NO LTR ENTIRE DOCUMENT FILED IN BINDER

PRELIMINARY

→ D. BROOKS C.A.

YUCCA MOUNTAIN PROJECT

A SUMMARY OF GEOHEMISTRY SUPPORT ACTIVITIES

OCTOBER 1989 - SEPTEMBER 1990

BY

MIFFLIN & ASSOCIATES
LAS VEGAS, NV

SUBMITTED TO:

STATE OF NEVADA
AGENCY FOR NUCLEAR PROJECTS/
NUCLEAR WASTE PROJECT OFFICE
CARSON CITY, NV

FEBRUARY, 1991

delete all distribution except: CF, PDR, LPDR & NWDOCS

ADD: Charlotte Abrams Encl. 1

102 WM-11 NH03 0/1

Mifflin & Associates, Inc.
2700 East Sunset Road, Suite C25
Las Vegas, Nevada 89120
702/798-0402 & 3026

STATUS REPORT:
Geochemistry Program
Yucca Mountain
Proposed High-Level Nuclear Waste Repository

M. E. Morgenstein and D. L. Shettel, Jr.
Geochemistry / Mineralogy Program Manager and Co-Manager

07 February 1991

General

The geochemistry program is comprised of a total of ten (10) studies relating to licensing issues dealing with repository performance. Seven of these studies were active at the end of the contracting period.

During this contract period MAI Staff, Drs. Morgenstein, Shettel, and Burns attended DOE and NWTRB meetings that dealt with geochemical concerns. In addition various reports and publications were completed dealing with the host of issues outlined in this report. Copies of the more significant publications are appended to this report.

Issues and Studies

1. Authigenic mineral sorption behavior at standard geothermal temperatures in the presence of radionuclide proxies. These studies are ongoing at Massachusetts Institute of Technology (MIT) under the direction of Professor R. Burns.

2. Disturbed zone boundary. These studies are ongoing under the direction of Dr. D. L. Shettel, Jr.

3. Dissolved gas exchange into zeolite structure. These studies were active at the end of the contract period under the direction of Prof. J. C. Rucklidge at the University of Toronto.

4. Mass transport in a thermal gradient. These studies were active at the end of contract period under the direction of Professor J. D. Rimstidt at the Virginia Polytechnic Institute and State University.

5. Desert varnish texture and geochemistry. These studies were active at the end of the contract period under the direction of Senior Professor D. H. Krinsley at Arizona State University.

6. Soil carbonate, opal genesis, and fracture fillings. These studies were active at the end of the contract period under the direction of Dr. Jay Quade (soil carbonate) and Dr. M. Morgenstein (opal).

7. Zeolite crystal chemistry at super-cage exchange sites. These studies are ongoing under the direction of Dr. J. Smyth at the University of Colorado.

8. Thermal stabilities of zeolites, clays and oxyhydroxides. No work was being performed during the contract period. Previously, work was being performed at MIT under the codirection of Drs. R. Burns and T. Bowers.

9. Thermal and chemical stability of volcanic glass, authigenic mineral production and heat of

crystallization. No work was performed during the contract period. Previously, work was being performed by Dr. R. Burns and Dr.. M. Morgenstein.

10. Vadose zone water geochemistry as deduced from authigenic minerals. No site specific work was being performed, but laboratory techniques were being developed at the University of Toronto by Dr. J.C. Rucklidge.

Project Status

1. *Authigenic mineral sorption behavior at standard geothermal temperature in the presence of radionuclide proxies (R. Burns).*

This project was funded through 30 September 1990. At the onset of the State of Nevada geochemical program, it was recognized that in order for any sorption credit to be taken at the Yucca Mountain site, a complete understanding of sorption behavior of individual sorbing minerals must be acquired. It was evident then, as it is now, that the DOE program does not adequately attempt to acquire these data. The DOE sorption program has started pure mineral sorption studies but these are bath-type experiments that employ crushed minerals rather than single crystals. We anticipate that the DOE experiments do not depict real world mineral behavior and therefore are of little utility in the site characterization process.

The most important mineral in the sorption studies is clinoptilolite and much of the open literature work on the sorption behavior of clinoptilolite has been accomplished by L. L. Ames, Jr. These studies have not looked at competing cations during the exchange process nor crystal face differences in sorption. Consequently, in order to complete our understanding of the behavior of clinoptilolite we have initiated oriented single crystal sorption studies using controlled temperature baths, SIMS and electron microprobe analysis experiments with major zeolites found at Yucca Mountain.

With respect to licensing, the following conclusions can be drawn from our studies:

1. The presence of Sr^{2+} and Ba^{2+} reduces Cs^{+} uptake in zeolites. Consequently, in the early stages of the repository, ^{90}Sr with a 28.8 year half-life would reduce the capacity of clinoptilolite to uptake ^{135}Cs which has a half-life of 3×10^{6} years and ^{137}Cs which has a half-life of 30.2 years. In the later stages of the repository, the uptake of long-lived ^{135} Cs would be compromised by daughter ^{137}Ba.

2. We have noted that there appears to be cation competition problems with mordenite where Ba and Sr do not enter the structure in the presence of Cs.

3. We find significant reduction of sorption along the (010) crystal faces (parallel to the b-axis) of clinoptilolite. Long-term experiments have been underway to ascertain if this property changes with time. We find no changes after two months of exposure. Consequently, we can conclude that zeolite crystal orientation within the pathways of "most likely transport" will have significant bearing on retardation credit that can be taken. It is not sufficient enough to just know that that there are zeolites present but their orientation must also be acquired before one can calculate sorption potential. This obviously complicates the sorption-retardation issue since the "most likely pathways" remain an enigma and are undefined. If one can not locate a specific pathway, one certainly can not take credit for sorption along that pathway.

4. Mordenite behaves similarly to clinoptilolite with respect to differential sorption behavior along different crystal faces. Mordenite seems to have a diminished sorption potential on the c-axis at its termination faces. We are not prepared to explain this observation as yet, especially since the super channels along this axis are larger (6.6 Å) then channels parallel to the other faces (2.8Å x 4.0Å).

5. Finally, we note that sorption behavior is greatly influenced by water chemistry (vadose water chemistry is an unknown for the site) as is zeolite stability itself.

When data collection from this program is completed, it may be used with site-specific mineral distribution and orientation information to model sorption retardation. We anticipate that there will be credit for matrix flow situations where transport itself is extremely slow. We do not feel at this time that sorption credit during fracture flow will be sufficient to affect licensing decisions, as we feel that there is an insufficient quantity of zeolites, clays, and oxyhydroxides in the fractures that will remain stable, have appropriate orientations, and will be exposed to transporting fluids to allow meaningful sorption reactions to occur for retardation of the key radionuclides during fracture flow.

Two of the more important publications produced during this study during the contract period were:

Burns, R.G.; Bowers, T.S.; Wood, V.J.; Blundy, J.D.; and Morgenstein, M.E. (1990). Reactivity of zeolites forming in vitric tuffs in the unsaturated zone at Yucca Mountain, Nevada. In: Nuclear Waste Isolation in the Unsaturated Zone (American Nuclear Society Publication), p.101-112.

Burns, R.G.; Wood, V.J.; and Morgenstein, M.E. (1991). Sorption of Cesium and Strontium by Zeolite Single Crystals. DOE Publication in press.

2. Disturbed Zone Boundary

This project is progressing slowly due to lack of direct funding. Two subcontractors to MAI were suspended last fall due to decreased overall funding levels. These were Dr. M.H. Reed at the University of Oregon, who was performing calculations of open and closed system boiling of Rainier Mesa vadose water, and Dr. K. Udell at the University of California at Berkeley, who was involved in a preliminary theoretical analysis of transport mechanisms in the vadose zone. Both of these researchers were engaged in useful work with respect to the issue of the location of the disturbed zone boundary. Results of their work are summarized in MAI's last yearly technical program summary.

The current activity in this project involves the conversion of public domain hydrogeochemical computer software to Apple Macintosh personal computers and the quality assuring of these codes for use in the Yucca Mountain program for the State of Nevada. To date three U.S.G.S. hydrogeochemical modeling codes have been converted and quality assured (BALANCE, WATEQ4F, and PHREEQE). Work is proceeding on the DOE/LLNL geochemical code package EQ3/6 which is to be used by the DOE for geochemical performance assessment in the near-field environment. These codes will become extremely useful once DOE or the State's contractors obtain complete chemical analyses of vadose zone waters.

The key issue regarding the disturbed zone is the position of the boundary as it is the starting point for ground-water travel time calculations. DOE's concept of a fixed distance boundary from the repository implies a longer flow path and thus travel time of radionuclides to the accessible environment than adherence to the original NRC definition of boundary placement at the edge of rock volumes in which processes are too complex to model. MAI's work to date suggests the boundary's location is indeed complex and may vary in distance depending on the importance of fracture versus matrix fluid transport in the vadose zone of the near-field environment.

Three of the reports referenced in this section were:

Shettel, D.L., Jr. (1990) Quality assurance of hydrogeochemical calculations performed by the FORTRAN computer program PHREEQE: for NWPO, 269p.

Shettel, D.L., Jr. (1990) Quality assurance of hydrogeochemical calculations performed by the FORTRAN computer program WATEQ4F: for NWPO, 264p.

Shettel, D.L., Jr. (1990)Quality assurance of hydrogeochemical calculations performed by the U.S.G.S.'s FORTRAN computer program BALANCE: for NWPO, 29p.

3. Dissolved Gas Exchange with Zeolite Structures.

This project is funded through the end of the academic year (May/June 1990) at the University of Toronto IsoTrace Laboratory under the direction of Prof. J. C. Rucklidge. Experimental work on the extraction and analysis of ^{14}C in CO_2 dissolved in the supercage water of zeolites was completed last fall. Results of this work show that aqueous and/or gaseous CO_2 does indeed exchange with that in the zeolites and the extraction of CO_2 is temperature dependent. The high temperature fraction may be indicative of CO_2 closer to the time of formation of the mineral while lower temperature fractions are more related to recent environments. In-situ samples of zeolites are needed to test and fine-tune hypotheses developed during the experimental work To this end, a piece of core from DOE drillhole UE25A11 at 1629' was obtained and sent to Toronto. Opening and ^{129}I analysis of this waxed and wrapped core are awaiting additional funding to support another graduate student at the University of Toronto.

A Master's thesis was recently completed by Ms. Naomi Baba (1990) at the University of Toronto, Isotrace Laboratory and was partially funded by the State of Nevada. Iodiine extraction methods for various natural samples were tested by AMS analyses of ^{129}I for the purpose of understanding the ^{129}I distribution in various parts of the natural environment. Types of samples analyzed included marine biological specimens, geological samples from the K-T (Cretaceous-Tertiary) boundary, iodine-rich brines from Japan, and a shallow groundwater sample with low I content. A conclusion of this study was that from analyses of marine organisms entry of man-made ^{129}I increased significantly in the marine environment after 1945. The $^{129}I/^{127}I$ post-bomb ratio has become one to two orders of magnitude greater than the pre-bomb ratio in marine organisms. Only one iodine analysis was attempted on the shallow groundwater sample. Due to low total iodine concentration, the low $^{129}I/^{127}I$ ratio of the sample, a high AMS background, and the possibility of contamination, interpretation of the result was not possible. Clearly, more work is needed on analysis of groundwater samples for development of partition factors for iodine isotopes between water and single mineral crystals. Other possible uses include the development of environmental baseline for iodine concentrations in rocks and fluids surrounding Yucca Mountain which may aid detection of the breaching of nuclear waste canisters.

DOE is not to our knowledge pursuing any research of this type. These methods currently under development at Toronto may complement and eventually supplement standard hydrogeologic observations (water sampling and moisture monitoring) regarding an understanding of fracture flow in the vadose zone.

The characterization issues involved are:

- Development of analytical (A.M.S.) techniques to measure ^{13}C and ^{129}I in single crystals.
- Determine whether techniques can distinguish between liquid and vapor flow.
- Determine whether authigenic zeolites in fractures and matrix can be distinguished between with respect to exposure to relatively "recent" waters.

The significant publication for this section was:

Baba, N. (1990) A Survey of Iodine-129 in the Environment: Thesis for Master of Science, Isotrace Laboratory, University of Toronto, 45p.

4. Mass Transport in a Thermal Gradient.

Funding for this project will expire in May or June, 1990, as monies are used. Experiments with crushed tuff in vertical temperature gradient reactors have been completed with distilled water and an NaCl solution (same ionic strength as J-13 water) by Prof. J.D. Rimstidt and colleagues at V.P.I.S.U. The experiments are partially saturated with water, heated from below so that boiling occurs a few inches above the heater plate, and are maintained at atmospheric pressure to simulate the vadose zone at Yucca Mountain after emplacement of nuclear waste canisters. Results to date show that significant mass transport (geochemical differentiation) occurs in a thermal gradient under partially-saturated, vapor-dominated conditions. Dissolution and leaching, as evidenced by severe etch pitting of mineral grains, occur in the cooler, upper end of the vertical temperature gradiient experiment (VTGE) where water vapor is condensing. Amorphous silica and zeolites are precipitated lower in the rock column in the zone of boiling. These deposits are sufficient to cement the rock grains together and possibly have a self-sealing effect in the boiling zone. This sealed zone may result in a perched water layer of groundwater (above the repository) that may later invade the repository after the thermal pulse or if any fractures develop during cooling. The general behavior of this experimental system and the compositional variations of the solution are apparently independent of the starting tuff (glassy or nonlithophysal) and appear unrelated to variation of the starting solution (ranging from distilled-deionized to synthetic J-13 waters). This results from the rock buffering the solution composition due to the large mineral surface area relative to the solution mass. The results demonstrate that extremely nonequilibrium conditions prevail throughout the reactor experiment and that significant variations in solution chemistry most likely result from localized flow patterns of liquid and vapor in the reactor.

Experiments were planned (before funding expired) utilizing an artificially fractured core in the middle of the column to simulate a fracture environment. Future funding levels may permit a continuation of these experiments.

The results of these preliminary experiments affect licensing issues as follows:

- With respect to the boundary of the disturbed zone, will dissolution of host rock significantly extend the boundary as defined by the NRC?
- How significant will dissolution be as a result of refluxing of aqueous fluids that will occur during the thermal pulse associated with the heat generated by the emplaced nuclear waste?
- Will dissolution of the host rock impact the post closure integrity of the repository with respect to release of radionuclides to the accessible environment?

Additional work in both the laboratory and field will be necessary to satisfy these concerns because the results of these preliminary experiments show that there are potential problems in the near-field environment.

Significant publications and reports for this section include:

Rimstidt, J.D., W.D. Newcomb, and D.L. Shettel, Jr., 1989, A vertical thermal gradient experiment to simulate conditions in vapor dominated geothermal systems, epithermal gold deposits, and high

level radioactive waste repositories in unsaturated media (abstract submitted to International Water-Rock Conference, Malvern, England).

Rimstidt, J.D., and M.A. Williamson (1991) Vertical Thermal Gradient Experiments Results: A Report to Mifflin & Associates, Inc. [for NWPO], 81p.

5. Desert Varnish Textures and Geochemistry (D. H. Krinsley).

This project is funded through 30 September 1990. The DOE is utilizing desert varnish cation ratio dating at Yucca Mountain for a fairly large variety of research activities. Cation-ratio dating is based upon simple (?) geochemical reactions (A + B = C) that do not necessarily have an adequate basis of understanding. Consequently, this research program was initiated to ascertain if MAI could validate the technique and utilize the method for determining ages of soil geochemical reactions that were observed during volcanic glass studies at Yucca Mountain. Consequently, textural and geochemical properties of desert varnish have been studied from various global locations. We have tentatively concluded that we are unable to utilize the method to obtain ages for the following reasons:

1. Diagenetic reactions occurring as ferromanganiferous remobilization have masked and turbated stratigraphic control within desert varnish samples. Geochemical analyses therefore do not correlate with microstratigraphy within the sample.

2. Analytical techniques previously employed by students of desert varnish dating have not utilized the best techniques to obtain geochemical information. Cation ratios used were therefore compromised by unknown quantities of Ti.

3. Textural modification to varnish during diagenesis provide assorted conduits for liquid transfer within the sample. These pathways are non-uniform between samples therefore there are major differences in porosity among samples. These conduits probably effect the cation ratios themselves.

4. The role(s) of biological transfer (fixation) of iron and manganese oxyhydroxides are not understood and apparently varies within discrete samples of varnish and among populations of different samples.

5. The role of organic acids on the geochemical properties of the varnish is not understood.

6. The geochemical interaction of the rock substrate and the varnish is not understood.

A significant publication resulting from the efforts of this study is:

Krinsley, D.H.; Dorn, R.I.; and Anderson, S.W. (1990). Factors That Interfere with the Age Determination of Rock Varnish. Physical Geography, 11,2, pp. 97-119.

6. Soil Carbonate, Opal Genesis, and Fracture Fillings.

The focus of this project has been on the genesis of Trench 14 features and similar features (sand ramps, Trench 17, Trench 8, and Trench 1 deposits). Samples of soil-generated opal were studied by Burns, Blundy, and Morgenstein to establish authigenic mineralization in surficial desert soils at Yucca Mountain and to use these information for analogue comparative reactions with Trench 14 deposits and deep-seated fracture fillings obtained from cores taken from within Yucca Mountain. Quade ran stable isotopes on Trench 14 carbonates to establish carbonate genesis data and found the fracture fillings to be

of meteoric/soil origin. The conclusive evidence established by Quade suggests that these deposits are important with respect to paleoclimate studies as they are presumably indicative of wetter climatic periods.

Higher temperature minerals such as druzy quartz are probably not related to the soil zone processes of carbonate precipitation. These minerals are associated with breccia cementation within the wall rock of the fracture zones. We presume at this point in time that earlier periods of tectonic activity provided mineralization at higher than ambient thermal conditions and that at these periods it is possible that ore mineralization occurred (as attested by trace element geochemistry of these zones).

Consequently, two issues remain untested by the DOE program.

a. Ore mineralization associated with fracture fillings and wall rock authigenic mineralization.

b. Past climate issues relative to the genesis of carbonate/opal infilling of fracture/fault systems.

MAI has not been addressing the first issue; however, the second issue remains part of our concern. The first stage in the development of pertinent information concerning past climate is to establish the period(s) of time of carbonate and opal fracture filling deposition. This must be accomplished in an extremely detailed fashion because it is probable that carbonate deposition is still ongoing, and the a full range in time occurs with respect to the genesis of these deposits. Consequently, nonstable isotope geochemistry must be combined with stable isotope analysis for the same samples to resolve age and climatic conditions.

A significant publication resulting from the efforts of the study is:

Quade, T. and T.E. Cerling. (1990). Staable Isotopic Evidence for a Pedogenic Origin of Carrbonates in Trench 14 near Yucca Mountain, Nevada. Science, V250, pp.1549-1552.

7. Zeolite Crystal Chemistry at Super-cage Exchange Sites.

This program is primarily concerned with resolving the structure of zeolite minerals. Much work was done by J. Kirkpatrick using magic-angle techniques. As funding did not permit the continuation of these activities, structural resolution studies have continued at a lesser level by J. Smyth. These data are important in resolving the sorption/desorption behavior of clinoptilolite and mordenite. Work has progressed using clinoptilolite. We anticipate several publications will be forthcoming. Much work is needed; however, prior to obtaining the necessary information which will resolve the structural/chemical behavior of the zeolites during sorption reactions. These data will allow us to develop a theoretical approach towards sorption which will provide data on mineral stability and super-cage attachment sites for various radionuclides. These data will assist in our own modeling efforts with respect to obtaining data on sorption credit.

8. Thermal Stability of Zeolites, Clays, and Oxyhydroxides.

In addition to actual laboratory measurements, done by J. Kirkpatrick, thermodynamic data have been acquired by T. Bowers, and R. Burns relative to the stability fields of the major zeolites at Yucca Mountain. We find that silica and aluminum activity are important controlling parameters for clinoptilolite stability. Stability is also related to cation substitution in the super-cage sites.

A significant drawback in our studies has been the absence of vadose zone water chemistry. As the chemical composition of vadose water is determinative with respect to zeolite stability calculations, these information must be collected by the DOE program if site characterization is to proceed in any deterministic level. In particular, analytical data with respect to the key parameters of silica, alumina, potassium, sodium, and calcium must be acquired for matrix and fracture-flow vadose liquids. We anticipate significant chemical differences between fracture-flow and matrix flow vadose zone waters.

In addition to these information a comprehensive program needs to be established for the acquisition of site-specific data which will establish the thermal conductivity of the host rocks at the proposed repository. As thermal conductivity is certainly related to moisture content (probably more so than mineral content) these information need to be collected. We find that a function of the initial thermal regime is moisture migration away from the repository. This will greatly affect the thermal conductivity of the host rock so that as time proceeds the temperature of the host rock thermal envelope will be significantly higher than anticipated. These considerations will certainly affect sorptive mineral stabilities (zeolites and clays).

To our knowledge there has been no activity on the thermal stability of oxyhydroxides and certainly not much with respect to their sorption capacity.

A significant publication resulting from the efforts of this study is:

Bowers, T.S. and R.G. Burns. (1990). Activity diagrams for clinoptilolite: Susceptibility of this zeolite to further diagenetic reactions. American Mineralogist, V.75, pp 601-619.

9. Thermal and Chemical Stability of Volcanic Glass, Authigenic Mineral Production and Heat of Crystallization.

This project is not active due to funding constraints. Previous work on the project has produced data that indicates that:

a. Authigenic mineralization (zeolites, clay, and opal formation) occurs in the soil zone of Yucca Mountain and is similar to mineralogy and mineral associations found at depth. The age of neomineral formation is presently unknown. Surface water reactions with volcanic glass is responsible in part for the neomineralization.

b. Heat of crystallization as a function of hydration of volcanic glass could play an important role in effecting the thermal envelope.

c. Volcanic glass instability at Yucca Mountain is a function of temperature, water availability, and water chemistry (alkali concentrations).

Volcanic glass is potentially one of the most reactive components in Yucca Mountain associated with the proposed high-level nuclear waste repository. Most volcanic glass is presently hydrated and if heated above ambience should lose this water of hydration. We anticipate alkali exchange during this reaction phase; consequently, the chemistry of released waters would be corrosive with respect to natural and man-made barriers. Little study has been offered by the DOE program with respect to volcanic glass stability and reactivity in the Yucca Mountain environment. These parameters will probably affect sorption potential, whole rock strength, vadose water chemistry, and the thermal envelope.

A large portion of the State of Nevada geochemical program in the future must concern itself with these issues as they will become key concerns during site licensing.

10. Vadose Zone Water Geochemistry as Deduced from Authigenic Minerals.

This project was partially funded through the end of University of Toronto's academic year (May/June 1990) The project is only partially funded because the bulk of funds supplied to the IsoTrace Laboratory have been utilized on the third study - dissolved gas exchange with zeolite structures. To date, Toronto has only performed a theoretical analysis of the feasibility of determining the tritium concentration in the small amounts of water trapped in the super cage of zeolites by the tandetron (accelerator mass spectroscopy). Results of this analysis suggest that the measurement of tritium from small amounts of water is feasible, but about an additional $10,000 would be necessary for machine time to perfect the set-up and extraction techniques.

The idea for looking at tritium in zeolites is to determine if zeolites lining fractures can be used to determine the passage of the most recent transient aqueous flows in adjoining fractures. Detection of tritium in loosely-bound zeolitic waters might indicate fracture flow of water since above-ground nuclear testing began 35-40 years ago. Future work beyond tritium determinations was to involve stable oxygen and hydrogen isotopes of supercage water in zeolites as well as the relationship that might exist between the chemical composition of supercage zeolitic waters and free aqueous solutions surrounding the minerals. The underlying rationale for pursuing these studies was and still is the lack of vadose-zone water samples in the DOE technical program.

Summary

The geochemistry program is designed to provide detailed information needed for assessing models developed by the DOE program concerning the geochemical conditions at the Yucca Mountain site. These information are also needed to assess performance and in part design issues that are being studied by the DOE.

Since the main thrust of the geochemistry program is to provide data needed to evaluate the DOE site characterization activities related to licensing and performance assessment, the geochemistry program strives towards an understanding of how the natural geochemical system operates and how imposed repository conditions will modify that system. Consequently, given an understanding of the basic principals governing the active and potential geochemical reactions, we will be in a strong position to assess the DOE site characterization effort.

Some of the more important issues which require resolution prior to licensing are:

1. Site-specific configuration of the most likely pathways of transport in matrix and fracture network.

2. An agreement on the confines of the disturbed zone under site-specific conditions.

3. Site-specific thermal perturbations imposed upon the natural system by repository loading, and reimposed upon the modified rock system by changes in vadose moisture, changes in mineralogy, changes in thermal conductivity, thermal ponding, and authigenic heats of reaction.

4. Sorption behavior on site-specific transport pathways documented by sorption theory, laboratory data collection and in-situ field experimentation, including real data on vadose water chemistry variations, mineral stability and competing reactions. Within these confines, it is imperative that material ion concentrations such as C_s be investigated (both as aqueous and within solid phases) to ascertain the level of potential sorption interference with repository induced radionuclide transport.

5. Gas-phase transport within the vadose zone to the accessible environment.

6. Thermal, mechanical, and chemical stability of canisters, seals, plugs, liners, and other man-made materials. Evolved vadose-zone water chemistry and sorption geochemistry need to be revised based upon introduced foreign materials.

7. Authigenic mineral distributions, concentrations, and crystallographic orientations and exposures within specific transport pathways. Minerals studied must have physical access to transporting fluids.

8. Mass transport in a thermal gradient in the vadose zone of Yucca Mountain.

9. Ages of authigenic mineralization in relation to past climatic events, as determined by stable isotope analyses among other techniques.

10. Spatial geochemical data collection of sufficient magnitude to geostatistically characterize existing conditions between the central repository and the accessible environment along liquid/vapor flow pathways.

Our studies have been focused towards obtaining sufficient data to address these issues. Nevertheless, the Department of Energy (DOE) has the responsibility and statutory obligation to collect the site-specific raw data.

SORPTION OF CESIUM AND STRONTIUM BY ZEOLITE SINGLE CRYSTALS

Roger G. Burns,[1] Valerie M. Wood,[1] and Maury E. Morgenstein[2]

[1] Department of Earth, Atmospheric and Planetary Sciences,
Massachusetts Institute of Technology, Cambridge, Massachusetts 02139,
(617) 253-1906

[2] Mifflin & Associates, Inc.,
1000 Nevada Highway, Boulder City, Nevada 89005
(702) 294-3065

ABSTRACT

The aspect ratios of crystals of platey clinoptilolite and fibrous mordenite observed in mineral assemblages coating fractures through tuffs at Yucca Mountain, Nevada, influence the sorption properties of these two zeolites. The crystallographic dependencies of cation exchange reactions have been demonstrated in clinoptilolite by reacting CsCl with oriented single crystals mounted on (100), (010), (001) and (101) faces. Competing cation exchange reactions involving Cs^+, Sr^{2+} and Ba^{2+}, as well as Cs^+ in NaCl or $NaHCO_3$ solutions, were performed on the oriented zeolite crystals. Reactions were carried out at 60 °C for 1 to 8 weeks in a shaking water bath with dissolved metal chloride solutions ranging in concentrations from 1*M* to $10^{-4}M$. Electron microprobe analyses were performed on the surfaces of the reacted zeolite crystals.

In clinoptilolite, cation exchange is initially retarded on (010) faces which are normal to the one direction (parallel to the *b*-axis) along which channels do not exist in the clinoptilolite structure. This orientation effect was particularly severe for Sr, concentrations of which on (010) faces remained 90% lower than values measured on other crystal faces even when reaction times exceeded 2 months. In competition with Sr and Ba, the uptake of Cs into clinoptilolite was lowered significantly (and vice versa for Ba and Sr), particularly in the presence of Ba. The addition of 1*M* NaCl did not significantly affect the relative concentrations of these competing cations in reacted zeolite crystals. In $NaHCO_3$ solutions, however, the Cs uptake was lowered significantly.

Although clinoptilolite has a very high selectivity for Cs^+ compared to other cations, competition with Sr^{2+} and Ba^{2+} reduces the concentration of Cs^+ exchanged into this zeolite. As a result, in the early stages of an underground repository for radioactive waste, ^{90}Sr ($t_{1/2}$ = 28.8 yr $\rightarrow$ ^{90}Y) released to groundwater could reduce the capacity of clinoptilolite to immobilize dissolved ^{137}Cs ($t_{1/2}$ = 30.2 yr $\rightarrow$ ^{137}Ba) and ^{135}Cs ($t_{1/2} = 3 \times 10^6$ yr $\rightarrow$ ^{135}Ba), while absorption of Sr^{2+} itself might be impaired by radiogenic Cs and its daughter Ba isotopes. At later stages, however, the entry of long-lived ^{135}Cs into the zeolite might be compromized by daughter ^{137}Ba inherited from ^{137}Cs.

INTRODUCTION

Clinoptilolite is well-known to possess high sorption selectivities and capacities for Cs and Sr, following research performed mainly in the 1960's by Ames and other workers (e.g. Ames, 1959-1965; Howery and Thomas, 1965; Barrer and Makki, 1966; Chelishchev et al., 1974). These studies involved measurements of radionuclides either absorbed by powdered zeolites in an exchange column or removed from spiked aqueous solutions emerging from the ion exchange column. Little attention was paid in those experiments to the chemical composition,

crystallographic orientation or homogeneity of individual zeolite crystals. Most of the measurements centered on clinoptilolite in zeolitized vitric tuff from Hector, California (Ames et al., 1958), composed of microcrystalline lamellae with diameters around 10 microns (Mumpton and Ormsby, 1978) and containing about 15% unaltered glass, quartz and feldspar impurities. Ames used aqueous salt solutions labelled initially with ^{137}Cs (Ames, 1960, 1961), but he later changed to ^{134}Cs (Ames, 1962a,b,c; 1963, 1964, 1965) due to interference by daughter ^{137}Ba. Ames (1960) showed that particle sizes of cemented aggregates of the Hector clinoptilolite crystallites affected the Cs capacity, which increased significantly when clumps were smaller than 1 mm. In the presence of competing alkali and alkaline earth cations, usually as 1*M* salt solutions containing $10^{-2}M$ CsCl, clinoptilolite was shown to have a high selectivity for Cs, leading to the replacement series at 25 °C

$$Cs^+ > Rb^+ > K^+ > NH_4^+ > Ba^{2+} \geq Sr^{2+} > Ca^{2+} > Na^+ > Mg^{2+} = Li^+.$$

For mordenite, the selectivity order was found to be (Ames, 1961)

$$Cs^+ > K^+ > Na^+ > Ba^{2+} > Sr^{2+} > Ca^{2+} > Li^+ = Mg^{2+}.$$

These selectivities are generally assumed to apply to cation exchange reactions at elevated temperatures, too. Cesium capacities of clinoptilolite decreased with decreasing concentrations of CsCl, and were further lowered by increasing concentrations of NaCl. Changing the sodium salt from chloride to SO_4^{2-} or NO_3^- did not influence the Cs capacity, but the comment was made (Ames, 1964) without specification that dissolved carbonates might influence cation exchange equilibria. Reactions performed at elevated temperatures decreased the Cs capacity of clinoptilolite, the concentration dropping by about one-third between 25 °C and 60 °C. Competing reactions between Cs and Rb, K, Ba, Sr, etc., were not conducted at elevated temperatures, however. Kinetic studies of Cs^+ exchange reactions (Ames, 1962a,b) yielded diffusion coefficients which increased with temperature, decreased with dilution, and varied inversely with particle size of the clinoptilolite. The diffusion rate data indicate that in 1-day experiments at 60 °C, Cs would diffuse ~90 microns and Sr ~9 microns into clinoptilolite particles. The Cs capacity of clinoptilolite was found (Ames, 1964) to be influenced by compositional differences, being smaller in the more silicic Hector clinoptilolite than in a calcic clinoptilolite from the John Day Formation, Oregon, having a lower Si/Al ratio. Ames (1960, p. 699) also commented that "the exchange properties of heulandite and clinoptilolite are quite dissimilar", but provided no data in support of this statement.

Note that in these early studies, Ames and subsequent researchers did not (1) measure cation exchange reactions in single crystals; (2) perform reactions in HCO_3^--bearing solutions; (3) examine temperature variations of competing cation exchange reactions; (4) carryout competing exchange reactions involving binary Cs-Sr, Cs-Ba and Sr-Ba systems or the ternary Cs-Sr-Ba system at elevated temperatures; or (5) determine orders of cation selectivities for zeolites at elevated temperatures.

Observations of euhedral calcic clinoptilolite (and heulandite) crystals with prominent (010) faces coating fractures in a drill core through Yucca Mountain (Carlos, 1985) led to our investigations of the crystallographic dependencies of cation exchange reactions into single crystals of clinoptilolite (Burns et al., 1990). The research was motivated by the fact that large continous open channels running parallel to the *c*- and *a*- axes in the clinoptilolite crystal structure (Koyama and Takeuchi, 1977; Smyth et al., 1990) do not exist along the *b*-axis, raising the possibility that cations entering and leaving the dominant (010) crystal faces of clinoptilolite might be retarded. Also, because fracture-flow water through bedded tuff sequences such as the deposits at Yucca Mountain appears to be relatively enriched in sodium bicarbonate (White et al., 1980; Ogard and Kerrisk, 1984; Kerrisk, 1987) and because cation exchange reactions had not been reported in such solutions, some of the single crystal cation exchange reactions with CsCl were performed in $NaHCO_3$ solutions. In addition, some exchange reactions between competing cations were studied, the rationale behind these experiments being that a mixture of radionuclides, including ^{137}Cs, ^{135}Cs and ^{90}Sr plus daughter Ba isotopes present in fission products, will compete with one another for sorption sites in zeolites should they be released into heated groundater percolating through buried radioactive waste.

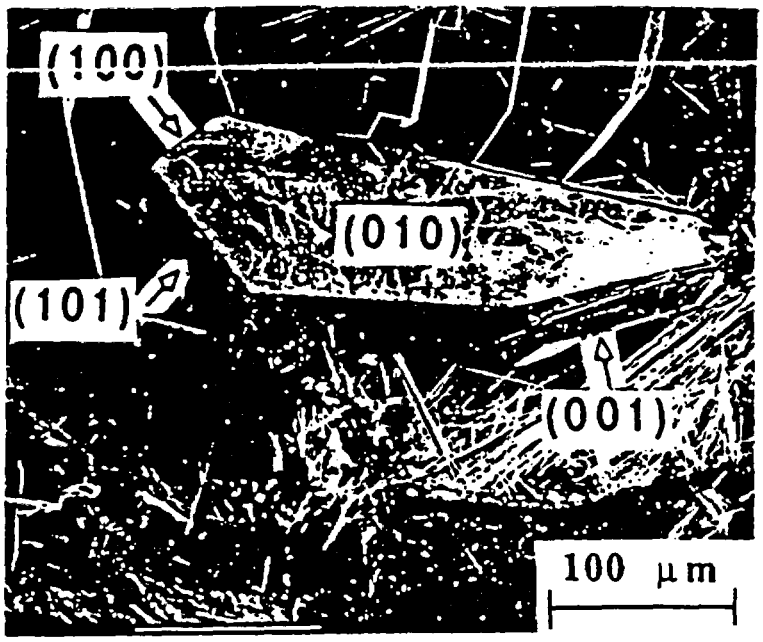

Figure 1. Clinoptilolite crystals from Succor Creek, Malheur Co., Oregon used in the cation exchange experiments. Polished mounts were made of crystals oriented on (100), (101), (010) and (001) faces.

EXPERIMENTAL DETAILS

Single crystals of clinoptilolite from Succor Creek, Malheur County, Oregon, oriented in polished mounts were used in most of the cation exchange reactions. The characteristic euhedral coffin-shaped habits of this clinoptilolite illustrated in Figure 1 enabled individual crystals with diameters between 1 and 2 mm to be mounted onto (100), (101), (010) and (001) faces. The chemical composition of the Succor Creek clinoptilolite, which is represented on the ternary diagram shown in Figure 2, more closely resembles those of calcic clinoptilolites occurring in fractures near the proposed repository horizon in the Topopah Spring Member tuff at Yucca Mountain (Levy, 1984; Carlos, 1985; Broxton, 1987; Broxton et al., 1986, 1987), than do other clinoptilolites used in previous cation exchange (Ames, 1959-65; Barrer and Makki, 1966) and crystallographic (Bish, 1984, 1988) measurements. The clinoptilolites were encapsulated in cold-setting epoxy cement in small brass cylinders. In each capsule, two or three crystals with masses ranging from 3 to 15 mg were mounted in the same orientation. The majority of the cation exchange measurements were carried out using crystals mounted on (010) faces, since these have the largest surface areas (Figure 1) and are more readily manipulated. Some exchange reactions were also carried out on mounted single crystals of a heulandite from Iceland and on polished clumps of microcrystalline clinoptilolites from Hector (California) and Castle Creek (Idaho) used in earlier studies (Ames, 1959-65; Bish, 1984, 1988). The specimens were polished, carbon-coated, and analysed first by electron microprobe. The carbon-coating was then removed by gentle rubbing with tissue paper before commencing the cation exchange reactions.

The cation exchange reactions were performed at 60 °C in a constant-temperature shaking water-bath for accumulated time periods ranging from 3 days to 2 months. Concentrations of dissolved chlorides of Cs, Sr, and/or Ba ranged from 1*M* to 10^{-4}*M*, and the cation exchange reactions were performed in the presence or absence of 1*M* $NaHCO_3$ or 1*M* NaCl. Each polished clinoptilolite mount was placed in a stoppered 50 ml flask with reactants (e.g. 20 ml of the metal

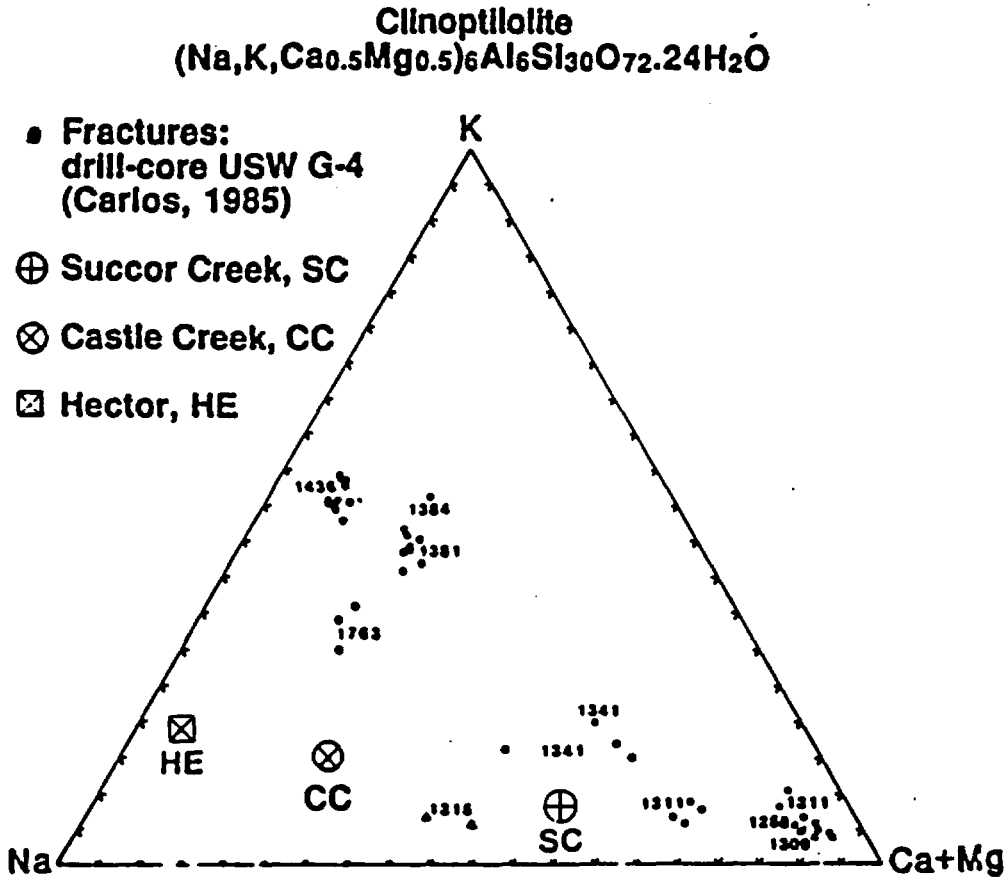

Figure 2. Triangular diagram showing the compositions of clinoptilolites used in the cation exchange experiments. Compositions of the Succor Creek (Oregon), Hector (California) and Castle Creek (Idaho) clinoptilolites are superimposed on analytical data for zeolites found in fractures in the unsaturated zone at Yucca Mountain (from Carlos, 1985).

chloride with or without added $NaHCO_3$ or NaCl solutions) and inserted into the shaking water-bath. After a specific reaction time-interval, flasks were removed from the bath and the crystal mounts washed several times with cold distilled water, dried at ambient temperatures, and carbon-coated prior to microprobe analyses. After completion of each set of microprobe analyses, the carbon coating the surfaces of the mounts was gently removed. The mounts were replaced in the stoppered flasks with fresh solutions and the cation exchange reactions allowed to continue for another increment of time.

Chemical compositions of the clinoptilolites were determined using a JEOL 733 Superprobe. Operating beam currents were 10 KeV and 5-10 nA with counting times of 20 seconds for all elements except Na, which was analysed first and counted for only 10 seconds. In attempts to further minimize loss of Na and zeolitic H_2O in the microprobe analyses, a defocussed beam approx. 10-20 microns in diameter was used to analyse the mounted Succor Creek clinoptilolite and heulandite crystals. Smaller beam diameters had to be used for the polished clumps of microcrystalline Hector and Castle Creek clinoptilolites, however, often resulting in low oxide totals for these zeolites. Criteria for satisfactory microprobe analyses were based on oxide totals exceeding 82% (since 24 H_2O molecules in ideal clinoptilolites corresponds to ~ 18 wt % water), constancy of Si/Al ratio, and the ratio $[\{(Na+K+Cs) + 0.5(Ca+Mg+Sr+Ba)\}/(Al+Fe)]$ lying in the range 0.9-1.2.

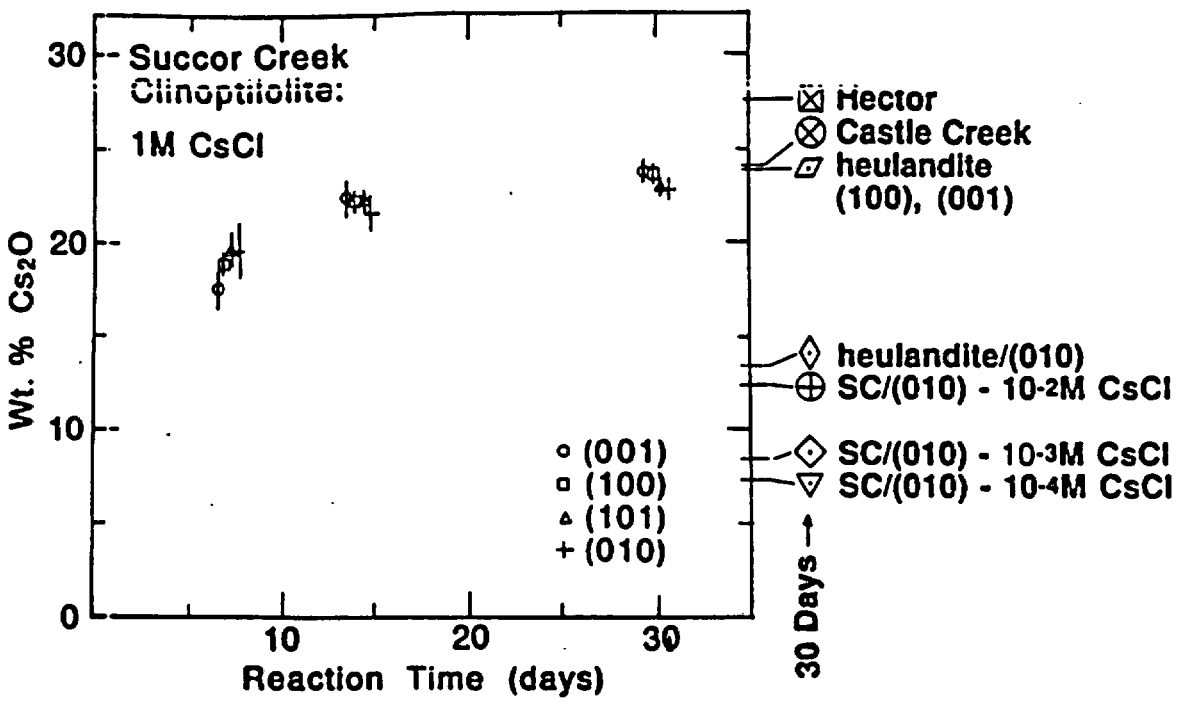

Figure 3. Cesium contents of oriented crystals of the Succor Creek clinoptilolite after reaction with 1*M* CsCl for increasing time periods. Inset on the right-hand axis are Cs_2O concentrations of other zeolites after 30-day reactions with CsCl solutions.

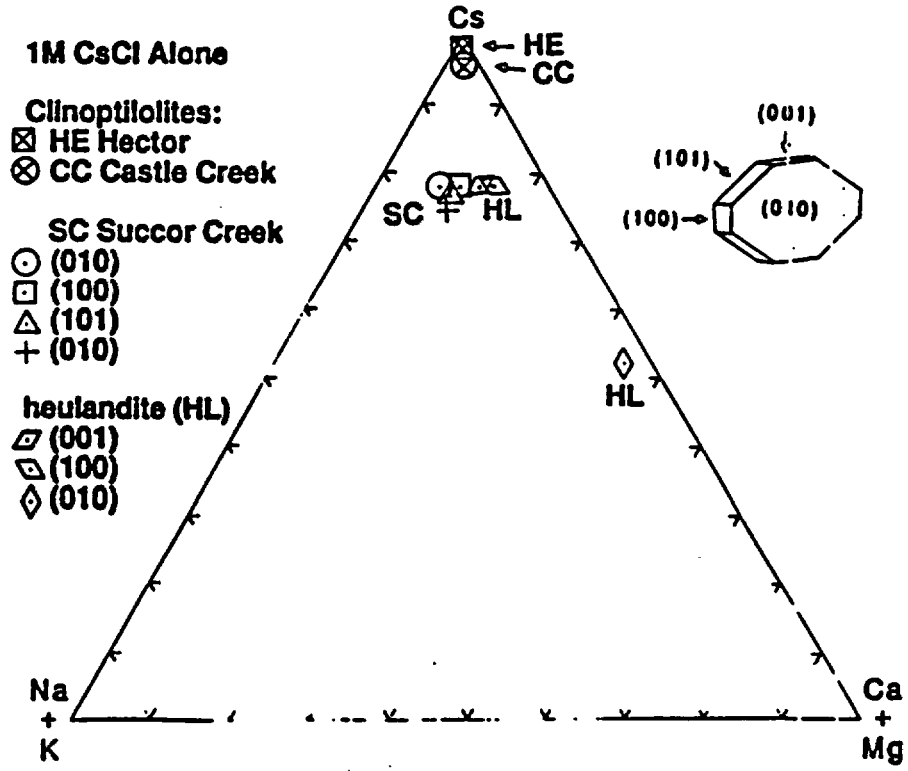

Figure 4. Triangular diagram showing the atom percentages of Cs present in the zeolites after 30-day reactions with 1*M* CsCl.

RESULTS

Reactions with CsCl Alone

Concentrations of cesium (expressed as weight % Cs_2O) entering the clinoptilolite crystals after reactions with solutions of CsCl alone are plotted in Figures 3, 4 and 5. In 30 day reactions with 1*M* CsCl, the clinoptilolites from Hector and Castle Creek became saturated with ~27.5 and ~24 % Cs_2O, respectively (Figure 3). The Succor Creek clinoptilolite crystals showed significant compositional zoning after reaction times of only 7 days which became less pronounced after 30 days when each crystal face acquired between 22 and 23 wt. % Cs_2O (Figure 3). Effects of crystal orientation on cesium uptake by the Succor Creek clinoptilolite were not always obvious in reactions involving relatively concentrated 1*M* CsCl solutions (Figure 3), in constrast to reactions involving 10^{-2}*M* CsCl described later. However, in heulandite there was a marked reduction of cesium concentration in the (010) face (~13 wt. % Cs_2O) compared to the (100) and (010) faces (~24 wt. % Cs_2O) (Figure 3).

The selectivity of heulandite and the clinoptilolites for cesium is demonstrated by the triangular diagrams illustrated in Figures 4 and 5 which show cation percentages of Cs plotted against (Na+K) and (Ca+Mg) cation percentages for the zeolites after reactions with CsCl solutions alone. Cesium replaced most of the cations in the Hector and Castle Creek clinoptilolite specimens with initially high (Na+K) contents (Figure 2). However, appreciable amounts of Ca^{2+} ions remained after Cs-exchange reactions with the more calcic Succor Creek clinoptilolite (Figure 4), particularly when dilute CsCl solutions were used (Figure 5). In heulandite, almost 45% of the Ca was still retained in the heulandite (010) face compared to ~10% Ca remaining in the heulandite (100) and (001) faces (Figure 4).

In reactions involving more dilute solutions, the Cs uptake into crystals of the Succor Creek clinoptilolite was reduced, and this is demonstrated in Figure 5. In 30 day reactions with 10^{-2}*M* CsCl, the (010) crystal faces acquired lower concentrations of Cs (~12.5 wt. % Cs_2O) and retained higher proportions of Ca than did the other three faces containing 17-19 wt. % Cs_2O (Figures 5 and 7a). The Cs uptake was further reduced in 30 day reactions with 10^{-3}*M* CsCl and 10^{-4}*M* CsCl solutions (Figures 3 and 5).

Reactions with CsCl in the Presence of $NaHCO_3$

The data plotted in Figures 6, 7 and 8 demonstrate the influence of sodium bicarbonate on the cesium exchange reactions. In the presence of 1*M* $NaHCO_3$, the Cs concentration acquired by each crystal face of the Succor Creek clinoptilolite was almost halfed compared to reactions performed in the absence of $NaHCO_3$ (compare Figures 5 & 6 and Figures 7a & 7b). For example, in reactions with 1*M* CsCl, the cesium content of the Succor Creek clinoptilolite dropped from ~23 wt. % Cs_2O (Figure 3) to ~13 wt. % Cs_2O in the presence of $NaHCO_3$. The triangular diagram illustrated in Figure 6 suggests that the reduced uptake of Cs into each crystal face was the result of sodium loading caused by the high concentration of dissolved $NaHCO_3$. However, in Cs-exchange reactions performed in 1*M* NaCl solutions, the Cs concentration of the (010) crystal faces reacted with 1*M* CsCl was significantly higher (i.e. 20.6 wt. % Cs_2O) than that resulting from Cs exchange in the presence of 1*M* $NaHCO_3$. This indicates that HCO_3^- ions may be responsible for retarding the entry of Cs into crystals of the Succor Creek clinoptilolite.

The crystallographic effects noted earlier for oriented crystals of heulandite (Figure 4) became significant in the Succor Creek clinoptilolite when Cs-exchange reactions were performed with 10^{-2}*M* CsCl solutions, particularly in 1*M* $NaHCO_3$. These trends are demonstrated in Figures 7 and 8. Again, compositional zoning was most pronounced in each crystal face after only 7-day reaction periods, but became less severe after 30-60 days. The data plotted in Figure 7a show that the cesium uptake by the (010) face is lowered relative to the other three crystal orientations. This orientation effect is even more pronounced in the presence of 1*M* $NaHCO_3$ (Figure 7b). The rate

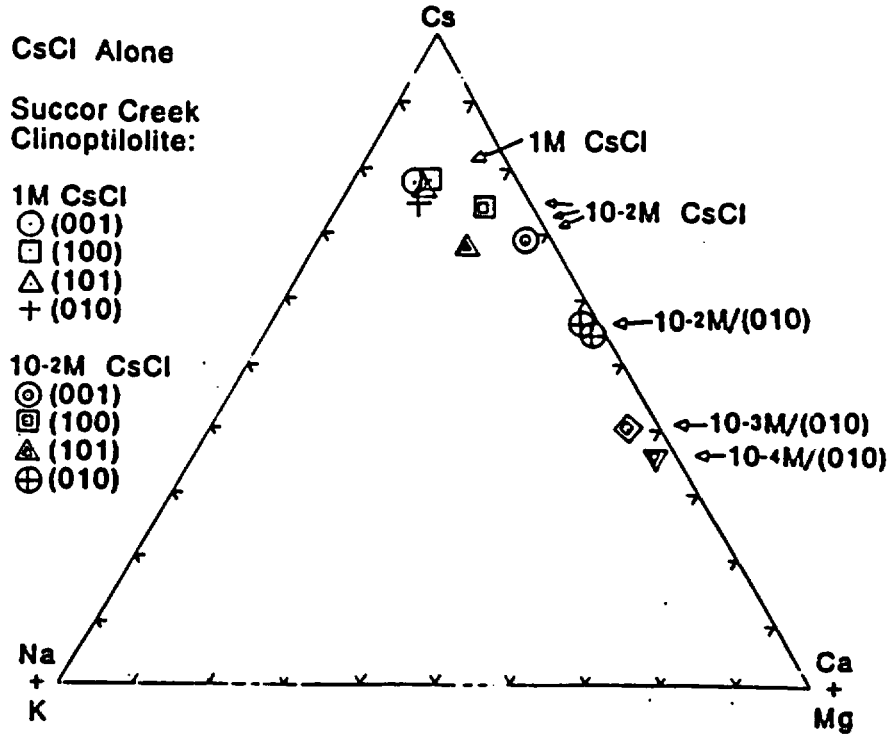

Figure 5. Atom percentages of Cs in oriented crystals of the Succor Creek clinoptilolite after 30-day exchange reactions with CsCl solutions alone.

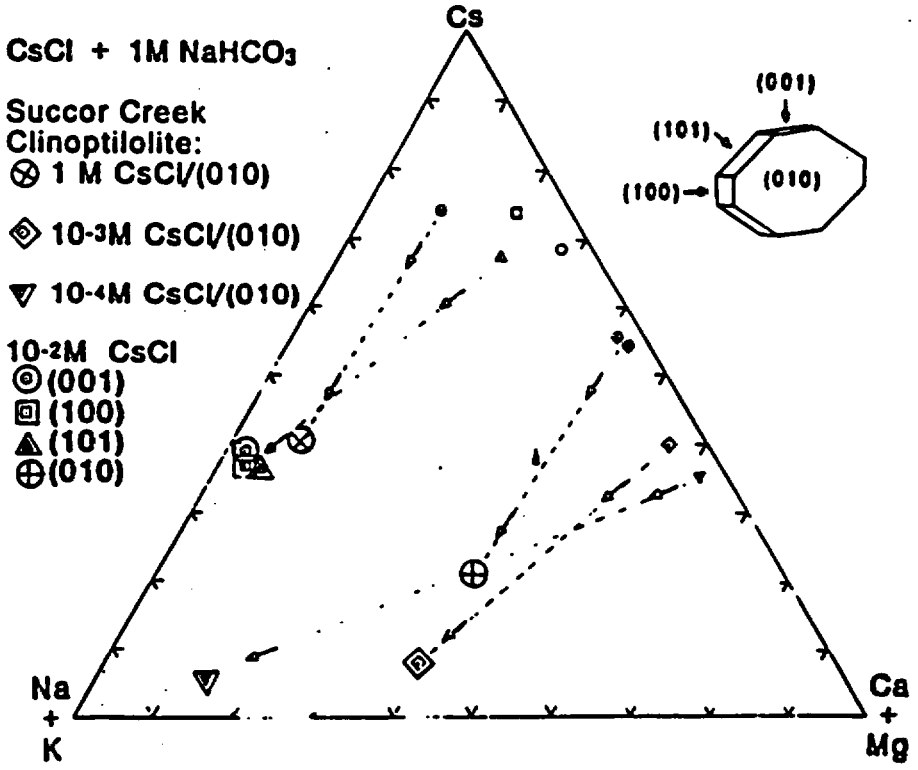

Figure 6. Cs atom percentages of oriented crystals of the Succor Creek clinoptilolite after reactions with different concentrations of CsCl in 1*M* $NaHCO_3$.

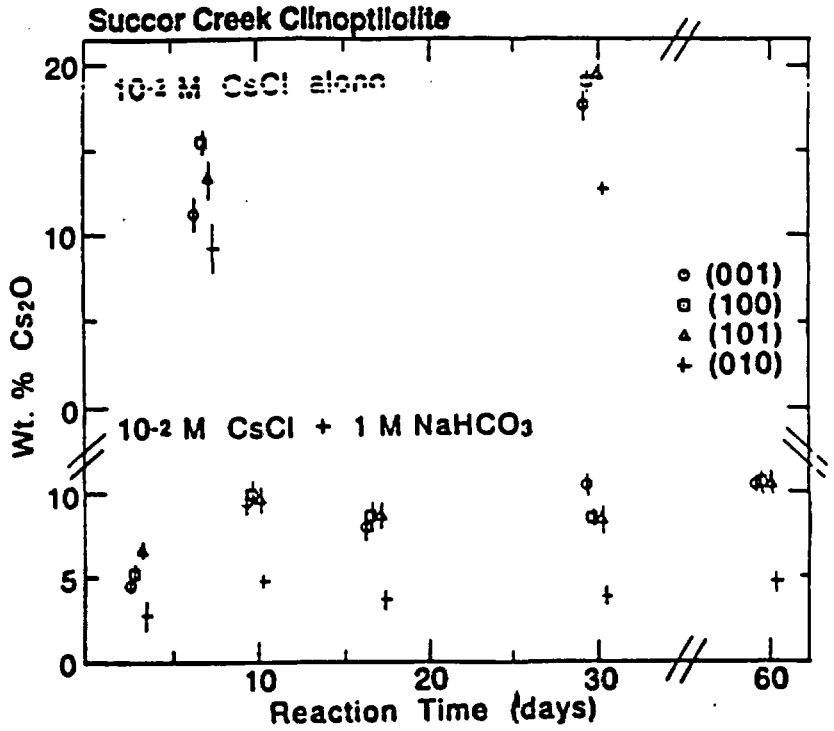

Figure 7. Cesium concentrations of oriented crystals of the Succor Creek clinoptilolite after reactions with $10^{-2}M$ CsCl (a) alone for 30 days and (b) in the presence of $1M$ $NaHCO_3$ for 60 days.

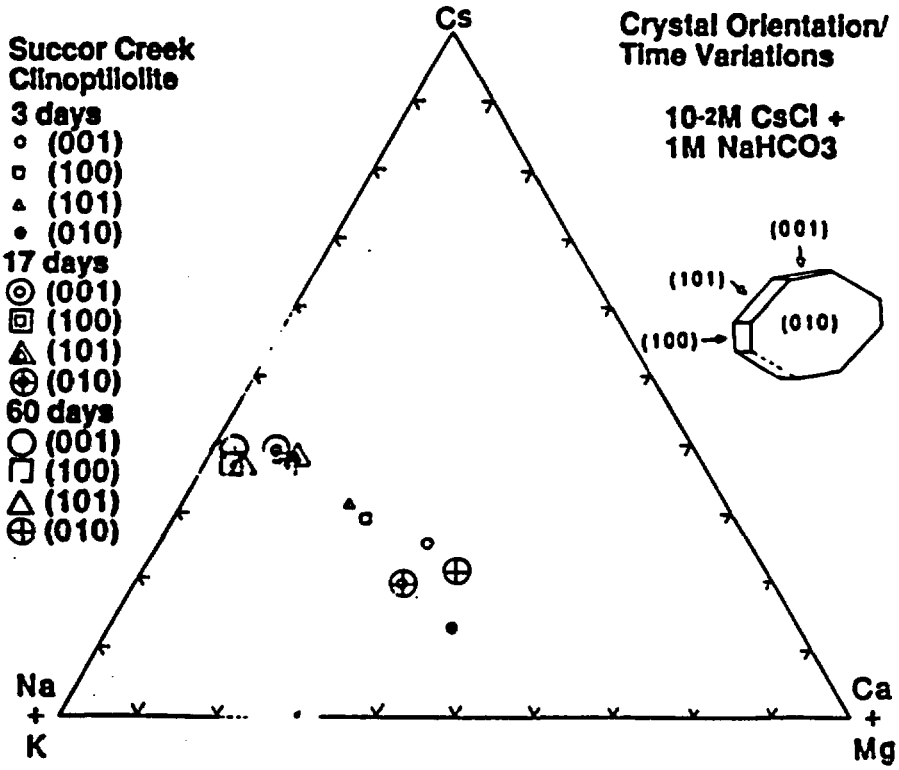

Figure 8. Temporal variations of Cs atom percentages of oriented crystals of the Succor Creek clinoptilolite after reactions with solutions of $10^{-2}M$ CsCl in $1M$ $NaHCO_3$.

of entry of Cs into the (010) face lags behind the Cs uptake of the other three crystal faces, which is demonstrated in Figure 8. It is strikingly apparent from Figures 7 and 8 that Cs is reluctant to enter the (010) face, particularly in sodium bicarbonate solutions.

Competing Exchange Reactions Involving Cs, Sr and Ba

In reactions between oriented crystals of the Succor Creek clinoptilolite and 1*M* $SrCl_2$ alone, the uptake of Sr after 30 days lags behind, and is drastically reduced, in the (010) face compared to the other three crystal faces. These effects are demonstrated in Figures 9 and 10a. Thus, only ~0.4 wt. % SrO was present in the (010) face after 30 days' reaction time, compared to 4-5 wt. % SrO in the other three crystal faces (Figure 10a).

In competing reactions between Cs and Sr in 1*M* chloride solutions involving (010) crystal faces of clinoptilolite, the Cs concentration was reduced from ~23 wt. % Cs_2O (Figure 3) to ~14.5 % Cs_2O in the presence of $SrCl_2$ (Figure 10a), while the SrO content was further reduced to ~0.3 wt % SrO on the (010) face (Figure 10a). In the presence of 1*M* $BaCl_2$, the Cs_2O content drops to ~13.5 wt. % Cs_2O while ~1.1 wt. % BaO enters the (010) face of the Succor Creek clinoptilolite (Figure 10a).

The microcrystalline Castle Creek clinoptilolite with a lower initial Ca content than the Succor Creek clinoptilolite accomodates higher concentrations of either Sr or Ba when in competition with Cs in reactions involving 1*M* solutions (Figure 10b). However, in more dilute solutions the concentration of Ba entering the Castle Creek clinoptilolite remains high in the presence of 10^{-2}M CsCl, whereas the Cs concentrations is drastically lowered in the presence of 10^{-2}*M* $BaCl_2$ (Figure 10b).

DISCUSSION

The results of the cation exchange experiments, which demonstrate that the uptake of Cs^+ and Sr^{2+} ions into clinoptilolite are crystallographic dependent, may be explained by the crystal structure illustrated in Figure 11 (Koyama and Takeuchi, 1977). Clinoptilolite has the basic zeolite structure consisting of a three-dimensional framework silicate in which all four oxygens of individual $(Si,Al)O_4$ tetrahedra are mutually shared to form secondary rings of corner-sharing tetrahedra (Gottardi and Galli, 1987). The complex 4- and 5-tetrahedron ring systems of clinoptilolite are arranged in sheet-like arrays parallel to (010) and are connected by relatively few oxygen bridges. As a result, clinoptilolite crystals display the characteristic platey or lamellar "coffin-shaped" habits with basal (010) cleavage shown in Figure 1. Linkages between the tetrahedral ring systems along the *c*-axis, as well as the *a*-axis, define cages that are open and form channels through the clinoptilolite structure. The channel systems in clinoptilolite consist of one set parallel to the *a*-axis formed by rings of 8 tetrahedra with free aperture dimensions of 4.4 x 5.5 Å (designated as the *C* channels by Koyama and Takeuchi, 1977). There are two sets of channels parallel to the *c*-axis formed by rings of 10 and 8 tetrahedra with corresponding free apertures of 4.4 x 7.2 Å and 4.4 x 4.4 Å (designated as the *A* and *B* channels, respectively). No such channels exist along the *b*-axis of clinoptilolite, however. The channels along the *a*- and *c*-axes are clearly wide enough to permit the entry of cations such as Cs^+ (diameter, d = 3.65Å), Ba^{2+} (d = 3.05 Å) and Sr^{2+} (d = 2.80 Å), the large ionic diameters of which also enable them to fit more snugly in the channels than smaller cations such as Na^+ and Ca^{2+}. In the clinoptilolite structure illustrated in Figure 11, Na^+ and Ca^{2+} occupy M(1) and M(2) positions, K^+ are located in M(3) positions and Mg^{2+} are situated in M(4) positions, and each cation is coordinated to several water molecules which are also located in the channels. Different site occupancies appear to exist in Cs-exchanged clinoptilolites, however (Smyth et al., 1990).

Smyth et al. (1990) reacted a natural clinoptilolite from Bend, Oregon, the initial composition of which contained comparable amounts of Ca^{2+}, Na^+ and K^+ ions, with 2*M* CsCl solution at 70 °C

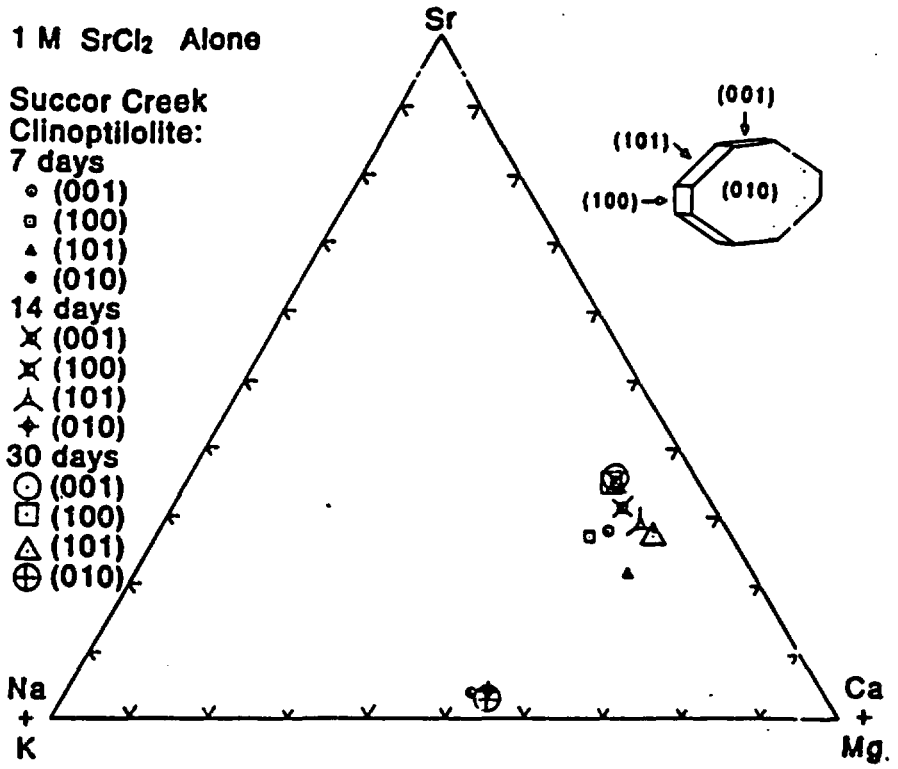

Figure 9. Temporal variations of Sr atom percentages of oriented crystals of the Succor Creek clinoptilolite after reactions with 1*M* $SrCl_2$ alone. Note the very low Sr content of the clinoptilolite (010) crystal face.

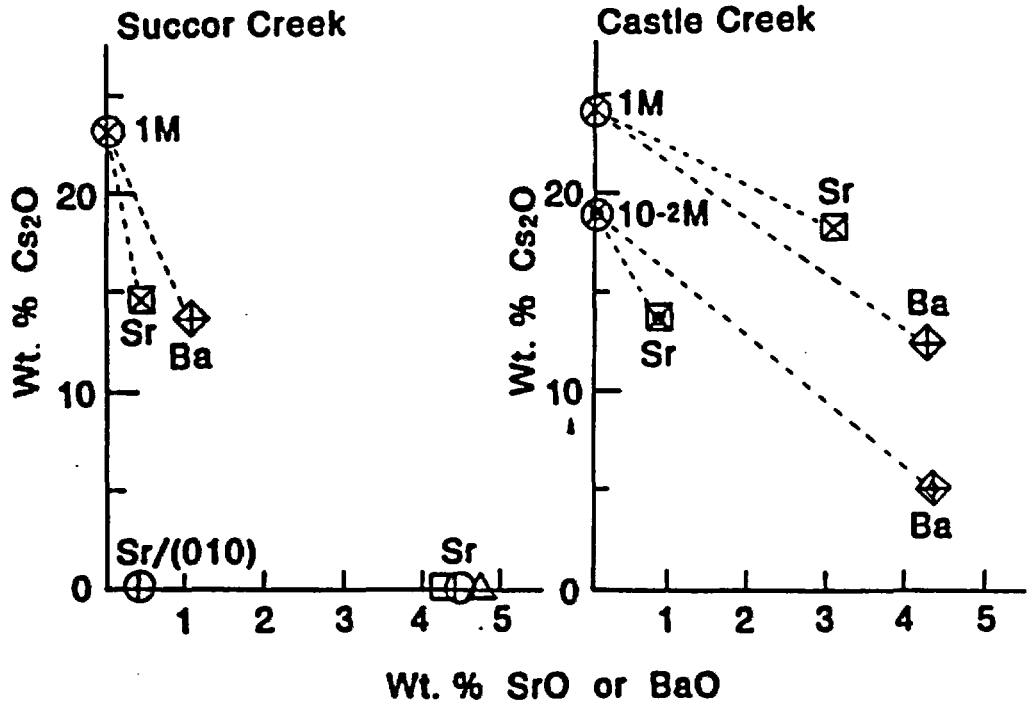

Figure 10. Cesium contents of zeolites after competing exchange reactions between Cs, Sr and Ba
(a) Succor Creek clinoptilolite (010) crystals reacted with 1*M* chloride solutions.
(b) Castle Creek microcrystals reacted with 1*M* and $10^{-2}M$ chloride solutions.

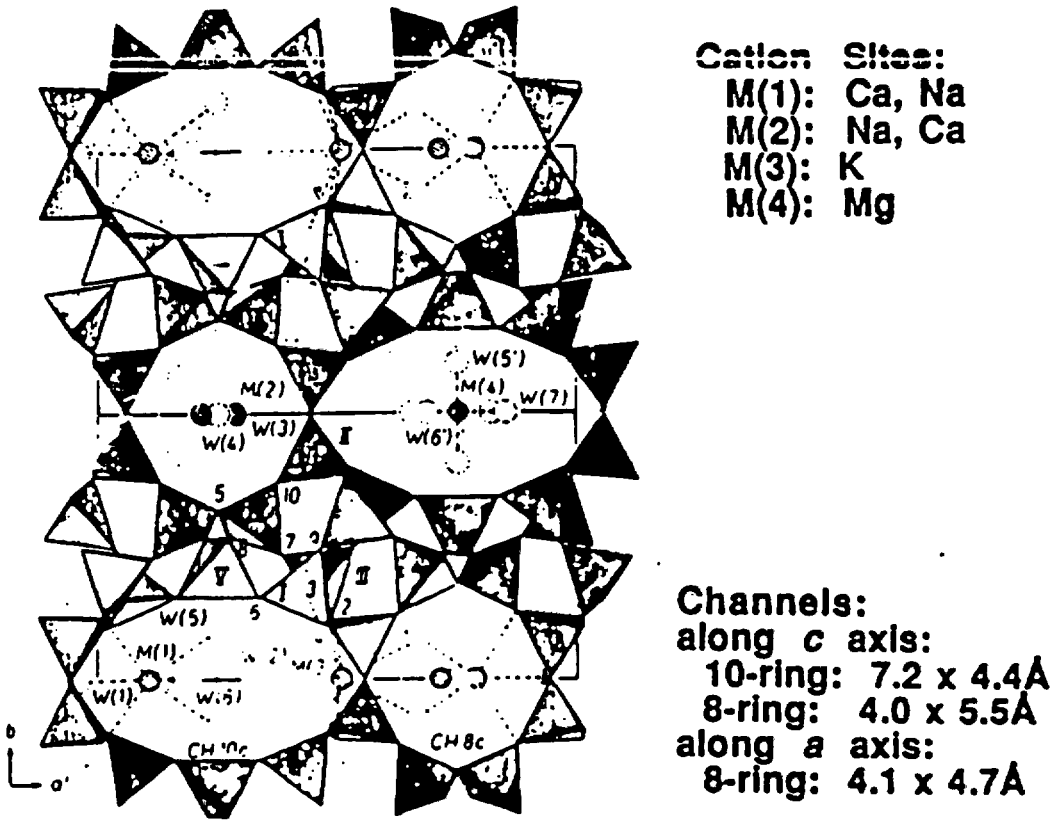

Figure 11. The crystal structure of clinoptilolite projected onto the (001) plane (from Koyama and Takeuchi, 1977). Note the large channels running parallel to the *c*-axis. Channels also occur parallel to the *a*-axis but do not exist parallel to the *b*-axis.

for 10 days, and produced a Cs-exchanged clinoptilolite that still retained most of its Ca^{2+} ions. The crystal structure refinement (Smyth et al., 1990) revealed that Cs^{+} ions occupy five different sites, none of which correspond to cation positions in the unreacted clinoptilolite. Each of the Cs sites has a low occupancy factor and lies close to another partially occupied Cs site, indicating appreciable positional disorder of the Cs atoms. The structure refinement also indicated that fewer water molecules are present in the crystal structure of the Cs-exchanged clinoptilolite. These results correlate with our observations of Ca retention and higher oxide totals in microprobe analyses of the Succor Creek clinoptilolite after Cs-exchange reactions.

Our measurements have clarified some ambiguities resulting from Ames' (1959-65) detailed investigations. Contrary to his claim (Ames, 1960, p. 699), our studies have demonsrated that heulandite and clinoptilolite do possess similar cesium exchange properties. Comparable concentrations of Cs enter the (100) and (001) crystal faces of the two zeolites. However, the (010) faces retard the entry of Cs, correlating with the absence of open channels along the *b*-axes in the crystal structures of both zeolites.

Ames (1964, p. 140) also predicted that differences of cation exchange properties of zeolites might exist between chloride and carbonate solutions if less-dissociated carbonate salts were used. Our measurements have revealed that Cs-exchange reactions performed in 1*M* $NaHCO_3$ solutions reduce the Cs capacities of each crystal face of the Succor Creek clinoptilolite, including the (001), (100) and (101) faces down which large open channels project in the crystal structure. Since this calcic clinoptilolite contains (and retains) a relatively high concentration of Ca^{2+} ions, it is conceivable that precipitation of nanophase particles of $CaCO_3$ (undetected in x-ray diffractograms) clog the channels and prevent the entry of Cs into the clinoptilolite structure. Further research is

required to elucidate this problem. Also, Cs-exchange reactions need to be performed in dilute (e.g. $10^{-3}M$ $NaHCO_3$) solutions that more closely resemble compositions of groundwater flowing though vitric tuffs at Yucca Mountain (White et al., 1980; Ogard and Kerrisk,1984; Moore et al., 1986).

The competing exchange reactions performed on single crystals and microcrystalline samples of clinoptilolite demonstrate that the uptake of Cs^+ into this zeolite is adversely affected by Sr^{2+} and Ba^{2+}. Such an assemblage of cations present as radiogenic ^{90}Sr, ^{137}Cs and ^{135}Cs and daughter Ba isotopes in high-level radiactive waste may interfere with one another when clinoptilolite in tuff deposits is called upon to immobilize dissolved components in contaminated groundwater.

Similar competing cation exchange experiments need to be undertaken on each oriented crystal face of clinoptilolite, as well as other zeolites such as mordenite found as a major constituent of zeolitized vitric tuffs at Yucca Mountain. Our exploratory cation exchange measurements of oriented fibers of mordenite indicate that differences exist in the relative concentrations of Cs, Sr and Ba entering crystallites parallel and perpendicular to the fiber axis, down which large open channels exist parallel to the *c*-axis (Meier, 1961; Schlenker et al., 1979).

SUMMARY

In cation exchange reactions involving oriented crystals of clinoptilolite
(1) the uptake of Cs, and particularly Sr, into the zeolite is crystallographic dependent. The cation concentrations are least on (010) faces perpendicular to the *b*-axis along which open channels do not exist in the crystal structure;
(2) the presence of dissolved $NaHCO_3$ reduces the Cs uptake from CsCl solutions, particularly into (010) faces of the zeolite;
(3) in competition with Sr and Ba, the Cs uptake is reduced, particularly in microcrystalline clinoptilolite; and
(4) calcic clinoptilolite and heulandite possess similar cation exchange properties. Cesium is reluctant to enter (010) faces, and significant proportions of Ca^{2+} remain in the crystal structures after Cs-exchange reactions.

Some of the implications of the cation exchange experiments include
(1) the uptake of soluble Cs radionuclides from sodium bicarbonate-type fracture flow groundwater by euhedral crystals of calcic clinoptilolites coating fractures in tuff deposits may be impaired at Yucca Mountain;
(2) the uptake of ^{135}Cs and ^{137}Cs may be compromized by coexisting radiogenic ^{90}Sr and daughter Ba isotopes in groundwater contaminated by leakages from buried high-level radioactive waste;
(3) fibrous mordenite crystallites may possess similar crystallographically-dependent cation exchange properties as coexisting clinoptilolite in zeolitized tuffs; and
(4) crystallogrpahic dependencies may exist for exchange reactions involving zeolites and other elements, including radionuclides of Zr, Ni, Ra, etc., but such effects require experimental verification.

Acknowledgments. The study was funded by the State of Nevada, Nuclear Waste Project Office, under a Department of Energy grant from the Nuclear Waste Fund.

REFERENCES CITED

Ames Jr., L. L. (1959) Zeolitic extraction of cesium from aqueous solutions. *U.S. Atomic Energy Commission Rept.*, HW62607, 25pp.

Ames Jr., L. L. (1960) The cation sieve properties of clinoptilolite. *Amer. Mineral.*, 45, 689-700.

Ames Jr., L. L. (1961) Cation sieve properties of the open zeolites chabacite, mordenite, erionite and clinoptilolite. *Amer. Mineral.*, 46, 1120-1131.

Ames Jr., L. L. (1962a) Kinetics of cesium reactions with some inorganic cation exchange materials. *Amer. Mineral.*, 47, 1067-1078.

Ames Jr., L. L. (1962b) Effect of base cation on the cesium kinetics of clinoptilolite. *Amer. Mineral.*, 47, 1310-1316

Ames Jr., L. L (1962c) Characterization of a strontium-selective zeolite. *Amer. Mineral.*, 47, 1317-1320.

Ames Jr., L. L. (1963) Mass action relationships of some zeolites in the region of high competing cation concentrations. *Amer. Mineral.*, 48, 868-881.

Ames Jr., L. L. (1964) Some zeolite equilibria with alkali metal cations. *Amer. Mineral.*, 49, 127-145.

Ames Jr., L. L. (1965) Self diffusion of some cations in open zeolites. *Amer. Mineral.*, 50, 465-478.

Ames, Jr., L. L., Sand, L. B., and Goldich, S. S. (1958) A contribution on the Hector, California, bentonite deposits. *Econ. Geol.*, 53, 22-37.

Barrer, R. M. and Makki, M. B. (1966) Molecular sieve sorbents from clinoptilolite. *Canad. J. Chem.*, 42, 1481-1487.

Bish, D. L. (1984) Effects of exchangeable cation composition on the thermal expansion - contraction of clinoptilolite. *Clays & Clay Minerals*, 32, 444-452.

Bish, D. L. (1988) Effects of composition on the dehydration behavior of clinoptilolite and heulandite. In: *Occurrence. Properties, and Utilization of Natural Zeolites* (D. Kallo and H. S. Sherry, eds.; Akademiai Kiado, Budapest), p. 565-576.

Broxton, D. E, (1987) Clinoptilolite compositions in diagenetically-altered tuffs at a potential nuclear waste repository, Yucca Mountain, Nevada. In: *The Technology of High-Level Nuclear Waste Disposal* (P. L. Hofmann, ed.; Batelle Memorial Inst. Publ.), p. 179-194.

Broxton, D. E., Bish, D. L., and Warren, R. G. (1987) Distribution and chemistry of diagenetic minerals at Yucca Mountain, Nye County, Nevada. *Clays & Clay Minerals*, 35, 89-110.

Broxton, D. E., Warren, R. G., Hagan, R. C., and Luedemann, G. (1986) Chemistry of diagenetically altered tuffs at a potential nuclear waste repository, Yucca Mountain, Nye County, Nevada. *U.S. Nat. Tech. Inform. Serv. Rept.* LA-10802, 160 pp.

Burns, R. G., Bowers, T. S., Woods, V. J., Blundy, J. D., and Morgenstein, M. E. (1990) Reactivity of zeolites forming in vitric tuffs in the unsaturated zone at Yucca Mountain, Nevada. In: *Nuclear Waste Isolation in the Unsaturated Zone* (Amer. Nuclear Soc. Publ.), p. 101-112.

Carlos, B. A. (1985) Minerals in fractures of the unsaturated zone from drill core USW G-4, Yucca Mountain, Nye County, Nevada. *U.S. Nat. Tech. Inform. Serv. Rept.* LA-10415, 55pp.

Chelishchev, N. F., Marynova, N. S., Fakina, L. K., and Berenshtein, B. G. (1974) Ion exchange properties of clinoptilolite. *Dokl. Akad. Nauk, SSSR, Chem. Phys.*, 217, 1140-1141.

Gottardi, G. and Galli, E. (1987) *Natural Zeolites*. Springer-Verlag.

Howery, D. G. and Thomas, H. C. (1965) Ion exchange on the mineral clinoptilolite. *Journ. Phys. Chem.*, 69, 531-537.

Kerrisk, J. F. (1987) Groundwater chemistry at Yucca Mountain, Nevada, and vicinity. *U. S. Nat. Tech. Inform. Serv. Rept.*, LA-10929, 113 pp.

Koyama, K. and Takeuchi, Y. (1977) Clinoptilolite: the distribution of potassium atoms and its role in thermal stability. *Zeit. Kristallog.*, 145, 216-239.

Levy, S. S. (1984) Studies of altered vitrophyre for the prediction of nuclear waste repository-induced thermal alteration at Yucca Mountain, Nevada. *Mat. Res. Soc. Symp. Proc.*, 26, 959-966.

Meier, W. M (1961) The crystal structure of mordenite (ptilolite), *Zeit. Kristallog.*, 15, 439-450.

Moore, D. E., Morrow, C. A., and Byerlee, J. D. (1986) High-temperature permeability and groundwater chemistry of some Nevada Test Site tuffs. *Journ. Geophys. Res.*, 82, 2163-2171.

Mumpton, F. A. and Ormsby, W. C. (1978) Morphology of zeolites in sedimentary rocks by scanning electron microscopy. In: *Natural Zeolites: Occurence, Properties, Use* (L. B. Sand and F. A. Mumpton; Pergamon Press) p. 113-132.

Ogard, A. E. and Kerrisk, J. F. (1984) Groundwater chemistry along flow paths between a proposed repository site and the accessible environment. *U. S. Nat. Tech. Inform. Serv. Rept.*, LA-10188.

Schlenker, J. L., Pluth, J. J., and Smith, J. V. (1979) Positions of cations and molecules in zeolites with the mordenite-type framework. VIII. Dehydrated sodium-exchanged mordenite. *Mat. Res. Bull.*, 14, 751-758.

Smyth, J. R., Spaid, A. T., and Bish, D. L. (1990) Crystal structures of a natural and a Cs-exchanged clinoptilolite. *Amer. Mineral.*, 75, 522-528.

White, A. F., Claassen, H. C., and Benson, L. V. (1980) The effect of dissolution of volcanic glass on the water chemistry in a tuffaceous aquifer, Rainier Mesa, Nevada. *U.S.G.S. Water-Supply Paper* 1535-Q, 33 pp.

FACTORS THAT INTERFERE WITH THE AGE DETERMINATION OF ROCK VARNISH

David H. Krinsley, Ronald I. Dorn+ and Steven W. Anderson**
***Department of Geology and +Department of Geography**
Arizona State University
Tempe, Arizona 85287

Abstract: Over the past few years the rock varnish literature has proliferated. More than a dozen research groups in at least six countries are now investigating the potential of rock varnish as a Quaternary dating technique for geomorphical and archaeological studies. New backscattered electron microscopy imagery of varnishes from southwestern North America illustrates the need for great caution in the selection of samples for all varnish dating methods. Nine general factors that may interfere with varnish dating are presented. For varnish dating to be successful, these factors must be evaluated by careful examination of samples in the field and by analyses of many cross-sections in the laboratory. [Key words: rock varnish, Quarternary dating methods, geomorphology, backscattered electron microscopy, geochronology.]

INTRODUCTION

Rock varnish, a dark thin (<1 to >500 microns) layer composed of clay minerals, manganese, and iron oxides, and a variety of minor and trace constituents, forms on rocks in the terrestrial weathering environment. In acid environments, varnish accretes over periods of thousands of years, where age has been established independently by historical, radiocarbon, and K-Ar dating (Blackwelder, 1948; Dorn and Oberlander, 1982; Whalley, 1983; Dorn, 1989). Rock varnish has been used for over a century in geomorphological (e.g., Merrill, 1898; White, 1924; Blackwelder, 1954; Hunt and Mabey, 1966; Bull, 1977) and archaeological studies (e.g., Basedow, 1914; Heizer and Baumhoff, 1962; Hayden, 1976) to assign relative ages to natural and human-manufactured surfaces in arid lands.

Significant advances have been made recently in the numerical and calibrated dating of rock varnishes. Paleomagnetism (Potter, 1979), uranium-series (Knauss and Ku, 1980), scavenging of heavy metals (Dorn and Oberlander, 1982), depth profiles of trace elements (Bard, 1979), layering of Mn-Fe laminations (Dorn, 1984, 1990), radiocarbon dating of carbonate rinds over varnishes (Dragovich, 1986), recognition of ash in varnish (Harrington, 1988), and K-Ar dating of varnish clays (Dorn, 1989) have been proposed. Most geomorphological and archaeological applications, however, have used cation-ratio (CR) dating (e.g., Dorn and Oberlander, 1981; Dorn, 1983, 1986, 1988, 1989; Dorn and Whitley, 1984; Dorn et al., 1986, 1987a,b, 1988a,b; Glazovskiy, 1985; Harrington, 1987, Harrington and Whitney, 1987; Whitney et al., 1988; Detheir et al., 1988; Pineda et al., 1988; Liu

Physical Geography, 1990, 11, 2, pp. 97-119.

and Zhang, 1990) and accelerator radiocarbon dating (Dorn et al., 1989) of rock varnish.

In the recent flurry of interest in varnish-dating methods, many have pointed out that rock varnish is incredibly complex: it is chemically, texturally and mineralogically heterogeneous on a scale of meters, millimeters, and microns (Dorn and Oberlander, 1982; Dorn, 1990; Dragovich, 1988a,b; Smith and Whalley, 1988; Krinsley and Manley, 1989; Krinsley and Anderson, 1989; Raymond et al., 1988a,b, 1989). The purpose of this paper is to add support to these concerns by urging caution to those trying to derive an age signal from rock varnish. We used backscattered electron microscopy (BSE) and several other techniques listed below to illustrate new and previously recognized factors that may interfere with the dating of rock varnish.

METHODS

Aspects of the analytical techniques and methods used to obtain the information in this paper are discussed below. Secondary electrons (SE) are conventionally used to form images in scanning electron microscopy (SEM), producing topography or relief with a simulated three dimensional view of the object. Generally, a rough object is coated with a heavy metal, observed on a cathode ray screen, and then photographed. Backscattered electron production (BSE) involves making a flat, well polished, uncovered thin section of a rock or other object. The section is then coated with carbon in a vacuum evaporator and observed, as above. In the BSE method, however, some of the electrons striking the section are reflected out of the specimen; the number of these electrons divided by the number of primary electrons that strike the target gives the backscattered coefficient which varies with the atomic number (Z) of the target.

Values of this coefficient range from about 5% for pure, light elements such as carbon (Z = 6), to about 50% for pure, heavy elements such as gold (Z = 79) (Robinson and George, 1978). When the target consists of a homogeneous mixture of several elements, as is the case with most minerals, an average atomic number applies. Thus, quartz and feldspar appear relatively darker than minerals containing heavy elements such as pyrite and ilmenite (Pye and Krinsley, 1984). Compositional contrast is seen most clearly on polished surfaces, because topographic contrast is suppressed. Robinson and Nickel (1979), for example, were able to distinguish between Fe_7S_8 and Fe_9S_{10}. The differences in contrast between individual minerals make it possible to observe very fine textural relations, with a spatial resolution of about 0.1 microns, and atomic number resolution of 0.1Z. Texture, combined with energy dispersive X-ray analysis (providing chemical information on individual minerals) and X-ray diffraction (bulk mineralogical data), permits the determination of individual minerals in section. The BSE technique produces approximately the same kind of information that one is able to obtain from a petrographic microscope, but with a resolution of more than ten times the 2000 Angstrom resolution of the light microscope.

The electron beam in both an SEM and an electron microprobe produces a wide range of radiation, including X-rays, which are characteristic of the elements

present, and their intensity is an approximate linear function of concentration. Energy dispersive X-ray (EDX) and wave length dispersive X-ray (WDX) analyses provide a means of determining the chemical composition of very small volumes on the surface of polished thin sections of rocks or mineral mounts. Units may be mounted on SEMs and electron microprobes so that chemical analyses and photographs of the areas analyzed can be accomplished almost simultaneously. In general, WDX is more accurate, can analyze more elements, but is slower than the EDX system (Long, 1967; Goldstein et al., 1981).

RESULTS AND DISCUSSION

What is the difference between a varnish sample that will yield a reliable and reproducible date and one that will not? Dorn et al. (1989) and Dorn (1989) defined certain empirical factors that can be assessed in the field or the laboratory that have caused a varnish-age signal to deviate from a control K-Ar or radiocarbon date. These nine factors are discussed and illustrated below; the first three (unstable surfaces, different types of varnish, and particular microenvironments) may be assessed in the field; the remaining six factors in the laboratory using electron microscopy.

Unstable Surfaces

When a rock surface spalls, flakes, or undergoes disintegration, a varnish age reflects only the time since weathering. Fluvial or aeolian abrasion can also restart the varnish clock, or can incompletely remove a varnish (Fig. A), yielding an uncertain age signal. For instance, silicic lava flows frequently tend to be highly vesicular, and thus unstable (Anderson and Krinsley, 1989). Weathering might therefore be very rapid, and until a porous vesicular layer has weathered down to a less porous layer, varnish would not be preserved. In addition, range fires can induce spalling of rock surfaces (Gillespie, 1987), and hence the varnish. Even in deserts as dry as southern Nevada this can be a problem, as Spaulding (1985) reports the occurrence of dwarf conifer woodlands from over 45 ka to ~ 10 ka where only desert scrub vegetation now grows. The varnish that is present on unstable surfaces is usually quite thin and would produce erroneously young ages. The key is to be aware in the field of what composes a constructional geomorphic surface, as compared to a weathered surface.

Different Types of Varnish

Thorough testing of age signals in varnish has been conducted at sites of known age only for black, manganese-rich varnishes (Mn:Fe ratio $\geqq$ 0.3) formed in a subaerial environment from the deposition of airborne fallout. There are, however, many other types of Mn-rich and Mn-poor varnishes (Dorn and Oberlander, 1982) that have not been well tested. For example, orange varnishes formed on the undersides of cobbles in a desert pavement (Mn-poor, Mn:Fe ratio $<$ 0.3) have potential for radiocarbon dating (Dorn et al., 1989). Figure B presents varnish

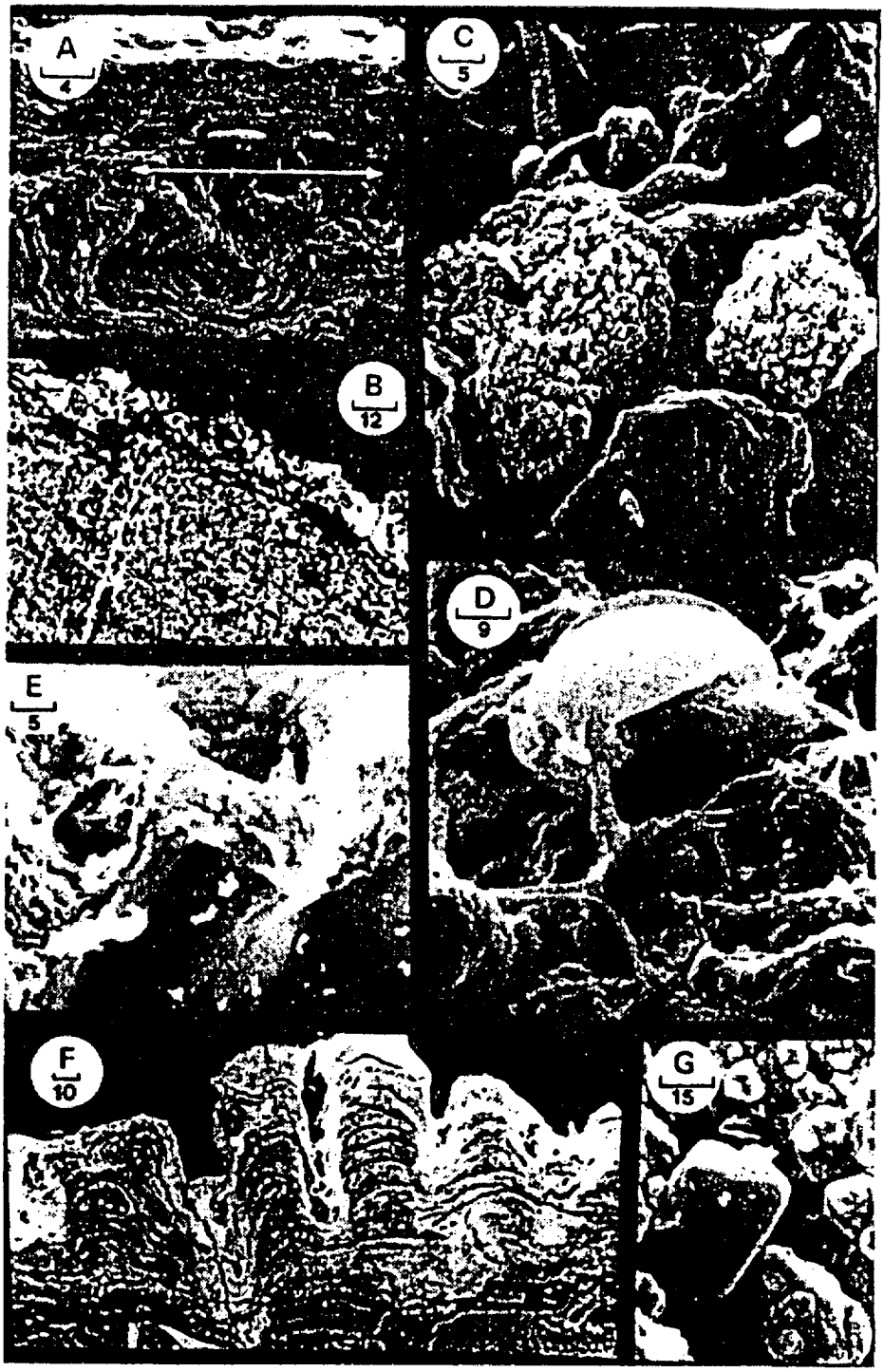
A
4
B
12
C
5
D
9
E
5
F
10
G
15

Plate 1.

Fig. A. SE (secondary electron) section illustrating a rare situation where aeolian abrasion has not completely eroded varnish; sample from a protected depression in a rock from the Cronese Basin, Mojave Desert, California. Three phases of varnish build-up and two (possibly three) phases of varnish erosion are recorded. First, the lower layer was deposited. Second, the area beneath the double arrow was eroded, most likely by the secretion of organic acids by fungi or lichens. Third, varnish filled in this depression. Fourth, aeolian abrasion truncated the varnish above the double arrow. Fifth, a newer layer of varnish has been deposited above the double arrow. Sixth, it is possible that some aeolian abrasion has occurred on top of the newest varnish layer.

Fig. B. BSE (backscatter) section of varnish from the west-central side of the Marble Mountains, SE Mojave Desert, California. The varnish is the lighter, thin ridge running roughly from upper left to lower right. The gray material is the supporting rock. A bright layer of varnish has penetrated from the surface into the rock through a crack (left of the wavy arrow). There is also another crack to the left, which contains considerably less varnish.

Fig C. SE image of microcolonial fungi (Staley et al., 1982; Taylor-George et al., 1983) from near Florence, Arizona. Depressions around fungi are probably due to the secretion of organic acids.

Fig. D. SE image of pollen grain resting on the surface of varnish, Hanaupah Canyon alluvial fan, Death Valley, California. Note the abundant filaments of fungi which may be obtaining organic matter from the pollen grain. As pollen and fungal filaments are buried by accreting varnish, organic matter is incorporated.

Fig. E. SE image of varnish on quartz, from Death Valley Canyon alluvial fan, Death Valley, California. One erosional hollow has been filled in by younger varnish (including the barium-rich crystal identified by the arrow), and would not be visible to a purely surface inspection. Another hollow is more recent, and would be visible during SE examination of the varnish surface.

Fig. F. BSE section of rock varnish from Death Valley Canyon alluvial fan, Death Valley, California. Note the roughly parallel layering near the rock/varnish contact, and the layering within the "stromatolite-like" structures. The very bright layers are generally high in Mn, while the black layers are open cracks. The depressions between the stromatolitic structures were probably formed by biological erosion of the varnish. After their formation, they have been subsequently filled in by younger/Mn-rich varnish. The depression on the far left side has been completely refilled. The other depressions are at various stages of refilling.

Fig G. SE view of the surface of varnish collected from the Bishop Tuff, on the Sherwin Grade, north of Bishop, California. Note the crystal of calcium carbonate that has dropped into the depression in the varnish. This particular varnish was a few centimeters away from an eroding vein of calcrete that had formed in an eroded outcrop of the Bishop Tuff.

Scale bar in microns.

formed in a rock fracture beneath a subaerial surface. 'Crack' varnishes have both Mn-rich and Mn-poor zones (Dorn and Oberlander, 1982; Dorn and Dragovich, 1990).

Crack varnishes pose a potential problem when the overlying rock spalls off, exposing varnish formed in a rock crevice. Crack varnishes can appear better developed to the naked eye than a varnish formed in an exposed subaerial environment, if the lithology is smooth like quartzite or chert. Dust and microbes are slow to adhere to these smooth rock types in an exposed subaerial environment. A rock crevice, however, is a more favorable environment for varnish adsorption. Alternatively, if the rock is weathered granite that readily sheds grus, or foliated metamorphic rock that salt-weathers rapidly, varnish formed in a crevice will typically be better developed than varnish developed on such easily weathered exposed surfaces. The danger in CR dating here rests in preferentially sampling these seemingly better varnished surfaces that originated in crevices. The crack environment is a totally different cation-leaching environment than the exposed surfaces. For example, cation ratios [(K+Ca)/Ti] of crack varnishes in the Coso Range were about 30% higher than subaerial varnishes from the same lava flow (Dorn, 1989).

Particular Microenvironments

Empirical data indicate that proximity to lichens, abundant detrital organic matter and cryptogamic soil lower varnish cation ratios, probably due to enhanced leaching from more abundant organic acids (Dorn, 1989). Underhangs, extremely rough lava flow surfaces, and proximity to desert soil surfaces, in contrast, increase cation ratios as compared to values for varnishes collected over a meter above soils. The reasons for this are uncertain, but they may involve different inputs of cations close to a soil and differential fluid movement over the surface of rock with a significantly different geometry (Dorn, 1989).

Organisms That Erode Varnish

Microcolonial fungi (Staley et al., 1982; Fig. C), cyanobacteria, and filamentous fungi (Fig. D) can lower cation ratios (Dorn, 1989) and make radiocarbon dates too young (Dorn et al., 1989). This is because younger varnish is deposited in the depressions created by the biogeochemical erosion (Figs. E,F,L). In addition, organic acids probably enhance the cation-leaching process (e.g., Truter, 1973; Talibudeen, 1981).

Anomalously High Concentration of Elements in Cation Ratios

All of the elements in the CR of (K+Ca)/Ti may occur in anomalous concentrations which vary tremendously from one place to another in the varnish (Dragovich, 1988a,b; Dorn, 1989). In many cases, concentrations of what appear to be different types of detrital minerals are observed at the micron-level. These anomalies are detectable by examining varnish scrapings and varnish cross-sections by electron microscopy (Figs. G,H,I,J,K). High levels of these cations are

produced by proximity to a source: for example, calcrete rubble for calcium (Fig. G). Varnishes influenced by these elemental anomalies should not be used for dating. It should also be noted that when these elements are studied in varnish cross-sections with the ion microprobe, they vary irregularly from top to bottom (O'Hara et al., 1989), just as they do in electron probe studies (Dragovich, 1988a,b; Dorn, 1990a).

A more difficult problem involves barium. Ba, sometimes contained in crystals of sulfate, is common in arid varnishes (Engel and Sharp, 1958; Lakin et al., 1963; Potter and Rossman, 1979; Bard, 1979; Duerden et al., 1986; Dragovich, 1988a,b; Dorn, 1990a). Typical values for bulk chemical measurements are <1% (Bard, 1979; Duerden, 1986; Dorn et al., 1990), but may reach over 4% on a micron-scale using a wavelength dispersive microprobe (Krinsley and Anderson, 1989; Krinsley, unpublished data). If an EDX unit attached to a scanning electron microscope is used to analyze varnish cation ratios (Harrington and Whitney, 1987), the Ti K-alpha and Ti K-beta peaks overlap the Ba L-alpha and Ba L-beta peaks, respectively (Harrington et al., 1989). When the concentration of Ti is considerably less than Ba, which can happen frequently in arid varnishes, the Ba and Ti peaks partially overlap, are difficult to separate, and may produce a false cation ratio. It is possible to deconvolute the overlapping lines, but resolution is considerably better if WDX is used. When the same varnish scrapings are analyzed by other methods, proton-induced X-ray emission, WDX, and inductively coupled plasma, virtually identical chemical analyses are obtained for varnish cation ratios (Dorn et al., 1990).

Surface Topographies That Trap Aeolian Detritus

Since rock varnishes collected for dating are from subaerial exposures, the material that accumulates is aeolian fallout, or from material that has weathered from rock surfaces that may be topographically above the sampled varnish. If surface topography is irregular, coarse angular aeolian fallout is more readily trapped (Figs. G,H,I,J). More than a third of surfaces we have examined fall into this category.

Many surface depressions are produced by erosion of varnish, typically by the secretion of acids by organisms such as microcolonial fungi (Figs. C,L). Material that fills in these depressions is younger than the surrounding varnish and much younger than what is of interest, the geomorphic or archaeological exposure of the underlying rock. The SEM method of CR dating only views varnish from the top (Harrington and Whitney, 1987). This source of contamination is, therefore, not assessed, since infilled depressions are often not visible by viewing the surface (Fig. E).

It is necessary to evaluate multiple varnish cross-sections to check for these infilled depressions before varnish material is chemically analyzed for dating. If infilled depressions are found, the sample should not be used. This is not just a theoretical concern. When samples that contained these infilled depressions were analyzed for CR dating or radiocarbon dating, the varnish ages were significantly younger than the control dates for the same site (Dorn et al., 1989; Dorn, 1989).

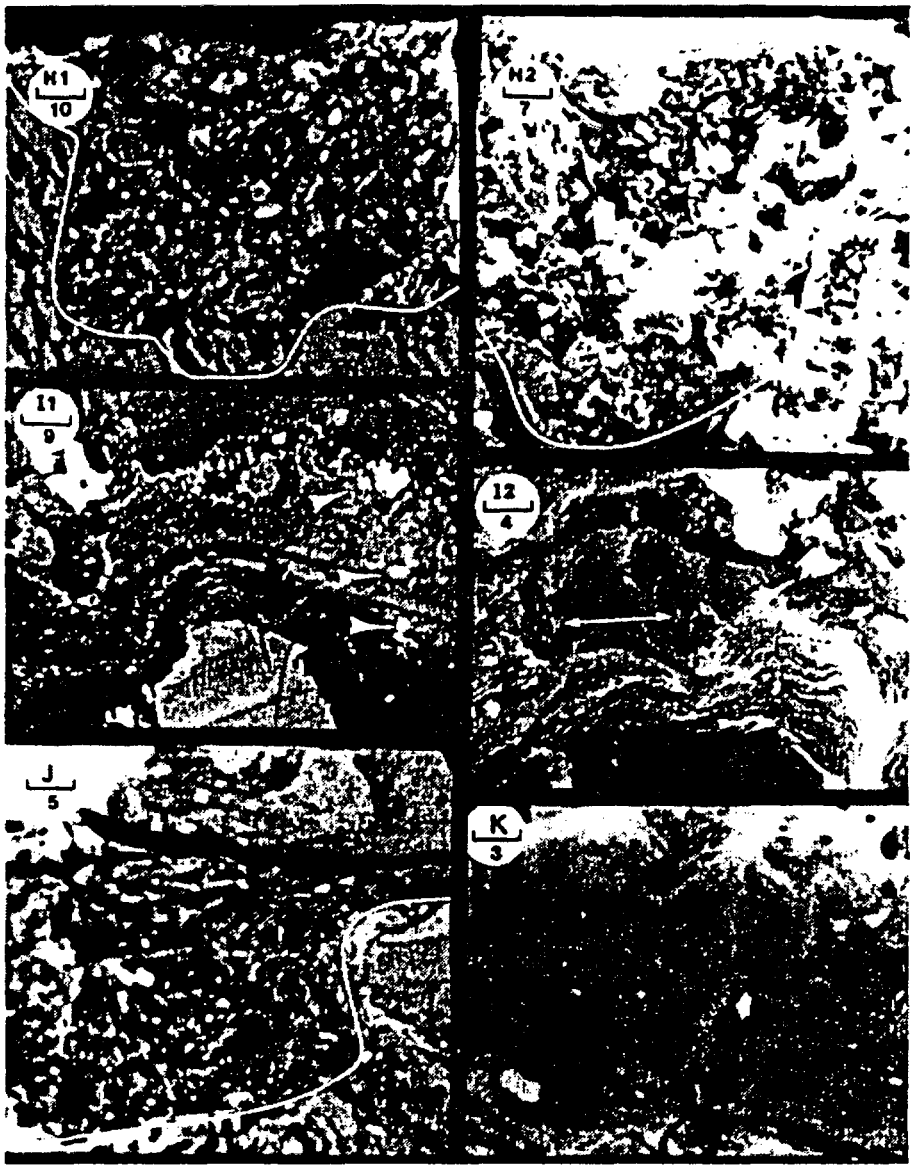
H1
10
H2
7
I1
9
I2
4
J
5
K
3

Plate 2.

Figs. H1 and H2. Deposits of relatively deep varnish in rock depressions, illustrated by both BSE (H1, from the Marble Mountains, Mojave Desert, California) and SE (H2, from Crater Flat in southern Nevada). Note that the texture is not layered, but a chaotic mix of typical varnish constituents (Mn-Fe oxides and clays) and a high concentration of aeolian detritus (for example the barium-sulfate crystals identified by the arrows in H2). This 'granular' texture may have been produced during rapid aeolian deposition in a rock depression, as opposed to slow rates of growth of the more layered varnishes. The rock/varnish boundary is indicated by the line. Immediately to the left and right of these pockets, the varnish is less than 5 microns thick.

Figs. I1 and I2. Layered structures of varnish at the rock/varnish boundary, illustrated by BSE (I1, from Coso basalt flow 28; see Dorn, 1989 for site) and SE (I2, also from Coso basalt flow 28). The arrows in I1 identify microprobe points; the uppermost arrow is adjacent to a bright (high Z contrast) grain that is barium sulfate. There is a change in the structure of the varnishes, that occurs about the position of the uppermost arrows in I1 and I2. Below is layered varnish; above is more porous varnish. There are a series of paleodepressions at this level that have been infilled by varnish and aeolian detritus. The arrows in I2 point to barium-rich detritus trapped in paleo-depressions. The bright detritus in I1, iron oxide and barium sulfate, appear to be trapped in paleodepressions. Because the layering appears to be truncated in I1, the depressions probably represent a paleoerosional episode.

Fig. J. BSE section from Death Valley, California. The line represents a textural change from layered varnish on the right to more porous, granular varnish on the left. There are three possibilities to explain the change. This may represent a former erosional depression, filled in by the porous varnish (hypothesis favored by Dorn). It could represent a diagenesis, whereby the porous-granular varnish is gradually plugged by the mobilization and reprecipitation of Mn-Fe oxides, and layering is produced (hypothesis favored by Krinsley and Anderson). Alternatively, it could represent two different styles of varnish deposition, occurring side by side. Dorn cites the difficulty in reorganizing the chaotic texture on the left into layers. Krinsley and Anderson observe that above the big crack (from right to left, three-quarters to the top of the image), porous layers merge into well-cemented and bright layers enriched in Mn-Fe oxides.

Fig. K. BSE section of varnish from Death Valley Canyon alluvial fan, Death Valley, California. Note the partially filled fracture in the middle of the image (highlighted by arrow). The crack, which is perpendicular to the layering, is partially filled with high Z material and vanishes into a layered, mound-like structure of high Z material. Krinsley and Anderson also feel that in places, the high Z material in the filled cracks appears to have moved parallel to the layering. Dorn feels the layering is depositional. Note that aeolian detritus has been trapped as these layers accrete. Most of this detritus is low Z material, probably quartz or feldspar, while a few are high Z material, perhaps barium or iron.

Scale bar in microns.

The type of varnish that yields ages similar to control dates is evenly layered, showing regular laminae which are not eroded (Figs. M,N,O,P).

Another implication of these surface irregularities for the dating of rock varnish concern with the nature of the constituents that accumulate in pockets filled with younger material. Given proximity to the source of a titanium or calcium anomaly, for example, the aeolian detritus will be rich in these elements (Fig. G). If the varnish is collected from a desert area that produced abundant barium sulfate, such as a playa surface, barium is found in high concentrations in these erosional pockets (Figs. E, H2, I, J, S, Z4). A geochemical signal such as abundant barium indicates that a sample should not be used for dating.

We see no evidence that the constituents of the varnish are derived from the rock immediately underlying the varnish (Figs. E, I2, P, Q), as has been postulated by some (Merrill, 1898; Blackwelder, 1954; Smith and Whalley, 1988), although there is occasionally some weathering of rock at the rock/varnish interface and there very well may be occasional inclusions of rock material in the varnish (Figs. Q,R,S). Our elemental analysis of various varnishes (Krinsley and Anderson, 1989) using the electron probe with WDS supports the view that there is no elemental exchange between the varnish and the rock (e.g., Potter and Rossman, 1977, 1979; Allen, 1978; Dorn and Oberlander, 1982; Elvidge and Iverson, 1983; Raymond et al., 1988b).

Cracks Oriented Normal to the Varnish Surface

Such cracks were first noted by Whalley (1983, 1984) and are illustrated here by Figures Q, T, U, V and W. We agree that these may be created by wetting and drying, which could cause expansion and contraction; the same set of processes is linked to fixing manganese and iron oxides with mixed-layer illite-montmorillonite clays in varnish (Potter and Rossman, 1977, 1979). It is also possible that organisms such as microcolonial fungi, cyanobacteria, or lichen thalli could weaken the varnish and promote fracturing during wetting and drying. It is possible that different distributions and abundances of these cracks might influence fluid movement and the cation-ratio dating of varnish. This needs to be assessed under controlled circumstances.

Remobilization of Varnish Constituents

Some of the fractures which are oriented parallel or subparallel to the varnish and the underlying rock may be the result of sample preparation (Fig. Q), but many of these predate sample collection and have partial or complete fillings, and 'bridges' high in Mn and Fe resulting from mobilization and reprecipitation after fracturing (Fig. K,T,U,V2,W). These phenomena have not been reported previously, but are common in selected samples observed thus far from southwestern North America. BSE imagery of highly porous varnish (e.g., Figs. E,H,I,J,K,R,S,T,V) illustrates ready avenues for the movement of fluid through varnish.

It is also possible that thin laminae of Mn-Fe rich layers may represent the mobilization, lateral movement, and reprecipitation of oxides. Here, the authors'

preliminary interpretation diverges. All authors believe the appearance of some discontinuous laminae may reflect diagenetic processes that gradually plug the pore spaces and fractures in the layered varnishes (e.g., smaller arrows in Fig. Q, V2, W). Anderson and Dorn (following Perry and Adams, 1978) believe that the layered laminae that are laterally continuous (Figs. M,N,O,P) are produced by depositional processes. All of the authors agree that the mobilization cannot be over significant distances, or the Mn and Fe would be leached completely out of the varnish, something that clearly does not occur.

There is strong chemical evidence that at least some varnish constituents are mobile, inferentially supporting the BSE observations of constituent mobility. Abundant empirical data indicate that K and Ca are leached from varnish over time (Dorn and Oberlander, 1981; Dorn, 1983, 1989; Glazovskiy, 1985; Harrington and Whitney, 1987; Pineda et al., 1988; Liu and Zhang, 1990). Under certain geochemical circumstances, Ti, which is generally insoluble, may also act as a mobile cation. A few of the acid waters and brines for which analyses were given by White et al. (1963) contain more than 1,000 μg/l of titanium, indicating that Ti is mobile under highly acidic and extremely basic circumstances. Chelation of titanium by organic complexes (organic ligands) might also increase its solubility (Hem, 1985). It is possible that chelating complexes and organic acids, produced by the decay of organisms (Figs. C,D,X), could mobilize titanium in rock varnish on a micron scale. The pH values of bulk samples of black varnishes from 97 sites in western North America average 7.3±0.7 (Dorn, 1990), and therefore Dorn believes that titanium mobility is unlikely to influence the chemistry of bulk samples of black varnish.

For varnish radiocarbon dating to work, the organic matter dated must reflect the time of varnish deposition. Any remobilization would inject younger carbon. Stable carbon isotope analyses of the type of organic matter that yields good radiocarbon dates (similar to control dates) indicate that the dated organic matter is derived from the adjacent plants (Dorn and DeNiro, 1985). Dorn et al. (1989) assumed that the organic matter successfully dated was composed of fragments of organic material trapped mechanically as varnish accumulates (Figs. X, Y) and organic matter locked in the lattice structures of Mn-oxides. In contrast, organic carbon adsorbed to clays appears to move through varnish, and if the sample is not treated with HF to remove the younger organic matter adsorbed to clays, the radiocarbon dates are too young (Dorn et al., 1989).

Our observations reveal it is unlikely that the dated organic matter is derived from Mn-oxides, as speculated by Dorn et al. (1989); instead all the dated material must be from trapped detrital fragments (Figs. X,Y). If Mn is mobilized in the evenly layered laminae used in varnish radiocarbon dating, even for short distances, younger carbon could become incorporated into the reprecipitated oxides. Since the varnish radiocarbon dates processed with HCl, HF, hydroxylamine hydrochloride, and dithionite do match the control dates (Dorn et al., 1989), it means either there is not enough organic carbon trapped in the Mn-oxides to influence significantly the radiocarbon date or that the Mn-oxides in the layered laminae are not remobilized. Preliminary transmission electron microscopic (TEM) data suggest that the Mn occurs as very simple oxides, and is at least partly isolated from the

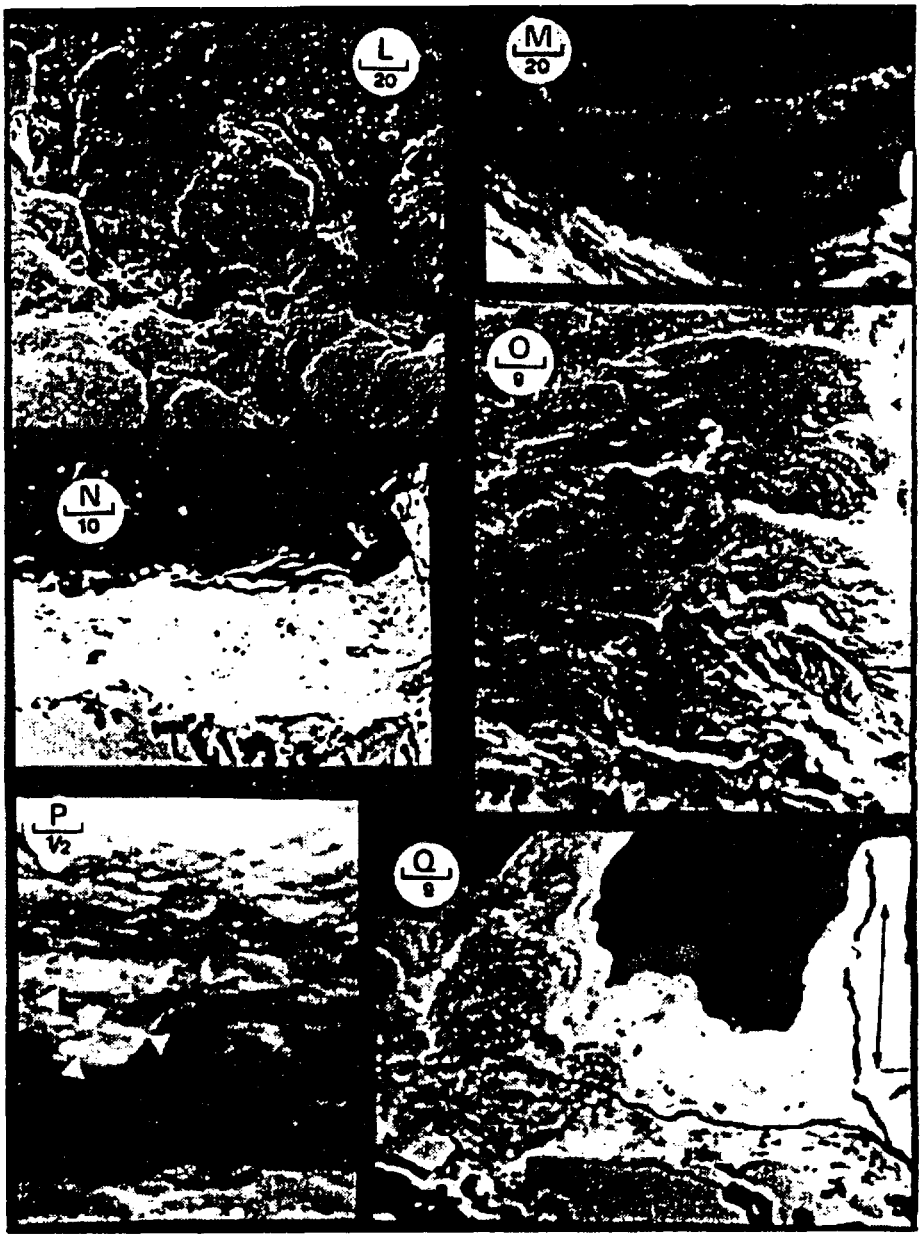
L
20
M
20
O
9
N
10
P
½
Q
9

Plate 3.

Fig. L. SE view of the varnish surface from Crater Flat, southern Nevada. The depressions are being made by microcolonial fungi (rounded forms) that secrete acids and chemically erode the varnish. As the Mn and Fe oxides are reduced, they are mobilized and probably reprecipitate in the fractures, as in Figures K,T and V.

Fig. M. Light microscope photograph of a varnish section from Hanaupah Canyon alluvial fan, Death Valley. The uppermost layer of the varnish is lighter in color; it is Mn-poor. The next lowest layer is black and enriched in Mn. The third layer into the varnish is poor in Mn and is lighter. The lowest layer of the varnish is rich in Mn and black. The lighter material beneath this dark layer is the rock. When viewed in color, the lighter layers are orange, reflecting an abundance of iron.

Fig. N. BSE section of varnish from South Mountain Park, Phoenix, Arizona. Note the parallel layers in the varnish, with little deformation. However, there is some fracturing.

Fig. O. SE section of varnish from Little Cones basalt flow, Crater Flat in southern Nevada. Note the parallel layers in the varnish with a little deformation.

Fig. P. SE image of varnish from the Cronese Basin, Mojave Desert. The arrows highlight Mn-oxide crystals imbedded in a matrix of clay minerals, but structurally isolated from the clays and the Fe-oxides, which at least partly confirms the transmission electron microscope data discussed in the text.

Fig Q. BSE image of varnish on Death Valley Canyon alluvial fan, Death Valley. Note the abrupt structural break between the underlying rock and the varnish, but a piece of the rock has been incorporated into the varnish on the lower left part of the image. The double arrow oriented vertically on the right is adjacent to a crevice that may have been created during thin-section preparation. The two smaller arrows on the left side of the image identify discontinuous high-Z laminae that may be from the mobilization and reprecipitation of Mn-Fe oxides. Dorn agrees with Krinsley and Anderson in this situation, that when the high-Z Mn-rich laminations feather out, the Mn-rich laminae may be enhanced by mobilized and reprecipitated Mn.

Scale bar in microns.

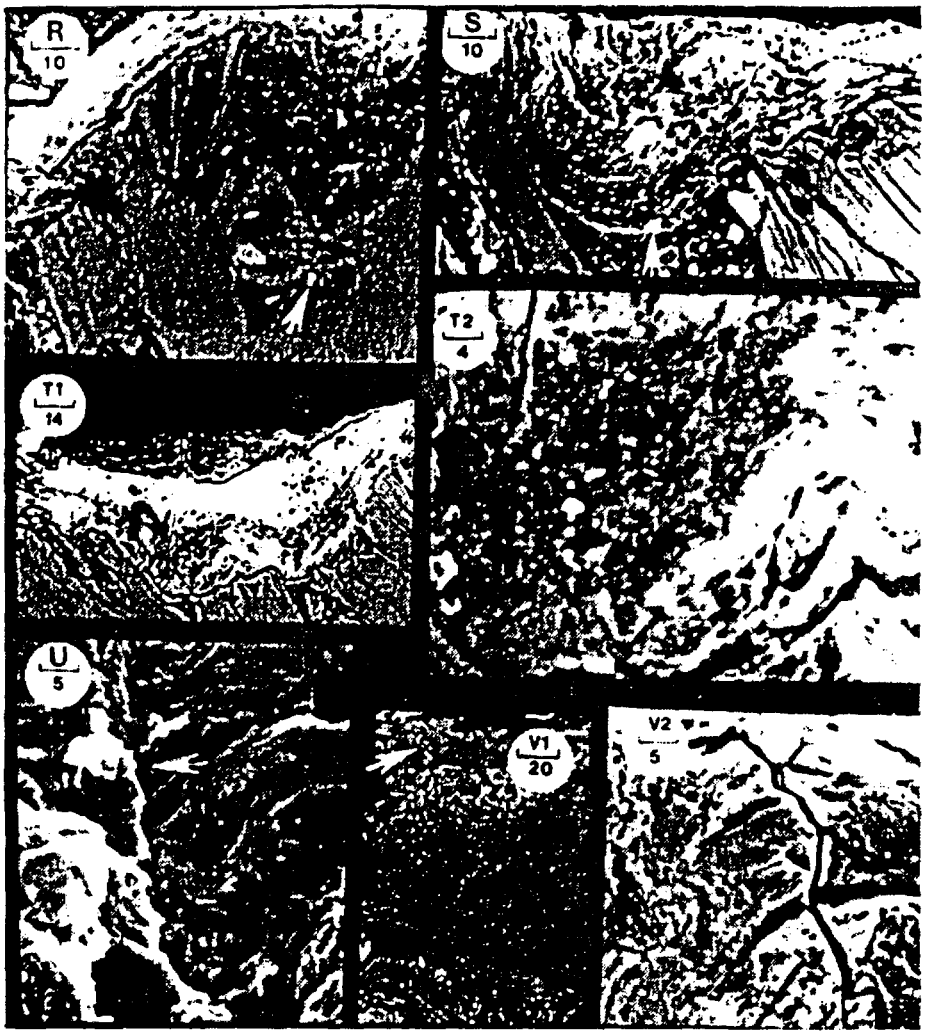
R
10
S
10
T2
4
T1
14
U
5
V1
20
V2
5

Plate 4.

Fig. R. BSE section of varnish near the rock varnish contact from Hanaupah Canyon alluvial fan, Death Valley, California. Roughly parallel layers of varnish (lighter) are found in the upper portion of the micrograph. Below the varnish on the right side of the image is a depression filled with either rock debris, aeolian fallout debris, or a mixture. This depression probably formed by the weathering of the rock after the varnish started to form. Small, bright minerals scattered throughout the varnish and the rock debris are barium sulfate crystals (e.g., arrow).

Fig. S. BSE section of varnish from Hanaupah Canyon alluvial fan, Death Valley, California. A depression in the rock is bridged by the varnish. The depression was probably not original, since varnish requires a substrate to adhere. It is likely that the rock has weathered, and the varnish is gradually collapsing into the growing depression, accounting for the down-folding of the varnish layers. Note how this growing depression contains more aeolian debris (e.g., bright barium detritus) than the layered varnish on the right part of the image, and is more porous. The growing void under the varnish is a mixture of rock detritus, and varnish, including barium-detritus (see arrow). There are also several vertically oriented fractures that have been filled with Mn-rich high-Z material.

Figs. T1 and T2. BSE images at different scales of varnish cross sections from Hanaupah Canyon alluvial fan, Death Valley, California.

In T1, a depression in the rock has filled with varnish. Note the two fractures roughly perpendicular to the varnish layering. One of the cracks is open; the other (to the right) is filled with high Z (Mn-Fe) material. Note the high Z mound where the left fracture reaches the surface. Also note that this fracture extends down to the rock.

In T2, the depression highlighted by the arrow in T1 is identified by the black curved arrow. The double white arrow points to a fracture filled with Mn-Fe material.

Fig. U. SE image of varnish from Crater Flat, southern Nevada. The arrow highlights a vertical crack in the varnish. Since sample preparation did not involve the preparation of thin sections, but only a very gentle mechanical fracturing of the varnish (in this case, breaking a flaked piece with a fingertip), it is unlikely that the vertical fractures are an artifact of sample preparation.

Figs. V1 and V2. BSE images at different scales of varnish cross sections from Coso basalt flow 28 (see Dorn, 1989). The fracture on the left side of V1 (arrow) is perpendicular to the layering, and extends from the rock surface to the rock/air interface with a mound of high Z material at the top. The poor preservation of the thin section makes the texture difficult to discern in the middle of the varnish, but the layering is easier to observe adjacent to the varnish/rock interface. The arrow in V1 is where the close-up in V2 is located. The arrow in V2 identifies the precipitation of high Z, Mn-Fe rich material, in the vertical fracture, indicating the movement of solutions through the crack. Note also that high Z materials have moved out from this vertical fracture parallel to the layering in a series of stringers.

Scale bar in microns.

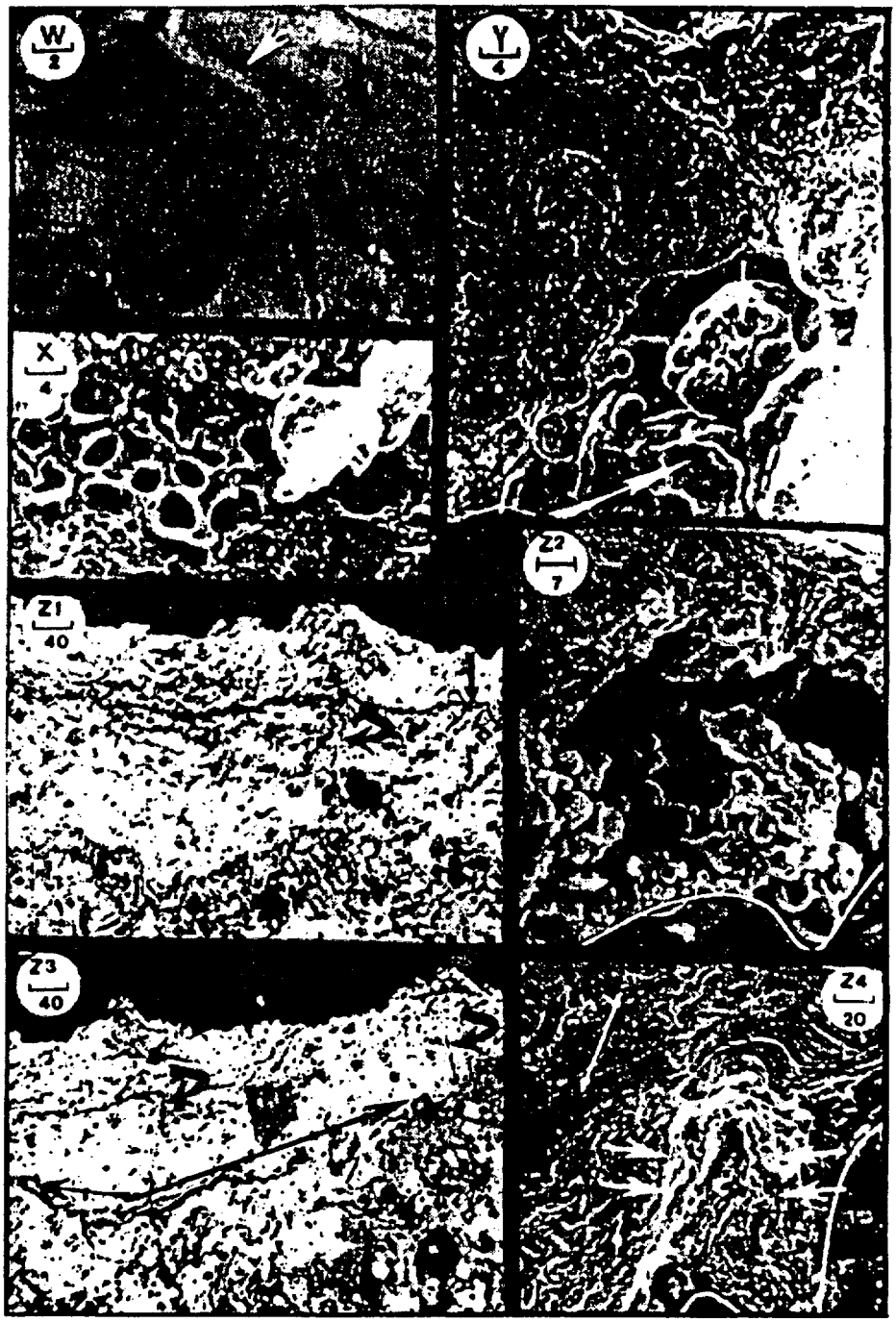
W
2
Y
4
X
4
Z2
7
Z1
40
Z3
40
Z4
20

Plate 5.

Fig. W. BSE image of rock varnish from Hanaupah Canyon alluvial fan, Death Valley, California. The arrow details a crack that has been filled with Mn-rich material. The crack is roughly perpendicular to the layering. Note that a portion of the large open crack near the bottom of the image is also partially lined with Mn-rich material.

Fig. X. SE image of cross-section of varnish from Crater Flat, southern Nevada. The honeycombed structures are decayed microcolonial fungi, now partly buried by accreting varnish.

Fig. Y. SE image of cross-section of varnish from Crater Flat, southern Nevada. The smooth-textured mass in the lower right part of the image is unidentified organic matter, encrusted in Mn-Fe oxides. Where the oxide crust has broken off (arrows), the very low counts obtained with EDX indicates it is organic matter.

Figs. Z1-Z4. Deformation structures, illustrated by BSE (Z1,Z3) and SE (Z4). The rock/varnish contact in Z1 and Z3 is represented by a tonal change from bright, high Z varnish to the rock with lower Z values (with scattered high Z iron minerals). The rock/varnish contact in Z2 and Z4 is indicated by the line.

Z1. Section from Coso 28 (see Dorn, 1989 for site description) illustrating "scalloped layers" characterized by wavy layers separated by voids. Also evident are cracks normal to the surface (curved arrow) and interlayer fracturing (the arrow pointing down illustrates the end of a major fracture in the varnish).

Z2. Section of varnish collected from the -180 m shoreline of Lake Lisan, Israel, illustrating lamellate structures on top of rounded botryoidal forms with abundant pore space. Other examples of alternating lamellate and botryoidal layers are found in Dorn (1986).

Z3. Section from Coso 28, illustrating vertical cracks (curved arrows), scalloped structures (above double arrow) and contorted varnish structures (below double arrow). Some of the contortion may be due to infilled paleoerosional depressions, similar to those in Fig. I. Some is probably due to lateral pressures exerted by the wetting and drying of varnish clays. Also note the large mineral fragment (dark, low Z) imbedded in the high Z varnish.

Z4. Section from varnish on an older alluvial fan unit of the Chocolate Mountains, Mojave Desert, California. The four arrows highlight a contorted structure, similar in scale and position to some at the base of the varnish in Z3. An infilled paleodepression with abundant Ba-rich and Ca-rich grains is found to the immediate left of the double arrow (upper left corner of the image).

Scale bar in microns.

iron and clay minerals; manganese oxide diameters range from several unit cells on the order of 12 to 30 angstroms, to diameters of as much as 500 to 600 angstroms (Fig. P). These preliminary TEM data also suggest that these oxides do not include carbon.

Another implication of oxide mobility is the problem of paleomagnetic dating of rock varnish. Potter (1979) first investigated the potential of paleomagnetic variations as an indicator of varnish age. Although Potter concluded that the strength of the signal in the rock underlying the varnish was far greater than in the varnish, new methods of analyzing micron-scale changes in paleomagnetism (Renne and Onstott, 1989) should open varnish Fe-oxides to future investigation. Our results demonstrate that some of the Mn-Fe oxides are remobilized; this would reset at least part of the paleomagnetic clock. Any future paleomagnetic analyses of varnish, therefore, must avoid zones of remobilization.

Deformation of Varnish

A number of varnish cross-sections include evidence of internal deformation; this is particularly true of thicker varnishes. We have classified deformation into three preliminary groups: scallops, contortions and fractures. Scalloped layers (Figs. Z1,Z3) may result from layer deformation and pore enlargement. It is, however, quite possible that scalloped layers separated by pores may represent botryoidal structures (Dorn and Oberlander, 1982; Dorn, 1986), where voids are an intrinsic part of the botryoidal layer (Fig. Z2). Not enough is known about how botryoidal layers are represented in polished thin sections.

Contortion is most commonly found near the varnish/rock contact in thick varnishes (Figs. Z3,Z4). Wetting and drying could cause expansion and contraction of clay-rich layers with time, as Whalley (1983, 1984) speculated. These lateral pressures can cause older layers to be thrust up stratigraphically (Fig. Z4), thereby confusing the dating situation, as older varnish may be found at the same level as the younger material.

Fracturing of thick varnishes occurs mostly parallel to the layers (Figs. F, Z1,Z3). The next most common type is found perpendicular to the varnish surface (Figs. T,U,V,Z1,Z3), while some fractures cut irregularly across the varnish (Figs. F,T2,W). Scallops, contortions and fractures open up pore spaces, and must surely permit relatively large amounts of water to move through the varnish. This must result in solution and reprecipitation, moving material from where it was deposited stratigraphically. If an age determination is to be accurate, the diagenetic history must be worked out in detail for each site to be dated.

CONCLUDING REMARKS

The occurrence of rock varnish on a wide variety of geomorphic and archaeological surfaces in arid and semiarid lands makes it a very valuable dating tool. However, samples must be collected and screened properly. We have documented nine general factors that have been shown to either affect the dating of rock varnish or are likely candidates to influence a varnish date, and hence deserve

further investigation. Some of these factors can be avoided by careful field sampling. Optical and secondary electron microscopy of varnish surfaces will determine whether surface micro-hollows are common and whether biological agencies are eroding the varnish at present. However, examination of varnish cross-sections is necessary to determine whether these and other confounding factors were present in the past. While light microscope analysis of ultra-thin sections yields useful information (Fig. M), the BSE technique produces textural data with a resolution at least 10x greater than light microscopy (less than 200 angstroms as compared to 2000 angstroms for light microscopy), in addition to chemical information with X-ray analysis.

Our BSE observations also lead us to propose a possible new perspective on cation-ratio dating of rock varnish. Instead of scraping square centimeters for a cation-ratio analysis (Dorn, 1989) or using an SEM with energy-dispersive X-ray analysis to examine the top of a varnish sample (Harrington and Whitney, 1987), microtextural areas could be defined in cross-section with BSE. There would be no uncertainty here as to whether the varnish or rock was being analyzed. Also, WDX would separate barium from titanium easily. If certain microtextural areas yield statistically significant correlations between known age and the chemistry of a given texture, there would be considerably greater control over the nature of the varnish which was being sampled. While many have noted extreme chemical variability in varnish on a micron-scale (Dorn and Oberlander, 1982; Dragovich, 1988a,b; O'Hara et al., 1989; Dorn, 1990a,b), it is possible that this variability could be reduced by comparing similar varnish microtextures, for example using only the layered laminae next to the underlying rock (e.g., Figs. I,N). This new approach deserves further investigation.

Acknowledgments: This research was partially funded by the State of Nevada, Nuclear Waste Project Office, under a grant from the Nuclear Waste Fund, and NSF grant EAR/SES 87-57014. We wish to acknowledge assistance from Mifflin & Associates Inc., Las Vegas, NV. We thank Don Meiser for TEM photography and interpretation, Patrick Trusty for laboratory assistance, and J. Bell and D. Dorn for help in the field.

BIBLIOGRAPHY

Allen, C.C. (1978) Desert varnish of the Sonoran Desert: optical and electron probe microanalysis. *Journal of Geology*, Vol. 86, 743-752.

Anderson, S.W. and Krinsley, D.H. (1989) Criteria for recognition of constructional silicic lava flow surfaces: implications for cation-ratio dating of rock varnish. *Geological Society of America Abstracts with Programs*, Vol. 21, A282.

Bard, J.C. (1979) The development of a patination dating technique for Great Basin petroglyphs utilizing neutron activation and X-ray fluorescence analyses. Ph.D. dissertation, University of California, Berkeley.

Basedow, H. (1914) Aboriginal rock carvings of great antiquity in South Australia. *Journal of the Royal Anthropological Institute*, Vol. 44, 195-211.

Blackwelder, E. (1948) Historical significance of desert lacquer. *Geological Society of America Bulletin*, Vol. 59, 1367.

——— (1954) Geomorphic processes in the desert. *California State Division of Mines Bulletin*, No. 170, 11-20.

Bull, W.B. (1977) The alluvial-fan environment. *Progress in Physical Geography*, Vol. 1, 222-270.

Dethier, D.P., Harrington, C.D., and Aldrich, M.J. (1988) Late Cenozoic rates of erosion in the western Espanola basin, New Mexico: evidence from geologic dating of erosion surfaces. *Geological Society of America Bulletin*, Vol. 100, 928-937.

Dorn, R.I. (1983) Cation-ratio dating: a new rock varnish age determination technique. *Quartenary Research*, Vol. 20, 49-73.

_____ (1984) Cause and implications of rock varnish microchemical laminations. *Nature*, Vol. 310, 767-770.

_____ (1986) Rock varnish as an indicator of aeolian environmental change. In W.G. Nickling, ed., *Aeolian Geomorphology*. London: Allen & Unwin, 291-307.

_____ (1988) A rock varnish interpretation of alluvial-fan development in Death Valley, California. *National Geographic Research*, Vol. 4, 56-73.

_____ (1989) Cation-ratio dating of rock varnish: A geographical perspective. *Progress in Physical Geography*, Vol. 13, 559-596.

_____ (1990) Quaternary alkalinity fluctuations recorded in rock varnish microlaminations on western U.S.A. volcanics. *Palaeogeography, Palaeoclimatology, Palaeoecology*, Vol. 76, 291-310.

Dorn, R.I., Bamforth, D.B., Cahill, T.A., Dohrenwend, J.C., Turrin, B.D., Jull, A.J.T., Long, A., Macko, M.E., Weil, E.B., Whitley, D.S., and Zabel, T.H. (1986) Cation-ratio and accelerator-radiocarbon dating of rock varnish on archaeological artifacts and landforms in the Mojave Desert, eastern California. *Science*, Vol. 223, 730-733.

Dorn, R.I., Cahill, T.A., Eldred, R.A., Gill, T.E., Kusko, B.H., Bach, A.J., and Elliott-Fisk, D.L. (1990) Dating rock varnish by the cation ratio method with PIXE, ICP, and the electron microprobe. *International Journal of PIXE* (in press).

Dorn, R.I., Bell, J., and Peterson, F. (1988b) Implications of rock varnish dating at Crater Flat, Near Yucca Mountain, Nevada. *Geological Society America Abstracts with Programs*, Vol. 20, A54.

Dorn, R.I., and DeNiro, M.J. (1985) Stable carbon isotope ratios of rock varnish organic matter: A new paleoenvironmental indicator. *Science*, Vol. 227, 1472-1474.

Dorn, R.I. and Dragovich, D. (1990) Interpretation of rock varnish in Australia: Case studies from the Arid Zone. *Australian Geographer* (in press).

Dorn, R.I., Jull, A.J.T., Donahue, D.J., Linick, T.W., and Toolin, L.J. (1989) Accelerator Mass Spectrometry Radiocarbon Dating of Rock Varnish. *Geological Society America Bulletin*, Vol. 101, 1363-1372.

Dorn, R.I., Nobbs, M., and Cahill, T.A. (1988a) Cation-ratio dating of rock engravings from the Olary Province of arid South Australia. *Antiquity*, Vol. 62, 681-689.

Dorn, R.I. and Oberlander, T.M. (1981) Rock varnish origin, characteristics and usage. *Zeitschrift fur Geomorphologie*, Vol. 25, 420-436.

_____ (1982) Rock varnish. *Progress in Physical Geography*, Vol. 6, 317-367.

Dorn, R.I., Tanner, D.L., Turrin, B.D., and Dohrenwend, J.C. (1987a) Cation-ratio dating of Quaternary materials in the east-central Mojave Desert, California. *Physical Geography*, Vol. 8, 72-81.

Dorn, R.I., Turrin, B.D., Jull, A.J.T., Linick, T.W., and Donahue, D.J. (1987b) Radiocarbon and cation-ratio ages for rock varnish on Tioga and Tahoe morainal boulders of Pine Creek, eastern Sierra Nevada, California, and their Paleoclimatic Implications. *Quarternary Research*, Vol. 28, 38-49.

Dorn, R.I., and Whitley, D.S. (1984) Chronometric and relative age determination of petroglyphs in the western United States. *Annals Association American Geographers*, Vol. 74, 308-322.

Dragovich, D. (1986) Minimum age of some desert varnish near Broken Hill, New South Wales. *Search*, Vol. 17, 149-151.

_____ (1988a) A preliminary electron probe study of microchemical variations in desert varnish in western New South Wales, Australia. *Earth Surface Processes and Landforms*, Vol. 13, 259-270.

_____ (1988b) Desert varnish and environmental change near Broken Hill, western New South Wales. *Earth-Science Reviews*, Vol. 25, 399-407.

Duerden, P., Cohen, D.D., Dragovich, D., and Clayton, E. (1986) Ion beam analysis studies of desert varnish. *Nuclear Instruments and Methods in Physics Research*, Vol. B15, 643-646.

Elvidge, C.D. and Iverson, R.M. (1983) Regeneration of desert pavement and varnish. In R.H. Webb and H.G. Wilshire, eds., *Environmental Effects of Off-Road Vehicles*. New York: Springer Verlag, 225-243.

Engel, C.G. and Sharp, R.P. (1958) Chemical data on desert varnish. *Geological Society America Bulletin*, Vol. 69, 487-518.

Gillespie, A.R. (1987) $^{40}Ar - ^{39}Ar$ "exposure age" of geomorphic surfaces; the effect of range fires. *EOS*, Vol. 68, 1286.

Glazovskiy, A.F. (1985) Rock varnish in the glacierized regions of the Pamirs (in Russian). *Data of the Glaciological Studies (Moscow)*, Vol. 54, 136-141.

Goldstein, J.I., Newbury, D.E., Echlin, S., Joy, D.C., Fiori, C., and Lifshin, E. (1981) *Scanning Electron Microscopy and Microanalysis*. New York: Plenum Press.

Harrington, C.D. (1987) Application of rock varnish dating of Quaternary surficial deposits in determining times of fault movement. *U.S. Geological Survey Open File Report*, No. 87- 673, 70-75.

_____ (1988) Recognition of components of volcanic ash in rock varnish and the dating of volcanic ejecta plumes. *Geological Society of America Abstracts with Programs*, Vol. 20, 167.

_____, Raymond, R.J., and Krier, D.J. (1989) Barium concentration in rock varnish: implications for calibrated rock varnish dating curves. *Geological Society of America Abstracts with Programs*, Vol. 21, A343.

Harrington, C.D. and Whitney, J.W. (1987) Scanning electron microscope method for rock varnish dating. *Geology*, Vol. 15, 967-970.

Hayden, J. (1976) Pre-altithermal archaeology in the Sierra Pinacate, Sonora, Mexico. *American Antiquity*, Vol. 41, 274-289.

Heizer, R.F and Baumhoff, M.A. (1962) *Prehistoric Rock Art of Nevada and Eastern California*. Berkeley, CA: University of California Press.

Hem, J. (1985) Study and interpretation of the chemical characteristics of natural water. *U.S. Geological Survey Water Supply Paper*, No. 2254, 1-137.

Hunt, C.B. and Mabey, D.R. (1966) Stratigraphy and structure, Death Valley, California. *U.S. Geological Survey Professional Paper*, No. 494A.

Krinsley, D. and Anderson, S. (1989) Desert varnish: a new look at chemical and textural variations. *Geological Society of America Abstracts with Programs*, Vol. 21, 103.

Krinsley, D. and Manley, C.R. (1989) Backscattered electron microscopy as an advanced technique in petrography. *Journal of Geological Education*, Vol. 37, 202-209.

Lakin, H.W., Hunt, C.B., Davidson, D.F., and Odea, U. (1963) Variation in minor-element content of desert varnish. *U.S. Geological Survey Professional Paper*, No. 475-B, B28-B31.

Liu, T. and Zhang, Y. (1990) Establishment of a cation-leaching curve of varnish for the Dunhuang region, western China. *Seismology and Geology* (in press).

Long, J.V.P. (1967) Electron microprobe analysis. In J. Zussman, ed., *Physical Methods in Determinative Mineralogy*. New York: Academic Press, 215-260.

Merrill, G.P. (1898) Desert varnish. *U.S. Geological Survey Bulletin*, No. 150, 389-391.

O'Hara, P., Krinsley, D.H., and Anderson, S.W. (1989) Elemental analysis of rock varnish using the ion microprobe. *Geological Society America Abstracts with Programs*, Vol. 21, A165.

Perry, R.S., and Adam, J. (1978) Desert varnish: evidence of cyclic deposition of manganese. *Nature*, Vol. 276, 489-491.

Pineda, C.A., Jacobson, L., and Peisach, M. (1988) Ion beam analysis for the determination of cation-ratios as a means of dating southern African Rock Varnishes. *Nuclear Instruments and Methods in Physics Research*, Vol. B35, 463-466.

Potter, R.M. (1979) The tetravalent manganese oxides: clarification of their structural variations and relationships and characterization of their occurrence in the terrestrial weathering environment as desert varnish and other manganese oxides. Ph.D. dissertation, California Institute of Technology.

_____and Rossman, G.R. (1977) Desert varnish: The importance of clay minerals. *Science*, Vol. 196, 1446-1448.

_____ (1979) The manganese- and iron-oxide mineralogy of desert varnish. *Chemical Geology*, Vol. 25, 79-94.

Pye, K. and Krinsley, D.H. (1984) Petrographic examination of sedimentary rocks in the SEM using backscattered electron detectors. *Journal Sedimentary Petrology*, Vol. 54, 877-888.

Raymond, R., Jr., Harrington, C.D., Bish, D.L., and Chipera, S.J. (1988a) Mineralogic characterization of rock varnish from Nye County, Southern Nevada. *Geological Society America Abstracts with Programs*, Vol. 20, 345.

Raymond, R., Jr., Harrington, C.D., and Bish, D.L. (1988b) Role of geologic substrate in rock varnish formation. *EOS*, Vol. 69, 1049.

Raymond, R., Jr., Harrington, C.D., and Reneau, S.L. (1989) An SEM view of rock varnish sedimentary micro-basins. *Geological Society of America Abstracts with Programs*, Vol. 21, A333.

Renne, P.R. and Onstott, T.C. (1989) Laser-selective demagnetization: a new technique in paleomagnetism and rock magnetism. *Science*, Vol. 242, 1152-1155.

Robinson, V.N.E. and George, E.P. (1978) Electron scattering in the SEM. *Scanning Electron Microscopy*, Vol. 1978/I, 859-866.

Robinson, V.N.E. and Nickel, E.J. (1979) A useful new technique for mineralogy: the backscattered electron/low vacuum mode of SEM operation. *American Mineralogist*, Vol. 64, 1322-1328.

Smith, B.J. and Whalley, W.B. (1988) A note on the characteristics and possible origins of desert varnishes from southeast Morocco. *Earth Surface Processes and Landforms*, Vol. 13, 251-258.

Spaulding, W.G. (1985) Vegetation and climates of the last 45,000 years in the vicinity of the Nevada Test Site, South-Central Nevada. *U.S. Geological Survey Professional Paper*, No. 1329, 1-83.

Staley, J.T., Palmer, F., and Adams, J.B. (1982) Microcolonial fungi: common inhabitants on desert rocks? *Science*, Vol. 215, 1093-1095.

Talibudeen, O. (1981) Cation exchange in soils. In D.J. Greenland and M.H.B. Hayes, *Chemistry of Soil Processes*. New York: John Wiley, 115-177.

Taylor-George, S., Palmer, F.E., Staley, J.T., Borns, D.J., Curtiss, B., and Adams, J.B. (1983) Fungi and bacteria involved in desert varnish formation. *Microbial Ecology*, Vol. 9, 227-245.

Truter, M.R. (1973) Structures of organic complexes with alkali metal ions. In J.D. Dunitz, ed., *Alkali Metal Complexes with Organic Ligands: Structure and Bonding*. Berlin: Springer-Verlag, 71-111.

Whalley, W.B. (1983). Desert varnish. In A.S. Goudie and D. Pye, eds., *Chemical Sedimentation and Geomorphology*. London: Academic Press, 197-226.

_____ (1984) High altitude rock weathering processes. In K.J. Miller, ed., *International Karakoram Project, Volume One*. Cambridge: Cambridge University Press, 365-373.

White, C.H. (1924) Desert varnish. *American Journal of Science*, Vol. 9, 413-420.

White, D.E., Hem, J., and Waring, G.A. (1963) Chemical composition of subsurface waters. *U.S. Geological Survey Professional Paper*, No. 440-F, F1-F67.

Whitney, J.W., Harrington, C.D., and Glancy, P.A. (1988) Deciphering Quaternary alluvial history in Las Vegas Wash, Nevada by radiocarbon and rock varnish dating. *Geological Society of America Abstracts with Programs*, Vol. 20, 243.

6. A. G. Whittaker, *ibid.* 276, 695 (1978); *Science* 200, 763 (1978); *ibid.* 229, 485 (1985).
7. R. B. Heimann, J. Kleinman, N. M. Salansky, *Nature* 306, 164 (1983).
8. P. P. K. Smith and P. R. Buseck, *Science* 216, 984 (1982); *ibid.* 229, 486 (1985).
9. J. Heremans, C. H. Olk, G. L. Eesley, J. Steinbeck, G. Dresselhaus, *Phys. Rev. Lett.* 60, 453 (1988), and references therein.
10. J. Steinbeck, G. Braunstein, M. S. Dresselhaus, T. Venkatesan, D. C. Jacobson, *J. Appl. Phys.* 58, 4374 (1985).
11. G. Galli, R. M. Martin, R. Car, M. Parrinello, *Phys. Rev. Lett.* 63, 988 (1989).
12. ———, *Phys. Rev. B*, in press.
13. J. Tersoff, *Phys. Rev. Lett.* 61, 2879 (1989).
14. J. S. Gold, W. A. Bassett, M. S. Weathers, J. M. Bird, *Science* 225, 921 (1984).
15. M. van Thiel and F. H. Ree, *J. Appl. Phys.* 62, 1761 (1987).
16. F. P. Bundy, *J. Chem. Phys.* 38, 631 (1963).
17. ———, *J. Geophys. Res.* 85, 6930 (1980).
18. As pointed out by Dickey *et al.* (2), this might bring the T_m of C into the range of Earth's geotherm at depths greater than 1200 km, and liquid C could play an important role in the dynamics of Earth's mantle.
19. J. W. Shaner, J. M. Brown, C. A. Swenson, R. G. McQueen, *J. Phys. C* 8, 235 (1984).
20. A. C. Mitchell, J. W. Shaner, R. N. Keeler, *Physica* 139, 386 (1986).
21. W. A. Bassett, *Bull. Am. Phys. Soc.* 35, 465 (1990).
22. M. Togaya, paper presented at the First International Conference on the New Diamond Science and Technology (Tokyo, 1988).
23. R. Car and M. Parrinello, *Phys. Rev. Lett.* 55, 2471 (1985).
24. For a review, see S. Lundqvist and N. H. March, Eds., *Theory of the Inhomogeneous Electron Gas* (Plenum, New York, 1983).
25. M. T. Yin and M. L. Cohen, *Phys. Rev. B* 24, 6121 (1981).
26. J. R. Chelikowsky and S. Louie, *ibid.* 29, 3470 (1984).
27. M. T. Yin and M. L. Cohen, *ibid.*, p. 6996.
28. S. Fahy, S. Louie, M. L. Cohen, *ibid.* 34, 1191 (1986), and references therein.
29. M. Posternak, A. Baldereschi, A. J. Freeman, E. Wimmer, M. Weinert, *Phys. Rev. Lett.* 50, 761 (1983), and references therein.
30. R. Biswas, R. M. Martin, R. J. Needs, O. H. Nielsen, *Phys. Rev. B* 30, 3210 (1984); *ibid.* 35, 9559 (1987).
31. M. T. Yin and M. L. Cohen, *Phys. Rev. Lett.* 50, 2006 (1983).
32. G. Galli, R. M. Martin, R. Car, M. Parrinello, *ibid.* 62, 555 (1989).
33. S. Nosé, *Mol. Phys.* 52, 255 (1984); *J. Chem. Phys.* 81, 511 (1984).
34. W. Hoover, *Phys. Rev. A* 31, 1695 (1985).
35. We have adopted a nonlocal pseudopotential [G. B. Bachelet, D. Hamman, M. Schluter, *Phys. Rev. B* 26, 4199 (1982)] of the form suggested by L. Kleinman and D. M. Bylander [*Phys. Rev. Lett.* 48, 1425 (1982)] to describe the interaction between core (1*s*) and valence electrons. The single particle orbitals at the Γ point of the Brillouin zone have been expanded in plane waves, with a cutoff of 35 Ry. Time evolution has been simulated with a time step of 10^{-16} s.
36. The equilibrium density of diamond is 3.5 g cm^{-3}.
37. As a check on our work, we compared with experiment our estimate of the linear expansion coefficient

$$\alpha = \frac{1}{3B}\left(\frac{\partial P}{\partial T}\right)_n$$

where B is the bulk modulus, of solid diamond for T higher than the Debye temperature (2000 K). Assuming a weak dependence of B upon T, we can use $B(T = 0)$ in the expression of α. The calculated value, $\approx 510^{-6}$ K^{-1}, is in satisfactory agreement with the experimental one of $\approx 710^{-6}$ K^{-1}.
38. The expression is

$$g(r) = \sum_{ij} g_{ij}(r)$$

where i and j denote the differently coordinated sites present in the system; g_{ij} is defined as the number of particles with coordination i per unit volume, found at a distance r from an origin site with coordination j.
39. I. Stich *et al.*, *Phys. Rev. Lett.* 63, 2240 (1989).
40. This work was supported by NSF grant DMR86-12860 (G.G. and R.M.M.) and by the Scuola Internazionale Superiors di Studi Avanzati (SISSA)–Centro Interuniversitario Nord-Est per il Calcolo Applicato (CINECA) by collaborative project, under the sponsorship of the Italian Ministry for Public Education (R. C. and M. P.). The computational work was done at the National Center for Supercomputing Applications. We benefited from useful discussions with J. Belak, M. Grumbach, M. Ross, J. W. Shaner, M. S. Weathers, and R. Young.

6 August 1990; accepted 12 October 1990

Stable Isotopic Evidence for a Pedogenic Origin of Carbonates in Trench 14 near Yucca Mountain, Nevada

JAY QUADE AND THURE E. CERLING

Layered carbonate and silica encrust fault fractures exposed in Trench 14 near Yucca Mountain, site of the proposed high-level nuclear waste repository in southern Nevada. Comparison of the stable carbon and oxygen isotopic compositions of the fracture carbonates with those of modern soil carbonates in the area shows that the fracture carbonates are pedogenic in origin and that they likely formed in the presence of vegetation and rainfall typical of a glacial climate. Their isotopic composition differs markedly from that of carbonate associated with nearby springs. The regional water table therefore remained below the level of Trench 14 during the time that the carbonates and silica precipitated, a period probably covering parts of at least the last 300,000 years.

ONE OF THE CHIEF ASSUMPTIONS used to justify locating a high-level nuclear waste repository at Yucca Mountain is that the buried waste will remain well within the unsaturated zone for the next several hundreds of thousands of years, regardless of even large changes in water-table elevation in response to climate change. A serious challenge to the validity of this assumption was the discovery of a complex network of carbonate and silica fillings in the fractures associated with several faults bordering Yucca Mountain. The best known and the most controversial of these fracture fillings are located in Trench 14, which crosses the Bow Ridge fault (Fig. 1). The thick, well-layered, and well-indurated nature of the fillings caused immediate concern because of similarity in these respects to vein cements and travertines associated with springs (*1*) and because of the apparent Quaternary age of some of the carbonate (*2*). A spring origin would imply that there was a rise in the regional water table, presumably during glacial maxima, to at least the level of Trench 14. Trench 14 is about 150 m above the level of the proposed repository and 400 m above the water table. A return to glacial hydrologic conditions might then result in ground-water flooding of the repository and rapid transport of radionuclides to nearby discharge points, such as Trench 14.

There has been a substantial effort at establishing the origin of the fracture cements in Trench 14 (*1*). An alternate hypothesis to a spring origin is that the carbonates and silica formed in soils in the vadose zone for hundreds of thousands of years (*2*). In this case, meteoric water infiltrating through the fractures deposited carbonate and silica as a normal part of desert soil formation.

To test these two hypotheses, we compared the carbon and oxygen isotopic data from Trench 14 to those in modern desert soils. We sampled soils in settings where the water table has remained tens to hundreds of meters below the surface during pedogenesis and therefore where ground water has played no role in carbonate formation. We took special care to sample soils younger than 7000 years old in order to establish the relation between the isotopic composition in soil carbonate and modern vegetation and rainfall (*3*). Pack-rat midden and pollen evidence shows that the distribution of vegetation has not greatly changed in the region during that span (*4*). We sampled soils displaying weak Stage I morphology (*5*), a degree of development consistent with a mid-to-late Holocene age. Five accelerator dates on thin carbonate coatings from three representative soils yielded ages between 3820 and 820 years (Table 1) (*6*).

The $\delta^{13}C$ content of modern soil carbonate varies substantially with elevation (Fig. 2) because of variations in (i) the isotopic composition of desert plants and (ii) the proportion of atmospheric CO_2 in the des-

Department of Geology and Geophysics, University of Utah, Salt Lake City, UT 84112.

ert soil atmosphere (*3*). Plants fractionate C along three differing metabolic pathways: C_3, C_4, and CAM. The C_3 plants, including conifers, mountain shrubs, and some grasses, make up virtually all of the biomass at higher elevations in the southern Great Basin. The $\delta^{13}C$ of these plants average −24 to −25 per mil at high-elevation sites, and coexisting soil carbonate has a $\delta^{13}C$ higher than in this biomass by 14 to 16 per mil (*7*). At lower elevations, C_4 and CAM (*8*) plants, as well as many C_3 shrubs and herbs, are present; here, C_4 plants are the most abundant, and they have an average $\delta^{13}Cd$ of −13 per mil. A larger proportion of atmospheric CO_2, with an average $\delta^{13}C$ of −6 per mil, is present deep in soils at low elevations because of lower plant respiration rates. This C reservoir further increases the $\delta^{13}C$ of soil CO_2—and therefore also of soil carbonate—that is derived from the mix of C_3 and C_4 plants. Holocene-age soil carbonates from each of the major vegetation zones therefore display a distinct $\delta^{13}C$ signature (Fig. 2). For example, the $\delta^{13}C$ of soil carbonates average −9 per mil in the ponderosa pine zone (>2400 m) and −7.4 ± 0.8 per mil (15 samples) in the pinyon-juniper-sage zone (1800 and 2300 m). Near sea level in Death Valley, the $\delta^{13}C$ of soil carbonates is −2 to +2 per mil, reflecting the contribution of C_3 creosote and C_4 desert holly shrubs, as well as some mixing of atmospheric CO_2 deep in the soil (*3*). The $\delta^{18}O$ composition of soil carbonate also decreases with elevation (Fig. 3), irrespective of parent material, primarily because the $\delta^{18}O$ composition of rainfall also decreases with increasing elevation. Evaporation or differing penetration of meteoric water seasonally also may influence the $\delta^{18}O$ of pedogenic carbonates (*3*).

Fig. 1. The fracture system filled with layered calcite and silica, exposed on the south wall, east end of Trench 14. The trench wall is about 3.5 m high.

Table 1. The ^{14}C dates (in ^{14}C years before present) by accelerator mass spectrometry on pedogenic carbonate from three (SM-2, 3, 4) soils in the Spring Mountains, 100 km south of Yucca Mountain (*6*). For each sample, we scraped 50 to 100 mg of material from clast undersides, taking care not to include any carbonate from the host clast or from older cements. Further details on soil sites, designated by these field numbers, is in (*3*).

Lab no.	Field no.	Age	Soil depth (cm)
AA-3697	SM-3(B)	1210 ± 50	15
AA-3698	SM-2A	1900 ± 60	Surface
AA-3699	SM-2B	3820 ± 55	10 to 15
AA-3700	SM-2C	1785 ± 65	30 to 40
AA-3701	SM-4	820 ± 50	50 to 60

We sampled five Holocene-age soils in the vicinity of Trench 14. The local vegetation is dominated by C_3 shrubs such as black bush (*Coleogyne ramosissma*) and Nevada joint fir (*Ephedra nevadensis*); creosote (*Larrea divaricata*), burrobush (*Ambrosia dumosa*), and twin fruit (*Menodora spinescens*) are less abundant. Shadscale (*Atriplex confertifolia*), a C_4 shrub, is also common. All the herbs, and some of the grasses (mainly *Stipa* sp. and *Oryzopsis hymenoides*), are C_3 plants. Fluffgrass (*erioneuron pulchellum*), a C_4 grass, grows in the early summer. This mix of C_3 and C_4 plants, and moderate plant respiration rates, produces $\delta^{13}C$ values in soil carbonate of −4.2 to −7.1 per mil (14 samples) below a depth of 50 cm. The $\delta^{18}O$ (PDB) of the same carbonates nearly all fall between −7 and −10.6 per mil.

We analyzed 22 samples from most of the major veins exposed in Trench 14. The $\delta^{13}C$ of all but one of samples ranges from −6.3 to −7.7 per mil (average −7.0 ± 0.4 per mil, Fig. 2). The Trench 14 carbonates have low $\delta^{13}C$ values compared to those in nearby Holocene-age soil carbonate; these low values indicate that the Trench 14 carbonates did not form in equilibrium with the modern vegetation in the area. However, the C isotope data do overlap with values from modern soils about 750 m above the site, where cover is dominated by pinyon (*Pinus monophylla*), juniper (*Juniperus osteosperma*), and sagebrush (*Artemisia tridentata*). Samples from this vegetation zone yielded a $\delta^{13}C$ average of −7.4 ± 0.8 per mil. A single sample from Trench 14 yielded a result of −4.6 per mil, a value that is

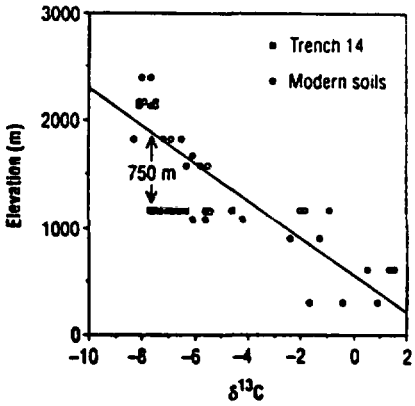

Fig. 2. The $\delta^{13}C$ (PDB) of pedogenic carbonate in modern soils developed on volcanic parent materials along elevation transects in the southern Great Basin. The linear regression (shown) for 39 soil analyses is: elevation (in meters) = (554.4 ± 103.8) − (174.98 ± 18.3)z, where z is the $\delta^{13}C$ (PDB) of soil carbonate. The $\delta^{13}C$ compositions of all but one sample from Trench 14 are lower than that for carbonate in Holocene-age soils in the vicinity but overlap with the $\delta^{13}C$ range of soil carbonate ~750 m higher on the transects.

observed in modern soils nearby. The other 21 samples from Trench 14 display a narrow range of $\delta^{18}C$ (PDB), between −10.5 and −11.8 per mil (average of −11.3 ± 0.3, Fig. 3). Again, this is close to the values for modern soil carbonate in the pinyon-juniper-sage zone (average −11.5 ± 1.4 per mil) and is unlike nearby modern soils at −9.8 ± 1.2 per mil (*9*).

Evidence from fossil pack-rat middens indicates that vegetation zones were displaced about 1,000 m downward during the last full-glacial period (16,000 to 19,000 years ago) (*4*). Juniper, sagebrush, and pinyon then dominated the vegetation at Yucca Mountain. Our evidence indicates that the Trench 14 carbonates, if formed in soils, would have precipitated in equilibrium with this plant assemblage during the glacial maxima. The $\delta^{18}O$ of ground water in the region during glacial times was 1.5 to 2.0 per mil less than that of modern ground water (*10, 11*); this is close to the 1.5-per-mil average difference we observe between carbonates in Trench 14 and nearby modern soils.

A further test of a soil versus spring origin comes in comparing the C isotopic composition of coexisting carbonate and occluded organic matter. The difference should be 14 to 16 per mil in soils with relatively high respiration rates, including those found under pinyon-juniper-sage cover (*7*). The Trench 14 carbonates contain 0.12 to 0.18% organic C (Table 2). The average difference between carbonates and occluded organic matter was found to be 14.6 ± 0.2 per mil (3 samples), which supports a pe-

Table 2. The $\delta^{13}C$ (PDB) of coexisting carbonate and occluded organic (org.) matter from Trench 14. Roughly 30-g samples of carbonate were pyrolized at 650 °C for 1 hour in covered crucibles, thus converting organic matter to pure carbon. Carbon was then concentrated by hydrolysis of the carbonate with 3N HCl.

Sample	Org. C (percent*)	$\delta^{13}C$ carbonate (per mil)	$\delta^{13}C$ org. matter (per mil)	Difference (per mil)
YM-14-8B	0.18	−6.3	−21.2	14.9
YM-14-11B	0.13	−7.0	−21.6	14.6
YM-14-12B	0.12	−7.3	−21.7	14.4

*By weight.

dogenic origin for the vein fillings in Trench 14. The spring carbonates we collected from veins at Ash Meadows (see below) did not contain sufficient occluded organic matter for analysis.

Uranium-trend dates and other geologic evidence (*2, 12*) suggest that carbonate in several fractures exposed in Trench 14 accumulated during the last 300,000 years, but that other fractures were filled earlier. As glacial periods have occurred about every 100,000 years (*10*), cementation events in the fractures could have occurred in one or more of many glacial periods during the latter half of the Pleistocene, and possibly earlier.

How do the isotope results on carbonates from Trench 14 compare to those expected for carbonates of unequivocal spring origin? To answer this question we considered two situations that account for the different types

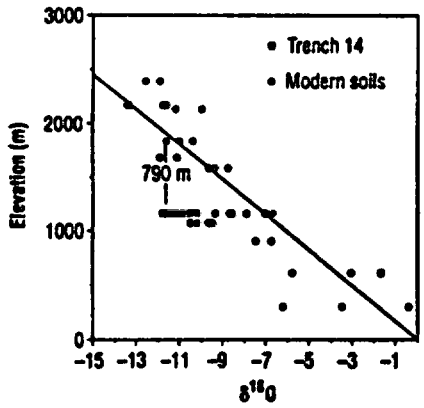

Fig. 3. The $\delta^{18}O$ (PDB) of pedogenic carbonate in modern soils developed on volcanic parent materials along elevation transects in the southern Great Basin. The linear regression (shown) for 39 soil analyses is: elevation (in meters) = (−149.0 ± 207.7) − (173.7 ± 18.5)x, where x is the $\delta^{18}O$ (PDB) of soil carbonate. On average, Trench 14 carbonates have $\delta^{18}O$ values consistent with soil carbonate now ~790 m above the site in the lower pinyon-juniper-sagebrush zone, the same setting indicated by the C isotopes in Trench 14.

of spring conditions found in the region: (i) spring discharge from the regional water table in fractured, transmissive bedrock; and (ii) cool spring discharge fed by local perched water.

Vein carbonate associated with springs that discharge from the regional water table have been analyzed in the Ash Meadows area south of Yucca Mountain (*10, 13*). Carbonates there and at Trench 14 fill major extensional fractures within a few meters of the surface, from which, in the case of Ash Meadows, ground water discharges directly from a major aquifer. Although different ground-water systems underlie the two areas, the age, temperature, and most aspects of the isotope chemistry of the two systems are alike. The $\delta^{18}O$ (SMOW) of ground water at Ash Meadows is nearly identical to that of the ground water underlying Trench 14, at −13 to −13.5 per mil (*10, 11, 14*). However, the $\delta^{13}C$ of dissolved inorganic carbon in Ash Meadows ground water is greater by 3 to 4 per mil in comparison to ground water under Trench 14, probably because of exchange with Paleozoic carbonate rocks along the flow path.

The $\delta^{18}O$ of spring carbonates from Devil's Hole, located near to Ash Meadows, is about −14.5 and −16.5 per mil (PDB) for interglacial and glacial climates, respectively (*10*) (Fig. 4). These values are appreciably lower than values for Trench 14 carbonates because of the low $\delta^{18}O$ ratios of the ground waters and high temperatures of the springs. The $\delta^{18}O$ values of carbonates in Trench 14 require temperatures of formation of ≤15°C (*15*), if the inferred $\delta^{18}O$ range of ground water during the last 250,000 years (*10, 11*) is correct. Spring discharge from the regional aquifer at such low temperatures is highly unlikely at Trench 14 in view of the geologic setting. Temperatures in springs at Ash Meadows–Devil's Hole and in ground water under Trench 14 (*14*) generally exceed 28°C because of deep circulation of ground water, and these temperatures are unaffected by short-term (<300,000 year) climate fluctuations (*10*). Temperatures as low as 20°C are known from minor springs fed by deeply circulated water at Ash Meadows. But in these springs, water passes slowly to the surface through aquitards composed of fine-grained Pliocene basin-fill, probably after leakage from the more transmissive carbonate aquifer below. The slow circulation apparently causes spring water to partially or wholly equilibrate with near-surface temperatures (*16*). No fine-grained strata have been observed in the Trench 14 area. The transmissive nature of the fractured volcanic rocks and fault system at Trench 14 would have led to rapid ascent of ground water, as in the examples from Ash Meadows, where

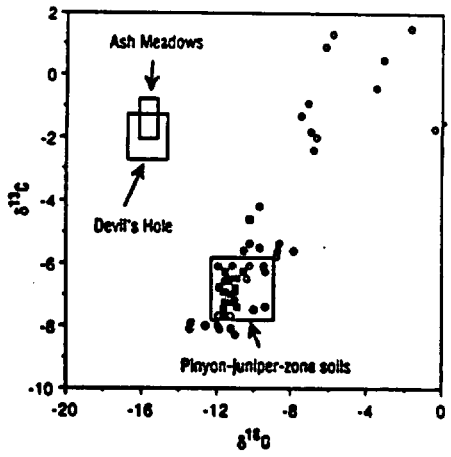

Fig. 4. The $\delta^{18}O$ (PDB) versus $\delta^{13}C$ (PDB) of carbonates from Holocene soils (○)/(■), Trench 14, and springs. In all, 21 of the 22 analyses from Trench 14 fall within the isotopic field for Holocene-age soil carbonate found in the pinyon-juniper-sagebrush zone on volcanic parent material. A single result lies in the field defined by modern soils in the vicinity. Spring carbonates from Ash Meadows (*13*) and Devil's Hole (*10*) plot completely outside the observed range for carbonates in modern soils and in Trench 14.

springs flowing from bedrock have temperatures ≥28°C irrespective of discharge rate (*16*).

The $\delta^{13}C$ of spring carbonate at Ash Meadows and Devil's Hole ranges from −1.5 to −2.9 per mil (*17*) (Fig. 4). This carbonate precipitated in isotopic equilibrium with HCO_3^- in ground water that had a $\delta^{13}C$ of −4 to −5 per mil. The HCO_3^- in ground water under Yucca Mountain is much more variable, ranging between −11 and −2 per mil (*14*). If such a broad range of spring water compositions did produce over a long period the narrow range of $\delta^{13}C$ values observed in Trench 14 carbonates, it would be highly fortuitous.

The overriding difficulty with the second situation described above, spring discharge of local perched water, is that the hydrogeologic setting is generally wrong. Springs in perched water systems normally display a large upgradient catchment area and an aquitard unit that crops out at the point of discharge. Perched water in the region is typically found above and discharges from strata with a low permeability, such as zeolitized air-fall tuffs (*16*). In contrast, the rocks at Trench 14 are highly fractured ash-flow tuff and permeable alluvium; the nearest thin ash-fall aquitards are several hundred meters below Trench 14. However, the possibility of a perched water setting cannot be refuted by our isotopic results. The water in perched zones could have originated locally as precipitation and therefore had a similar oxygen isotopic composition to soil water. The HCO_3^- in perched

water may also be in equilibrium with locally derived plant CO_2, as HCO_3^- is in soil water.

Other evidence also supports a pedogenic origin for the Trench 14 carbonates. The morphology (*2*) and petrography of the carbonates and silica fillings are consistent with a soil origin, as is micromorphological, clay mineralogical, trace element (*18*), and isotope tracer (*19*) evidence. Oxygen isotopes from the silica cements indicate that the temperatures of formation were ~15°C, consistent with that in a pedogenic environment (*2*).

REFERENCES AND NOTES

1. P. S. Justus and N. K. Stablein, *Geotimes* **34**, 14 (1989); papers presented at the DOE/NRC meeting on the calcite and opaline silica peer review, 25 to 27 May 1987, Las Vegas, NV; D. T. Vaniman, D. L. Bish, S. Chipera, *Los Alamos Natl. Lab. Rep. LA-11289-MS (UC-70)* (1988).
2. E. M. Taylor, *U.S. Geol. Surv. Bull.*, in press.
3. J. Quade, T. E. Cerling, J. R. Bowman, *Geol. Soc. Am. Bull.* **101**, 464 (1989).
4. W. G. Spaulding, *U.S. Geol. Surv. Prof. Pap.* 1329 (1985). Spaulding mainly sampled middens from all around the adjacent Nevada Test Site and Amargosa Desert, within ~100 km of Trench 14, and from the Sheep Range near Las Vegas.
5. L. H. Gile, F. F. Peterson, R. B. Grossman, *Soil Sci.* **101**, 347 (1966). Weak Stage I refers to pedogenic carbonate only as coatings on clast undersides.
6. J. Quade, *Quat. Res.* **26**, 340 (1986); E. M. Taylor, thesis, University of Colorado, Boulder (1986); S. G. Wells, L. D. McFadden, J. C. Dohrenwend *Quat. Res.* **27**, 130 (1987). Soil carbonate development is dependent on time and other factors, such as parent material, dust flux, and so forth. However, weak stage I morphology is observed to be associated with surfaces younger than late Pleistocene, irrespective of parent material. Carbonate coatings of our samples were discontinuous patches on clast undersides and were ≤1 mm in thickness. Clasts were occasionally encrusted with older cements, and these were avoided. The patterns displayed by stable C isotopes in these soils (*3*) indicate that there has been negligible detrital contamination or inheritance from dissolution of parent material. As such, these dates represent a composite age of all the layers of carbonate present. Because of the very young ages we obtained, it is unlikely that any pre-Holocene component to the carbonate is present.
7. T. E. Cerling, J. Quade, Y. Wang, J. R. Bowman, *Nature* **341**, 138 (1989). Complete isotopic equilibrium between C species is obtained before the precipitation of soil carbonate, and this accounts for 10 to 11 per mil of the enrichment. Diffusion effects on soil CO_2 account for about 4.4 per mil further enrichment in the carbonates. Parent material has no influence on the outcome (*3*). All stable isotope analyses on carbonates are reported relative to PDB (Pee Dee Belemnite) using standard notation, where $\delta^{13}C(PDB)$ or $\delta^{18}O(PDB) = [(R_{sample}/R_{standard}) - 1] \times 1000)$ and $R = (^{13}C/^{12}C_{sample})/(^{13}C/^{12}C_{standard})$ or $^{18}O/^{16}O_{sample}/^{18}O/^{16}O_{standard}$ respectively. The isotopic composition of water is reported relative to SMOW (standard mean ocean water).
8. CAM plants, which include cactus and most yucca, are present at lower elevations but don't exceed 10% of the biomass at any site. They average −18 per mil in $\delta^{13}C$.
9. We observed that the $\delta^{13}C$ (PDB) and the $\delta^{18}O$ (PDB) of carbonates appear to be constant below about 40-cm depth in modern soils at this general elevation (*3*). Above 40 cm, mixing with the atmospheric CO_2 causes progressive enrichment up to the soil surface. All the Trench 14 samples come from 0.9 to 3.4 m below the surface, and display no systematic trends with depth. All our modern soil carbonates that we used to fingerprint isotopically each of the vegetation zones come from 0.5 to 2.2 m depth.
10. I. J. Winograd, B. J. Szabo, T. B. Coplen, A. C. Riggs, *Science* **242**, 1275 (1988).
11. H. C. Claassen, *Chem. Geol. (Isot. Geosci. Sect.)* **58**, 311 (1986); L. Benson and H. Klieforth, in *Aspects of Climate Variability in the Pacific and Western Americas*, D. H. Peterson, Ed. (*Monogr. 55*, American Geophysical Union, Washington, DC, 1989), pp. 41–59.
12. J. N. Rosholt *et al.*, *U.S. Geol. Surv. Open-File Rep. 85-540* (1985). At least three episodes of faulting and subsequent fracture filling are evident from cross-cutting relations in the south wall of Trench 14 (*2*). The age of the last event is currently assessed at no older than 300,000 years ago and is likely around 150,000 years ago. This estimate is based on the estimated age of the Stage IV petrocalcic horizon [see (*3*) for this terminology] cut by the youngest fissures and the presence in one fissure of a basaltic ash thought to be 150,000 years old. The two earlier faulting episodes do not cut the Stage IV carbonates or deposits dated by U-trend methods at about 450,000 years ago. This method, however, remains experimental. The few published U-series dates on the veins are problematic because they contain excess ^{232}Th, and therefore do not exhibit closed-system behavior. More dates, particularly by the U-series and ^{14}C methods, are clearly warranted.
13. R. L. Hay, R. E. Pexton, T. T. Teague, T. K. Kyser, *Geol. Soc. Am. Bull.* **97**, 1488 (1986).
14. L. V. Benson and P. W. McKinley, *U.S. Geol. Surv. Open-File Rep. 85-484* (1985).
15. To calculate the maximum possible temperatures of carbonate formation, we used −11.5 per mil (SMOW) for ground water (interglacial water) and the most depleted carbonates from Trench 14, −11.5 per mil (PDB). This gives a temperature of 15.4°C. Waters showing a typical glacial-age composition [−13.5 per mil (SMOW)] give a temperature of 7.3°C.
16. I. J. Winograd and W. Thordarson, *U.S. Geol. Survey Prof. Pap. 712-C* (1975).
17. P. D. Coplen and I. J. Winograd, in preparation.
18. D. T. Vaniman, D. L. Bish, S. Chipera, *Los Alamos Natl. Lab. Rep.* LA-11289-MS (UC-70) (1988).
19. D. R. Muhs, J. W. Whitney, R. R. Shroba, E. M. Taylor, C. A. Bush, *Proceedings of the International High-level Nuclear Waste Management Conference*, Las Vegas, NV, 8 to 12 April, (American Society of Civil Engineers, New York, 1990).

20. We thank M. Mifflin, I. Winograd, and L. Benson for their useful discussions and help, and R. J. Johnson for his logistical assistance. Analyses were performed at the University of Utah and Yale University. This work was supported primarily by the Nevada Nuclear Waste Project Office, and by National Science Foundation grant BNS-8703304.

25 June 1990; accepted 3 October 1990

The Kangmar Dome: A Metamorphic Core Complex in Southern Xizang (Tibet)

Z. CHEN, Y. LIU, K. V. HODGES, B. C. BURCHFIEL, L. H. ROYDEN, C. DENG

The Kangmar metamorphic-igneous complex is one of the most accessible examples of an enigmatic group of gneiss domes (the North Himalayan belt) that lies midway between the Greater Himalaya and the Indus-Tsangpo suture in southern Tibet. Structural analysis suggests that the domal structure formed as a consequence of extensional deformation, much like the Tertiary metamorphic core complexes in the North American Cordillera. Unlike its North American counterparts, the Kangmar dome developed in an entirely convergent tectonic setting. The documentation of metamorphic core complexes in the Himalayan orogen supports the emerging concept that extensional processes may play an important role in the evolution of compressional mountain belts.

ALTHOUGH THE HIMALAYAN OROgen developed as a consequence of continent-continent collision between India and Eurasia during Eocene time and subsequently has accommodated continued convergence between these plates, recent studies of the geology of southern Tibet have revealed that extensional faults characteristic of divergent settings like the Basin and Range province of western North America are common at high structural levels in the Himalaya (*1–3*). These faults are interpreted as facilitating the lateral spreading of isostatically compensated, tectonically thickened lithosphere under the influence of gravity (*2*, *4–6*).

The presence of extensional structures in southern Tibet raises an important question: how many features that we commonly think of as characteristic of divergent settings can develop in convergent settings? Some of the most striking extensional features of the Basin and Range province are gneiss domes referred to as metamorphic core complexes. Since their recognition as extensional phenomena (*7*), these complexes have been found in numerous extensional settings worldwide but never in convergent settings. A series of gneiss domes forms an east-west trending belt roughly halfway between the crest of the Himalayas and the Indus-Tsangpo suture [Fig. 1; the Lhagoi Kangri or North Himalayan belt (*8*)]. Some of the gross features of these domes suggest that

Z. Chen, Y. Liu, C. Deng, Chengdu Institute of Geology and Mineral Resources, Chengdu, People's Republic of China.
K. V. Hodges, B. C. Burchfiel, L. H. Royden, Department of Earth, Atmospheric, and Planetary Sciences, Massachusetts Institute of Technology, Cambridge, MA 02139.

American Mineralogist, Volume 75, pages 601–619, 1990

Activity diagrams for clinoptilolite: Susceptibility of this zeolite to further diagenetic reactions

TERESA S. BOWERS, ROGER G. BURNS
Department of Earth, Atmospheric, and Planetary Sciences, Massachusetts Institute of Technology, Cambridge, Massachusetts 02139, U.S.A.

ABSTRACT

Clinoptilolite is the predominant zeolite in diagenetically altered volcanic rocks at Yucca Mountain, Nevada, having formed by posteruptive reactions of ground water with vitric tuffs in the pyroclastic deposits. Compositional variations of clinoptilolites in the fractured and zeolitized tuffs not presently in contact with ground water and the vulnerability of zeolites to burial diagenesis raise questions about the long-term stability of clinoptilolite. Equilibrium activity diagrams were calculated for clinoptilolite solid solutions in the seven-component system Ca-Na-K-Mg-Fe-Al-Si plus H_2O, employing available thermodynamic data for related minerals, aqueous species, and water. Stability fields are portrayed graphically on plots of $\log(a_{Na^+}/a_{H^+})$ versus $\log(a_{Ca^{2+}}/(a_{H^+})^2)$, assuming the presence of potassium feldspar, saponite, and hematite, and using ranges of activities for SiO_2 and Al^{3+} defined by the saturation limits for several silica polymorphs, gibbsite, kaolinite, and pyrophyllite. Formation of clinoptilolite is favored by higher SiO_2 activities than allowed for by the presence of quartz, thus accounting for the coexistence of clinoptilolite with opal-CT in zeolitized vitric tuffs. The clinoptilolite stability field broadens with increasing atomic substitution of Ca for Na, and K for Ca, reaches a maximum for intermediate activities of dissolved Al, and decreases with increasing temperature. The thermodynamic calculations show that ground water of the sodium-bicarbonate type, such as reference J-13 well water collected from fractured devitrified tuffs at the adjacent Nevada Nuclear Test Site, is approximately in equilibrium at 25 °C with calcite and several zeolites, including heulandite and calcic clinoptilolite. Mg-rich clinoptilolites are stabilized in ground water depleted in Ca^{2+}. Decreasing Al^{3+} activities result in the association of clinoptilolite with calcite and opal-CT observed in weathered zeolitized vitric tuffs at Yucca Mountain. The activity diagrams indicate that prolonged diagenetic reactions with ground water depleted in Al, enriched in Na or Ca, and heated by the thermal envelope surrounding buried nuclear waste may eliminate sorptive calcic clinoptilolites in fractured tuffs and underlying basal vitrophyre.

INTRODUCTION

Clinoptilolite, ideally $(Na,K,Ca_{0.5})_6Si_{30}Al_6O_{72}\cdot 24H_2O$, is an abundant zeolite in diagenetically altered rhyolite tuffs, where it forms by posteruptive reactions of hydrated glass shards (Hay, 1966; Hay and Sheppard, 1977; Iijima, 1975, 1980). Silicic air-fall and ash-flow tuffs are the predominant rocks at Yucca Mountain, Nevada, the site of the proposed repository for burial of high-level nuclear waste (U.S. DOE, 1988). The repository horizon at this site is a densely welded and devitrified tuff unit underlain by a basal vitrophyre and vitric to zeolitized non-welded tuffs containing high proportions of clinoptilolite (Broxton et al., 1987). Because of its favorable cation exchange reactions, clinoptilolite is advocated as one mineral in the tuffaceous deposits capable of immobilizing several of the soluble cations and being an effective barrier to radionuclide migration (Ogard et al., 1984), should water entering the repository cause leakage of fission products.

Clinoptilolites analyzed in drill-core samples throughout Yucca Mountain and its vicinity display wide compositional variations, particularly in fractures adjacent to the repository horizon in the Topopah Spring Member of the Paintbrush Tuff unit and in underlying zeolitized vitric tuffs (Broxton et al., 1987). In the vadose zone beneath Yucca Mountain, clinoptilolites with high Ca and Mg contents line fractures in the Topopah Spring Member (Carlos, 1985; Broxton et al., 1986, 1987). In underlying bedded tuffs, the clinoptilolites display regional and depth variations (Broxton et al., 1986, 1987). On the western side of Yucca Mountain the clinoptilolites are Na-K-bearing and become Na-rich with depth. To the east, the clinoptilolites are Ca-K-bearing and become Ca-rich with depth. Such compositional variations are portrayed in

0003-004X/90/0506-0601$02.00

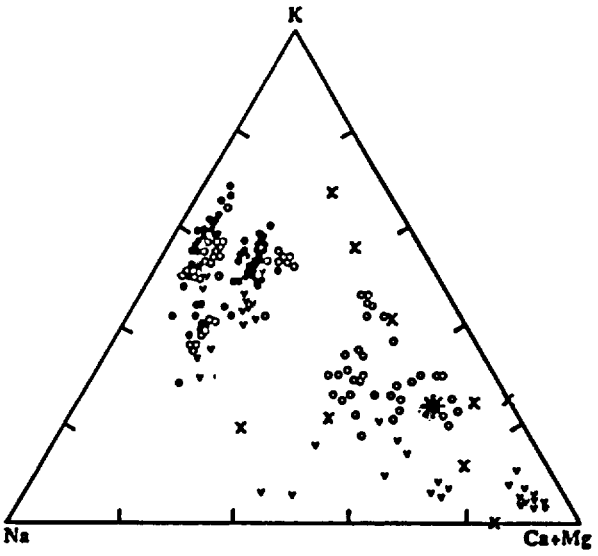

Fig. 1. Triangular diagram showing compositional variations of clinoptilolite and heulandites (modified from Broxton et al., 1986). Superimposed on data for these zeolites in the unsaturated zone at Yucca Mountain, Nevada, are compositions used in the thermodynamic calculations: ●, ○ western and eastern parts of the repository block (Broxton et al., 1986); V lining fractures in and below the proposed repository horizon (Carlos, 1985); * measured calorimetrically (Hemingway and Robie, 1984); X different atomic substitutions used to calculate activity diagrams in Fig. 11.

Figure 1. Similar regional and depth variations occur in zeolitized tuffs at the adjacent Nevada Test Site (Hoover, 1968). Such compositional variations of clinoptilolite not presently in contact with ground water and the susceptibility of zeolites to further diagenetic reactions (Moncure et al., 1981; Smyth, 1982) suggest that the long-term thermodynamic stability of clinoptilolite should be examined.

Although the Topopah Spring Member tuff and underlying zeolitized tuffs lie in the unsaturated or vadose zone, well above the present-day water table beneath Yucca Mountain, these formations dip to the east so that at the location of the nearest water-supply well, designated J-13 and located 6 km to the east at Jackass Flat on the Nevada Test Site, the Topopah Spring Member lies beneath the water table. The major producing horizon for J-13 well water is a highly fractured interval within the Topopah Spring Member (Delany, 1985). The chemical composition of the ground water obtained from well J-13 has been monitored for several years (Daniels et al., 1982; Bish et al., 1984; Kerrisk, 1987) and serves as a standard in laboratory experiments and geochemical modeling studies for the Yucca Mountain exploration block (e.g., Oversby, 1985; Delany, 1985; Knauss et al., 1985a, 1985b; Moore et al., 1986; Thomas, 1987; U.S. DOE, 1988, p. 4–51). Whether J-13 well water is of an appropriate composition for the prediction of authigenic mineral reactions in the unsaturated zone beneath Yucca Mountain requires critical evaluation.

In order to assess the stability limits of clinoptilolite and its vulnerability to changes of ground water chemistry relative to the composition of J-13 well water, equilibrium activity diagrams have been calculated for clinoptilolite solid solutions in the system Ca-Na-K-Mg-Fe-Al-Si-H_2O, employing available thermodynamic data for oxide and aluminosilicate phases. Although low-temperature processes are subject to many kinetically controlled variables, the assumption of thermodynamic equilibrium provides a reference from which to assess observed mineral relations. Results reported here indicate that authigenic minerals such as clinoptilolite modify and are modified by ground-water compositions.

Calculations of activity diagrams

Sources of thermodynamic data

The method for calculating activity diagrams is described in Bowers et al. (1984), who also tabulated thermodynamic data for many of the phases considered here. Thermodynamic data for zeolites including clinoptilolite, heulandite, natrolite, scolecite, and mesolite are provided by calorimetric measurements made by Johnson et al. (1982, 1983, 1985) and Hemingway and Robie (1984). Table 1 lists formulae of all of the minerals considered in this study. Note that several of these minerals (notably laumontite, stilbite, and chabazite) were found not to exhibit stability fields within the pressure, temperature, and compositional ranges of the calculations.

The clinoptilolite measured by Hemingway and Robie (1984) from altered tuffs of the Big Sandy Formation, Mohave County, Arizona (Sheppard and Gude, 1973) was formulated by them as

$$Na_{0.56}K_{0.98}Ca_{1.50}Mg_{1.23}Fe_{0.3}Al_{4.7}Si_{29}O_{72}\cdot 22H_2O,$$

with Si/Al = 4.33 and (Na + K) > Ca. The heulandite measured by Johnson et al. (1985) was formulated as

$$Ca_{0.583}Sr_{0.173}Ba_{0.063}Na_{0.383}K_{0.133}Si_{6.833}Al_{2.163}O_{18}\cdot 6.0H_2O,$$

with Si/Al = 3.16 and (Ca + Sr + Ba) > (Na + K). Note that clinoptilolite and heulandite are isostructural, and a continuous solid-solution series exists between the two minerals. By convention, the compositional boundary for clinoptilolite is determined by the ratios Si/Al ≥ 4 and (Na + K) ≥ Ca, whereas heulandite has Si/Al < 4 and Ca > (Na + K). As indicated in Figure 1, the composition of the clinoptilolite for which thermodynamic data are available resembles those of the (Ca + Mg)-rich zeolites that line fractures in the Topopah Spring Member and are present in underlying zeolitized vitric tuffs, particularly beneath the northeastern block of Yucca Mountain (Broxton et al., 1987).

Several minerals of interest in this study, including clinoptilolite, have measured heat-capacity and entropy data, but no Gibbs free energy of formation at 25 °C (ΔG_f°). When this is the case, free energies can be estimated by

TABLE 1. Minerals and formulas

Quartz	SiO_2
Amorphous silica	SiO_2
Gibbsite	$Al(OH)_3$
Diaspore	$AlO(OH)$
Kaolinite	$Al_2Si_2O_5(OH)_4$
Pyrophyllite	$Al_2Si_4O_{10}(OH)_2$
Wollastonite	$CaSiO_3$
Grossular	$Ca_3Al_2Si_3O_{12}$
Anorthite	$CaAl_2Si_2O_8$
Gehlinite	$Ca_2Al_2SiO_7$
Prehnite	$Ca_2Al_2Si_3O_{10}(OH)_2$
Margarite	$CaAl_2Si_2O_{10}(OH)_2$
Ca end-member beidellite	$Ca_{0.165}Al_2(Al_{0.33}Si_{3.67}O_{10})(OH)_2$
Lawsonite	$CaAl_2Si_2O_7(OH)_2 \cdot H_2O$
Wairakite	$CaAl_2Si_4O_{12} \cdot 2H_2O$
Laumontite	$CaAl_2Si_4O_{12} \cdot 4H_2O$
Chabazite	$CaAl_2Si_4O_{12} \cdot 6H_2O$
Ca end-member phillipsite	$CaAl_2Si_4O_{12} \cdot 5H_2O$
Scolecite	$CaAl_2Si_3O_{10} \cdot 3H_2O$
Epistilbite	$CaAl_2Si_6O_{16} \cdot 5H_2O$
Heulandite	$CaAl_2Si_7O_{18} \cdot 6H_2O$
Albite	$NaAlSi_3O_8$
Nepheline	$NaAlSiO_4$
Paragonite	$NaAl_2(AlSi_3O_{10})(OH)_2$
Na end-member beidellite	$Na_{0.33}Al_2(Al_{0.33}Si_{3.67}O_{10})(OH)_2$
Na end-member phillipsite	$Na_2Al_2Si_6O_{16} \cdot 5H_2O$
Analcime	$NaAlSi_2O_6 \cdot H_2O$
Natrolite	$Na_2Al_2Si_3O_{10} \cdot 2H_2O$
Mordenite	$NaAlSi_5O_{12} \cdot 3H_2O$
Potassium feldspar	$KAlSi_3O_8$
Kalsilite	$KAlSiO_4$
Muscovite	$KAl_2(AlSi_3O_{10})(OH)_2$
K end-member beidellite	$K_{0.33}Al_2(Al_{0.33}Si_{3.67}O_{10})(OH)_2$
K end-member phillipsite	$K_2Al_2Si_6O_{16} \cdot 5H_2O$
Phillipsite	$Na_{1.33}K_{0.66}Al_{2.99}Si_{5.13}O_{16} \cdot 6H_2O$
H end-member beidellite	$H_{0.33}Al_2(Al_{0.33}Si_{3.67}O_{10})(OH)_2$
Stilbite	$NaCa_2Al_5Si_{13}O_{36} \cdot 14H_2O$
Mesolite	$Na_{0.676}Ca_{0.657}Al_{1.99}Si_{3.01}O_{10} \cdot 2.647H_2O$
Clinoptilolite	$(Na_{0.66}K_{0.53}Ca_{1.5}Mg_{1.25})(Al_{6.7}Fe_{0.3})Si_{30}O_{72} \cdot 22H_2O$
Ca end-member saponite	$Ca_{0.165}Mg_3(Al_{0.33}Si_{3.67}O_{10})(OH)_2$
Hematite	Fe_2O_3

various component-summation methods. The method of Chen (1975) was used here for Na end-member phillipsite, K end-member phillipsite, and (Na,K) end-member phillipsite. This method involves summing several sets of components, including oxides, simple silicates, and components of similar structural type. The resulting free-energy determinations are fit with an exponential curve that asymptotically approaches a low value that is used as ΔG_f°. Chen (1975) reported an estimated error in ΔG_f° obtained in this manner of less than 0.6% for a number of minerals when compared to their experimental values. An attempt was made to estimate free energies for the clinoptilolite formulated by Hemingway and Robie (1984) and for end-member heulandite, Ca end-member phillipsite, stilbite, chabazite, and epistilbite formulated in Table 1 using Chen's (1975) method. Clinoptilolite and end-member heulandite were treated as separate phases on the basis of different Si-Al ratios even though a continuous solid-solution series exists between the two minerals. The independent estimates of ΔG_f° from summing various components for clinoptilolite and each of the end-member minerals listed above did not fall along exponential curves, but decreased linearly such that an exponential fit could not be made. Chen (1975) noted a similar difficulty with some minerals. The free energy of formation for these minerals was therefore taken as the lowest value obtained from the various component-summation schemes and generally involved summing over zeolite and other hydrous components, including natrolite, scolecite, K end-member phillipsite, brucite, kaolinite, quartz, and hematite. The error associated with this method will be somewhat higher than the 0.6% estimated by Chen (1975). All estimated ΔG_f° and ΔH_f° data used in this study are in Table 2. In addition, since alkali-rich mordenite fre-

TABLE 2. Estimated free energies and enthalpies of some zeolites*

	$\Delta G_f^\circ(298)$ (cal/mol)	$\Delta H_f^\circ(298)$ (cal/mol)
Na end-member phillipsite	−1 851 376	−2 003 469
K end-member phillipsite	−1 871 460	−2 025 549
Ca end-member phillipsite	−1 860 596	−2 010 073
Phillipsite	−2 112 851	−2 294 159
Mordenite	−1 465 647	—
Epistilbite	−2 065 242	−2 234 763
Chabazite	−1 712 637	−1 868 861
Stilbite	−4 633 571	−5 247 477
Heulandite	−2 326 575	−2 519 882
Clinoptilolite	−9 057 789	−9 811 932

* Mineral formulas given in Table 1.

TABLE 3. Estimated free energies for compositionally variable clinoptilolite

	ΔG_f°(298) (cal/mol)
$(Na_{0.66}K_{0.66}Ca_{1.5}Mg_{1.25})$-$(Al_{6.7}Fe_{0.2})Si_{29}O_{72}\cdot 22H_2O$	−9 057 789
Na-Ca substitution	
$Na_{1.66}Ca_{1.0}$	−9 052 517
$Na_{2.66}Ca_{0.5}$	−9 047 244
$Na_{3.66}$	−9 041 972
$Na_{0.66}Ca_{1.66}$	−9 059 265
$Ca_{1.76}$	−9 060 742
K-Ca substitution	
$K_{1.66}Ca_{1.0}$	−9 068 653
$K_{2.66}Ca_{0.5}$	−9 079 517
$K_{3.66}$	−9 090 381
$K_{0.6}Ca_{1.76}$	−9 052 574
$Ca_{1.66}$	−9 047 142
Ca-Mg substitution	
$Ca_{0.75}Mg_{2.0}$	−9 036 211
$Ca_{1.7}Mg_{1.66}$	−9 063 394
$Ca_{2.0}Mg_{0.75}$	−9 071 801
$Ca_{2.5}Mg_{0.33}$	−9 085 813
$Ca_{2.75}$	−9 092 259

quently coexists with clinoptilolite in zeolitized tuffs at Yucca Mountain (Sheppard et al., 1988), its ΔG_f° was also estimated by Chen's (1975) method. However, because no measured thermodynamic data are available for mordenite, this zeolite was used only in activity diagrams calculated at 25 °C, although, as noted later, mordenite occurs at elevated temperatures in hydrothermal environments (Sturchio et al., 1989). The end-member heulandite formulated in Table 1 was the only one used in the calculations presented here because, as noted earlier, the specimen measured by Johnson et al. (1985) contained Ba and Sr components not included in this study.

Previous estimates of thermodynamic properties of clinoptilolite, heulandite, and mordenite were made by Kerrisk (1983). However, those calculations were made prior to recently published calorimetric data (Johnson et al., 1982, 1983, 1985; Hemingway and Robie, 1984). Direct comparisons between Kerrisk's (1983) estimates and those presented here cannot be made because he estimated equilibrium constants of specific hydrolysis reactions rather than free energies of formation of the minerals themselves.

Table 3 contains estimated free energies of formation for compositionally variable clinoptilolites. Independent substitutions of Na for Ca, K for Ca, and Ca for Mg were allowed, where constant charge balance and Si/Al ratio of 4.33 are maintained. Corresponding ΔG_f° values for each of these derived compositions were estimated from the value given for clinoptilolite in Table 2 by a component-summation method using natrolite, scolecite, and H_2O for Na-Ca substitution; K end-member phillipsite, scolecite, quartz, and H_2O for K-Ca substitution; and scolecite, brucite, kaolinite, and quartz for Ca-Mg substitution. These correction mechanisms resulted in lower ΔG_f° values for Ca over Na, K over Ca, and Ca over Mg-rich clinoptilolites.

Composition of ground water

Because the Topopah Spring Member tuff is the major producing horizon for water pumped from the J-13 well, it has been generally assumed (Oversby, 1985) that the composition of J-13 well water approximates the prevailing water chemistry of the proposed repository horizon in the same formation at Yucca Mountain even though the Topopah Spring Member there is in the unsaturated zone. As a result, J-13 well water continues to be widely used as the reference aqueous phase for calibrating numerous environmental parameters relevant to the Yucca Mountain repository horizon (Oversby, 1985; Delany, 1985; Knauss et al., 1985a, 1985b; Moore et al., 1986; Thomas, 1987; U.S. DOE, 1988, p. 4–51). The chemical composition of J-13 well water has been monitored for several years (Daniels et al., 1982; Kerrisk, 1987), and typical concentrations of dissolved species in it are summarized in Table 4. Small fluctuations in concentrations over time have been recorded, but the variations are minor compared with other variables in experiments in which J-13 well water was used (Daniels et al., 1982). However, during experiments in which J-13 well water was contacted with tuff samples of the Topopah Spring Member taken from a drill core at the appropriate region of main water production of the J-13 well, concentrations of many constituents changed slightly (Table 4), particularly Mg and Al, which decreased after three weeks at room temperature (Daniels et al., 1982). Moreover, filtration affected the compositions of some elements, particularly Fe, Al, and Mg, which were drastically reduced in samples passed through 0.05 μm Nuclepore membranes compared to those obtained from 0.45 μm Millipore filters (Daniels et al., 1982). The Al concentration, for example, decreased from ~40 mg/L (0.45 μm filter) to <0.01 mg/L (0.05 μm filter) (Daniels et al., 1982). The Al concentration of J-13 well water (0.012 mg/L) represents one of the lowest values reported for drill holes throughout Yucca Mountain (Ogard and Kerrisk, 1984).

Cation concentrations in solutions contacted with vitrophyre samples from the Topopah Spring Member at 152 °C showed significant increases of dissolved Si, Fe, Al, K, and Na and a decrease of dissolved Mg, which were attributed to dissolution of glass and precipitation of clays (Daniels et al., 1982). A specimen of zeolitized tuff reacted with J-13 well water at 152 °C showed marked dissolution of clinoptilolite and disappearance of mordenite and cristobalite (Daniels et al., 1982). In later experiments, Knauss et al. (1985a, 1985b) studied compositional changes of J-13 well water after reacting it with crushed tuff and polished wafer samples of the densely welded, devitrified ash-flow tuff in a drill core taken from the respository level in the Topopah Spring Member. The modal minerals of this horizon consist of ~98% microcrystalline sanidine-cristobalite-quartz and accessory (<2%) biotite-montmorillonite (Bish et al., 1984; Broxton et al., 1989). Reactions were performed over 2–3 months at temperatures of 90, 150, and 250 °C and pres-

TABLE 4. Chemical composition of J-13 well water (mg/L)

	A	B	C	D	E	F	G
Li	0.042	—	—	—	0.06	0.05	0.05
Na	43.9	55	58.5	44	45	51	54.1
K	5.11	7.5	5.58	4.4	5.3	4.9	6.4
Ca	12.5	11.5	6.46	13	11.5	14	11
Mg	1.92	1.1	0.315	2.0	1.76	2.1	0.95
Sr	0.035	—	—	—	—	0.05	0.002
Al	0.012	0.999	1.64	—	0.03	0.03	0.01
Fe	0.006	—	—	—	0.04	0.04	0.004
SiO_2	57.9	53	148	59	64.3	66	71.6
NO_3	9.6	9.0	9.5	8.7	10.1	5.6	—
F	2.2	2.3	2.4	2.2	2.1	2.2	—
Cl	6.9	7.2	7.4	—	6.4	7.5	—
HCO_3	125.3	178.8	61.0	120	143	120	—
SO_4	18.7	18.3	18.5	19	18.1	22	—
pH	7.6	7.27	6.97	7.5	6.9	7.1	—

A. Delany (1985).
B. J-13 reacted with TS tuff at 90 °C; Knauss et al. (1985a).
C. J-13 reacted with TS tuff at 150 °C; Knauss et al. (1985a).
D. Moore et al. (1986).
E. Ogard and Kerrisk (1984).
F. Daniels et al. (1982).
G. Daniels et al. (1982), after J-13 water reacted with TS tuff at 25 °C.

sures of 90–100 bars. Results from the experiments at 150 °C are in Table 4, where it can be seen that dissolved SiO_2 concentrations increase and are close to the cristobalite saturation value (Knauss et al., 1985a). Na also increased during the experiments, Ca and Mg decreased, and Al and K both increased rapidly and then decreased. These effects were attributed to dissolution of montmorillonite and precipitation of calcite and illite. The experiments at 90 and 250 °C produced similar results. Phases identified by scanning electron microscopy included illite, Mg-Ca or Fe-rich clays, gibbsite, calcite, and a pure SiO_2 phase considered to be cristobalite (Knauss et al., 1985a, 1985b).

Studies to determine compositional changes of ground water as it passes through the unsaturated zone in tuffaceous deposits have been conducted at Rainier Mesa, located 50 km to the north-northeast of Yucca Mountain (Benson, 1976; White et al., 1980). At Rainier Mesa welded and vitric tuffs overlie zeolitized tuffs, resembling the sequence of ash-flow tuffs at Yucca Mountain. Concentrations of Ca and Mg in interstitial waters decreased as a function of depth and were generally lower than those in J-13 well water, whereas opposite effects were observed for Na (Benson, 1976; White et al., 1980). The concentration of dissolved K was lower at depth, and that of SiO_2 higher, than J-13 well-water compositions, whereas Cl^- decreased and HCO_3^- increased with depth. The maximum compositional variations of the interstitial water occurred in alteration zones containing clinoptilolite and montmorillonite (Benson, 1976; White et al., 1980). Water seeping through fractures in tunnels beneath the zeolitized tuffs was HCO_3^--rich and had lower Ca, Mg, and SiO_2 contents, variable K concentrations, and higher Na concentrations than J-13 well water (Benson, 1976; White et al., 1980). The clinoptilolites along the fractures were Ca-Mg-K-rich, correlating with the depletion of these cations in the ground water, whereas the fracture-flow water was enriched in HCO_3^- relative to the more Cl^--rich interstitial water. Comparisons made with dissolution experiments on vitric and crystalline tuffs demonstrated the rapid release of Na and SiO_2 but the retention of K in glass-bearing tuffs, whereas dissolution of crystalline tuffs containing sanidine, quartz, biotite, and clinopyroxene phenocrysts and sanidine-cristobalite groundmass resulted in solutions rich in Ca, Mg, and HCO_3^- (White et al., 1980). White et al. (1980) thus concluded that fracture-water compositions, such as J-13 well water, are dominated by dissolution of vitric tuffs but are modified by infiltration through zeolitized tuffs.

The composition of J-13 well water not only plots in the field of the Rainier Mesa interstitial and fracture-flow waters, but analyses also lie in the middle of compositional ranges for ground water pumped from several wells throughout Yucca Mountain originating from various depths in the saturated zone (Ogard and Kerrisk, 1984) at temperatures rarely exceeding 40 °C. In the Yellowstone hydrothermal environment, downhole water compositions at 140 °C show appreciably higher concentrations of SiO_2, HCO_3^-, Na, and K, and lower Ca contents than the lower temperature J-13 well water (31 °C). Clinoptilolites there are enriched in K and Na but are depleted in Ca (Keith et al., 1978; Sturchio et al., 1989). These results, and the experimental observations described earlier, clearly show that zeolitized rhyolitic tuffs affect ground-water chemistry, and they suggest that compositional variability of clinoptilolites influence and are influenced by ground-water compositions. They also indicate that potassic clinoptilolites are stable to at least 140 °C.

Recently attempts were made to measure compositions of pore water extracted by triaxial compression of nonwelded tuffs from the unsaturated zone at Yucca Moun-

tain (Yang et al., 1988). The samples of extracted water have much higher Ca, Mg, K, Sr, Cl^-, SO_4^{2-}, and SiO_2 concentrations than J-13 well water, and the compositions of extracted water are influenced by changes of axial stress on the compressed tuffs. Unfortunately, pH, HCO_3^-, and dissolved Al data were not reported for these tuff samples. Consequently, the pore-water compositions could not be used in our thermodynamic calculations.

Representation of activity diagrams

A number of activity diagrams are presented here, initially for simple three-component systems and subsequently for the more complex multicomponent systems that are required for depicting stability fields of clinoptilolite in felsic rocks. The primary focus is on the clinoptilolite composition highlighted earlier for which thermodynamic data are available (Hemingway and Robie, 1984). Although the chosen three-component systems serve as a necessary reference for establishing stability fields for clinoptilolite in the multicomponent systems discussed later, they also may contain useful information for diagenetic reactions involving other zeolites in felsic and mafic rocks.

Systems of three and four components plus H_2O can be readily represented in two dimensions. For example, in the system Ca-Al-Si-H_2O, two components are selected for the x and y axes, all reactions are balanced with respect to a third component, and the activity of H_2O is fixed, commonly equal to one. A reaction between amorphous silica and heulandite can be represented by writing a hydrolysis reaction for each mineral:

$$SiO_{2(am)} = SiO_{2(aq)} \quad (1)$$

$$CaAl_2Si_7O_{18}\cdot 6H_2O + 8H^+ = Ca^{2+} + 2Al^{3+} + 7SiO_{2(aq)} + 10H_2O \quad (2)$$

Combining Reactions 1 and 2 and eliminating $SiO_{2(aq)}$ from the equations gives

$$CaAl_2Si_7O_{18}\cdot 6H_2O + 8H^+ = 7SiO_{2(am)} + Ca^{2+} + 2Al^{3+} + 10H_2O \quad (3)$$

An equilibrium constant as a function of pressure and temperature can be calculated from thermodynamic data for this reaction and is expressed as

$$\log K = 2\log(a_{Al^{3+}}/(a_{H^+})^3) + \log(a_{Ca^{2+}}/(a_{H^+})^2) \quad (4)$$

If the x and y axes are chosen as $\log(a_{Al^{3+}}/(a_{H^+})^3)$ and $\log(a_{Ca^{2+}}/(a_{H^+})^2)$, respectively, Reaction 4 is the equation of a line with a slope of -2 and a y intercept of log K that forms the boundary on an activity diagram between amorphous silica and heulandite (see Fig. 3a, discussed later). Similar calculations are performed for all mineral pairs, and the resulting intersecting lines form the boundaries of the phases that appear on the stability diagrams presented here.

Systems with more than four components plus H_2O are calculated in a similar manner, but with the inclusion of any additional minerals assumed to be at saturation to constrain additional components. For example, the system Ca-Na-Al-Si-H_2O might have Ca and Na on the axes, be balanced on Al, and have coexisting amorphous silica, as in Reaction 3. Alternatively, this four-component system could be balanced with respect to SiO_2 and have the Al component constrained by a saturation phase such as gibbsite:

$$CaAl_2Si_7O_{18}\cdot 6H_2O + 2H^+ = 2Al(OH)_3 + 7SiO_{2(aq)} + Ca^{2+} + 4H_2O \quad (5)$$

Gibbsite, however, provides a theoretical maximum activity of the Al^{3+} component that may not be desirable in all circumstances. Saturation with respect to any Al-bearing mineral in the four-component system can be assumed, although, if the chosen saturation phase includes the components plotted on the axes of the diagram, it will change the topology of the other fields. At Yucca Mountain, drill-core samples in the vadose zone contain opal and smectite as coexisting authigenic SiO_2 and Al^{3+}-bearing phases, respectively, with some authigenic potassium feldspar and minor amounts of cristobalite, quartz, and calcite (Broxton et al., 1987; Bish, 1989). These phases, together with the composition of J-13 well water (Table 4), serve to define the ranges of silica and Al^{3+} activities shown in Figure 2, which were used to construct the activity diagrams presented here. Thus, lines labeled D and H on Figure 2 represent the extremes of dissolved silica saturation limits corresponding to quartz and amorphous silica, respectively; cristobalite has an intermediate saturation level approximated by line E; line F corresponds to coexisting kaolinite and pyrophyllite; and line G is the activity of dissolved SiO_2 in J-13 well water. Similarly, for dissolved Al^{3+}, lines A, B, and C correspond to saturation values for coexisting amorphous silica plus pyrophyllite, coexisting pyrophyllite plus kaolinite, and gibbsite, respectively, and line I represents an arbitrarily low value of dissolved Al, which, as shown later, is consistent with the coexistence of opal, calcite, and clinoptilolite. Note that, although gibbsite, kaolinite, and pyrophyllite have not been reported at Yucca Mountain, their ideal end-member compositions serve as useful constraints for dissolved Al^{3+} and SiO_2 activities. Smectite, however, which is pervasive at Yucca Mountain (Bish, 1989), has a sheet silicate structure resembling pyrophyllite. If smectite were used to constrain Al activities, its value would fall into the general range for pyrophyllite, depending on the smectite composition. The reported analysis of Al in J-13 well water, 0.012 mg/L, which, as noted earlier, is one of the lowest concentrations reported for ground water at Yucca Mountain (Ogard and Kerrisk, 1984), is too high to be equilibrium-controlled. The fluid speciation program used to calculate cation activities (EQ3NR of Wolery, 1983) indicates that at the measured pH of J-13 well water (~7.5), dissolved Al occurs predominantly as $Al(OH)_4^-$, with a calculated equilibrium value for $[Al^{3+}]$ of $\sim 2 \times 10^{-11}$ M. Using an activity coefficient of ~0.6 for Al^{3+} gives a value for $\log(a_{Al^{3+}}/(a_{H^+})^3)$ of 9.6, significantly in excess of the gibbsite saturation value of approximate-

ly 7.9 (Fig. 2). This value is inconsistent with the equilibrium coexistence of J-13 well water and any of the observed mineral assemblages at Yucca Mountain and other areas for which dissolved Al concentration data are available, and it cannot be used to constrain calculations presented here. As noted earlier, a possible interpretation of this discrepancy is that the Al in J-13 well water contains unfiltered particulate matter that passes through membrane filters (Daniels et al., 1982). In calculating the activity diagrams, the activity of H_2O is taken to be unity, and the calcite boundary is added to appropriate diagrams by assuming a dissolved HCO_3^- content equivalent to that of J-13 well water (Table 4) and using the 90 °C and 150 °C analytical data in the activity diagrams calculated at 100 °C and 150 °C, respectively.

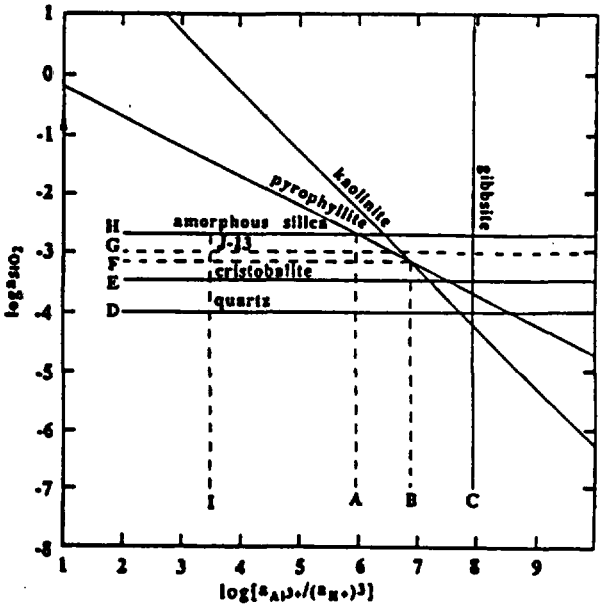

Fig. 2. Ranges of dissolved silica and aluminum activities used in the calculations of activity diagrams. Silica activities correspond to amorphous silica (H), J-13 well water (G), coexisting pyrophyllite-kaolinite-saturated solution (F), cristobalite-saturated solution (E), and quartz-saturated solution (D). Al activities are those for solutions saturated by assemblages of pyrophyllite + amorphous silica (A), pyrophyllite-kaolinite (B), and gibbsite (C) and an arbitrary low value (I).

Results

Diagrams of systems of three components plus H_2O

A series of diagrams of systems of three components plus H_2O are shown in Figures 3 to 5 for the systems Ca-Al-Si, Na-Al-Si, and K-Al-Si, respectively. All of these diagrams are balanced with respect to SiO_2. Quartz has been suppressed throughout the calculations described here in favor of amorphous silica because opal is the commonly observed authigenic SiO_2 phase in zeolitized ash-flow tuffs at Yucca Mountain (Broxton et al., 1986, 1987; Bish, 1989). As a result, each of the diagrams in Figures 3–5 has amorphous silica as the stable phase in the bottom left corner. Amorphous silica occupies a relatively smaller stability field than would quartz, had quartz not been suppressed. Figures 3a–3c illustrate the changes in phase relations for the system Ca-Al-Si with increasing temperatures at 25, 100, and 200 °C with pressures corresponding to the steam-saturation curve. Note that the heulandite field at 25 °C is replaced by Ca end-member phillipsite at higher temperatures. The scolecite field decreases in size with increasing temperature, and this zeolite is no longer stable at 200 °C (Fig. 3c). The field of Ca end-member beidellite apparent at 200 °C may exist at lower temperatures as well but does not appear in Figures 3a and 3b, possibly because of inaccuracies in the thermodynamic data for Ca end-member beidellite or adjacent phases. The stable limits of these and other activity diagrams described later are delineated by the dashed lines labeled gibbsite (or diaspore at 200 °C) and calcite. Higher Al or Ca activities can only result from supersaturation of the fluid with respect to these phases. As noted earlier, J-13 well water is unconstrained on the Al axis because its measured Al content cannot be reconciled with existing thermodynamic data. It is apparent from Figures 3a and 3b that in the simple Ca-Al-Si system J-13 well water is somewhat undersaturated with respect to calcite at 25 °C and would be slightly oversaturated at 100 °C.

Activity diagrams for the system Na-Al-Si are illustrated in Figures 4a and 4b. The 25 °C diagram (Fig. 4a) contains a stability field for mordenite. However, owing to lack of thermodynamic data for mordenite, this zeolite was not included in high-temperature calculations in Figure 4b. Its absence from Figure 4b is not indicative of stability limits for mordenite; indeed, mordenite occurs at ~170 °C in drill holes throughout the Yellowstone geothermal system (Keith et al., 1978; Sturchio et al., 1989). Thus, in the absence of mordenite the stability field of albite widens at 100 °C and Na end-member beidellite also becomes stable (Fig. 4b). Figures 5a and 5b show activity diagrams for the system K-Al-Si at 25 °C and 100 °C in which K end-member phillipsite is joined by potassium feldspar at high temperatures. J-13 well water is consistent with equilibrium with respect to either mordenite or albite (Fig. 4) and either K end-member phillipsite or potassium feldspar (Fig. 5).

Multicomponent diagrams

Figures 3 to 5 provide simplified activity diagrams used as references for comparison with the more complex systems of four and five components plus H_2O necessary for plotting the stability fields of clinoptilolite. Figures 6–9 are activity diagrams for the system Ca-Na-K-Al-Si. Values of $\log(a_{Na^+}/a_{H^+})$ and $\log(a_{Ca^{2+}}/(a_{H^+})^2)$ are plotted on the x- and y-axes, respectively, in each diagram. Either Al (Figs. 6 and 7) or Si (Figs. 8 and 9) has been used as the balancing component. In each case, two additional components need to be specified. The component K^+ is constrained by assuming the presence of potassium feldspar,

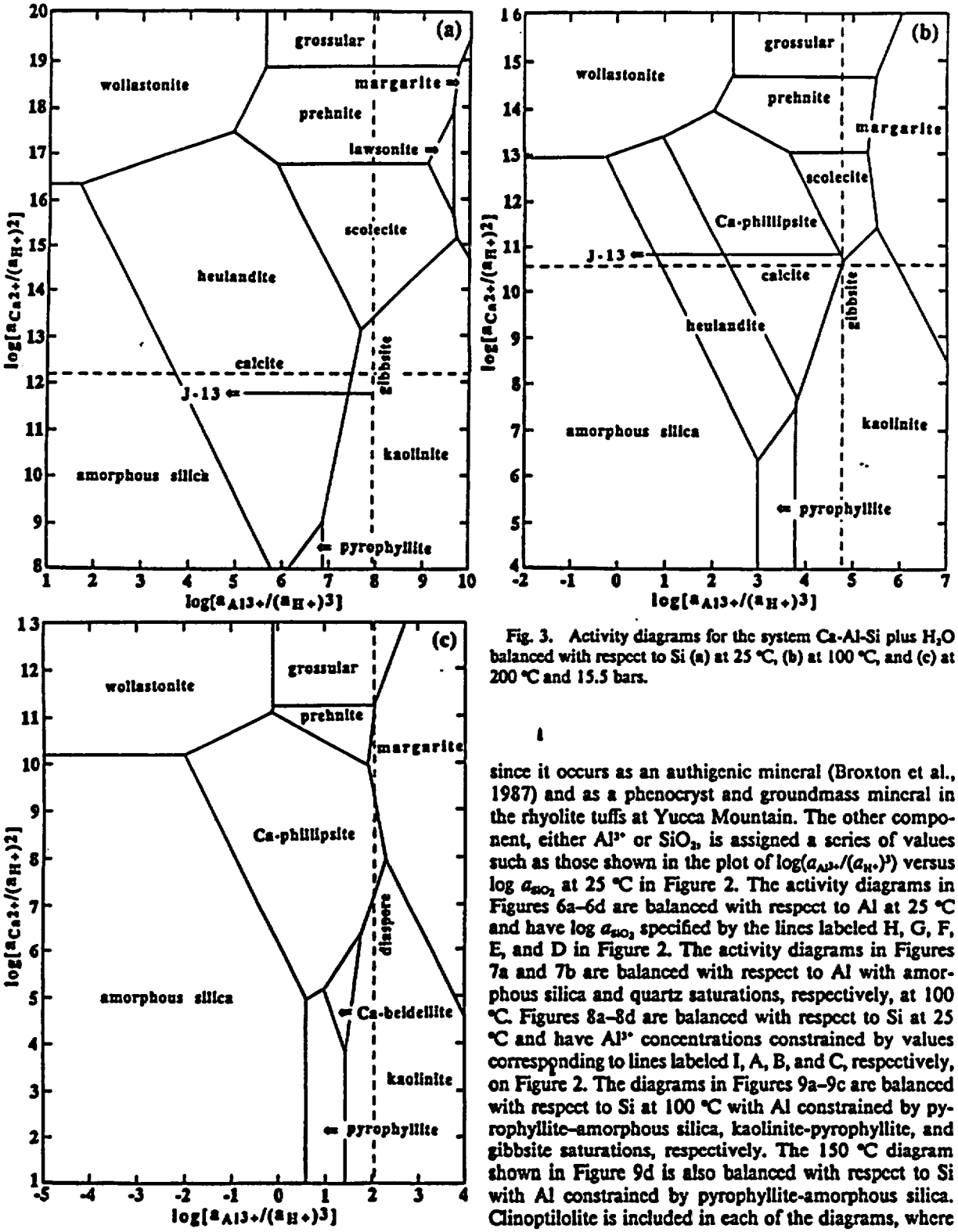

Fig. 3. Activity diagrams for the system Ca-Al-Si plus H_2O balanced with respect to Si (a) at 25 °C, (b) at 100 °C, and (c) at 200 °C and 15.5 bars.

since it occurs as an authigenic mineral (Broxton et al., 1987) and as a phenocryst and groundmass mineral in the rhyolite tuffs at Yucca Mountain. The other component, either Al^{3+} or SiO_2, is assigned a series of values such as those shown in the plot of $\log(a_{Al^{3+}}/(a_{H^+})^3)$ versus $\log a_{SiO_2}$ at 25 °C in Figure 2. The activity diagrams in Figures 6a–6d are balanced with respect to Al at 25 °C and have $\log a_{SiO_2}$ specified by the lines labeled H, G, F, E, and D in Figure 2. The activity diagrams in Figures 7a and 7b are balanced with respect to Al with amorphous silica and quartz saturations, respectively, at 100 °C. Figures 8a–8d are balanced with respect to Si at 25 °C and have Al^{3+} concentrations constrained by values corresponding to lines labeled I, A, B, and C, respectively, on Figure 2. The diagrams in Figures 9a–9c are balanced with respect to Si at 100 °C with Al constrained by pyrophyllite–amorphous silica, kaolinite-pyrophyllite, and gibbsite saturations, respectively. The 150 °C diagram shown in Figure 9d is also balanced with respect to Si with Al constrained by pyrophyllite-amorphous silica. Clinoptilolite is included in each of the diagrams, where stable, by considering it to be in equilibrium with Ca end-member saponite (smectite) and hematite to account for

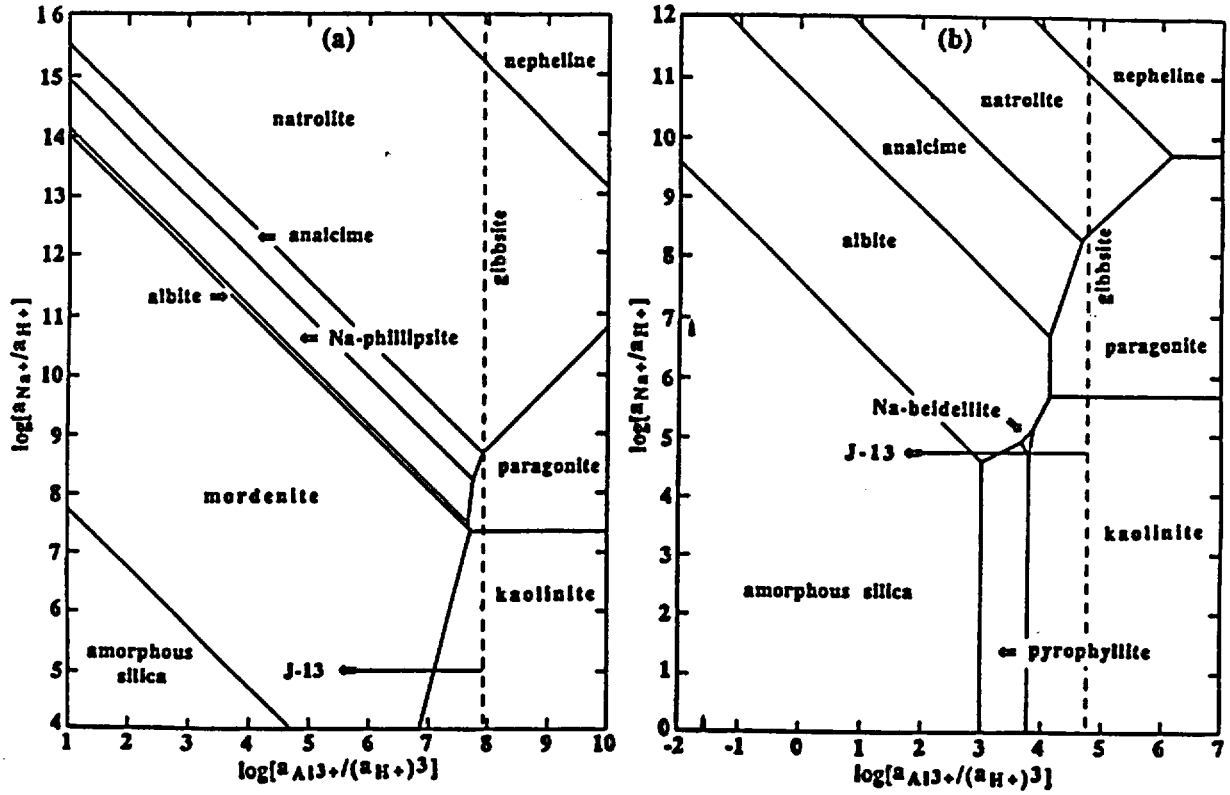

Fig. 4. Activity diagrams for the system Na-Al-Si plus H_2O balanced with respect to Si (a) at 25 °C; and (b) at 100 °C.

the small amounts of Mg and Fe found in the clinoptilolite specimen measured by Hemingway and Robie (1984). As noted earlier, limited thermodynamic data for mordenite enable its stability field to be shown on diagrams at 25 °C only. On all of the activity diagrams shown in Figures 6–9, calcite is plotted with a dashed line by assuming a bicarbonate ion content comparable to J-13 well water, and the circular symbol labeled J-13 corresponds to Ca and Na activities of this reference ground water.

By comparing the activity diagrams shown in Figures 6–9 through changing temperature, or for different activities of Al or Si, trends in the relative stabilities of various zeolite phases may be recognized easily. For example, Figure 6 shows that (1) clinoptilolite is stable at high activities of silica and its field decreases with decreasing silica activity, (2) the heulandite field also diminishes with silica activity but still remains when cristobalite is present, correlating with heulandite + cristobalite assemblages found in some drill cores at Yucca Mountain, (3) the mesolite stability field, which exists at low activities of silica, narrows and then disappears with increasing silica activity, and (4) at low silica activities, scolecite and albite are stabilized relative to heulandite and mordenite, respectively.

The effects of temperature can be seen by comparing Figure 6a (solid lines) with Figure 7a (corresponding to amorphous silica saturation) and Figure 6d with Figure 7b (quartz saturation), where it is apparent that both clinoptilolite and mesolite have smaller regions of stability at 100 °C than at 25 °C, and that Ca end-member phillipsite replaces heulandite at low activities of silica.

The effects of variable Al activity at 25 °C can be observed in Figure 8. Clinoptilolite is not stable at high Al activities corresponding to gibbsite saturation (Fig. 8d) but appears with decreasing Al activities (Figs. 8a–8c). Its stability field maximizes at an intermediate Al activity constrained by the coexistence of amorphous silica and pyrophyllite (cf. smectite) (Fig. 8b) and then becomes smaller with further decrease in Al activity (Fig. 8a). Similar less conspicuous trends exist for heulandite. The stability field of mesolite, on the other hand, increases with rising Al activity and maximizes at gibbsite saturation, where the clinoptilolite, heulandite, mordenite, and phillipsite fields disappear (Fig. 8d). Note that circles representing Ca and Na concentrations of J-13 well water plot close to the join of mordenite, clinoptilolite, and amorphous silica (Fig. 8a), and with heulandite, mordenite, and clinoptilolite (Fig. 8b), which are consistent with mineral assemblages observed at Yucca Mountain. Ef-

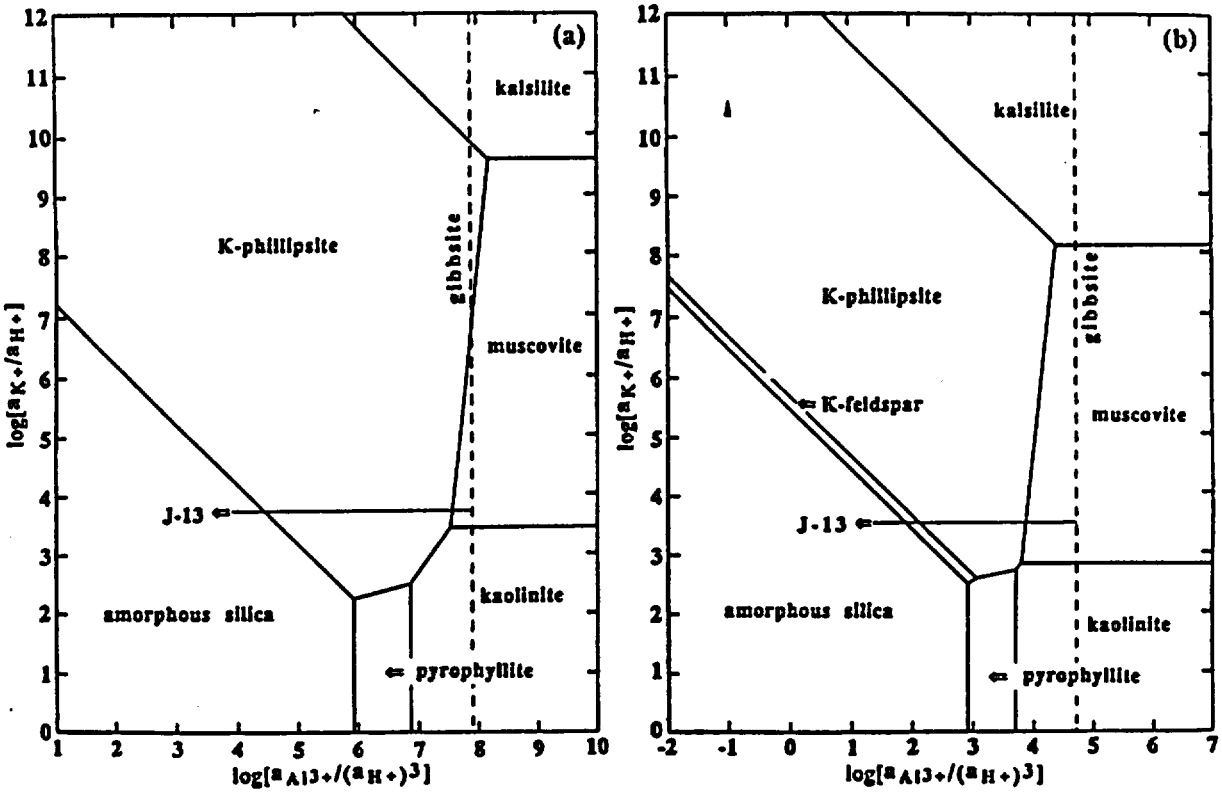

Fig. 5. Activity diagrams for the system K-Al-Si plus H_2O balanced with respect to Si (a) at 25 °C; and (b) at 100 °C.

fects of temperature may be seen in Figures 9a–9c, which show that the clinoptilolite and heulandite stability fields decrease with increasing temperature and appear only at low Al activities. At 150 °C with Al activity corresponding to coexisting pyrophyllite and amorphous silica, clinoptilolite, but not heulandite, still has a small stability field (Fig. 9d). Thus, alkali-rich clinoptilolites are expected to persist to at least 150 °C, as indicated by their occurrence in drill holes at Yellowstone (Keith et al., 1978; Sturchio et al., 1989), but under a significantly reduced range of Al activities.

In Figures 10a and 10b, the system Ca-Na-K-Al-Si is represented at 25 °C with $\log(a_{K^+})/(a_{H^+})$ replacing $\log(a_{Na^+})/(a_{H^+})$ on the x-axis and albite replacing potassium feldspar as the saturation phase. Figure 10a is balanced on Al, and amorphous silica is the saturation phase, whereas Figure 10b is balanced on Si with Al^{3+} activity controlled by coexisting amorphous silica plus pyrophyllite. These two representative activity diagrams based on K^+ activities are very similar to their Na-counterparts, except that K-end-member-silicate phases replace Na-end-member-silicate minerals. The stability field of clinoptilolite is again largest at high silica activities, intermediate Al^{3+} activities, and low temperatures.

Activity diagrams for clinoptilolites of variable compositions

As noted earlier, clinoptilolite compositions vary considerably at Yucca Mountain (Fig. 1). Therefore, activity diagrams were calculated for clinoptilolites of variable Na-Ca, K-Ca, and Ca-Mg contents (Fig. 1), and the results are shown in Figure 11. The stability fields are identified in Figure 11a, which is related to the activity diagram in Figure 8b, where Si is balanced and Al activities are constrained by the assemblage pyrophyllite + amorphous silica + potassium feldspar, which corresponds to conditions of maximum clinoptilolite stability at 25 °C.

Figure 11b shows that with increasing atomic substitution of Na in clinoptilolite, the clinoptilolite stability field narrows. Conversely, the clinoptilolite stability field widens for clinoptilolites with higher Ca contents and merges into the heulandite field. Clinoptilolites more sodic than $Na_{0.56}Ca_{1.3}$ are no longer in equilibrium with J-13 well water, suggesting that ground water with higher Na and lower Ca concentrations, perhaps derived from altered vitric tuffs (White et al., 1980), is necessary to stabilize sodic clinoptilolites.

K has the opposite effect on the clinoptilolite stability

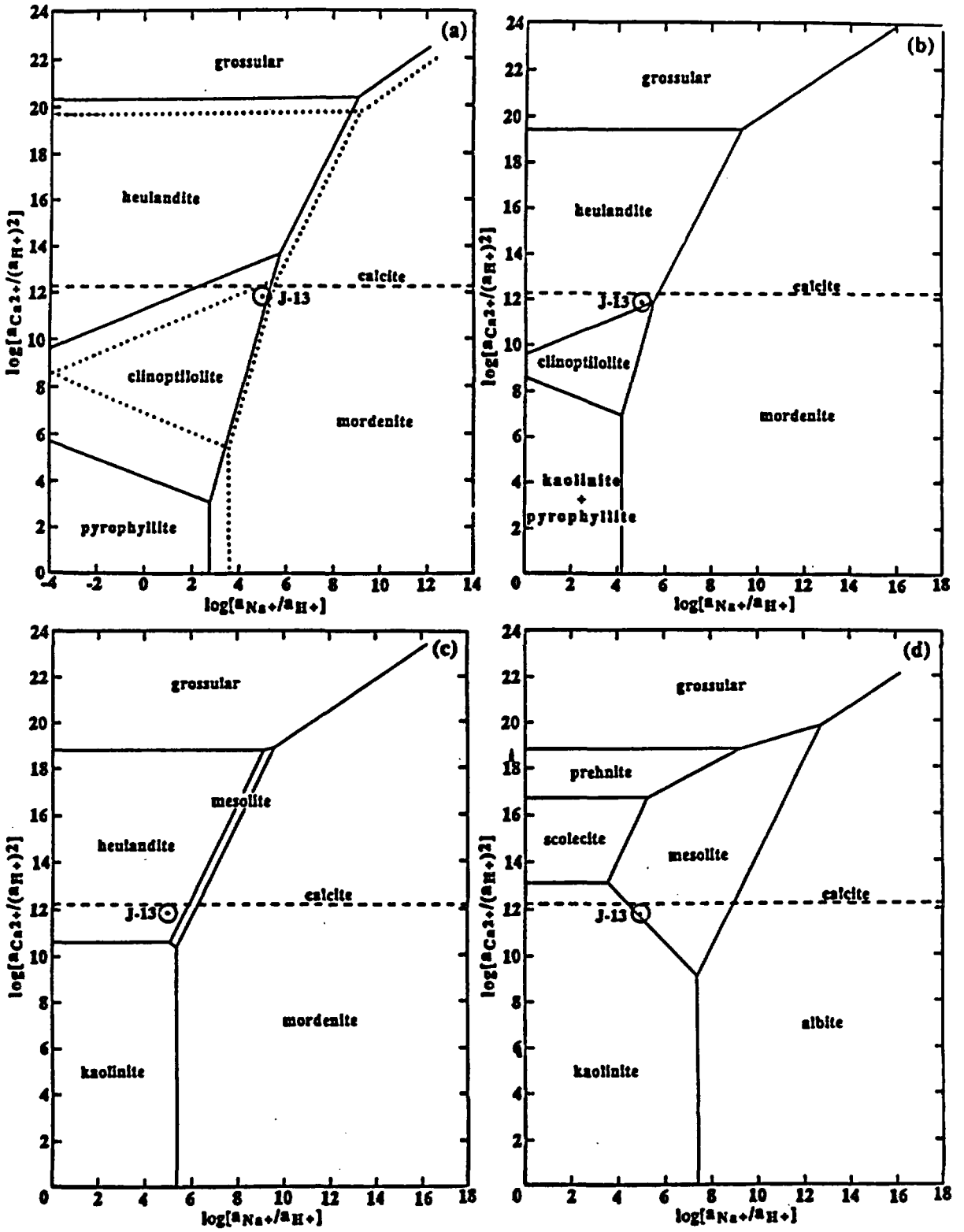

Fig. 6. Activity diagrams for the system Ca-Na-K-Al-Si plus H_2O balanced with respect to Al at 25 °C for different silica activities: (a) amorphous silica and J-13 well water (dotted lines), (b) pyrophyllite-kaolinite, (c) cristobalite, and (d) quartz. Saturation phases also include potassium feldspar, hematite, and Ca end-member saponite.

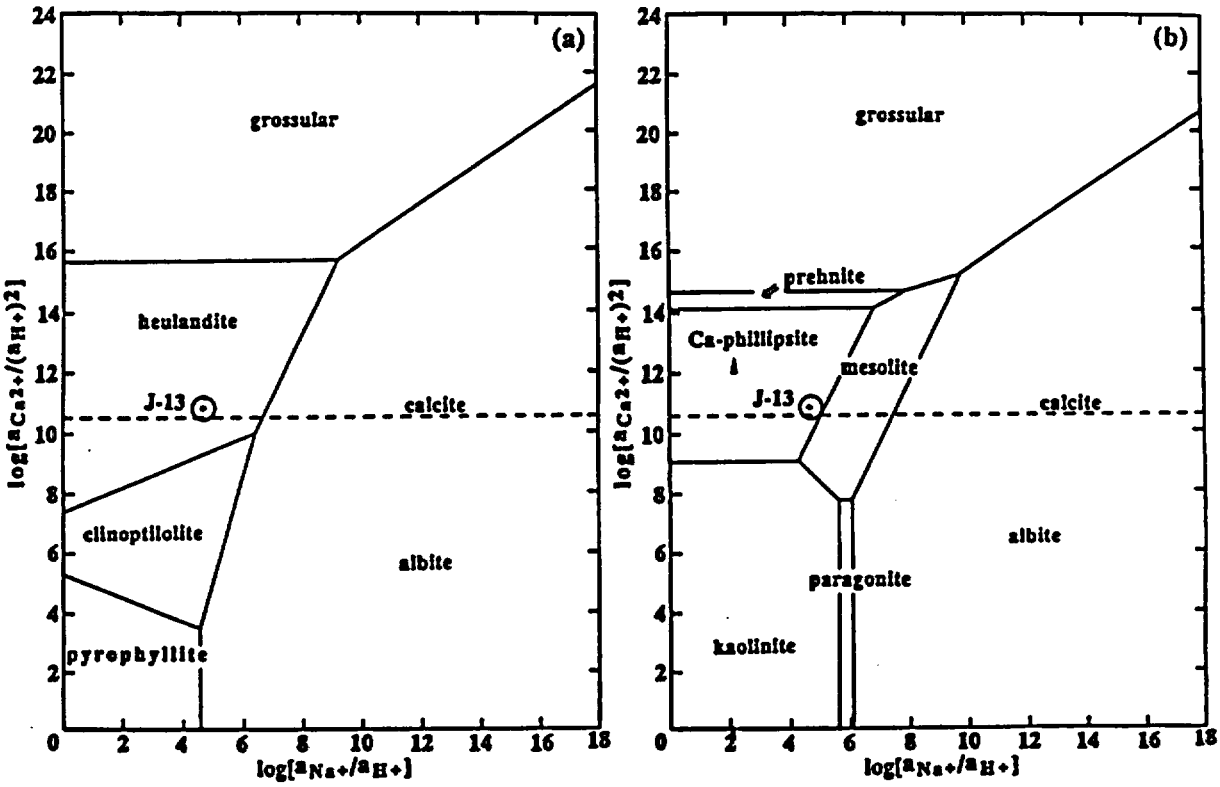

Fig. 7. Activity diagrams for the system Ca-Na-K-Al-Si plus H_2O balanced with respect to Al at 100 °C for different silica activities: (a) amorphous silica, and (b) quartz.

field (Fig. 11c), which widens considerably with increasing atomic substitution of K for Ca. Clinoptilolites less potassic than $K_{0.93}Ca_{1.3}$ would no longer be in equilibrium with J-13 well water. In contrast, replacement of Ca by Mg in clinoptilolite displaces its stability field to lower Ca activities (Fig. 11d). Clinoptilolites more magnesian than $Ca_{1.7}Mg_{1.63}$ would not be in equilibrium with J-13 well water.

Discussion

The activity diagrams demonstrate that the formation of clinoptilolite is favored by SiO_2 activities higher than allowed for by the presence of quartz. This is demonstrated by Figure 6 and is achieved, for example, when clinoptilolite coexists with opal in diagenetically altered volcanic glasses. Heulandite, however, can exist in the presence of opal and cristobalite but not quartz. Such assemblages are commonly observed in vitric tuff samples from drill cores at Rainier Mesa and Yucca Mountain (Benson, 1976; White et al., 1980; Broxton et al., 1987) and from surface desert pavement and outcrop locations (Burns et al., 1990).

Clinoptilolite has a maximum stability field at an intermediate Al activity value but shrinks with either increasing or decreasing activities of Al. This is indicated by Figure 8, in which the clinoptilolite stability field is largest when Al activities are controlled by the assemblage amorphous silica + pyrophyllite (cf. smectite) (Fig. 8b). Furthermore, since the composition of J-13 well water appears to be approximately in equilibrium with respect to calcite, the J-13 Ca^{2+}/Na^{+} points plotted in Figures 8b and 8c suggest that if J-13 well water is in equilibrium with clinoptilolite, then the Al activities should lie between the values for kaolinite-pyrophyllite and pyrophyllite-amorphous silica. Such Al activities also indicate that J-13 well water could be in equilibrium with other zeolites represented on the activity diagrams, including heulandite and mordenite (Fig. 6b) and possibly mesolite (Figs. 8c and 10b), particularly when the stability field of Na-rich clinoptilolites is diminished (Fig. 11b). These observations for calcic clinoptilolite, heulandite, and mordenite correlate with the occurrence of these zeolites as fracture linings in welded and devitrified tuffs and in basal vitrophyres in the vadose zone throughout Yucca Mountain (Broxton et al., 1987; Levy, 1984). Chabazite occurring with coatings of fine-grained heulandite in fractured vitrophyre below the water table in the J-13 well (Carlos, 1989) does not appear to have a stability field

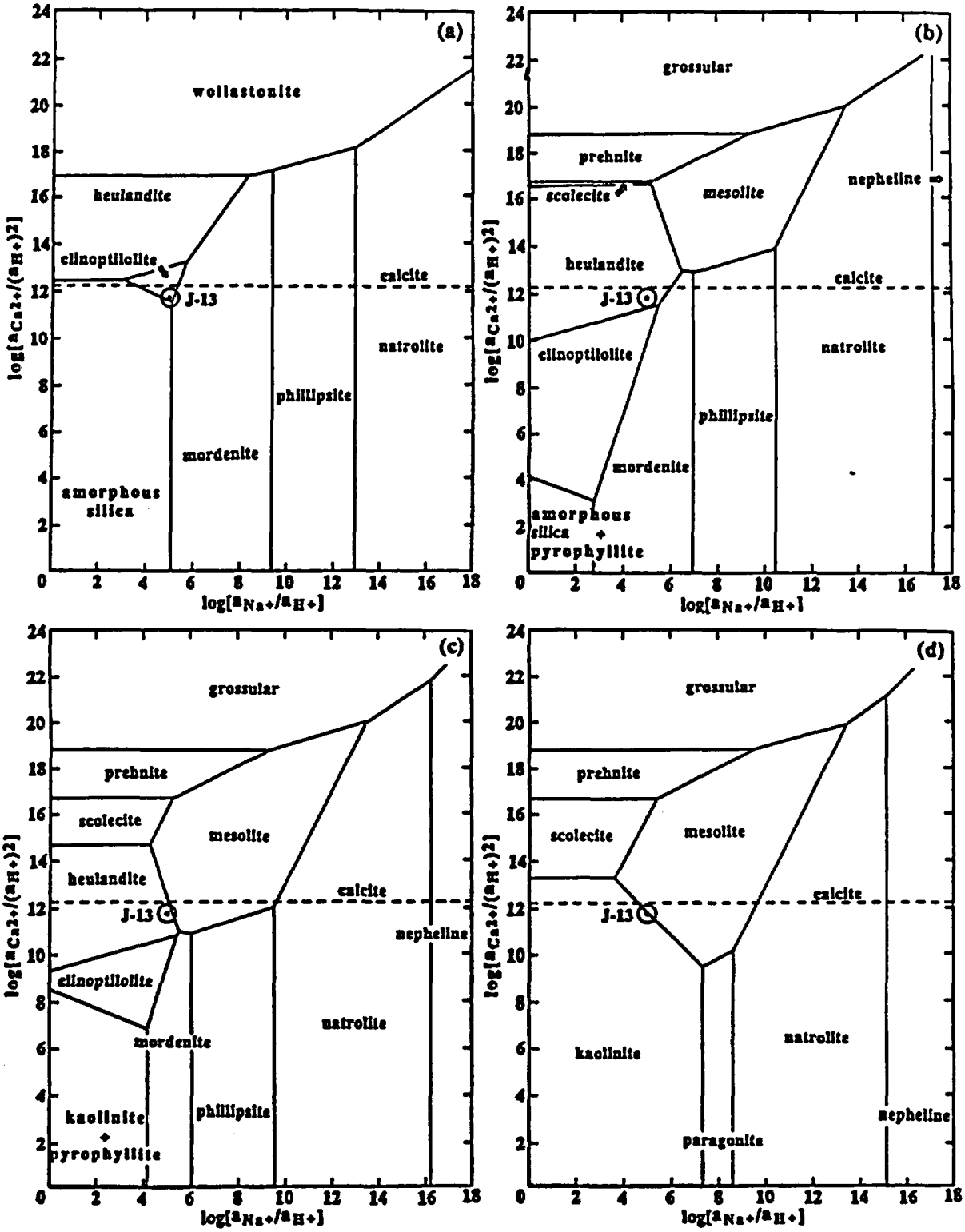

Fig. 8. Activity diagrams for the system Ca-Na-K-Al-Si plus H_2O balanced with respect to Si at 25 °C for different Al activities: (a) low Al activity corresponding to line I in Fig. 2, (b) pyrophyllite-amorphous silica, (c) kaolinite-pyrophyllite, and (d) gibbsite. Saturation phases again include potassium feldspar, hematite, and Ca end-member saponite.

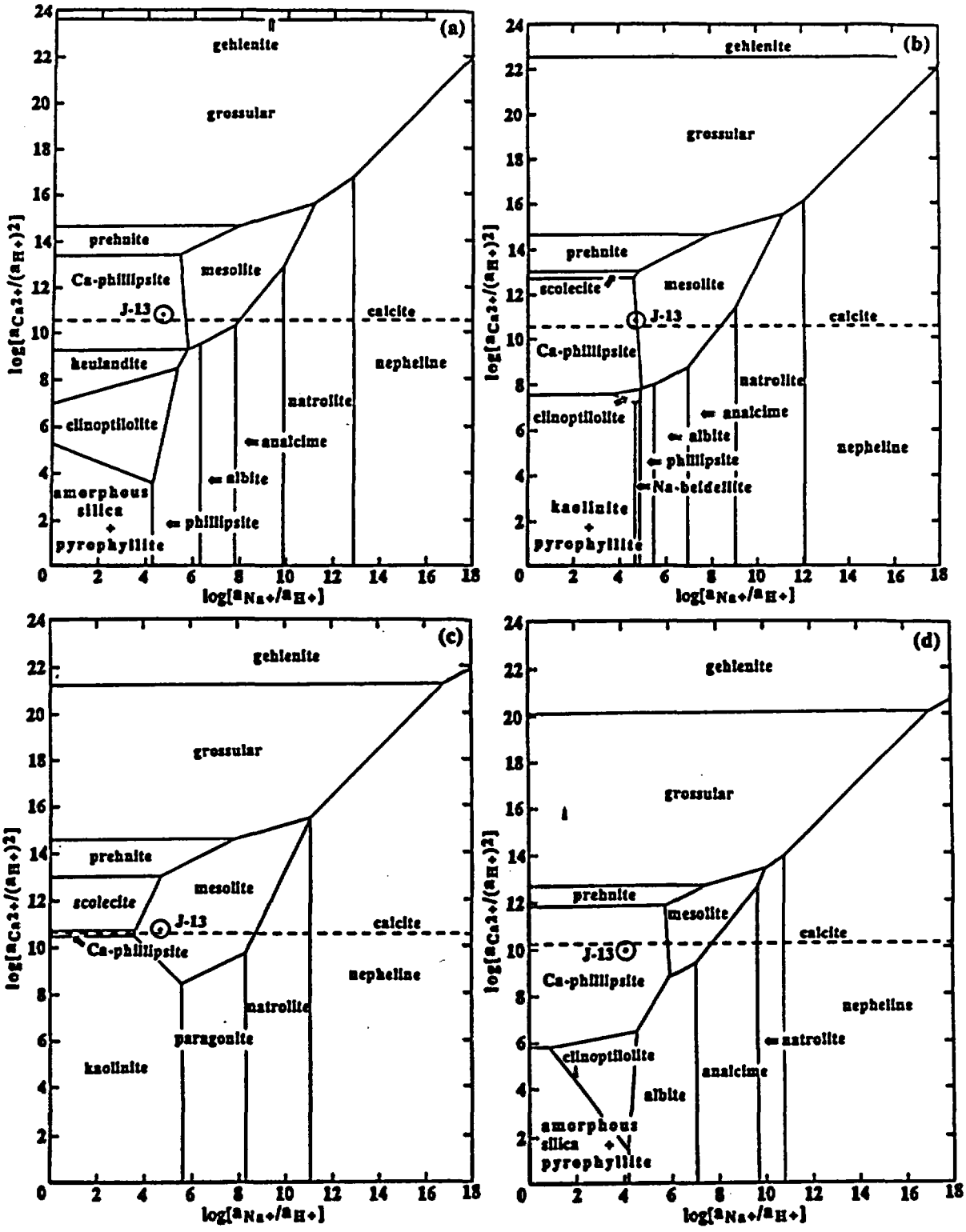

Fig. 9. Activity diagrams for the system Ca-Na-K-Al-Si plus H_2O at elevated temperatures balanced with respect to Si for different Al activities: (a) pyrophyllite-amorphous silica at 100 °C, (b) kaolinite-pyrophyllite at 100°C; (c) gibbsite at 100 °C, and (d) pyrophyllite-amorphous silica at 150 °C.

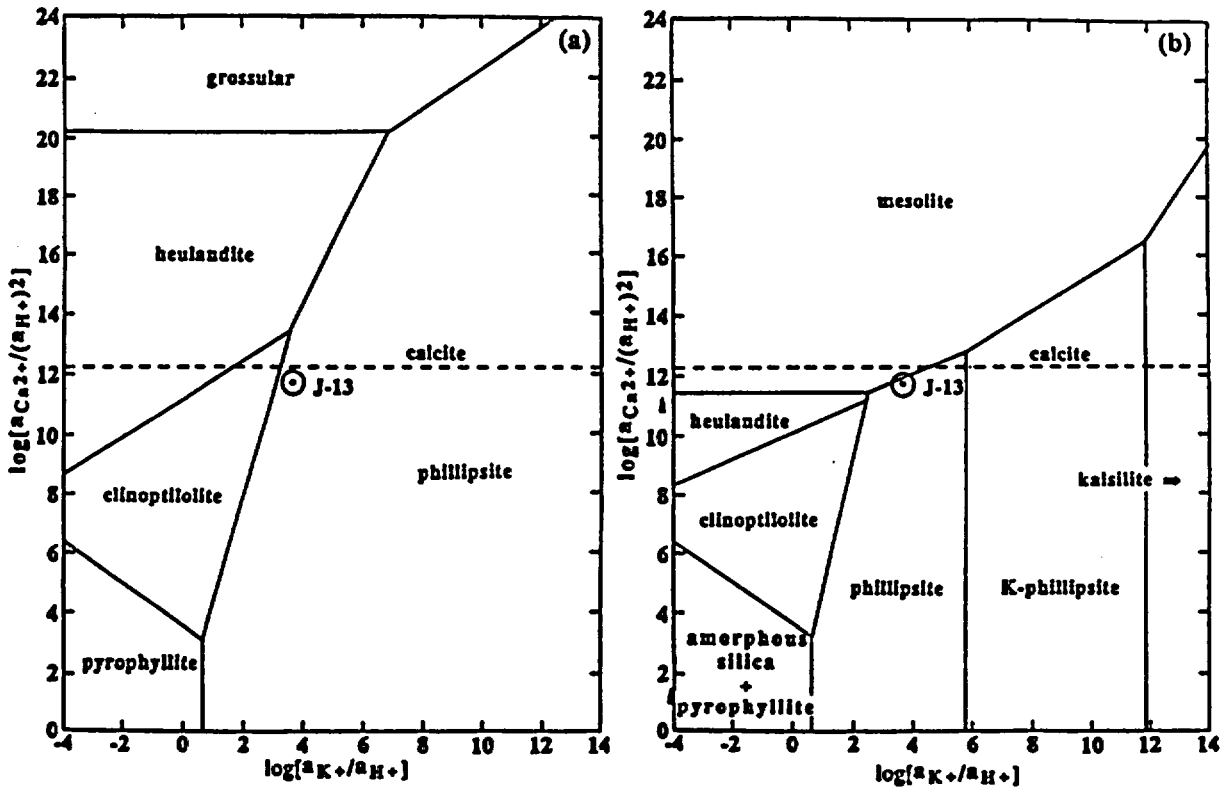

Fig. 10. Activity diagrams based on K and Ca activities in the system Ca-Na-K-Al-Si plus H_2O at 25 °C (a) balanced with respect to Al with silica saturation by amorphous silica, and (b) balanced with respect to Si with Al saturation by pyrophyllite + amorphous silica. Saturation phases include albite, hematite, and Ca end-member saponite.

and may be metastable with respect to mesolite or scolecite.

The clinoptilolite stability field decreases with increasing temperature between 25 and 150 °C (Figs. 7a, 9a, 9b, and 9d) and likely disappears by 200 °C. This correlates with hydrothermal experiments (Boles, 1971; Knauss et al., 1985a, 1985b; Hawkins et al., 1978) and observed geological occurrences of clinoptilolite (Hay, 1966; Hay and Sheppard, 1977). Potassic clinoptilolites have been identified at 120–140 °C in drill cores from the Yellowstone hydrothermal environment (Keith et al., 1978; Sturchio et al., 1989), however, correlating with the increased stability field of K-rich clinoptilolites (see Fig. 11c).

Zeolite diagenetic zones have been suggested for alteration of vitric tuffs based on the appearance and disappearance of clinoptilolite in buried pyroclastic deposits (Iijima, 1975, 1980; Smyth, 1982). Zone I, for example, is characterized by large-scale preservation of glass in vitric tuffs above the water table and incipient alteration of glass shards, particularly in groundmass, to smectite and opal. The Topopah Spring Member at Yucca Mountain, lying well above the water table, falls into Zone I. However, Ca-rich clinoptilolites occur in fractures through lower welded tuff and vitrophyre horizons of the Topopah Spring Member and may be indicative of groundwater interactions, perhaps with microcrystalline devitrified tuffs, which produce relatively high concentrations of dissolved Ca^{2+}, Na^+, and HCO_3^- in fracture-flow water (White et al., 1980). The activity diagrams calculated for 25 °C consistently show that calcic clinoptilolites are stable in the presence of fracture-flow J-13 well water originating from microcrystalline devitrified Topopah Spring Member tuffs, even though such zeolites have not been observed as fracture-lining minerals at this level in J-13 drill cores (Carlos, 1989). The abundance of drusy quartz coating fractures at that level (Carlos, 1989) may depress the silica activity below that necessary to crystallize clinoptilolite (and heulandite).

Diagenetic Zone II, which characterizes the bedded tuffs below the Topopah Spring Member, represents extensive zeolitization of vitric tuffs to clinoptilolite-bearing assemblages and is promoted by water enriched in alkali cations and by slightly elevated temperatures (Smyth, 1982). Progressive hydration and dissolution reactions of the rhyolitic vitric tuffs increase the concentrations of SiO_2, Na^+,

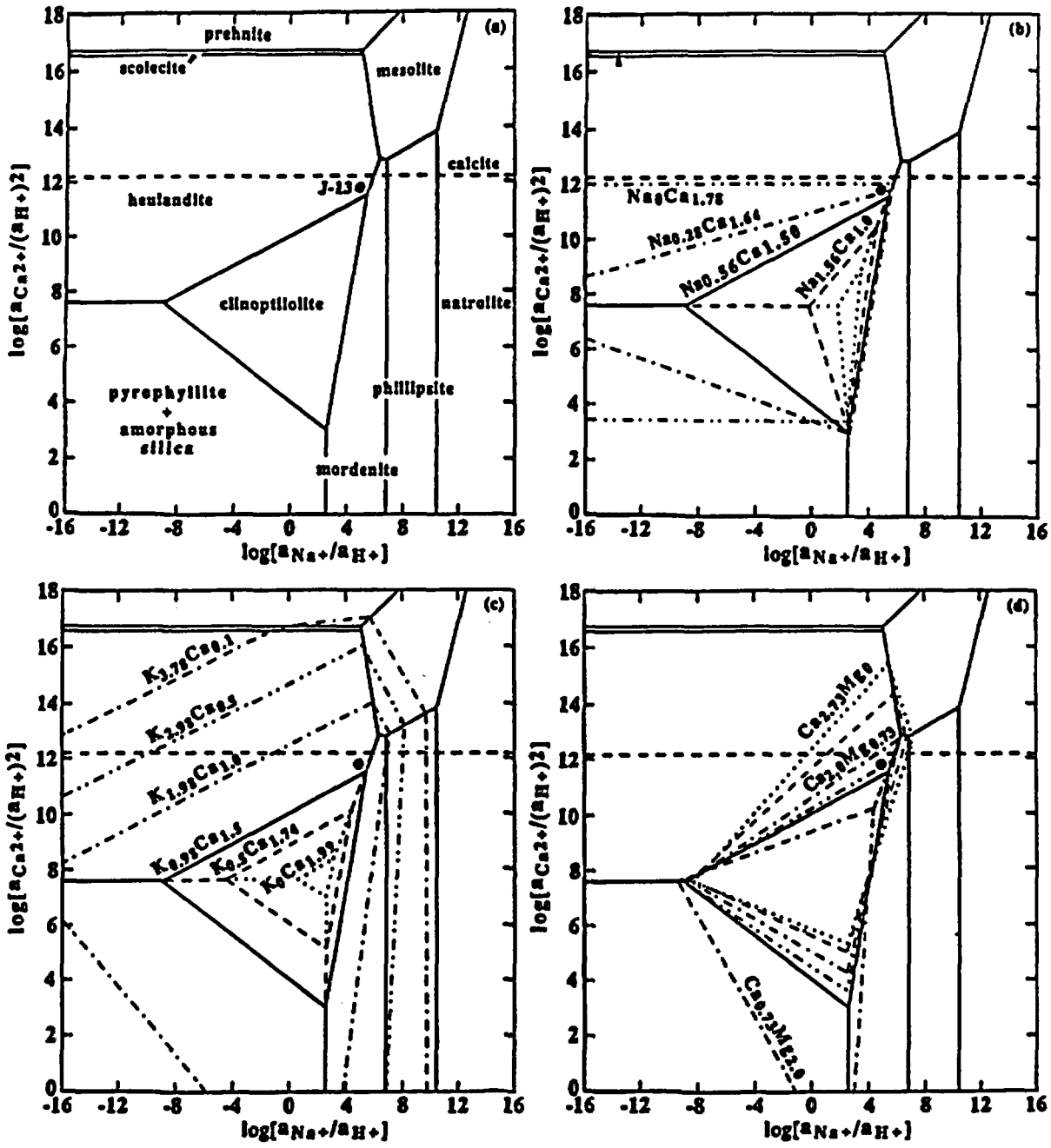

Fig. 11. Activity diagrams for clinoptilolites having variable cation compositions. The calculated stability fields at 25 °C correspond to aluminum saturation by pyrophyllite plus amorphous silica and are balanced with respect to Si (compare Fig. 7b). (a) reference diagram for the clinoptilolite composition $Na_{0.36}K_{0.56}Ca_{1.50}Mg_{1.23}$; (b) Ca-Na variations: ·····-·····= $Na_0Ca_{1.78}$, ·····= $Na_{0.28}Ca_{1.64}$, ——= $Na_{0.56}Ca_{1.5}$, ------= $Na_{1.56}Ca_{1.0}$, ····· = $Na_{2.56}Ca_{0.5}$. (c) K-Ca variations: ·····-·····= $K_{3.78}Ca_{0.1}$, ·····= $K_{2.96}Ca_{0.5}$, ·····= $K_{1.96}Ca_{1.0}$, ——= $K_{0.96}Ca_{1.5}$, ------= $K_{0.5}Ca_{1.75}$, ····· = $K_0Ca_{1.75}$. (d) Ca-Mg variations: ····· = $Ca_{2.73}Mg_0$, ------= $Ca_{2.5}Mg_{0.23}$, ·····= $Ca_{2.0}Mg_{0.73}$, ·····= $Ca_{1.7}Mg_{1.03}$, ——= $Ca_{1.5}Mg_{1.23}$, ·····= $Ca_{0.73}Mg_{2.0}$.

and ultimately K^+ in ground water (White et al., 1980) from which clinoptilolite-clay silicate-opal assemblages are derived. The presence of Ca-poor, K-Na-rich clinoptilolites in diagenetic Zone II conforms with the activity diagrams, which consistently show the clinoptilolite stability field moving away from J-13 well-water compositions at elevated temperatures, as well as by increased Na, but depleted Ca, concentrations in ground water.

Deeper drill cores through Yucca Mountain have yielded analcime instead of clinoptilolite, which is indicative of diagenetic Zone III, whereas Zone IV is represented by the breakdown of analcime to albite. It has been suggested that the clinoptilolite-analcime transition depends on the concentration of dissolved Na, and the Zone II–Zone III boundary was estimated to lie between 100 and 150 °C for present-day ground-water compositions at Yucca Mountain (Smyth, 1982). However, Kerrisk (1983) concluded from reaction-path calculations that the clinoptilolite-analcime transition is controlled by the activity of dissolved silica. Mordenite coexists with clinoptilolite in zeolitized tuffs at Yucca Mountain. Textural evidence (Sheppard et al., 1988) suggests that some mordenites have formed at the expense of clinoptilolite during late-stage dissolution, and this observation is consistent with our activity diagrams. However, mordenite also persists at higher temperatures (~170 °C) than clinoptilolite (~140 °C) in drill holes through the Yellowstone hydrothermal environment (Keith et al., 1978; Sturchio et al., 1989), but this observation cannot be correlated with activity diagrams calculated at elevated temperatures because of lack of thermodynamic data for mordenite. The inability to include mordenite in such activity diagrams may be responsible for the apparent stability fields of albite or phillipsite abutting the clinoptilolite field instead of analcime in the diagrams calculated at 100 °C (Figs. 7a and 9a) and 150 °C (Fig. 9d).

Effects of temperature on the calcic clinoptilolite and heulandite stability fields, together with occurrences of K-Na-rich clinoptilolites at elevated temperatures (Sturchio et al., 1989), suggest that calcic zeolites are most vulnerable to thermal decomposition (cf. Figs. 8a and 8d). Such Ca-rich zeolites occur in fractures (Carlos, 1985) and in the vitrophyre at the base of the Topopah Spring Member tuff at Yucca Mountain (Levy, 1984). The density of fractures is highest in the densely welded tuff horizon in the Topopah Spring Member (Scott et al., 1983) where siting of the proposed nuclear waste repository is planned. In the vicinity of the heat envelope that would surround radioactive waste buried there, fluid temperatures could exceed 150 °C within a radius of 10 m from the proposed repository horizon (Travis et al., 1984; U.S. DOE, 1988, p. 4–118), and thereby affect the thermal stability of calcic zeolites in the fractures and underlying basal vitrophyre.

Several observed reactions suggested by phase assemblages in weathered vitric tuffs (Benson, 1976; White et al., 1980; Burns et al., 1990) can be demonstrated on the activity diagrams. For example, the reaction of glass + clay silicates to clinoptilolite + opal plots at the intersection of amorphous silica + pyrophyllite + mordenite + clinoptilolite in Figures 6a and 8b, but requires lower calcium activities in the coexisting fluid than that of J-13 well water. Low Ca and slightly reduced K activities of rainwater would account for the assemblage glass + clay silicates + opal + clinoptilolite + authigenic potassium feldspar forming on weathered vitric tuffs at outcrops and in detritus forming desert pavement (Burns et al., 1990). The assemblage of clinoptilolite + calcite + opal also found in weathered vitric tuffs is represented on Figure 8a, requiring, however, very low activities of Al.

Conclusions

The calculated activity diagrams presented here quantify observed field occurrences and verify deductions made about the stability of clinoptilolite during burial diagenesis of vitric tuffs. The coexistence of clinoptilolite with opal correlates with its calculated wide stability field in aqueous solutions saturated with amorphous silica. Clinoptilolite-smectite assemblages indicate that the zeolite crystallized from ground water with dissolved Al concentrations lower than saturation values with respect to gibbsite and lower than the reported measurements of J-13 well water. Calcic clinoptilolites associated with calcite are consistent with crystallization from fracture-flow ground water containing Ca^{2+} and HCO_3^- derived from incipient dissolution of microcrystalline devitrified tuffs. Alkali-rich clinoptilolites, on the other hand, correlate with ground water having elevated Na^+ and K^+ but depleted Ca^{2+} concentrations, which are associated with altered vitric tuffs. Although the crystallization of clinoptilolite may be promoted by ground water enriched in silica and alklai metals, the clinoptilolite stability field diminishes appreciably between 25 and 150 °C, correlating with burial diagenetic reactions, and confirming doubts (Smyth, 1982) about the thermal stability of calcic clinoptilolites close to buried radioactive waste. Questions remain, however, concerning the stability of calcic versus K-Na-rich clinoptilolites at elevated temperatures and the effects of compositional variations in heulandite and mordenite. Recently revised thermodynamic properties of heulandite (Johnson et al., 1989) and limited information on thermal stability limits of mordenite (Kusakabe et al., 1981) may constrain our ongoing calculations of zeolite activity diagrams.

Acknowledgments

We gratefully acknowledge the assistance of Drs. M. E. Morgenstein, C. L. Johnson, and D. L. Shettel, who reviewed early drafts of the manuscript and provided information about ground-water chemistry at Yucca Mountain. Helpful comments on the original manuscript were received from Drs. J. A. Apps, D. L. Bish, J. G. Liou, W. M. Murphy, J. K. Bohlke, and an anonymous reviewer. Dr. J. F. Kerrisk kindly provided his report on clinoptilolite stability field calculations. The study was funded by the State of Nevada, Nuclear Waste Project Office, under a Department of Energy grant from the Nuclear Waste Fund.

References cited

Benson, L.V. (1976) Mass transport in vitric tuffs of Rainier Mesa, Nye County, Nevada. U.S. Energy Research and Development Administration, Nevada, Report NVO-1253-10.

Bish, D.L. (1989) Evaluation of past and future alterations in tuff at Yucca Mountain, Nevada, based on the clay mineralogy of drill cores USW G-1, G-2, and G-3. U.S. National Technical Information Service, Report LA-10667, 40 p.

Bish, D.L., Ogard, A.L., Vaniman, D.T., and Benson, L. (1984) Miner-

alogy-petrology and groundwater chemistry of Yucca Mountain Tuffs. Materials Research Society Symposium Research Proceedings, 26, 283–291.

Boles, J.R. (1971) Synthesis of analcime from natural heulandite and clinoptilolite. American Mineralogist, 56, 1724–1734.

Bowers, T.S., Jackson, K.J., and Helgeson, H.C. (1984) Equilibrium activity diagrams for coexisting minerals and aqueous solutions at pressures and temperatures to 5 kb and 600 °C. Springer-Verlag, New York.

Broxton, D.E., Bish, D.L., and Warren, R.G. (1987) Distribution and chemistry of diagenetic minerals at Yucca Mountain, Nye County, Nevada. Clays and Clay Minerals, 35, 89–110.

Broxton, D.E., Warren, R.G., Hagan, R.C., and Luedemann, G. (1986) Chemistry of diagenetically altered tuffs at a potential nuclear waste repository, Yucca Mountain, Nye County, Nevada. U.S. National Technical Information Service, Report LA-10802, 160 p.

Broxton, D.E., Byers, F.M., Jr., and Warren, R.G. (1989) Petrography and phenocryst chemistry of volcanic units at Yucca Mountain, Nevada: A comparison of outcrop and drill hole samples. U.S. National Technical Information Service, Report LA-11503, 65 p.

Burns, R.G., Bowers, T.S., Wood, V.J., Blundy, J.D., and Morgenstein, M.E. (1990) Reactivity of zeolites forming in vitric tuffs in the unsaturated zone at Yucca Mountain, Nevada. In Proceedings of nuclear waste isolation in the undersaturated zone, Focus '89, p. 101–112. American Nuclear Society, La Grange Park, IL.

Carlos, B.A. (1985) Minerals in fractures of the unsaturated zone from drill core USW G-4, Yucca Mountain, Nye County, Nevada. U.S. National Technical Information Service, Report LA-10415, 55 p.

——(1989) Fracture-coating minerals in the Topopah Spring Member and Upper Tuff of Calico Hills from drill hole J-13. U.S. National Technical Information Service, Report LA-11504, 20 p.

Chen, C.-H. (1975) A method of estimation of standard free energies of formation of silicate minerals at 298.15 °K. American Journal of Science, 275, 801–817.

Daniels, W.R., et al. (29 coauthors) (1982) Summary report on the geochemistry of Yucca Mountain and environs. U.S. National Technical Information Service, Report LA-9328.

Delany, J.M. (1985) Reaction of Topopah Spring tuff with J-13 water: A geochemical modeling approach using the EQ3/6 reaction path code. U.S. National Technical Information Service, Report UCRL-53631.

Hawkins, D.B., Sheppard, R.A., and Gude, A.J., III (1978) Hydrothermal synthesis of clinoptilolite and comments on the assemblage phillipsite-clinoptilolite-mordenite. In L.B. Sands and F.A. Mumpton, Eds., Natural zeolites, p. 337–349. Pergamon Press, New York.

Hay, R.L. (1966) Zeolites and zeolite reactions in sedimentary rocks. Geological Society of America Special Paper 85, p. 130–146.

Hay, R.L., and Sheppard, R.A. (1977) Zeolites in open hydrologic systems. In F.A. Mumpton, Ed., Mineralogy and geology of natural zeolites. Mineralogical Society of America Reviews in Mineralogy, 4, 93–102.

Hemingway, B.S., and Robie, R.A. (1984) Thermodynamic properties of zeolites: Low temperature heat capacities and thermodynamic functions of phillipsite and clinoptilolite. Estimates of the thermochemical properties of zeolitic water at low temperatures. American Mineralogist, 69, 692–700.

Hoover, D.L. (1968) Genesis of zeolites, Nevada Test Site. Geological Society of America Memoir 110, 275–284.

Iijima, A. (1975) Effect of pore water to clinoptilolite-analcime-albite reaction series. Journal of the Faculty of Science, University of Tokyo, Series II, 19, 133–147.

——(1980) Geology of natural zeolites and zeolitic rocks. In L.V.C. Rees, Ed., Proceedings of the Fifth International Conference on Zeolites, p. 103–118. Heyden & Co., London.

Johnson, G.K., Flotow, H.E., O'Hare, P.A.G., and Wise, W.S. (1982) Thermodynamic studies of zeolites: Analcime and dehydrated analcime. American Mineralogist, 67, 736–748.

——(1983) Thermodynamic studies of zeolites: Natrolite, mesolite, and scolecite. American Mineralogist, 68, 1134–1145.

——(1985) Thermodynamic studies of zeolites: Heulandite. American Mineralogist, 70, 1065–1071.

——(1989) Thermodynamic studies of zeolites: Heulandite: Erratum. American Mineralogist, 74, 697.

Keith, T.E.C., White, D.E., and Beeson, M.H. (1978) Hydrothermal alteration and self-sealing in Y-7 and Y-8 drill holes in northern part of Upper Geyser Basin, Yellowstone National Park, Wyoming. U.S. Geological Survey Professional Paper 1054-A, A1–A26.

Kerrisk, J.F. (1983) Reaction-path calculations of groundwater chemistry and mineral formation at Rainier Mesa, Nevada. U.S. National Technical Information Service, Report LA-9912-MS, 41 p.

Kerrisk, J.F. (1987) Groundwater chemistry at Yucca Mountain, Nevada, and vicinity. U.S. National Technical Information Service, Report LA-10929, 113 p.

Knauss, K.G., Beiringer, W.J., and Peifer, D.W. (1985a) Hydrothermal interaction of crushed Topopah Spring tuff and J-13 water at 90, 150, and 250 °C using Dickson-type, gold-bag rocking autoclaves. U.S. National Technical Information Service, UCRL-53630, 27 p.

Knauss, K.G., Delany, J.M., Beiringer, W.J., and Peifer, D.W. (1985b) Hydrothermal interaction of Topopah Spring Tuff with J-13 water as a function of temperature. Materials Research Society Symposium Proceedings, 27, 539–546.

Kusakabe, H., Minato, H., Utada, M., and Yamanaka, T. (1981) Phase relations of clinoptilolite, mordenite, analcime and albite with increasing pH, sodium ion concentration and temperature. Scientific Papers of the College of General Education, University of Tokyo, 31, 39–59.

Levy, S.S. (1984) Studies of altered vitrophyre for the prediction of nuclear waste repository-induced thermal alteration at Yucca Mountain, Nevada. Materials Research Society Symposium Proceedings, 26, 959–966.

Moncure, G.K., Surdam, R.C., and McKague, H.L. (1981) Zeolite diagenesis below Pahute Mesa, Nevada Test Site. Clays and Clay Minerals, 29, 385–396.

Moore, D.E., Morrow, C.A., and Byerlee, J.D. (1986) High-temperature permeability and groundwater chemistry of some Nevada Test Site tuffs. Journal of Geophysical Research, 82, 2163–2171.

Ogard, A.E., and Kerrisk, J.F. (1984) Groundwater chemistry along flow paths between a proposed repository site and the accessible environment. U.S. National Technical Information Service, Report LA-10188.

Ogard, A.E., Wolfsberg, K., Daniels, W.R., Kerrisk, J., Rundberg, R.S., and Thomas, K.W. (1984) Retardation of radionuclides by rock units along the flow path to the accessible environment. Materials Research Society Symposium Proceedings, 26, 329–336.

Oversby, V.M. (1985) The reaction of Topopah Spring tuff with J-13 water at 90 °C and 150 °C—Samples from drill cores USW G-1, USW GU-3, USW G-4, and UE-25h#1. U.S. National Technical Information Service, Report UCRL-53629, 26 p.

Scott, R.B., Spengler, R.W., Diehl, S., Lappin, A.R., and Chornack, M.P. (1983) Geologic character of tuffs in the unsaturated zone at Yucca Mountain, southern Nevada. In J.W. Mercer, P.S.C. Rao, and I.W. Wendell, Eds., Role of the unsaturated zone in radioactive and hazardous waste disposal, p. 289–335. Ann Arbor Science, Ann Arbor, Michigan.

Sheppard, R.A., and Gude, A.J., III (1973) Zeolites and associated authigenic silicate minerals in tuffaceous rocks of the Big Sandy formation, Mohave County, Arizona. U.S. Geological Survey Professional Paper 830.

Sheppard, R.A., Gude, A.J.,III and Fitzpatrick, J.J. (1988) Distribution, characterization, and genesis of mordenite in Miocene silicic tuffs at Yucca Mountain, Nye County, Nevada. U.S. Geological Survey Bulletin 1777, 22 p.

Smyth, J.R. (1982) Zeolite stability constraints on radioactive waste isolation in zeolite-bearing volcanic rocks. Journal of Geology, 90, 195–201.

Sturchio, N.C., Bohlke, J.K., and Binz, C.M. (1989) Radium-thorium disequilibrium and zeolite-water ion exchange in a Yellowstone hydrothermal environment. Geochimica et Cosmochimica Acta, 53, 1025–1034.

Thomas, K.W. (1987) Summary of sorption measurements performed with Yucca Mountain, Nevada, tuff samples and water from well J-13. U.S. National Technical Information Service, Report LA-10960, 99 p.

Travis, B.J., Hodson, S.W., Nuttall, H.E., Cook, T.L., and Rundberg, R.S. (1984) Numerical simulation of flow and transport in fractured tuff. Materials Research Society Symposium Proceedings, 26, 1039–1046.

U.S. Department of Energy (1988) Site characterization plan, Yucca Mountain Site, Nevada, research and development area, Nevada, Report DOE/RW-0160, 8 vols.

White, A.F., Claassen, H.C., and Benson, L.V. (1980) The effect of dissolution of volcanic glass on the water chemistry in a tuffaceous aquifer, Rainier Mesa, Nevada. U.S. Geological Survey Water-Supply Paper 1535-Q, 33 p.

Wolery, T.J. (1983) EQ3NR, a geochemical program for geochemical aqueous speciation-solubility calculations. U.S. National Technical Information Service, UCRL-5, Distribution Category UC-70.

Yang, I.C., Turner, A.K., Sayre, T.M., and Montazer, P. (1988) Triaxial-compression extraction of pore water from unsaturated tuff, Yucca Mountain, Nevada. U.S. Geological Survey Water-Resources Investigations Report 88-4189, 68 p.

Manuscript received November 28, 1988
Manuscript accepted February 2, 1990

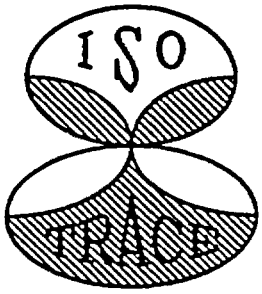

ISOTRACE LABORATORY

A SURVEY OF IODINE-129 IN THE ENVIRONMENT

by

Naomi Baba

A Thesis submitted in conformity with the requirements
for the Degree of Master of Science in the
University of Toronto

IsoTrace Laboratory, University of Toronto
60 St. George Street, Toronto, Canada M5S 1A7

Acknowledgements

I would like to express my appreciation to all the members at IsoTrace Laboratory for their support of this work. My special thanks go to Dr. L.Kilius and Professor J.C.Rucklidge, my supervisor, for their assistance and guidance; to J.Perez for helping me out from my struggles with WordPerfect and Autocad; to R.Cresswell for his sincere help with my various problems; and to Professor K.Howard in the Department of Geology for support and encouragement.

My appreciation also goes to Professor N, Nakai of Nagoya University in Japan, who has guided me in my carreer, for his great help in obtaining the brine samples.

I would like to acknowledge the following organizations for providing marine biological samples: Smithsonian Institution, Canadian Museum of Nature, Redpath Museum at McGill University, Atlantic Reference Center at Huntsman Marine Science Center and Hokkaido University in Japan.

I would like to acknowledge Petroleum Resource Development Company and Kanto Natural Gas Development Company (in Japan) for providing brine samples and also useful information. My special thanks go to members of Mitsubishi Gas Chemistry Company (in Japan) for their generous support when I collected the brine samples.

I would like to thank Dr. Gwen Milton and Dr. Jack Cornett of Chalk River Laboratory for discussing a perspective on ^{129}I research with us and also for providing a groundwater sample.

This work was supported by Mifflin & Associates, Inc. of Las Vegas, Nevada and the Natural Sciences and Engineering Research Council of Canada.

Contents

Abstract

Extraction methods of iodine for various natural samples were tested for the ^{129}I analysis by AMS with a purpose of understanding ^{129}I distribution in selected parts of the natural environment.

Extraction of iodine from marine biological specimens was carried out by dry-ashing of samples in a combustion tube with a presence of oxygen. The $^{129}I/^{127}I$ ratios of the iodine for coastal marine organisms show significant entry of man-made ^{129}I into the environment since 1945, one or two magnitudes higher than before that date. Both pre-bomb and post-bomb data indicate local variations of $^{129}I/^{127}I$ ratios. The local variation in the pre-bomb data may reflect differences in local geology, since fissiogenic contribution of this isotope from weathered material can be important in coastal areas. The local variation in the post-bomb data is probably due to incomplete mixing of man-made ^{129}I in the environment.

Some geological samples from K-T (Cretaceous-Tertiary) boundary were tentatively analyzed for their ^{129}I content from the point of view of the stability of cosmic ray flux and ^{129}I transport from outer space in the past, as radiation on the Earth from a nearby supernova has been one of the suggested causes of mass extinction of various biological species. Since the material was organic rich, the combustion method was applied for the extraction of iodine. Extraction efficiency was low possibly due to the incomplete combustion and transfer of vaporized iodine. Higher isotope ratios than pre-bomb ratio were obtained for samples not only at the vicinity of the boundary but also at far above and below the boundary. Although this does not exclude the possibility of the supernova hypothesis, ^{129}I contamination from modern meteoric water or from the extraction procedure is quite possible.

The $^{129}I/^{127}I$ ratios were also determined for some iodine-rich brines in Japan, where iodine is considered to be genetically related to the buried organic matter which later formed natural gas or oil. Iodine in brines can be readily extracted by oxidation using oxidizing reagent after decomposing organic matter in the samples by evaporating and gentle heating by a burner. Although dating of brines or estimation of parent organic matter of hydro-carbon has been suggested, that now seems difficult for the sample of <16 Ma range because of the large error in the measurement and also because the initial ratio could possibly vary in a certain range locally or time-dependently. The possibility of secondary alteration due to the interaction with host rocks or meteoric water can not be neglected.

An extraction method of iodine from a shallow groundwater sample with low iodine content was tested using anion-exchange resin with an addition of carrier.

Chapter I : Introduction

I-(1) Purpose and scope of investigation

Iodine has one stable isotope, ^{127}I, and several radioisotopes including ^{129}I. Iodine-129 has a half-life of 16 million years, and its decay product is ^{129}Xe.

Because of the low specific activity and the low energy of its radiations, it is impossible to make direct measurement of the concentration of ^{129}I in the natural environment by measuring its decay-rate.

Although the introduction of neutron-activation analysis opened up the possibility of measuring as little as 10^{-13} grams of ^{129}I (Studier, 1962), samples have been limited due to the requirement of gram quantities of iodine (Edwards and Rey, 1967) and the necessity to go through tedious purification processes in order to obtain a final product free of interference from other activation products.

Accelerator mass spectrometry (AMS) has become a promising tool for studying trace amount of long-lived radionuclides during the last decade. Iodine-129 is currently studied by AMS at the Nuclear Structure Research Laboratory at the University of Rochester and at the IsoTrace Laboratory at the University of Toronto. The main advantages of AMS over neutron activation analysis are that only 1-5 mg of iodine is needed for analysis and that we do not have to worry about interference from other elements which may be contained in a final product after the sample preparation procedure.

While various applications of this isotope have been proposed for geological, hydrological and geochemical studies (Edwards, 1962; Fabryka-Martin *et al.*, 1985; Fabryka-Martin *et al.*, 1987b; Fehn *et al.*, 1986), a study on the distribution of ^{129}I in the natural environment is still at an exploratory stage.

The main objectives of this study are:

1) to develop and test the chemical procedures for the extraction of iodine from natural samples;

2) to measure the natural level of ^{129}I in samples from the marine environment which were collected prior to 1945 and are hence unaffected by man-made disturbance which occured after this date;

3) to see the entry of ^{129}I in the marine environment arriving from anthropogenic activity, that is, nuclear weapon testing or nuclear industry; and

4) to measure ^{129}I concentration in natural samples, such as, sediments and

brines to see the feasibility of proposed geological and hydrological applications of this isotope, such as, (a) investigation of the stability of cosmic ray flux and ^{129}I transport from outer space in the past and (b) dating of brine or estimation of buried age of organic matter which was later transformed into fluid or gaseous hydro-carbon.

The study is formatted in the following way to address these objectives. In the rest of this chapter, previous studies are summarized regarding the distribution of ^{129}I in the environment. In Chapter II, the distribution of natural and anthropogenic ^{129}I in coastal marine environment is examined using iodine-rich marine organisms. It presents chemical procedures for the iodine extraction from algae, sponge and horny corals, the ^{129}I measurement by AMS and the interpretation of the data. In Chapter III, the iodine extraction methods for geological and hydrological material, such as, sediments, brines and shallow groundwater are presented. The ^{129}I concentrations are measured in these samples by AMS to discuss geological and hydrological meanings of the data. Conclusions are presented in Chapter IV.

I-(2) Previous studies on the distribution of ^{129}I in the environment

In this section, previous studies are summarized regarding the natural and anthropogenic production of ^{129}I and its distribution.

(A) Naturally produced ^{129}I

Iodine-129 in the environment originates from (a) the spontaneous fission of ^{238}U, (b) direct interaction of cosmic radiation with stable elements in the upper atmosphere and (c) cosmic radiation in extraterrestrial matter (cosmic dust) which ultimately reaches the Earth's surface. The fission contributions to the hydrosphere originate (1) from uranium in seawater, (2) from uranium in weathering rocks and (3) through the release of ^{129}I in volcanic processes.

Edwards and Rey (1968) made an estimate of the distribution of terrestrial ^{129}I under equilibrium conditions. Principal processes contributing to 90% of the total natural ^{129}I production are cosmic-ray interactions with xenon in the atmosphere and volcanic release of fissiogenic ^{129}I. These two contributions are of approximately the same magnitude.

According to their estimate, the $^{129}I/^{127}I$ ratio for a marine environment in an equilibrium condition is approximately 2.2×10^{-12}, while that for freshwater or land mass surface is slightly higher.

Since the present ^{129}I concentration in the natural environment has been greatly disturbed by the man-made ^{129}I from nuclear reactors since 1945, it is necessary to obtain natural samples which are free of this contamination in order to verify the estimation. Edwards (1962) suggested that iodine in pre-fallout (pre-bomb) marine

plants and animals should represent natural ^{129}I levels, since their environment is in a relatively homogeneous equilibrium. Despite the collection of some pre-bomb material by Edwards and Rey (1968), the demand for gram-sized quantities of iodine for activation analysis made the measurement difficult. They reported a ratio of $4x10^{-11}$ for Pre-1936 human thyroid. This is the first and only published data for pre-bomb biological specimens, as far as the writer knows.

Fehn *et al.*(1986) obtained the $^{129}I/^{127}I$ ratio of around $1x10^{-12}$ for pre-bomb marine sediments from the continental slopes near Cape Hatteras in the Atlantic Ocean. An atmospheric pre-bomb ratio of $6x10^{-13}$ was reported by Fabryka-Martin *et al.* (1985), based on measurements on young groundwater (ca. 4,000 years) in the recharge area of the Great Artesian Basin of Australia. However, the groundwater may have had a leaching of old iodine, that is, iodine with low ^{129}I content, from the host rocks.

(B) Production and distribution of anthropogenic ^{129}I

Man-made ^{129}I, a fission product of ^{235}U and ^{239}Pu, has been produced and released directly to the atmosphere and/or hydrosphere from nuclear bomb testing and waste from the processing of spent nuclear fuels.

The concentration of ^{129}I in the atmosphere, as well as that of other manmade radionuclides such as ^{14}C, ^{3}H and ^{137}Cs, seems to have peaked in 1960's and 1970's, when a $^{129}I/^{127}I$ ratio of about 10^{-7} was measured in rain from a region remote from nuclear facilities (Oliver *et al.*, 1982). Such releases are now under control; therefore, the concentration of this isotope in the atmosphere has been decreasing over the past decade owing to its deposition on the earth's surface and dilution by marine iodine. The current isotopic ratio for precipitation is on the order of 10^{-12} to 10^{-10} (Fabryka-Martin *et al.*, 1989).

The residence time of iodine in the atmosphere is about 15 days (Kocher, 1981). This is not long enough for a localized release of ^{129}I to become globally mixed in the atmosphere. Therefore, the distribution of ^{129}I, at present, is expected to be quite inhomogeneous on the earth due to incomplete mixing. This is different from ^{14}C, where the concentration has been relatively homogeneously distributed on global scale.

Chapter II : Natural and anthropogenic ^{129}I in marine organisms

Marine organisms, such as, algae, sponge and horny corals are great concentrators of iodine. They may contain from a few hundred parts per million (ppm) to a few percent of iodine, while the average iodine concentration in sea water is about 0.05 ppm.

A number of suitable marine biological specimens were obtained from collections in several museums in Canada and the U.S. for analysis of their $^{129}I/^{127}I$ ratios. The main purposes of this study were to measure the pre-bomb level of ^{129}I and to see the entry of this isotope in the marine environment arriving from anthropogenic activity. These samples were collected at various times over the last hundred years from different places around North America and Japan (Table 1, Fig.1, Fig.2). All were from coastal, shallow sea water environments.

Table 1 : Marine biological samples

* the name of organization from which the sample was obtained

Sm.....Smithsonian Institution
Department of Invertebrate Zoology
CMN-B.....Canadian Museum of Nature
Botany Division
CMN-Z.....Canadian Museum of Nature
Zoology Division
Mcg.....McGill University
Redpath Museum
ARC.....Huntsman Marine Science Center
Atlantic Reference Center
(St. Andrews, New Brunswick)
HU.....Hokkaido University, Japan

Sample	Sampling year	Sampling location	*Museum
Horny coral (Paragorgia arborea)	1879	Western part of Banquereau	Sm
Algae (Fucus vesiculoses)	1906	Mahone Bay, Nova Scotia	CMN-B
Sponge (Unidentified)	1910	LaHave, Nova Scotia	CMN-Z
Algae (Agarum cribrosum)	1933	Anticosti Is.	CMN-B
Algae (Chondrus crispis)	1949	Pocologan, N.B.	ARC
Algae (Agarum cribrosum)	1950	Splitknife ledge, N.B.	ARC
Algae (Scytosiphon lomentaria)	1950	New Brunswick	ARC
Sponge (Haliclona oculata)	1966	Shippegan, N.B.	CMN-Z
Algae (Ahnfeltia plicata)	1969	Bonavista Bay 47°23'N; 54°10'W	CMN-B
Algae (Laminaria digitata)	1981	Estuary of Matamek River Que, 50°17'N; 65°58'W	CMN-B

Horny coral (Pseudopterogorgia acerosa)	1884	Vicinity of Mango, Florida	Sm
Sponge (Aplysina lacunosa)	1973	Holetown, Barbados	Mcg
Sponge (Agelas sceptrum)	1985	Discovery Bay, Jamaica	Mcg
Sponge (Suberites domuncula)	1909	Barkley Sound, Vancouver Is.	CMN-Z
Algae	1961	Vancouver Is. Whidbey Is., Washington	CMN-B
Sponge (Suberites montiniger Carter)	1969	Amchitka Island, Alaska	CMN-Z
Algae (Alaria marginata)	1972	British Columbia	CMN-B
Algae (Laminaria)	1988	British Columbia	CMN-B
Algae (Hosome Konbu)	1942	Otaru, Hokkaido, Japan	HU
Algae (Laminaria)	1989	Sado Isl., Japan Sea	collected by author

Fig.1 Marine biological samples (North America)

Number is the year of collection

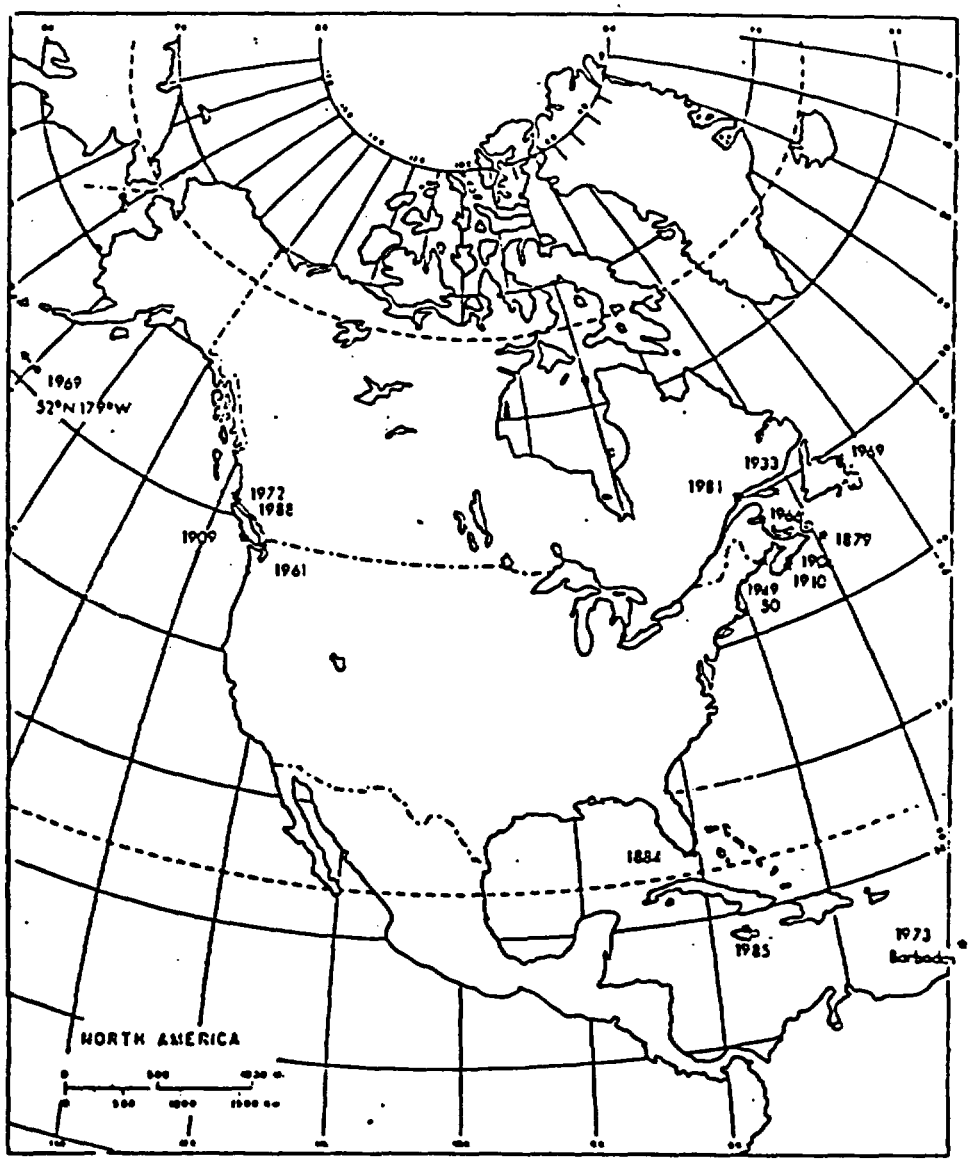

Fig.2 Marine biological samples (Japan)

Number is the year of collection

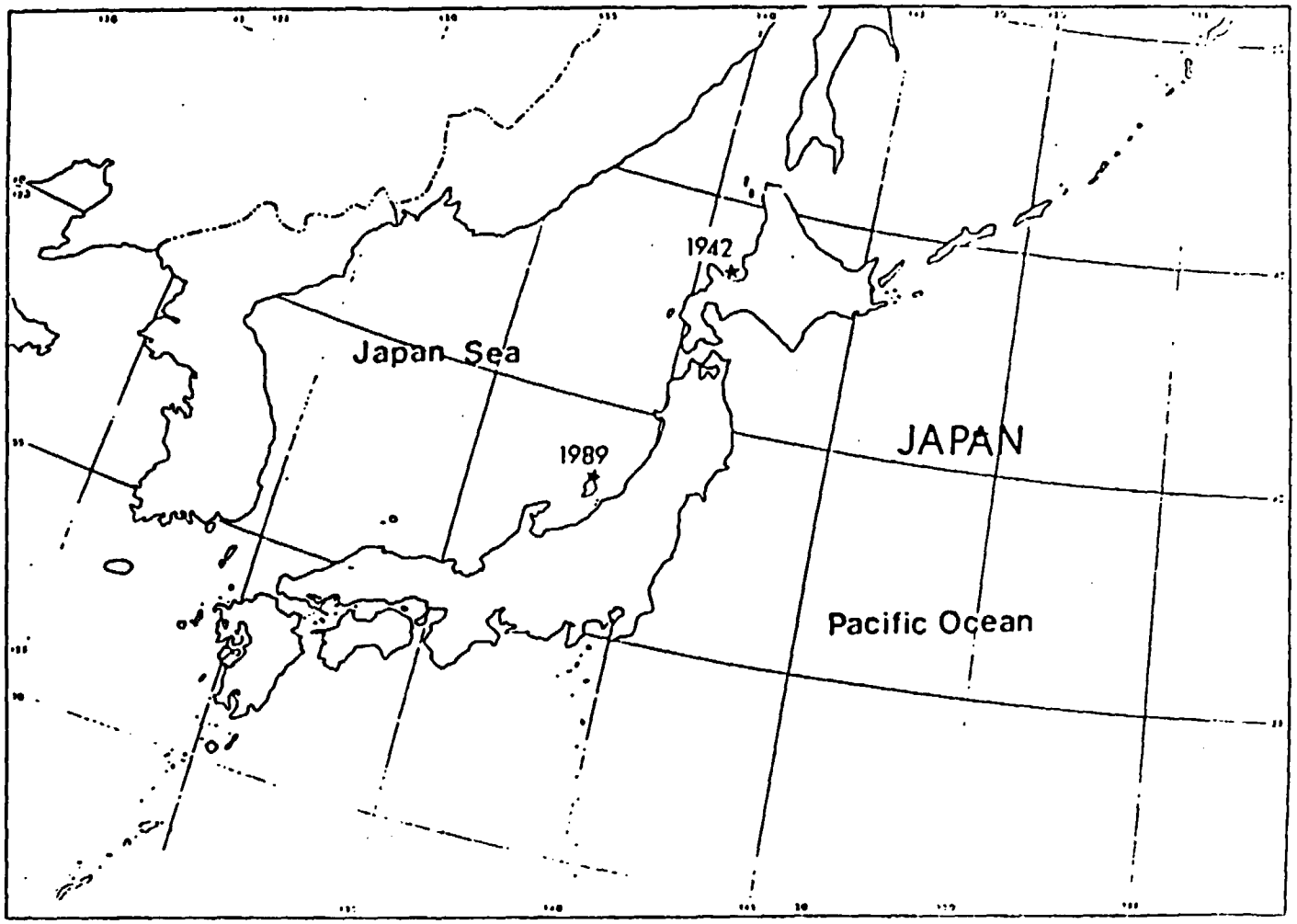

II-(1) Iodine in marine organisms

Among algae, brown and red algae are normally richer in iodine than green algae. Iodine concentration in brown algae is typically 100-4,000 ppm, and sometimes even up to 7,000 ppm (Goldschmidt, 1954).

It is generally believed that algae take iodine from seawater in the form of iodide (I^-) (Pederson and Price, 1980). The form of iodine in algae is not clearly known. Roche and Yagi (1952) immersed Laminaria in ^{131}I rich seawater and studied the fixation and release of ^{131}I by its radioactivity. Eighty percent of ^{131}I fixed to Laminaria was extractable by alcohol and ether as iodide (I^-). A small portion of iodide fixed was present as protein bound iodine. They concluded that this result supports the general belief that iodine is present in algae as mostly iodide (I^-) and is bonded to cells with weak (unstable) bonds.

More than 1,000 ppm, even up to 20,000 ppm of iodine has been reported to be present in the dry component of sponge (Goldshmidt, 1954).

Among corals, while so-called hard corals are not rich in iodine, horny corals (soft corals) may contain more than 20,000 ppm of iodine depending on species (Collins, 1967).

In horny corals and sponge, iodine is present in aromatic amino acid 3,5-diiodotyrosine (iodogorgoic acid) in the skeletal protein (Rankama, 1949).

II-(2) Chemical procedure for extraction of iodine from biological material

In order to extract iodine from organic matter, it is necessary to destroy organic bonds. There are basically two different methods for decomposing organic matter: oxidation by oxidizing reagent and dry-ashing.

For extraction of iodine, Gross *et al.* (1948) adapted the use of chromium trioxide as an oxidant with distillation of the iodine reduced from pentoxide in the presence of phosphorous acid. This method may not be adequate for our purpose because of possible iodine contamination from the large amounts of chemicals involved. Also, as a routine procedure, the fumes from chromic acid are not desirable for health reasons.

Dry-ashing of biological samples is commonly used to destroy organic bonds (Bock, 1979) and is adapted for this study.

The quartz apparatus used here is shown in Fig.3. It is a modification of an apparatus described in Studier *et al.* (1962). Oxygen is used to combust samples. During dry-ashing, the temperature should be kept as low as possible in order to minimize a release of iodine from the sample as volatile I_2 or HI. However, the temperature should be sufficiently high to turn the sample into ash. From my experience, 450-500°C is the optimum temperature. Gas absorption bottles containing 0.25% NaOH solution are used to trap I_2 and HI which could be released during the ashing process. The chemical reactions in the absorption bottles that take up released I_2 or HI are :

$$NaOH + HI \rightarrow NaI + H_2O$$
$$6NaOH + 3I_2 \rightarrow 5NaI + NaIO_3 + 3H_2O$$

Approximately 5-10 grams of sample is cut or ground into small pieces and is stuffed into the inner quartz tube. Quartz wool or fibre wool is placed at the bottom of the thick part of the tube to stop the sample from falling out.

At the beginning, oxygen is made to pass only outside of the inner tube. The area of 2mm holes is heated by a burner at all times. A sample is lightly heated by another burner from the right end in Fig.3. The volatile decomposition products are ignited at the area of holes. The burner is then gradually moved to the left. This process is called "destructive distillation" (Studier *et al.*, 1962) and is necessary for the combustion of organic rich material in a closed system because production of a large amount of volatile gas would cause an explosion of the tubes if the sample is heated all at once. After this destructive distillation, oxygen is passed inside the inner tube as well. The sample ignites at the left end. The flow rate of oxygen in the inner tube is gradually increased. However, it should be slow enough to maintain excess oxygen in the tube: otherwise, complete combustion of additional volatile material will not be

achieved.

After all combustible material has been burned, the whole quartz apparatus is heated at 450-500°C in a furnace for 1/2 to 1 hour to ensure the complete ashing. Distilled water is added to the residual ash in a beaker to leach out soluble matter. After a vigorous stirring, the ash residue is filtered out. The NaOH solution in the absorption bottles is poured into another beaker. The interior of the quartz tubes used for the combustion is rinsed with about 50 ml of distilled water. The water used for rinsing is added to the NaOH solution.

The NaOH solution is evaporated in a water bath. When nearly dry, the solution is transferred to a platinum crucible and taken to dryness. The evaporites are gently heated with a burner. After being cooled, distilled water is added and insoluble matter, if any, is filtered out. The resultant solution and the leached solution from the ash are combined.

To the solution, 6 N HNO_3 is slowly added until the pH of the solution is about 3. The solution is transferred to a separatory funnel and a few ml of carbon tetrachloride (CCl_4) is added. Iodide (I^-) in the solution is oxidized to I_2 by adding a few drops of 6 M $NaNO_2$. The separatory funnel is shaken until I_2 appears in the CCl_4 phase. The presence of I_2 is indicated by a purple color. The CCl_4 is transferred to a second separatory funnel. This extraction is repeated by using a fresh quantity of CCl_4 until no more purple color persists in CCl_4 phase. To the solution, 1-2 ml of 1 M $NH_2OH.HCl$ is added with the presence of a few ml of CCl_4. This will reduce IO_3^-, which might be present, to I_2. If there is any purple color appearing in the CCl_4 phase after shaking, the CCl_4 is transferred to the second separatory funnel and the extraction is repeated using a fresh quantity of CCl_4 until no more purple color persists. It should be noted that, with any sample the writer dealt with so far, IO_3^- was not present.

In the second separatory funnel, iodine-containing CCl_4 is shaken with 10 ml of distilled water containing a few drops of 1 M $NaHSO_3$ until both aqueous and CCl_4 phases are colorless. Molecular iodine (I_2) is reduced to iodide (I^-) in this procedure. The CCl_4 is discarded. This oxidation and reduction cycle is repeated once again to purify the iodine, using a few drops of 1 M $NaNO_2$ and a few drops of 6 N HNO_3 to oxidize I^- to I_2 and a few drops of 1 M $NaHSO_3$ to reduce I_2 to I^-.

At the end of the cycle, a few drops of concentrated H_2SO_4 are added to the solution containing iodide in order to remove excess SO_2. The solution is heated to steaming at low temperature (below 100°C) and then removed from the heat source. To the hot solution, 0.1 M $AgNO_3$ is added dropwise until the yellow precipitation of AgI ceases.

The precipitate is left overnight. The solution containing the precipitate is

Fig.3 Iodine extraction apparatus

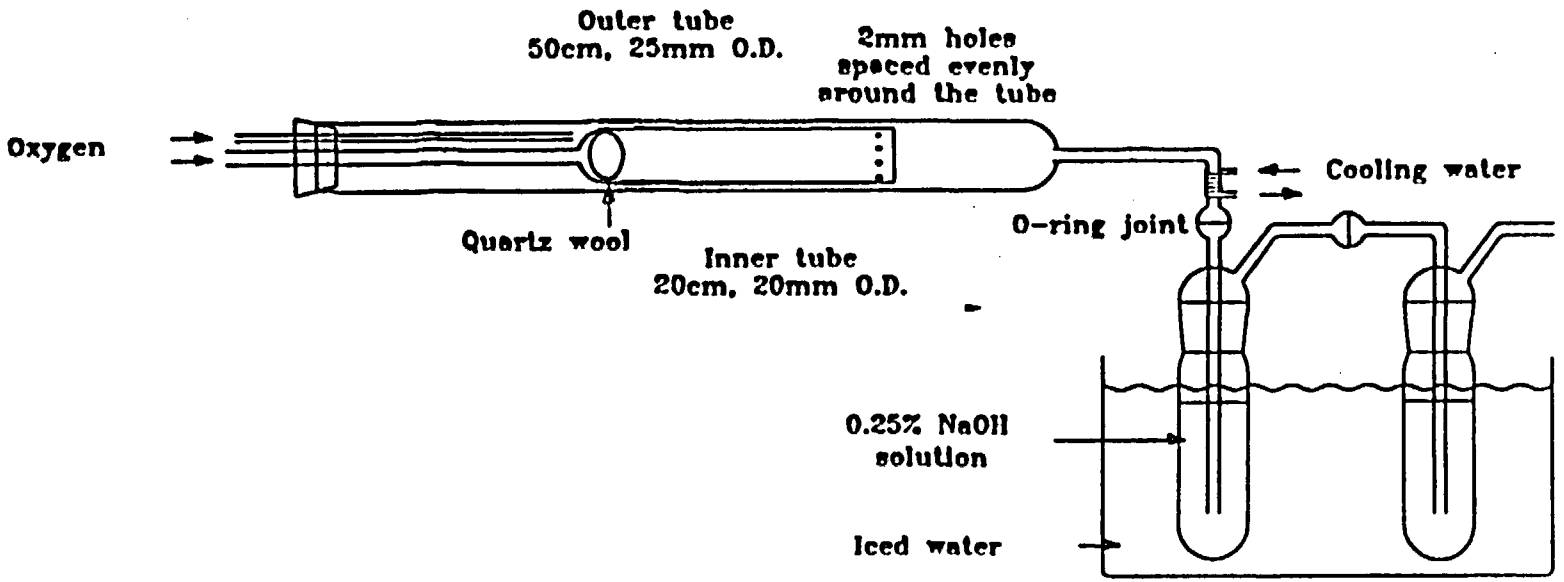

centrifuged and excess water is discarded. Another quantity of distilled water is added and the precipitate is stirred. It is centrifuged again and then water is discarded. This is repeated a few times. The precipitate is dried in a oven at 100°C.

The extraction efficiency through the procedure is about 75% for the seaweed sample collected in 1989 from the Japan Sea, determined by a comparison of the mass of iodine present in the precipitated AgI and the iodine content detected by neutron activation analysis.

About 3-10 mg of dried AgI (containing 54% of iodine) is well mixed with Nb powder (325 mesh) in an agate mortar at 1:2 in weight ratio and pressed into a Ta sample holder. It is heated at 170°C overnight in a vacuum oven and used as a target for AMS. From our experience, we have concluded that heating the sample at this temperature outgasses the powdered sample and hence gives a good result in terms of the stability of the sample in an ion source. If it is heated at lower temperature, the sample sometimes gives an unstable current.

Fig.4 Accelerator mass spectrometer at IsoTrace

EA1 Inflection line 45° electric analyzer
EA2 High energy line 15° electric analyzer
EA3 Heavy element line 45° electric analyzer
MA1 Inflection line 90° magnet
MA2 Radiocarbon line 45° analyzing magnet (set to null field for heavy element operation)
MA3 Radiocarbon line 45° energy ambiguity rejection magnet
MA4 Heavy element line 90° analyzing magnet

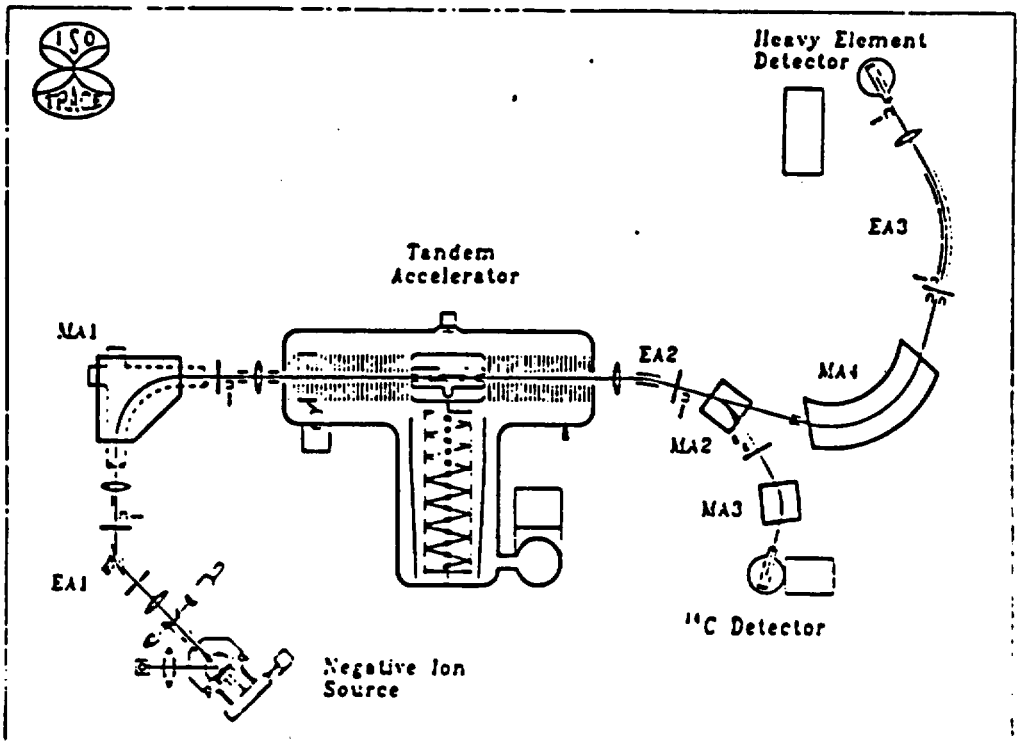

II-(3) Accelerator Mass Spectrometry (AMS)

(a)Theory

Mass spectrometry (MS) is an analytical method designed to separate charged atoms or molecules by their mass (M), energy (E) and charge state (q) based on their motion in electrostatic and magnetic fields.

MS involves four steps (Elmore, 1987); (1) the formation of a charged ion, (2) acceleration through an electrostatic potential of a few kilovolts, (3) separation of the ions based on their mass to charge ratio and (4) measurement of the number of ions per unit time in a detector (or measurement of the ion current in a Faraday cup).

Accelerator mass spectrometry uses these steps with the addition of an acceleration of negative ions to MeV energies. This allows separation of isotopes from their molecular isobars by fragmenting the molecular ions if a charge state (q)>+3 is chosen.

The AMS (Accelerator Mass Spectrometer) used in this work is located at the IsoTrace Laboratory at the University of Toronto. A schematic diagram is shown in Fig.4. Detailed descriptions of the AMS have been given elsewhere (Litherland, 1987; Kilius *et al.*, 1990). The description below is a summary of the iodine isotope measurement by AMS.

The sample (AgI target) is placed in a sputter ion source where a Cs primary beam strikes the sample surface. This produces an intense beam of negative ions (>1 μA of I^-) from the sample.

After leaving the surface of the sample, the I^- ions are accelerated to 20 KeV by the extraction electrode of the ion source. An electrostatic analyzer is used to reduce the energy distribution of ions accepted from the cesium sputter ion source. Subsequently, a magnetic analyzer with a resolution of about 300 ($M/\Delta M$) selects the negative ion beam by momenta.

The ions are then injected into the tandem accelerator. These negative ions are accelerated to the terminal of the accelerator, which is held at a constant voltage of 2 MV.

At the terminal, the ions pass through a gas canal, where several electrons are removed. The resulting positive ions are then accelerated a second time to ground potential. When a charge (q)>+3 is selected, the molecular ions are so unstable that they fragment quickly.

After acceleration, a charge (q) +5 is selected by a 15° electrostatic analyzer.

A subsequent 90° magnetic analyzer with a resolution of 2600 (M/ΔM) selects M/q and E/q and a 45° electric analyzer is used to select E/q. Finally, the ^{129}I ions are detected in a gap ionization detector. This combination of a detector, magnetic and electric analyzers reduces the continuum of ions generated in the residual gas or any other background generated by the system after the ion source.

The isotope ratios are obtained by alternately injecting the stable ^{127}I isotope and measuring the I^{+5} beam current in a Faraday cup after acceleration and then measuring the radioisotope counting rate in the detector after selecting mass 129 at the pre-acceleration magnet.

The measurement of ^{129}I requires only a reduction of ^{127}I tail due to sputtering at ^{129}I mass position at ion source as xenon is very rare and the ^{129}Xe isobar is eliminated by the use of negative ions (Kilius *et al.*, 1990b). The combination of electric and magnetic analyzer at both the injection and post-acceleration side reduces the ^{127}I component which is due to sputter tails, scattering and charge exchange. The rejection of the ^{127}I component throughout the system at the IsoTrace far exceeds the ^{129}I background in natural material. Therefore, all the counts obtained at the detector are considered to be real ^{129}I.

The transmission efficiency through the whole system is, at present, about 4%.

(b)Measurement

Standards (samples with a known isotope ratio) are measured throughout the run, typically before and after each sample (or sometimes every 2,3 samples). Our "standard" has been the iodine extracted from the seaweed collected in 1989 at Sado island in Japan Sea. The $^{129}I/^{127}I$ ratio of this material is known to be $(9.8+/-0.7)\times10^{-11}$ (Appendix A). A cycle is considered to be the data from beam current measurement and radioisotope counting for 100 seconds or longer depending on the counting rate. A sequence is a group of consecutive cycles for a given sample. Each unknown is usually run two or more times, with a total 5-10 cycles in each sequence.

Counts/current ratios per unit time in one sequence are averaged. The counts/current ratios for the standards before and after a sample are weighted-averaged. The obtained ratio is used for a normalization of a sample ratio.

A decrease in counts/current ratios during each sequence were often observed for samples with low $^{129}I/^{127}I$ ratio. This is possibly due to cross-contamination among the samples. This could happen during the drying process in the oven (since samples are put together in a wheel before drying) and/or in the ion source. For this reason, in the future measurements, a systematic blank measurement will be necessary to determine the level of cross-contamination.

II-(4) Results and discussions

The results are shown in Table 2 and Fig 5. For detailed descriptions of samples and collected locations, see Table 1, Fig. 1 and Fig.2.

Pre-bomb data range from $(3.0\pm0.6)\times10^{-12}$ to $(2.9\pm0.7)\times10^{-11}$, and this range is higher than the one obtained from marine sediment (about 1×10^{-12}) by Fehn *et al* (1986). There are some possible explanations for this discrepancy.

Iodine-129 concentration in coastal areas might reflect local geology. In other words, iodine in coastal areas may have more contribution from fissiogenic ^{129}I in weathered material than in the ocean. This also might explain the wide range in the pre-bomb ratios from place to place, although the possibility of sample contamination during preparation procedures cannot be neglected.

Another possible explanation is that man-made disturbance of the isotopic ratio may have predated the nuclear age, owing to the combustion of coal. Therefore, the biological samples collected before 1945 may have this effect. Coal usually contains uranium. Combustion of coal possibly releases fissiogenic ^{129}I into the environment and increases $^{129}I/^{127}I$ ratio.

The change in the $^{129}I/^{127}I$ ratios from pre-bomb to recent is significant. It has become clear that the level has reached one or two magnitudes higher than the prebomb level in the shallow marine environment. The level of the anthropogenic input seems to differ from place to place. Comparison of the post-bomb data at close sampling dates between each roughly divided region suggests that the north-east coast of North America has had higher input of anthropogenic ^{129}I since early 1950's than other sampling areas. On the other hand, two samples from the Caribbean Sea collected in 1970's and 1980's have the lowest post-bomb ratios among samples.

It seems that the ratios have been gradually increasing up to the present day in each region. Compared with the atmospheric ratio which probably had a peak in 1960's and 1970's and has decreased since then, the increase and dilution of ^{129}I concentration in the marine environment will require a much longer period owing to the vast sink and long residence time of iodine in the oceans.

Table 2 : ^{129}I in marine organisms
For detailed descriptions of samples and locations, see Table 1, Fig.1 and Fig.2.

	$^{129}I/^{127}I$
North-east North America	
Pre-bomb	
Horny coral(1879, Western Banquereau)	$(1.0\pm0.3)\times10^{-11}$
Algae(1906, Mahone Bay, N.B.)	$(7.7\pm1.2)\times10^{-12}$
Sponge(1910, LaHave, Nova Scotia)	$(3.0\pm0.5)\times10^{-12}$
Algae(1933, Anticosti Island)	$(3.3\pm1.6)\times10^{-12}$
Post-bomb	
Algae(1949&1950, New Brunswick)	$(1.3\pm0.2)\times10^{-10}$
Sponge(1966, Shippegan, N.B.)	$(2.1\pm0.2)\times10^{-10}$
Algae(1969, Newfoundland)	$(1.8\pm0.2)\times10^{-10}$
Algae(1981, Matamek River, Que)	$(1.9\pm0.2)\times10^{-10}$
South-east North America & Caribbean Sea	
Pre-bomb	
Horny coral(1884, Florida)	$(4.0\pm0.6)\times10^{-12}$
Post-bomb	
Sponge(1973, Barbados)	$(1.6\pm0.1)\times10^{-11}$
Sponge(1985, Jamaica)	$(2.3\pm0.4)\times10^{-11}$
North-west North America	
Pre-bomb	
Sponge(1909, Vancouver Island)	$(7.3\pm1.7)\times10^{-12}$
Post-bomb	
Algae(1961, Vancouver Island)	$(5.9\pm0.7)\times10^{-11}$
Sponge(1969, Alaska)	$(8.6\pm1.3)\times10^{-11}$
Algae(1972, British Columbia)	$(9.0\pm1.2)\times10^{-11}$
Algae(1988, British Columbia)	$(1.5\pm0.2)\times10^{-10}$
Japan	
Pre-bomb	
Algae(1942, Otaru, Hokkaido)	$(2.9\pm0.7)\times10^{-11}$
Post-bomb	
Algae(1989, Japan Sea, Sado Island)	$(9.8\pm0.7)\times10^{-11}$

Fig.5 $^{129}I/^{127}I$ ratios of pre-bomb and post-bomb marine organisms

- • North-east North America
- ★ South-east North America & Caribbean Sea
- ◆ North-west North America
- ■ Japan

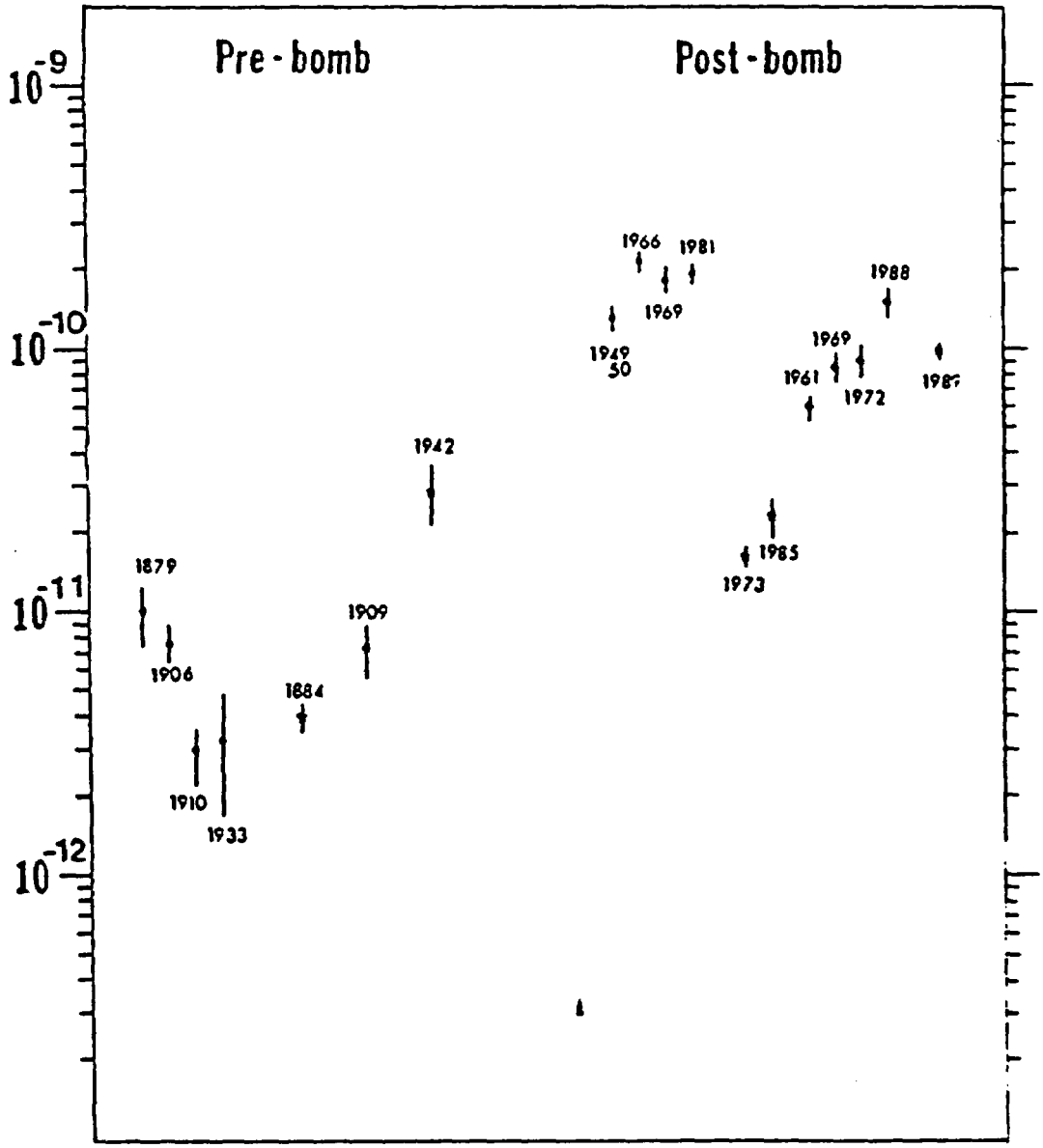

Chapter III: Iodine-129 in geological and hydrological samples

III-(1) The use of ^{129}I for geological and hydrological studies

The application of ^{129}I to the dating of geological samples on a 100 Ma time scale, by the use of its radioactive decay, has been suggested by several researchers for marine sediments, petroleum, brines and so on (Edwards, 1962; Fabryka-Martin, 1985; Fehn, 1986). The application of this isotope to dating, however, is not as simple as the case of ^{14}C (radiocarbon).

Since iodine is a mobile element, it is difficult to assume that the ^{129}I in a geological material of interest has been decaying in a totally isolated condition. For example, one may suggest the dating of marine fossils in sediments. However, according to Goldschmidt (1954), there has been complete exchange of inorganic matter including iodine in the space occupied by fossils; therefore, it is quite likely that iodine detected in the fossils may be due to secondary accumulation of iodine from external sources.

The subsurface production of this isotope from uranium is another problem. The dating of old groundwater, brines and petroleum requires the estimation of the fissiogenic contribution from host rocks.

When we deal with ^{129}I in geological material for dating purposes, one of the most important questions will be whether the level of this isotope has been constant over time and space.

Local variation of ^{129}I concentration may be present due to the inhomogeneous distribution of ^{238}U. The ^{129}I concentration in hydrosphere can be affected by local geology including volcanic activity.

Time-dependent variations are also likely. Production of cosmogenic radionuclides in the upper atmosphere is affected by the Earth's magnetic field and the local cosmic ray intensity. The Earth's magnetic field at present shields the atmosphere from a significant fraction of cosmic rays. It is known that the geomagnetic field has experienced many reversals. The cosmic ray intensity impinging upon the Earth is affected by the solar activity. These two factors will produce the time-dependent variation of cosmogenic radionuclide content of the atmosphere. The variation of radiocarbon content of the atmosphere has been reported from the analysis on old trees which are dated by dendrochronology (LaMarche and Harlan, 1973).

Moreover, there are researchers who attribute the principal source of cosmic rays to supernovae (Lingenfelter, 1969; Higdon and Lingenfelter, 1973). This suggestion opens up the possibility that cosmic ray intensity may have increased from

the normal background level in the past due to nearby supernova explosions. Higdon and Lingenfelter (1973) found high concentrations of cosmogenic ^{26}Al and ^{10}Be in deep-sea sediments at the depth corresponding to the age between 1.4 and 3.5 million years. They concluded that this may have resulted from an increase in local cosmic ray intensity, assuming there was no significant change in sedimentation rates. Although there has not been any study on ^{129}I concentration in deep oceanic sediment core, it is very likely that ^{129}I concentration varied in the past.

Although the use of this isotope for dating does not seem to be easy, it also has a potential of studying another interesting subject, that is, the stability of cosmic ray flux in the past. Also, the entry of anthropogenic ^{129}I in the sea might be used for studying the diagenetic processes in the sediments (Fehn *et al.*, 1986).

Iodine-129 in groundwater has been analyzed to demonstrate its application for estimation of residence time of water in subsurface, evaluation of ion filtration, evaluation of source of groundwater salinity and so on. Also, the ^{129}I in groundwater has been analyzed in the vicinity of uranium ores and granite bodies to study its subsurface production and its movement along with water. This is useful as a natural analogue of a nuclear waste repository site, since ^{129}I release from the waste is of concern because of its high mobility in the environment and its long half-life for radioactive decay (Fabryka-Martin *et al.*, 1987b).

III-(2) ^{129}I in K-T boundary material

A preliminary study on ^{129}I concentration in K-T boundary material was conducted to see if there is any enrichment of this isotope in the boundary; a nearby supernova has been one of the suggested causes of mass extinction of various biological species which occurred at this boundary.

(A) K-T boundary

K-T boundary (Cretaceous-Tertiary boundary) is one of the controversial parts of geological history.

A total reduction of 75% took place in biological species diversity, according to the estimation of Russel (1979). This includes the famous mass extinction of dinosaurs.

There are several theories proposed to explain the cause of the mass extinction. "Supernova theory" is one of them. According to the theory, the terrestrial environment could be affected by radiation from a supernova at a distance of 100 light years. Since astrophysists have estimated that supernovae occur within 50 light years every 70 million years, the K-T boundary event can be one of these incidents.

Higdon and Lingenfelter (1973) suggest that increases in cosmic ray intensities from nearby supernovae may produce concentrations of cosmogenic isotopes in the sedimentary record. Moreover, an supernova itself creates ^{129}I. A direst transport of this isotope from a supernova can be significant at a distance of 50 light years (Kilius, 1990a). Therefore, this is an interesting part of geological history for studying ^{129}I concentrations in sediments (Ganapathy, 1980; Kilius, 1990a).

(B) Sampling field

The material used in this study is from a site located on the west side of the Red Deer Valley about 18 Km east of Huxley, Alberta (Carlisle *et al.*). The formation including the K-T boundary seems to have been deposited in an alluvial, delta plain setting. The formation consists of silty sandstones, coals, ironstones and altered volcanic ashes. The samples were chosen from mudstone below the boundary clay, from coal layer which is a vicinity of boundary clay, and from shale above the boundary clay.

Table 3 : Stratigraphical location of samples
(Top of the K-T boundary clay is the datum)

Sample	Vertical distance(cm) below(-) or above(+) datum			Lithology
#21	+530	to	+540	shale
#13	+15	to	+20	coal
#9	0	to	-1	coal
#7	-3	to	-1	mudstone
#3	-180	to	-170	mudstone

(C) Chemical procedure

Iodine extraction from rock samples may be performed by acid digestion, alkali fusion or combustion method.

In this study, the samples are organic rich; therefore, it is quite likely that iodine is associated with organic matter. As there is a need to break the organic bonds, combustion method seems to be the best of these methods because either acid digestion or alkali fusion does not necessarily decompose organic matter (Tullai, 1988).

The apparatus used is a larger version of the one described in Fig.3. Here, the outer tube (120 cm, 30 mm O.D.) and the inner tube (50 cm, 25 mm O.D.) are used.

About 10-20 mg of KI with background level of $^{129}I/^{127}I$ (BANCO's brand. see Appendix A) is added to 50-100 grams of each sample to get a sufficient amount of iodine for analysis.

After all combustible material has been burned by destructive distillation described in Chapter II(2), the whole quartz apparatus is heated at 950-1000°C for 1 hour. The purposes of the heating at this high temperature are to complete the decomposition of the iodine compounds and to transfer the iodine from the sample to gas absorption bottles.

Recovery of iodine from absorption bottles and its purification process are the same as described in Chapter II(2). The AgI precipitated from the solution is dried and is analyzed for ^{129}I concentration by AMS.

The extraction efficiency calculated from the recovery of the added carrier

varies from 10% to 50%. This disappointingly low recovery is possibly due to the incomplete transfer of iodine to the absorption bottles. Some tarry matter that adhered to the wall of the tube, as a result of incomplete combustion, may have worked as a trap of iodine. This will be also discussed in the next section.

The concentrations of iodine and uranium were analyzed by neutron activation analysis. Iodine concentrations in these samples are below the detection limit (<6ppm). Uranium concentrations are shown in Table 4. The data indicate about the same level of uranium concentration in all samples. Therefore, the level of fissiogenic ^{129}I is probably about the same for all these samples.

Table 4 : Uranium concentrations (ppm)

#3	#7	#9	#13	#21
3.2±0.3	2.7±0.2	3.7±0.3	3.3±0.3	3.1±0.3

(D) Results and discussion

The sample mass, the mass of iodine in the added carrier and the measured ratio of the sample by AMS are listed in Table 5. All these items of information are needed to find the concentration of ^{129}I in the material.

Table 5 : Measured $^{129}I/^{127}I$ ratios of K-T boundary samples

Sample	Sample mass (g)	Added carrier (mg as I) : A	Measured $^{129}I/^{127}I$ ratio by AMS : c
#21	11.90	9.04	$(1.3\pm0.4)\times10^{-12}$
#13	53.02	8.55	$(1.2\pm1.3)\times10^{-12}$
#9	37.24	8.06	$(1.2\pm0.2)\times10^{-12}$
#7	49.66	9.10	$(1.3\pm0.5)\times10^{-12}$
#3	93.95	10.91	$(6.4\pm2.2)\times10^{-13}$

Data are compared in terms of ^{129}I(mg) per gram sample.

The measured isotopic ratio and ^{129}I concentration in a sample are related as follows.

$$a \times A + b \times B = c \times (A + B)$$

a : $^{129}I/^{127}I$ of carrier (KI)

A : the mass of iodine in the added carrier (mg)

b : $^{129}I/^{127}I$ of a sample

B : the mass of iodine in the sample (mg)

c : $^{129}I/^{127}I$ measured by AMS

Since B<<A and the value of a (2×10^{-14}) is negligible compared to the measured ratio, ^{129}I (mg) in the sample (bxB) is calculated as;

$$(b \times B) = c \times A$$

Table 6 : ^{129}I concentrations of K-T boundary samples

	Distance below(-) or above(+) the boundary clay (cm)	^{129}I(mg) per gram sample	$^{129}I/^{127}I$ ratio
#21	+530 to +540	$(1.5\pm0.5)\times10^{-13}$	$>(2.5\pm0.8)\times10^{-11}$
#13	+15 to +20	$(1.9\pm2.2)\times10^{-13}$	$>(3.1\pm3.6)\times10^{-11}$
#9	0 to +3	$(2.7\pm0.4)\times10^{-13}$	$>(4.5\pm0.6)\times10^{-11}$
#7	-3 to -1	$(2.5\pm1.0)\times10^{-13}$	$>(4.2\pm1.6)\times10^{-11}$
#3	-180 to -170	$(7.5\pm2.6)\times10^{-14}$	$>(1.3\pm0.4)\times10^{-11}$

Samples #7, #9, #13 and #21 show about the same level of ^{129}I concentration, while #3 from Cretaceous mudstone has less ^{129}I concentration than the others.

Since the detection limit of iodine concentration by neutron activation analysis is 6 ppm, we at least know that the concentrations for these sample were less than 6 ppm; therefore, we can deduce the minimum expected $^{129}I/^{127}I$ ratios for these samples. The calculated ratios are listed in the Table 6.

The calculated ratios are significantly higher than the pre-bomb ratios obtained in Chapter II (see Table 2, Fig.5). If we consider the radioactive decay, the initial ratios will be much higher. Since the samples #7 and #9 are at the vicinity of the K-T boundary, the age of these samples are considered to be about 65 million years. The initial $^{129}I/^{127}I$ ratios before the decay will be higher than $(7.0\pm2.7)\times10^{-10}$ for the sample #7 and $(7.5\pm10)\times10^{-10}$ for the sample #9. It may not be adequate to say that the ^{129}I levels were higher than the recent ^{129}I level (pre-bomb) throughout the age of these samples.

It is possible that the samples were contaminated by very recent meteoric water. The fissiogenic ^{129}I in these samples might be present in a significant amount. The possibility of contamination during extraction procedure cannot be eliminated. Iodine contaminant in oxygen in a cylinder, for example, can be a source of ^{129}I contamination. There are several problems to solve for future work on this project.

Suppose there was a layer of concentrated ^{129}I, does the profile of concentration stay at the original state considering the effect of the radioactive decay? Because iodine is a very mobile element, it is likely that iodine undergoes diffusion to the neighbour layers, depending on the attitude of groundwater flow. Probably, the better way to study ^{129}I concentration in K-T boundary is to look for the boundary in undisturbed deep-sea sediments, rather than in alluvial sediments which may reflect local condition and might be easily affected by groundwater.

A problem also lies in extraction process. When a carrier is added to a sample, the most important thing is that iodine in the carrier and the sample is isotopically well mixed. When a sample is heated with a carrier, iodine from the sample and iodine from the carrier may not be released at the same stage. Moreover, iodine in the sample is probably present at various states with various strength of bonds to the material. Iodine with stronger bonds will be released at later stage of the combustion.

During the experiments, some tarry matter was produced and adhered to the wall of a part of the combustion tube where the furnace could not reach. This tarry matter may work as a trap of iodine. Low extraction efficiency of the experiment is probably due to this "trap". The formation of this "trap" can be an obstacle for a complete isotope mixing of iodine.

The improvement of the system should be focused on the complete combustion of the samples and the complete transfer of iodine into the absorption bottles. If it is possible to obtain a sufficient amount of iodine without an addition of carrier, that will eliminate the concern about the isotope mixing. However, that will require the combustion of more than a kilogram of material.

III-(3) Iodine-129 concentration in iodine-rich brines

Brines with tremendous concentrations of iodine are found in various places around the world. Many of these brines are associated with petroleum. One example is Anadarko Basin in northern Oklahoma, and more than 1,400 ppm of iodine was found in this area (Collins, 1969).

Iodine-rich brines are not necessarily always associated with oil-field. In southern Kanto area and Niigata prefecture of Japan, brines with as much as 80 ppm of iodine are associated with "dissolved-in-water" type of gas (Marsden and Kawai, 1965; Fukuta and Nagata, 1982). The type of gas is not associated with an oil-deposit but is found dissolved in brine under pressure.

The concentration of iodine found in these brines is too high to be derived directly from seawater. The high level of iodine is considered as a result of leaching from dead marine organisms (Collins, 1975). Organic matter is well preserved in the sediments which form rapidly. It is not known exactly at what stage iodine is leached out from organic matter. Shishkina (1965) studied the distribution of iodide in marine and oceanic sediments, and found out that the concentration of iodine and I/Cl ratio in pore fluids are generally found to increase with depth, while iodine content of sediments decreases with depth. This fact suggests that iodine becomes enriched in pore fluids during early diagenesis due to decomposition of buried organic matter.

Compaction of a sediment results in a reduction of the interstitial volume concurrent with expulsion of interstitial water and deformation of the sediment skeleton. Expelled water probably containing hydrocarbon precursors migrates upward or laterally into a permeable rock. Hydrocarbons start to accumulate and mature to form petroleum or natural gas in this reservoir rock.

As is clear from this possible mechanism of petroleum formation, iodine in a brine quite possibly had contacts with source rock and reservoir rock which may contain uranium. However, if the level of uranium in the host rock was negligible, ^{129}I concentration in the brine may tell us the buried age of parent organic material which was later transformed into fluid or gaseous hydro-carbon.

(A) Sampling fields

Higashi-Niigata (Eastern Niigata) gas field

Niigata prefecture is located in northwestern Honshu (the largest main island) in Japan. The Higashi-Niigata gas field is one of the many gas fields around this area and is located to the east of the city of Niigata, situated on the coast of the Japan Sea (Fig.6).

There are two different kinds of gas fields present in this area; "dissolved-in-water type" found in Pleistocene formation and "structural" gas fields found in Tertiary formation.

"Dissolved-in-water type" gas fields are normally found in a relatively shallow sedimentary aquifer and are found dissolved in brine under pressure (Marsden and Kawai, 1965). Geologic trap of the sort associated with oil accumulation is not necessary here. The gas mainly consists of methane produced by bacterial fermentation. In Higashi-Niigata gas field, this type of gas fields are present in Quaternary (Pleistocene) sediments whose thickness is about 1,000 m. The rock sequence consists of unconsolidated gravel and sand. The depositional environment is alternation of shallow marine and lagoonal or estuarine systems.

In "structural" gas fields, gas is present as free gas. Generally, this type of gas may be associated with the formation of oil. However, sometimes free gas exists without a presence of oil nearby. Depending on the type of source rock (or type of original organic matter), organic matter is converted into either gaseous or fluid form. The structural gas fields in the Higashi-Niigata gas field are found in Tertiary formations called Nishiyama and Shiiya Formations. The sediments were deposited in an environment shifting from purely marine to shallow marine. The reservoir rock of the gas is sandstone in both formations. Brines are present at the side-bottom or bottom of gas trapped in anticlines. Brine saturates the voids and is able to move around due to the change in pressure.

All the wells from which samples were taken are located within an area of 6 km square. Concentrations of Cl and Br are measured by ion chromatography and those of iodine are measured by redox titration method using sodium thiosulfate to reduce free iodine produced from sample (Appendix B).

Fig.6 Oil and gas fields where iodine-rich brine samples were taken

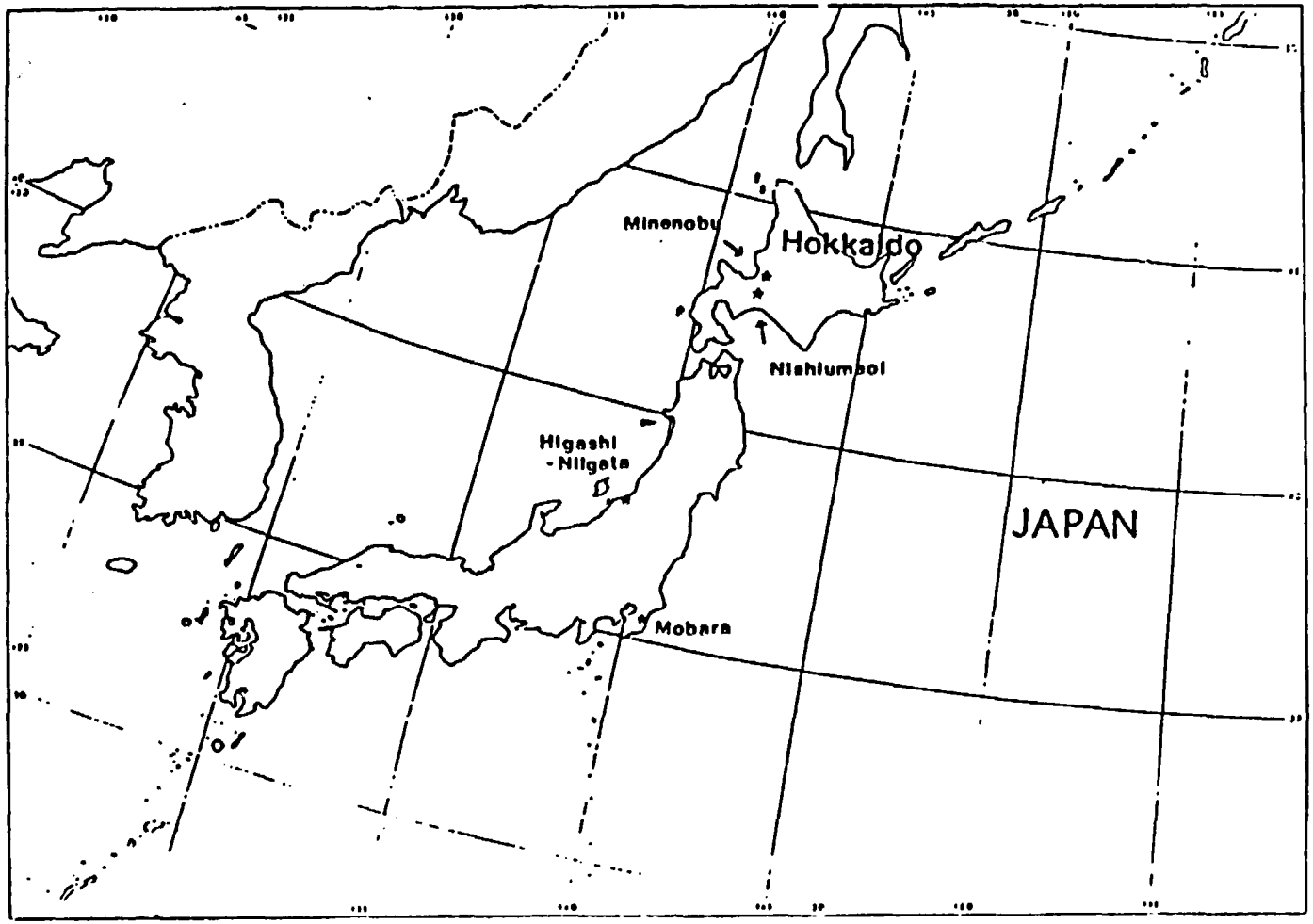

Table 7 : Higashi-Niigata gas field

	Formation	Depth (m)	pH	Cl (ppm)	Br (ppm)	I (ppm)
K103-3	G4(Pleistocene)	255-293	7.3	840	5	3.9
K101-3	G4(Pleistocene)	255-285	7.3	1100	6	4.3
K0-2	G5(Pleistocene)	397-432	7.6	5760	34	20.7
A1-2	G5(Pleistocene)	420-455	7.4	4800	26	14.8
M6-1	G6(Pleistocene)	557-585	7.4	13700	81	27.2
K7-1	G6(Pleistocene)	555-611	7.4	13500	85	33.0
K6-1	G7(Pleistocene)	1101-1045	7.4	18200	110	59.4
NS-2	Nishiyama	1404-1422	6.5	22800	125	77.5
MS-24	Nishiyama	2036-2064	6.8	20600	120	84.1
MS-31	Nishiyama	2135-2145	6.4	11300	18	23.8
NS-13	Shiiya	2683-2689	7.0	9960	65	15.1
NS-10	Shiiya	2923-2943	7.3	6240	25	8.9

The concentration of halogen increases with depth and reaches a maximum at the lower part of Pleistocene formation (G7) to Nishiyama Formation. The concentration decreases below Nishiyama. The low concentration near the surface is probably due to the dilution by meteoric water. According to Sudo (1967), the decrease of concentration below Nishiyama is due to the dilution by expelled water from compacted clay minerals or by the water produced from the decomposition of organic matter.

Mobara gas field

Southern Kanto, located just east of Tokyo, is the greatest gas production region in Japan (Fig.6). The Mobara gas field is the most representative gas field in the southern Kanto gas region.

The gas is present in the marine Kazusa Group of the early Pliocene to early Pleistocene age. This group consists of thick marine deposits laid down without interruption in sedimentation to a maximum thickness of 2,800 m. The group is made of alternation of sand and mudstone. The gas is "dissolved-in- water" type and is found in sand layers. The gas is believed to be indigenous to the Kazusa Group. It is thought that the mudstones in the group have had roles of both source rocks and cap rocks, while the produced gas has migrated to porous sand layers. Many faults are observed in this area. Although no upward movement of gas and water through faults is observed at present, it is likely that such movement has occurred in the past.

The Mobara gas field is also well-known for its iodine production. Iodine produced in this region exceeds the domestic need, and some part of it has been

exported to overseas.

Samples were taken from five wells (Table 8). These wells are located within a area of 2 Km square. In this area, salinity increases rapidly with depth, suggesting the gas fields have been well protected from the invasion of meteoric water. It is partly due to the lack of a topographically high place which would become a recharge area.

Table 8 : Mobara gas field

Well	Depth (m)	Iodine (ppm)
O-7	250- 570	75
A-26	578- 800	105
D-43	364- 823	130
D-110	706-1561	105
D-109	695-1577	105

Hokkaido oil-fields

For a comparison, two formation water (brine) samples were obtained from oil-fields in Hokkaido, Japan through Petroleum Resource Development Company (Fig.6, Table 9).

Table 9 : Hokkaido-oilfields

Sample	Formation (Ma)	Depth (m)	Iodine (ppm)
Minenobu SK-1	Atsuta (11-15)	1202-1213	62.5
Nishiumaoi SK-3	Taki-no-ue (15-16.5)	2479-2482	23.0

(B) Chemical procedure for extraction of iodine from brine

In water, iodine normally occurs as either iodide (I^-) or iodate (IO_3^-), the reduced and oxidized species respectively. Since the brines are found in reducing environment, we can assume that iodide is a predominant form of iodine in the samples.

Ten ml of 20% K_2CO_3 is added to 100-300 ml of a sample. The volume of a sample is determined so that it contains sufficient amount of iodine for isotope

analysis (>10mgI). After the water is boiled in a water bath, the resulting carbonate precipitate is filtered out. The filtered water is evaporated in a platinum dish. The evaporite is then heated lightly by a burner (300-400°C), allowing organic matter to be charred. After removing it from heat, water is added to the evaporite and the insoluble residue is removed by filtration.

Iodide (I^-) in the solution is oxidized to I_2 by $NaNO_2 + HNO_3$. The iodine is purified by the solvent extraction cycles mentioned in Chapter II(2). In the end, iodine is precipitated as AgI. AgI is used as a target of $^{129}I/^{127}I$ measurement by AMS.

(C) Results and discussions

Five samples were analyzed from the Higashi-Niigata gas field, one sample from the Mobara gasfield and two oil-field samples from Hokkaido. Results are shown in Table 10.

The ratios obtained here are significantly lower than the ones from prebomb marine organisms discussed in Chapter II (see Fig.7). Since the half-life of ^{129}I is about 16 Ma, the brines from the formation with an age of about 2 Ma are too young for the ^{129}I to have undergone significant decay.

As mentioned earlier, the origin of the iodine in the brines is possibly marine organisms. The question here is why there is a discrepancy between the ratios for prebomb marine organisms and ones for brines.

The discrepancy may be due to either the local variation or the time-dependent variation of the concentration of this isotope. Another possibility which was also mentioned in Chapter II(4) is that prebomb material has already been affected by man-made disturbance, such as, the combustion of coal.

Is there any possibility that low ^{129}I content is the indication of the presence of the old iodine which predates the age of the host rock? Iodine is able to move with water. During the formation of petroleum or natural gas, the migration of water is common. However, the movement is restricted between the mudstone or clayey layers where the permeability is low. In Higashi-Niigata and Mobara gas fields, there are numbers of these layers which function as cap rocks of the resources. Therefore, it is unlikely that iodine-containing brine travels from the great depth unless there are free paths such as faults.

The age of the host rock and the isotopic ratio do not seem to be correlated in this study. It is necessary to reduce the error in the data by repeating the measurements before drawing any conclusion. However, there is a possibility that the dating of material of the time range <16 Ma is potentially difficult because the initial ratio could vary in a certain range locally or time-dependently. Interaction with host

rocks or meteoric water can be another reason for the lack of correlation between isotopic ratio and formation age.

Table 10 : $^{129}I/^{127}I$ ratios of iodine-rich brine

Sample	Depth (m)	*Formation (Age)	$^{129}I/^{127}I$
Higashi-Niigata			
A1-2	422-425	G4(<2Ma)	$(6.0\pm2.9)\times10^{-13}$
M6-1	557-585	G5(<2Ma)	$(3.8\pm0.3)\times10^{-13}$
K6-1	1101-1045	G6(<2Ma)	$(1.2\pm0.7)\times10^{-12}$
MS-24	2036-2064	Nishiyama(2-5Ma)	$(3.4\pm2.0)\times10^{-13}$
NS-13	2683-2689	Shiiya(5-7Ma)	$(3.2\pm2.6)\times10^{-13}$
Mobara			
D-109	695-1577	Kazusa Group(<5Ma)	$(9.9\pm3.6)\times10^{-13}$
Minenobu			
SK-1	1202-1213	Atsuta(11-15Ma)	$(2.2\pm1.2)\times10^{-13}$
Nishiumaoi			
SK-3	2479-2482	Taki-no-ue (15-16.5Ma)	$(7.3\pm2.2)\times10^{-13}$

* The age of the formation has been determined by fission track method and microfossils.

Fig.7 $^{129}I/^{127}I$ ratios of brines

Data from marine organisms (see Chapter II) are also shown for a comparison

Pre-bomb....pre-bomb marine organisms
Post-bomb....post-bomb marine organisms

Brine samples

(Age of host rock)

1....Higashi-Niigata A1-2 (<2 Ma)
2....Higashi-Niigata M6-1 (<2 Ma)
3....Higashi-Niigata K6-1 (<2 Ma)
4....Higashi-Niigata MS-24 (2-5 Ma)
5....Higashi-Niigata NS-13 (5-7 Ma)
6....Mobara D-109 (<5Ma)
7....Minenobu SK-1 (11-15 Ma)
8....Nishiumaoi SK-13 (15-16.5 Ma)

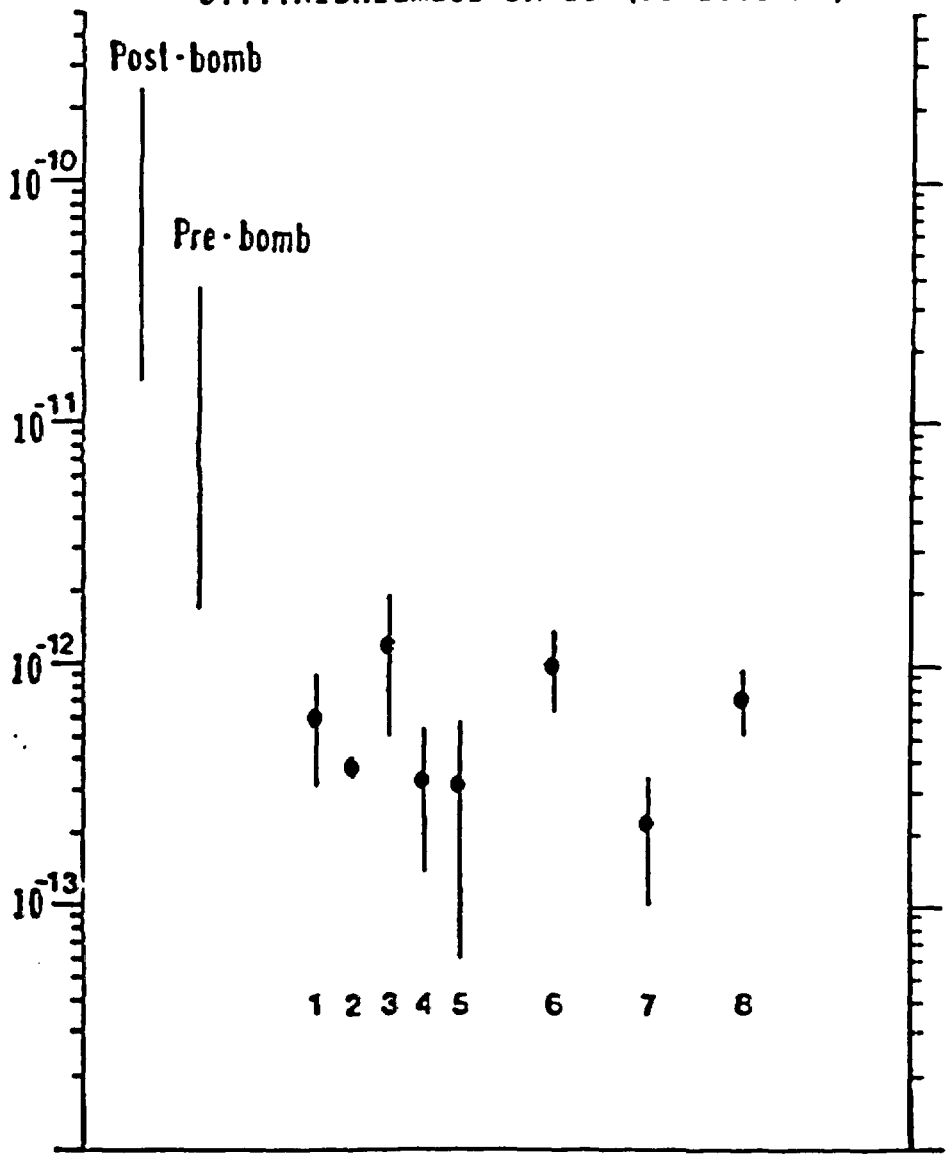

III-(4) ^{129}I in shallow groundwater

One groundwater sample was obtained from a borehole (location and depth unspecified) at Chalk River Laboratory, Chalk River, Ontario. The aim of the study was to establish a preparation technique for groundwater sample for the purpose of isotopic analysis. This is necessary for the future survey of possible ^{129}I contaminant around a waste repository site.

(A) Chemical procedure
Iodine concentration

The concentration of iodide in the sample was analyzed by the ceric arsenious oxidation-reduction method (Skougstad *et al.*, 1979) (see Appendix C).

The method is based on the catalytic effect of iodide on the ceric-arsenious oxidation reaction in acid solution. At a given temperature and for a given reaction time, the extent of reduction of ceric ion is directly proportional to iodide concentration at less than 0.06 mg of iodide per litre. The reaction can be monitored photometrically.

The result showed that the absorbance of Chalk River sample was nearly identical to that of distilled water which was used as a blank. From the comparison with the most diluted standard (1.6 µg/litre), the concentration of the Chalk River sample is considered to be less than 1.6 µg/L.

Iodine extraction
General approach

For the sufficient recovery of iodine, KI with background level of $^{129}I/^{127}I$ ratio was added to about 8 litres of the sample. Subsequently, the sample was passed through a small anion-exchange resin column. Iodine was stripped away from the resin by sodium hypochlorite, which oxidizes the anion to a less-strongly-sorbed form, periodate (IO_4^-). Iodine was purified by several solvent-extraction cycles to precipitate AgI at the end (Kleinberg and Cowan, 1960; Fabryka-Martin, 1987a).

Procedure

Water was filtered through about 3cm-thick pyrex wool to remove large particles (soil etc.). Potassium iodide (KI) with background level of $^{129}I/^{127}I$ ratio (Banco brand's, see Appendix A) was added to the sample. The volume of the processed water and the amount of the added iodide are listed in Table 11. The sample was then passed through an anion-exchange resin column (Dowex® 1X8-chloride, 100-200 dry mesh, 6cm x 5cm^2). Iodide (I^-) should be trapped in the resin.

The resin was transferred into a large beaker. One bed-volume of 4-6% Sodium hypochlorite (NaClO) was added to oxidize I^- to IO_4^-. The resin was stirred with a magnetic stirbar for half an hour on a hotplate set for low heat.

The resin was transferred into column and the NaClO solution was eluted. The remaining NaClO solution was eluted with an addition of 1.5 M Na_2SO_4. The eluting was continued until pH of the eluent became <7.

Concentrated H_2SO_4 was added to the eluent until pH became <1. The resultant Cl_2 gas should be removed by stirring and heating the solution at moderate temperature.

After the solution was cooled, it was transferred into a separatory funnel. A few ml of CCl_4 and 1 ml of 1 M $NH_2OH.HCl$ were added to the solution. The $NH_2OH.HCl$ can reduce IO_4^- to I_2. The separatory funnel was shaken until I_2 appears in the CCl_4 phase. The presence of I_2 was indicated by pink or purple color in CCl_4. The CCl_4 containing I_2 was transferred to a second separatory funnel. The extraction was repeated using fresh quantities of CCl_4 until CCl_4 remained colorless.

Subsequent reduction of I_2 to I^-, the repetition of the oxidation-reduction cycle and the precipitation of AgI with the addition of 0.1 M $AgNO_3$ were the same as described in Chapter II(2). The extraction efficiency throughout the procedure, calculated from a recovery of added carrier, was about 20%. The $^{129}I/^{127}I$ ratio of the sampls was measured by AMS.

(B) Results and discussions

Table 11 : Chalk River water sample

Volume of Water (litre)	Carrier added as mgI	Measured $^{129}I/^{127}I$ ratio	^{129}I (mg) per litre
8.380	15.28	$(1.55\pm0.12)\times10^{-11}$	$(2.8\pm0.2)\times10^{-11}$

The ^{129}I (mg) per litre sample was calculated and is listed in Table 11. As the iodide concentration is known to be less than 1.6 μg/L, the $^{129}I/^{127}I$ ratio of the sample is expected to be higher than $(1.8\pm0.1)\times10^{-8}$. This is a rather high value since the modern precipitation has a ratio of around 10^{-10} (Fabryka-Martin *et al.*, 1989).

During the run of the sample by AMS, the background level was more than one magnitude higher than at the best condition, as evidenced by the blank (Banco brand's iodide, 2×10^{-14}, see Appendix A) ratio of $(7.2\pm0.5)\times10^{-13}$. This was probably due to a problem with one of the vacuum pumps of AMS at this run and/or a cross-contamination among the samples in a sample-holding wheel.

From this reason, it is quite possible to assume that the sample was also contaminated. Therefore, the qualitative examination of the result is not possible here.

Chapter IV : Conclusions and recommendations

One of the objectives of this study was to develop and test the iodine extraction methods for natural samples, such as, iodine-rich marine organisms, organic-rich sediments, brine and shallow groundwater. Extraction of iodine from marine biological samples by the dry-ashing method and from brines by oxidation seem to work well. In these cases, the samples have enough iodine for isotope analysis; therefore, extraction efficiency is not a major concern as long as a sufficient amount of AgI precipitate is obtained at the end. However, in the cases of sediments and shallow groundwater, a carrier (iodide with a background level of $^{129}I/^{127}I$ ratio) has to be added to each sample, and then complete extraction of iodine from the sample becomes crucial in order to be assured that the iodine obtained is a homogeneous mixture of the carrier and the sample. Since the extraction of iodine from sediments by the combustion method and from shallow groundwater by anion-exchange resin had low extraction efficiency, 10-50% and 20% respectively, improvement of these methods will be necessary in the future. The improvement of the combustion method for sediments should be focused on the complete combustion of the samples and the complete transfer of iodine into the absorption bottles. At the same time, the system for combustion of much larger samples, kilogram quantities of material, should be developed so that the addition of a carrier is not necessary. The iodine trap capability of anion-exchange resin for groundwater samples should be tested through various tests, such as, the change in flow rate, configuration of resin column and so on.

The pre-bomb $^{129}I/^{127}I$ ratio in coastal marine environment was measured using iodine-rich marine organisms which were collected before 1945 around North-America and Japan. The data range from $(3.0\pm0.6)\times10^{-12}$ to $(2.9\pm0.7)\times10^{-11}$. Local variation of the ratio is present probably due to the differences in local geology, since, around coastal areas, fissiogenic contribution of this isotope from weathered material can be important. More systematic collection of samples and its correspondence to the local geology will give much clearer insight to the natural ^{129}I distribution in the marine environment. The same sort of study may be possible in the land environment using plants or thyroids of animals, although terrestrial plants contain much less iodine than marine plants and the availability of animal thyroids obtained before 1945 is not very abundant.

The entry of man-made ^{129}I after 1945 in the marine environment has been shown to be significant from the study of marine organisms. The $^{129}I/^{127}I$ ratio has become one or two magnitudes higher than pre-bomb ratio. The local variation in the post-bomb data is probably due to incomplete mixing of man-made ^{129}I in the environment. While atmospheric $^{129}I/^{127}I$ ratios have been decreasing since its peak in 1960 and 70's (Fabryka-Martin *et al.*, 1989), the marine ratios seem to have been gradually increasing up to the present day in each region. That is probably due to the vast sink and long residence time of iodine in the ocean. Studies of this sort will be a clue to geochemical cycle of iodine.

Higher ^{129}I concentrations than pre-bomb marine ratios were obtained for K-T boundary samples not only at the vicinity of the boundary layer but also at far below and above the layer, suggesting that there is ^{129}I contamination from modern meteoric water or from the extraction procedure. Although no discussion on the past cosmic ray intensity has been made so far, studies should be continued with an improved extraction method and preferably with an undisturbed deep-sea sediment core which would allow us to get a continuous measurement of the isotope throughout the strafigraphic sequence.

Although the finding a correlation between the $^{129}I/^{127}I$ ratios of brines and buried age of organic matter (origin of iodine) was an initial object, the correlation has not been found in this study. Before drawing any conclusion, it is necessary to reduce the error in the data, which was 81% at maximum, by repeating the measurements. However, there is a possibility that the dating of material of the time range <16 Ma is potentially difficult because the initial ratio could vary in a certain range locally or time-dependently. Interaction with host rocks or meteoric water can be another reason for the lack of correlation between the isotopic ratio and buried age.

Throughout the measurements of these samples, cross-contaminations possibly occurred among samples in the sample-holding wheels. A more careful handling of samples will be necessary during the preparation of the targets. Moreover, a systematic measurement of background should be performed in future studies to find the extent of cross-contamination during measurements.

Appendix A
Blank and standards for iodine isotope analysis

Blank (background) material

At Isotrace, the iodine with lowest ratio measured so far has been BANCO's brand KI (20% W/V solution, lot E8-31, IC No.54300). The ratio is $(3.5\pm5.8)\times10^{-14}$. This material was obtained from Nuclear Structure Research Laboratory at the University of Rochester, where it gave the ratio of 2×10^{-14}. Our ratio is consistent with their result within an error, although the error should be minimized by repeated analysis of the material.

Standards

Our standard for analysis has been the iodine extracted from seaweed collected in 1989 from the coast of Sado Island in Japan Sea. The $^{129}I/^{127}I$ ratio of the material is known to be $(9.8\pm0.7)\times10^{-11}$ from the calibration with IsoTrace Standard#2 (1.2×10^{-11}), which was made by the dilution of NBS 4994b standard. The ratio of the these standards were confirmed by a comparison with Nishiizumi standard (2500×10^{-15}).

Appendix B
Determination of iodide in brine

The determination of iodide in brine is possible through gravimetric, titrimetric and spectrophotometric method.

For the brine samples in this study, titrimetric method was applied using sodium thiosulfate to reduce free iodine extracted from samples. This is suitable for determining more than 0.1 mg of iodine.

1) A sample containing 0.1-5 mg of iodine is taken into a 300 ml Erlenmeyer flask with stopper. A drop of methyl orange solution(0.1 W/V%) is added. 1 N HCl is added until the solution shows a trace of red color. Distilled water is added until the volume of the solution gets about 50 ml.

2) Add 1 ml of sodium hypochlorite (Cl 3.5%) and 1 N HCl until the pH of the solution is adjusted between 1.3 and 2.0. Immerse the flask into a boiled water bath for 5 minutes.

$$HI + 3NaClO \rightarrow HIO_3 + 3NaCl$$

3) Add 5 ml of sodium formate (40 W/V%) and immerse the flask into a boiled water bath for 5 minutes to decompose the excess sodium hypochlorite.

$$NaClO + HCOONa + HCl \rightarrow 2NaCl + CO_2 + H_2O$$

4) After the solution is cooled, add 1 gram of KI and 6 ml of 6 N HCl to the solution. The mixture is shaken in a flask covered with a stopper and is stored in a dark place for 5 minutes.

$$HIO_3 + 5KI + 5HCl \rightarrow 3I_2 + 5KCl + 3H_2O$$

5) Iodine(I_2) is titrated with N/100 sodium thiosulfate. After the color of the solution gets thin, 1 ml of starch solution is added as an indicator. The disappearance of blue color is the end of the titration.

$$I_2 + 2Na_2S_2O_3 \rightarrow 2NaI + Na_2S_4O_6$$

6) As a blank test, 50 ml of distilled water is taken to a 300 ml Erlenmeyer flask and is processed in the same way as 1) to 5).

7) The concentration of iodide is calculated in the following way.

$$C = (a - b) \times 1000/v \times 0.2115$$

C : iodide (mg/L)
a : the volume (ml) of sodium thiosulfate used for titration of sample
b : the volume (ml) of sodium thiosulfate used for titration of blank
v : the volume of sample (ml)
0.2115 : the mass of iodide (mg) which can be titrated by 1 ml of N/100 sodium thiosulfate

Appendix C
Determination of iodine in groundwater with low iodine content

Ceric-arsenious oxidation method is suitable for determining iodide concentration of less than 0.06 ppm. The method is based on ability of iodide to catalyze the reduction of cesium (Ce) by arsenic (As). The reaction is:

$$2Ce^{4+} + AsO_3^{3-} \rightarrow 2Ce^{3+} + AsO_3^{-}$$

The reaction follows first-order reaction-rate kinetics, and at the given temperature and for a given reaction time, the extent of reduction of ceric ion is directly proportional to iodide concentration. The reaction can be stopped by the addition of silver ion. Since cerium (IV) ions show yellow color while cerium (III) ions are colorless, photometric measurement of absorbance of the solution at 450 nm permits the evaluation of the extent of the solution (Skougstad *et al.*, 1979).

References

Bock, R. (1979) A handbook of decomposition methods in analytical chemistry. 141-142. International Textbook Company. Glasgow.

Carlisle, D.B. and Braman, D.R. Amino acids at the Cretaceous-Tertiary boundary, Red Deer Valley, Alberta, Canada, three and four carbon mono-amino alkanoic acids.

Collins, A.G. and Egleson, G.C. (1967) Iodine abundance in oil-field brines in Oklahoma. *Science* **156**, 934-935.

Collins, A.G. (1975) Geochemistry of oilfield waters. Elsevier Scientific Pub. Co. New York.

Edwards, R.R. (1962) Iodine-129 : Its occurrence in nature and its utility as a tracer. *Science* **137**, 851-853.

Edwards, R.R. and Rey, P. (1968) Terrestrial occurrence and distribution of Iodine-129. Report NYO-3624-3

Elmore, D and Phillips, F.M. (1987) Accelerator Mass Spectrometry for measurement of long-lived radioisotopes. *Science* **236**, 543-550.

Fabryka-Martin, J., Bentley, H., Elmore, D. and Airey, P.L. (1985) Natural iodine-129 as an environmental tracer. *Geochim. Comochim. Acta* **49**, 337-347.

Fabryka-Martin, J. (1987a) Extraction of iodine from ground water for isotopic analysis. INC-7, LANL.

Fabryka-Martin, J., Davis, S.N. and Elmore, D. (1987b) Applications of ^{129}I and ^{36}Cl in hydrology. *Nuclear Instruments and Methods in Physics Research* **B29**, 361-371.

Fabryka-Martin, J.T., Davis, S.N., Elmore, D. and Kubik, P.W. (1989) *In situ* production and migration of ^{129}I in the Stripa granite, Sweden. *Geochim. Cosmochim. Acta* **53**, 1817-1823.

Fehn, U., Holdren, R., Elmore, D., Brunelle, T., Teng, R. and Kubik, P.W. (1986) Determination of natural and anthropogenic 129I in marine sediments. *Geophys. Res. Lett.* **13**, 137-139.

Fukuta, O. and Nagata, M. (1982) Iodine deposits of dissolved-in-water type in Japan. (in Japanese) *Journal of the Japanese Association of Petroleum Technologists* 47, 168-185.

Ganapathy, R. (1980) A major meteorite impact on the Earth 65 million years ago: evidence from the Cretaceous-Tertiary boundary clay. *Science* 209, 921-923. (Reference and Notes 15)

Goldschmidt, V.M. (1954) Iodine. IN Geochemistry, 602-620. Oxford at the Clarendon Press. London.

Gross, W.G., Wood, L.K. and McHargue, J.S. (1948) Spectrophotometric determination of iodine. *Anal. Chem.* 20, 900-901.

Higdon, J.C. and Lingenfelter, R.E. (1973) Sea sediments, cosmic rays and pulsars. *Nature* 246, 403-405.

Kilius, L.R. (1990a) personal communication

Kilius, L.R., Baba, N., Garwan, M.A., Litherland, A.E., Nadeau, M-J., Rucklidge, J.C., Wilson., G.C. and Zhao, X-L. (1990b) AMS of heavy ions with small accelerators. Invited paper presented at the Fifth International Conference on Accelerator Mass Spectrometry, Paris, April 1990.

Kleinberg, J. and Cowan, G.A. (1960) The radiochemistry of fluorine, chlorine, bromine and iodine. Report NAS-NS-3005. 31-32.

Kocher, D.C. (1981) A dynamic model of the global iodine cycle and estimation of dose to the world population from release of iodine-129 to the environment. *Environment International* 5, 15-31.

LaMarche, V.C., Jr., and Harlan, T.P. (1973) Accuracy of tree-ring dating of bristlecone pine for calibration of radiocarbon time scale. *J. Geophys. Res.* 78, 8849-8858.

Lingenfelter, R.E. (1969) Pulsars and cosmic-ray prehistory. Proc. 11th Int. Conf. on Cosmic Rays, Budapest. 557-563.

Litherland, A.E.(1987) Fundamentals of accelerator mass spectrometry. *Phil.Trans. R. Soc. Lond.* A323, 5-21.

Marsden, S.S. and Kawai, K. (1965) "Suiyosei-ten'nengasu", A special type of Japanese natural gas deposit. *Bulletin of the American Association of Petroleum Geologists* 49, 286-295.

Oliver, L.L., Ballad, R.V. and Manuel, O.K. (1982) ^{129}I in Missouri thyroids. *Health Phys.* 42, 425-432.

Pederson, T.F. and Price, N.B. (1980) The geochemistry of iodine and bromine in sediments of the Panama Basin. *Journal of Marine Research* 38, 397-411.

Rankama, K. and Samoha, Th.G. (1949) The halogens: fluorine, chlorine, bromine, iodine. IN Geochemistry, 756-769. The University of Chicago Press. Chicago.

Roche, J. and Yagi, Y. (1952) Sur la fixation de l'iode radioactif par les algues et sur les constituants iodes des Laminaires. *Comptes Rendus des Seances, Societe de Biologie* 146, 642-645.

Russel, D.A. (1979) The enigma of the extinction of the dinosaurs. *Ann. Rev. Earth Planet. Sci.* 7, 163-182.

Shishkina, O.V. (1965) Iodine distribution in marine and oceanic bottom muds and in their pore fluids. *Geokhimiya* 6, 739-746.

Skougstad, M.W., Fishman, M.J., Freedman, L.C., Erdmann, D.C. and Duncan, S.S. (1979) Methods for Determination of Inorganic Substances in Water and Fluvial Sediments, USGS Techniques of Water-Resources Investigations, Book 5, Chapter A1. 100-101.

Studier, M.H., Postmus, C., Mech, J., Walters, R.R. and Sloth, E.N. (1962) The use of ^{129}I as an isotopic tracer and its determination along with normal ^{127}I by neutron activation - The isolation of iodine from a variety of materials. *J. Inorg. Nucl. Chem.* 24, 755-761.

Sudo, Y. (1967) Geochemical study of brine from oil and gas fields in Japan. (in Japanese) *Journal of the Japanese Association of Petroleum Technologists* 32, 286-296.

Tullai, S. (1988) Extraction methods for iodine from crude oil systems for the determination of $^{129}I/^{127}I$ ratios. MSc thesis. Rochester Institute of Technology.

VERTICAL THERMAL GRADIENT EXPERIMENT RESULTS

A Report to Mifflin & Associates, Inc.
1000 Nevada Highway, Ste. 106
Boulder City, NV 89005

J. Donald Rimstidt
and
Mark A. Williamson

Department of Geological Sciences
Virginia Polytechnic Institute and State University
Blacksburg, VA 24061
March 12, 1991

INTRODUCTION

Burial of high level radioactive waste in the partly saturated tuffs of Yucca Mountain, Nevada will induce a steep thermal gradient near the waste repository. The resulting thermal anomaly will resemble natural geologic situations where magmatic intrusives cause high geothermal gradients in the nearby rocks. At Yucca Mountain, Nevada, the burial of heat producing radioactive wastes is likely to produce a situation similar to that found in present day vapor dominated geothermal systems or their ancient counterparts, epithermal gold deposits. These natural systems, being far from equilibrium, show a dramatic redistribution of elements. Such redistribution of elements and alteration of the rocks surrounding the waste disposal vaults in the Yucca Mountain tuffs could compromise the integrity of the repository.

Vapor dominated geothermal systems occur in areas of high heat flow in rocks where the recharge of ground water does not equal the heat-driven discharge to the surface (White et al., 1971). This situation may be the result of slow recharge, either resulting from low rock permeability or from a lack of water in the recharge portion of the overall system. Alternatively, an exceedingly high heat flux through the zone of discharge may remove hydrothermal solutions from the system at a very high rate. In either case, a zone develops where the voids in the rocks are filled with both liquid water and water vapor in proportions controlled by a complex interplay of heat flux, mass flux, and rock permeability (Cline et al., 1987). There are many cases of geothermal systems that show a vapor dominated zone including Larderello, Italy (Duchi, Minissale and Rossi, 1986, Truesdell and Nehring, 1979), Yellowstone, Wyoming (Muffler et al., 1971, Raymahashay, 1968), and Rotodawa, New Zealand (Ewers and Keays, 1977, Hedenquist and Henley, 1985, Krupp and Seward, 1987).

Vapor dominated geothermal systems can be divided into three geochemical zones, a boiling zone, a condensation zone and a solfataric zone. These zones are well

documented in Krupp and Seward (1987) and Hulen and Nielson (1986). It appears that fractures are the most likely conduits for fluid flow between the major zones. The slightly alkaline, dilute chloride solutions of the boiling zone are responsible for silicification and propylitic alteration of the original rocks. Boiling of these solutions produces a carbon dioxide-rich vapor that travels upward and often laterally until it condenses to produce a perched water table. If the system is low in sulfur and/or the condensate does not mix with oxidizing shallow groundwaters, the slightly acid, dilute bicarbonate solutions of this condensation zone generally produce weak phyllic alteration. However, if the system contains significant amounts of sulfur, either from a magmatic source or from sediments, and the vapor mixes with oxidizing shallow groundwaters, a very acidic solfataric zone with advanced argillic alteration forms.

Each of these zones show a distinct alteration mineralogy. It is important to note that alteration mineralogy is less influenced by the mineralogy of the original rock than by rock permeability, temperature, and fluid composition (Henley and Ellis, 1983). Although a wide variety of secondary minerals are found in these geothermal alteration assemblages, a few are very common. Propylitic alteration (Rose and Burt, 1979) assemblages occur in the deep part of the system and in the boiling zone. Because this part of the system is hydrodynamically stable for long periods of time, the alteration is generally pervasive. The physical extent of the condensation zone is generally controlled by the porosity and permeability of the rock as well as the location of fractures that carry the vapor upward from the boiling zone (see, for example, Figure 3 of Krupp and Seward, 1987 and Figure 6 of Hulen and Nielson, 1986). The fractures within the condensation zone generally show phyllic or weak argillic alteration and silicification (Rose and Burt, 1979). The solfataric zone shows advanced argillic alteration (Rose and Burt, 1979). This zone shows a loss of virtually every major rock component, including aluminum; apparently, only TiO_2 is insoluble enough to escape destruction. At Steamboat Springs, this leaching process increased the porosity of the local rock from 7.5% to 58.7%, with the concomitantly

produced mineralogy consisting of a box-work of amorphous silica, opal CT and anatase (Schoen, White, and Hemley, 1974).

The VTGE (Vertical Thermal Gradient Experiment) described in this report simulates a vapor dominated geothermal system that might develop around a high-level radioactive waste repository. The heat source (waste canisters) at the base of a column of partly saturated rock evaporates liquid water which rises convectively and condenses at the base of an overlying impermeable layer which confines the water but allows the conductive loss of heat (Figure 1). In this experiment, the bottom of the reactor is a boiling zone analogous to the area surrounding the entombed waste cannisters, while the top of the reactor is a condensation zone analogous to the layers of densely welded tuff overlying the repository host unit. Depending on the amount of carbon dioxide from decarbonation of calcite or from the pore gases, the condensate will be mildly acidic causing alteration of the minerals in the condensation zone. As the condensate returns downward, due to a combination of capillary action and gravity, it will react with the surface of the rock grains leaching alkali and alkaline earth elements and silica. By the time the solution reaches the boiling zone at the bottom of the reactor, it will be neutralized and saturated with the elements leached during its downward journey. Removal of the water from this solution by boiling causes the solution to become supersaturated with amorphous silica, clays, and zeolites and they may precipitate in the boiling zone. These alteration minerals can be identified using SEM, x-ray powder diffraction, and electron microprobe analysis and their abundance and composition related to run conditions. This experiment is inexpensive to construct and simple to operate so that it is economically feasible to operate several simultaneously to test a wide range of thermal gradients, solution compositions, and permeabilities.

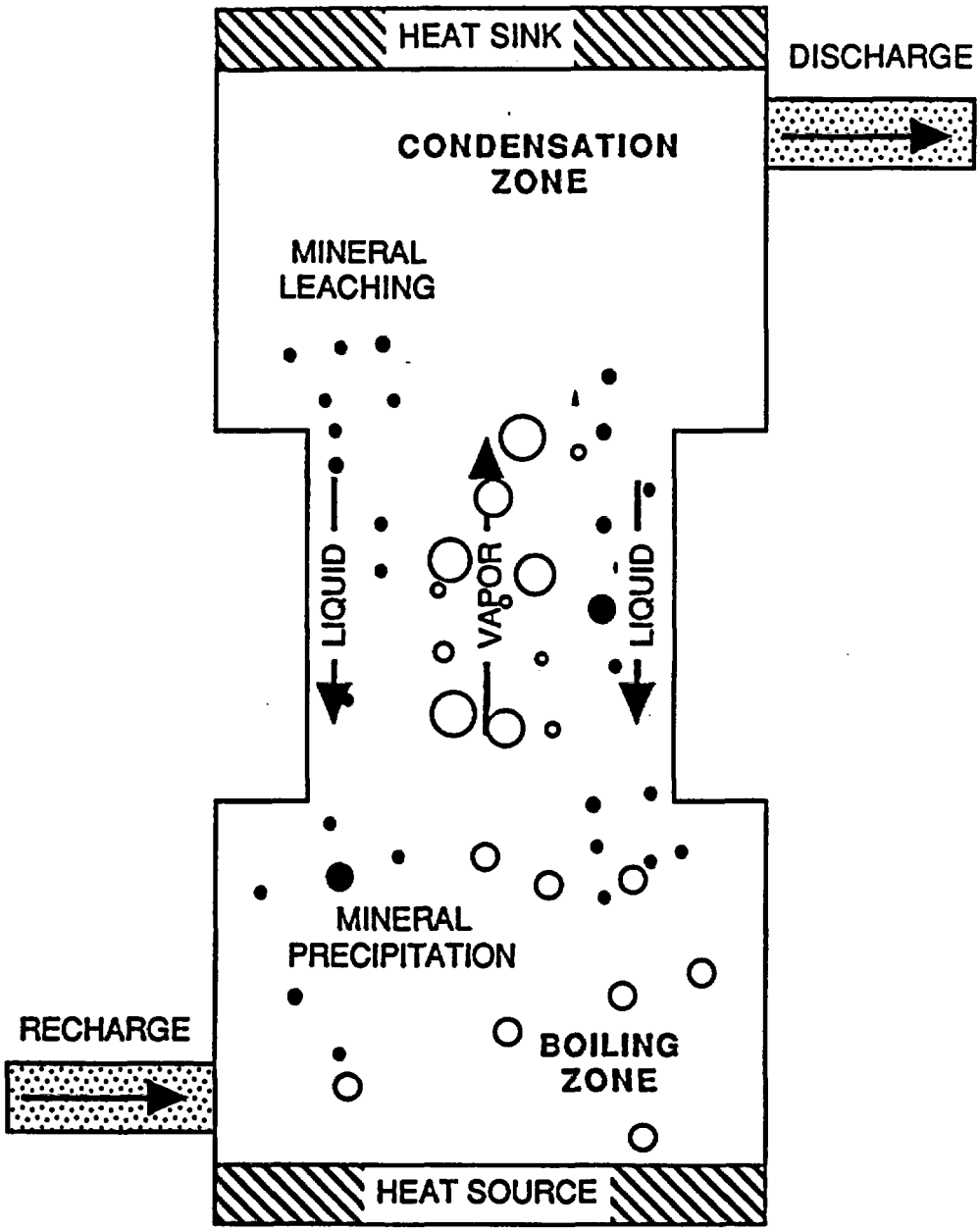

Figure 1. Schematic illustration of the parts of a vapor dominated geothermal system.

EXPERIMENTAL

Design

The overall design of the VTGE is shown schematically in Figure 2 (more detailed drawings of the various parts are shown in Appendix I). The heart of the experiment is a 10.2 cm (nominal 4 inch; schedule 40) i.d. polyvinyl chloride (PVC) pipe with a wall thickness of 6 mm and length 65 cm. The interior volume of the reactor is approximately five liters. The VTGE was designed with these dimensions for two reasons so that the reactor diameter is very large compared to particle or pore sizes minimizing boundary condition effects and so that the reactor is long enough to develop mineral zonations but short enough to be manageable in the laboratory. Thus, mineral zones that would occur over hundreds of meters in a real system are telescoped into a relatively small vertical distance.

Machined titanium blocks bolted onto each end of the PVC pipe (Figure 2 and Appendix 1) function as a heating assembly and a cooling assembly. The heating assembly located at the bottom of the experiment (Figure 2) contains a 250 watt disk resistance heater that is secured in place by silica wool packing (see Figure I-1 and I-2). A backing plate of insulation board bolted onto the end of the block holds the silica wool in place. The power output of the heating assembly is controlled by a variable voltage transformer (Figure 2). The cooling assembly contains a chamber that holds approximately 110 mL of water (Figure I-3 and I-4). The top of the chamber is closed by a plexiglass lid is bolted onto the top of the block and a viton o–ring seals the block to the lid. A metering pump circulates water from a reservoir through the cooling assembly and back to the reservoir. Brass swage-type type fittings secure copper tubes that carry the cooling water into and out of the cooling assembly. In-line thermometers record the temperature of the feed and effluent water. The heating and cooling assemblies extend 2.5 cm into the pipe and are sealed against the inside face of the PVC pipe by viton o–rings (Figure I-1 and I-3).

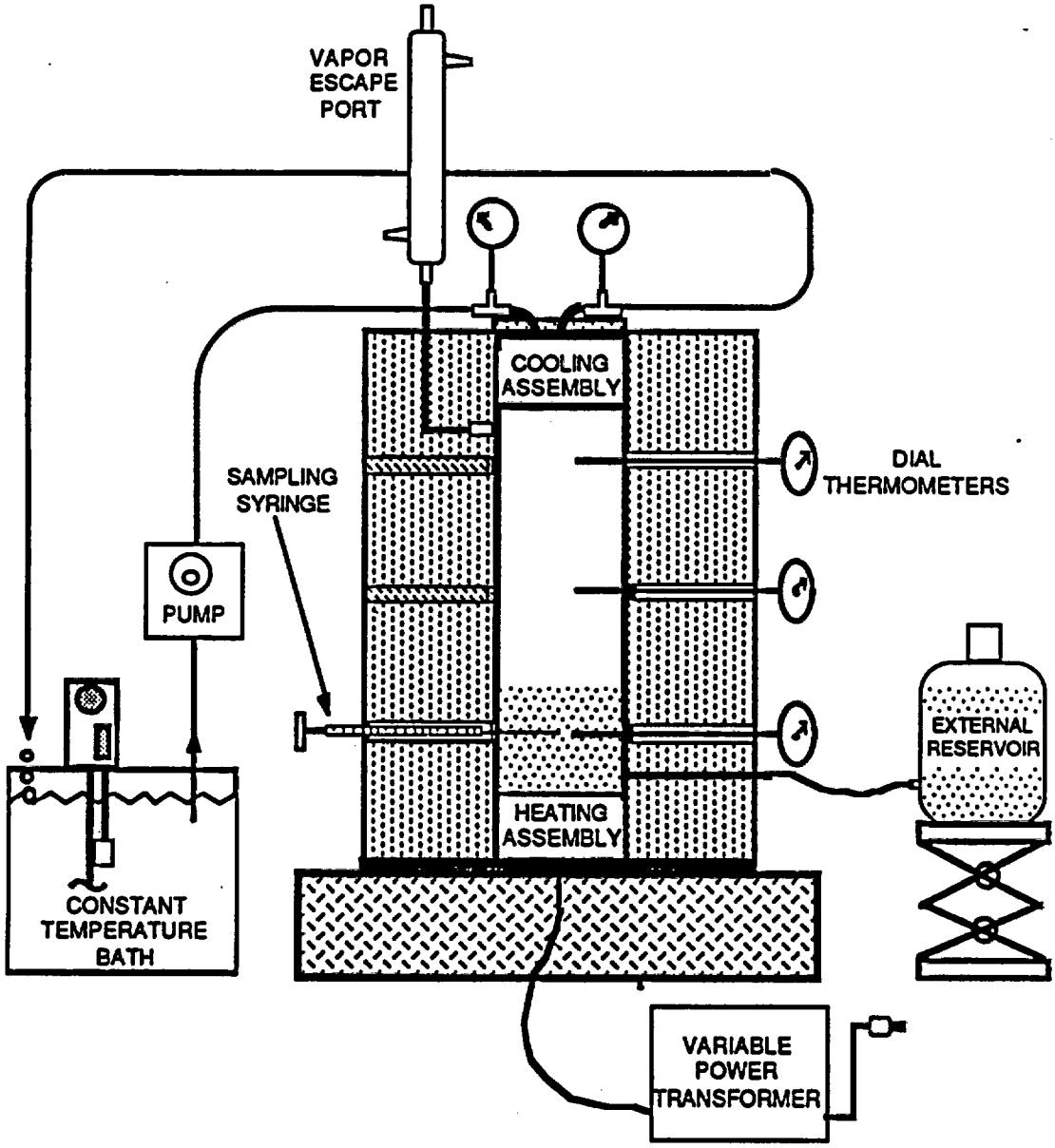

Figure 2. Schematic illustration showing the parts of the Vertical Thermal Gradient Experiment (VTGE).

The VTGE experiment is insulated on all sides in order to focus as much heat flow as possible through the column. The entire length of the apparatus is jacketed in three 2.5 cm thick layers of polyurathane foam. To accomplish this, two pieces of steel sheeting were formed into half cylinders and the foam layers were glued into the inside of the half cylinders as three concentric layers. The insulation shells were tightly bound around the pipe using nylon web belts equipped with fastex buckles. Two sheets of 2.5 cm thick polyurathane foam are placed on top of the VTGE to minimize heat loss through the top of the cooling assembly. The reactor sits on a piece of 2.5 cm thick insulation board which reduces the heat loss out of the bottom of the heating assembly.

This experiment was designed to produce heat fluxes far higher than might be expected in the proposed Yucca Mountain radioactive waste repository in order to accentuate any reactions or processes that might occur as a result of the thermal gradient. The rate of heat generation is limited by the 250 watt heater to 250 J sec^{-1}. This limits the vertical heat flux to a maximum of 2.5 J cm^{-2} sec^{-1}, although experiments with much higher heat fluxes could be performed by replacing the viton o–rings in the heater assembly with teflon ones. Lower heat fluxes can be produced by lowering the voltage across the heater using the variable transformer. The amount of heat introduced into the system by the disk heater in the heating assembly, P (J sec^{-1}), is determined from the equation

$$P = I^2R = \frac{V^2}{R} \qquad (1)$$

where I (= V/R) is the current (amp) delivered by the variable voltage transformer and R is resistance of the heater (55 ohms). The actual heat flux through the experiment can be determined by calculating the amount of heat, q (J sec^{-1}), carried away from the cooling assembly by the cooling water.

$$q = C_p r_f \Delta T \qquad (2)$$

where C_p is the heat capacity of the cooling water (≈4.2 J cm^{-3} K^{-1}), r_f is the flow rate (cm^3 sec^{-1}) and ΔT is the temperature difference (K) between the effluent and feed cooling water ($T_{effluent} - T_{feed}$).

Eight holes, 1.5 cm in diameter, were drilled into the side of the PVC pipe, three on one side and five on the other, 180° apart. The holes on one side of the pipe serve as ports for thermometers. These thermometers monitor the temperature gradient inside of the experiment and are centered at 9.5, 32.5 and 56.0 cm above the bottom of the PVC pipe (Figure 2). The three holes on the other side of the pipe at the same heights as the thermometers are fluid sampling ports that are sealed by septum stoppers. We used 30 ml syringes with 7.5 cm long needles to withdraw samples through these septa. A forth hole, centered 60.0 cm from the bottom of the pipe on the sample port side, allows the transfer of noncondensible gasses through a water-cooled glass condenser. The fifth hole, centered 5.8 cm above the bottom of the pipe, is connected to an external solution reservoir which is used to maintain a constant liquid level in the experiment. The reservoir consists of a three liter polyethylene small-mouthed bottle, with a spout at the bottom. Tygon tubing connects the reservoir to a port below the lowest sampling port of the PVC pipe. The liquid level in the reactor is adjusted by raising or lowering the lab jack on which the external reservoir sits.

Methods

The Yucca Mountain tuff used in the experiments reported here was crushed and sieved to a size fraction of $1 \leq x \leq 2$ mm. The sieved material was washed three times with distilled water and dried in an oven at 60°C. Approximately five liters of solid material was required to fill the reactor to the level of the vapor escape port.

We conducted experiments with glassy and devitrified (nonlithophysal) samples of the Topopah Springs member of the Yucca Mountain tuffs in combination with distilled-

deionized water, very dilute sodium chloride solutions (0.125 ppm NaCl) and synthetic J13 well water (Table 1), formulated to match the major element compositions given in Moore and Morrow (1986). The chemical composition of J13 well water is considered to be representative of the ground waters that might be encountered in the vicinity of Yucca Mountain. A summary of the experimental protocol is given in Table 2.

During the runs, 10 milliters of solution was extracted at various times from the lowest sampling port. Attempts to recover solutions from the middle and top sampling ports produced only a small amount of steam condensate but no liquid phase. These solutions were cooled to room temperature and their pH measured with a Ross combination electrode. Following pH determination, samples were acidified with 1 mL of reagent grade nitric acid and retained for for Na, K, Ca, Fe and Mn analysis by inductively coupled plasma emission spectroscopy (ICP). Silica was determined spectrophotometrically by the method of Govett (1961).

At the termination of an experiment, the apparatus was cooled and the run solution drained away from the solids. The heating and cooling assembly were removed from the ends of the reactor and the solids partitioned into approximately 5 cm intervals (Figure 3). These solids were air-dried at room temperature and stored in polyethylene bags.

RESULTS AND DISCUSSION

Design

During operation, the VTGE required little attention other than recording temperatures, adjusting the elevation of the external reservoir, and collecting solution samples. All runs, with the exception of run #4, were conducted using the external reservoir. Run #4 was performed by filling 80% of the pore spaces in the tuff and allowing the system to gradually dehydrate. Most experiments were conducted for a minimum of 450 hours. However, run #5 was terminated after only 340 hours due to a metering pump failure.

Table 1. Recipe for synthetic J-13 well water formulated to match the major element composition reported by Moore (1986).

To prepare Syn J-13 add the following, in the order given, to 3 L of distilled water with vigouous mixing 0.0522 g $Ca(OH)_2$, 0.0312 g KCl, 0.509 g $NaHCO_3$, and 1.65 mL HCl solution (1:100 dilution of concentrated acid). This produces a solution of the following composition:	
SPECIES	CONCENTRATION, ppm
Na^+	46.5
K^+	5.5
Ca^{2+}	9.4
HCO_3^-	121.3
Cl^-	7.3
pH	7.5

Table 2. Summary of VTGE runs with Yucca Mountain Tuff.

RUN #	REACTOR CHARGE	RUN SOLUTION	DURATION hours
4	Nonlithophysal tuff	Distilled-deionized*	625
5	Nonlithophysal tuff	Distilled-deionized	350
6	Nonlithophysal tuff	0.125 ppm NaCl	646
7	Glassy Tuff	Distilled-deionized	489
8	Glassy Tuff	0.125 ppm NaCl	544
9	Glassy Tuff	Synthetic J13 water	450
10	Nonlithophysal tuff	Synthetic J13 water	451

*Reactor filled with liquid so that 80% of the solids were submerged in the liquid phase at the beginning of the experiment.

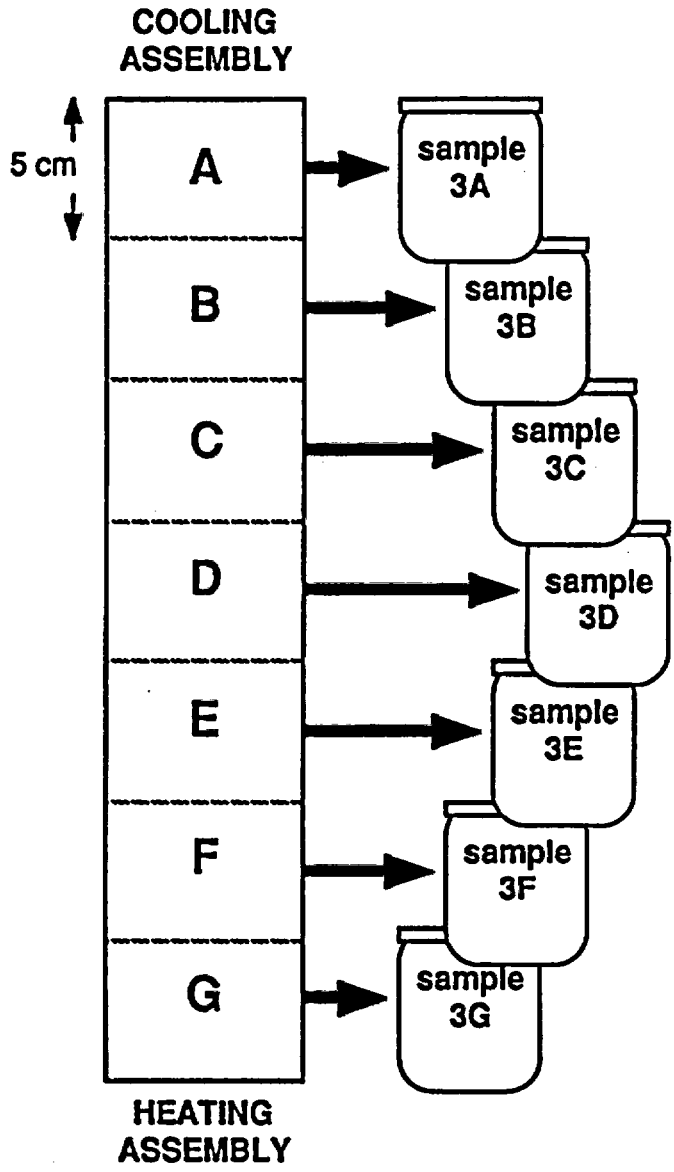

Figure 3. Schematic diagram showing how the run solids from the VTGE were partitioned into subsamples.

The thermal behavior of the VTGE was reasonably stable. The temperature histories for the various control points on the VTGE during experimental runs are tabulated in Appendix II. Figure 4 shows the temperature of the feed and effluent water for the cooling assembly for a typical experiment (run #6). The temperatures inside of the reactor, at the top, middle, and bottom control points, for run #6 are shown in Figure 5. Variations in the flow rate and temperature of cooling water through the cooling assembly affected the rate of heat removal by the cooling assembly. Efficiency for heat removal was 68-75% for most runs; the remaining heat was lost through the insulation. This variation in efficiency of heat removal by the cooling assembly was caused by variations in the temperature of the cooling water and the pumping rate of the metering pump. Variations in the temperature of the room tended to cause variations in the water bath temperature. This problem was somewhat alleviated by placing a copper cooling coil, carrying flowing tap water, in the water bath to remove the excess heat. Variations in the pumping rate were partly caused by the build up of bacteria and algae on the valves of the pump; this problem was mitigated by adding copper sulfate to the cooling water. Finally, the metering pumps that circulated the cooling water were required to operate at their highest pumping rates for extended periods of time and as they aged they showed increasing fluctuations in their pumping rate. The average lifetime of a pump was 1200 to 1500 hours.

SEM Study of Tuff Surfaces

At this time, we have completed only a cursory examination of the surfaces of the reacted tuff grains. However, nearly all of the reacted tuff grains showed the pervasive occurrence of small blobs of botryoidal silica (Figure 6). Silica cementation was so extensive near the bottom of the reactor that it cemented the grains together into a solid mass. In conjunction with silica precipitation in the bottom of the reactor, severe etch pitting is documented in the uppermost sections (Figure 7). Etch pitting and precipitation of amorphous silica was observed to vary inversely.

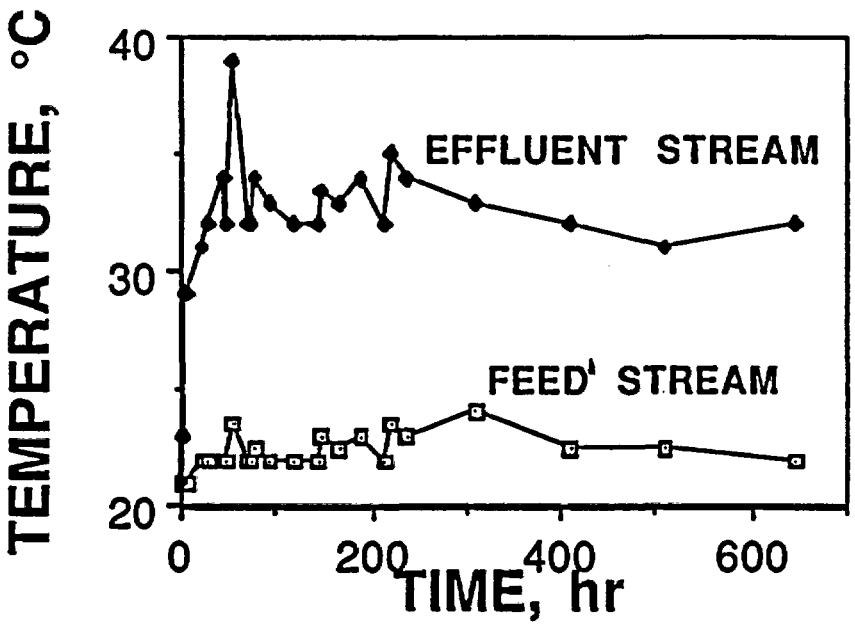

Figure 4. Graph showing the temperature of the feed and effluent cooling water stream for a typical experiment (#6). Varitations in the temperature of the effluent stream are mostly a result of variations in the pumping rate of the metering pump.

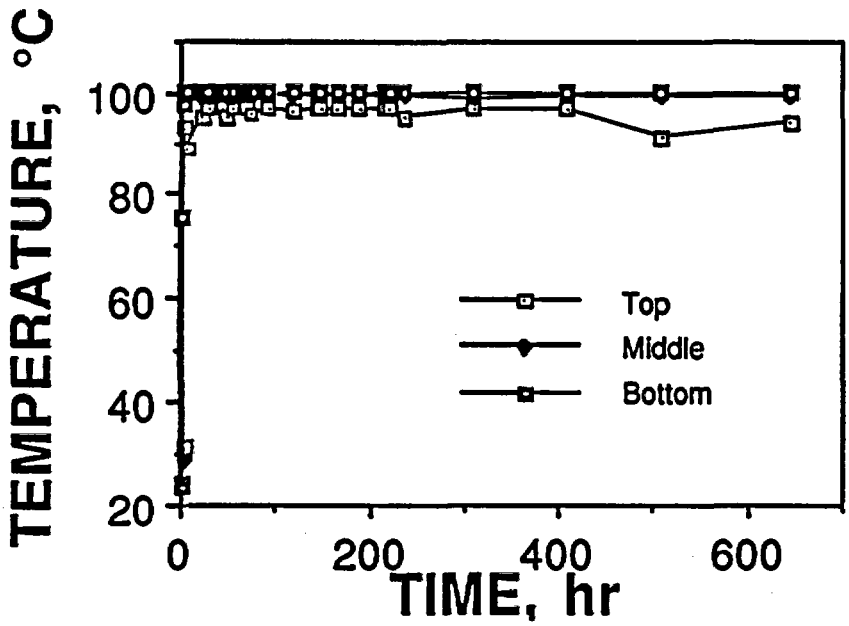

Figure 5. Graph showing the temperature at the top, middle, and bottom of a typical experiment (#6).

Figure 6. SEM photograph showing silica precipitated on the surface of tuff grains.

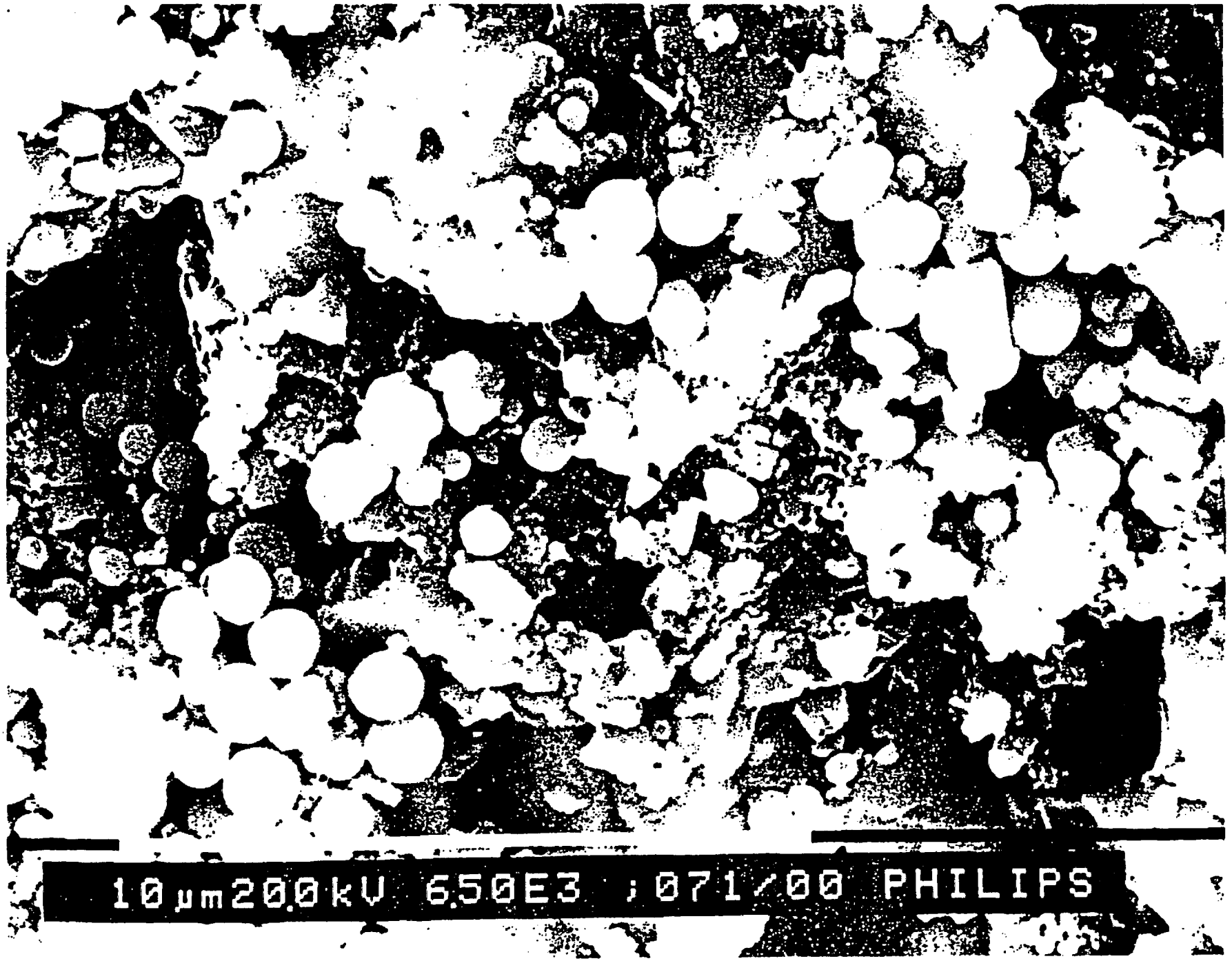
10µm20.0kV 6.50E3 ;071/00 PHILIPS

Figure 7. SEM photograph showing etch pitting on the surface of leached tuff grains.

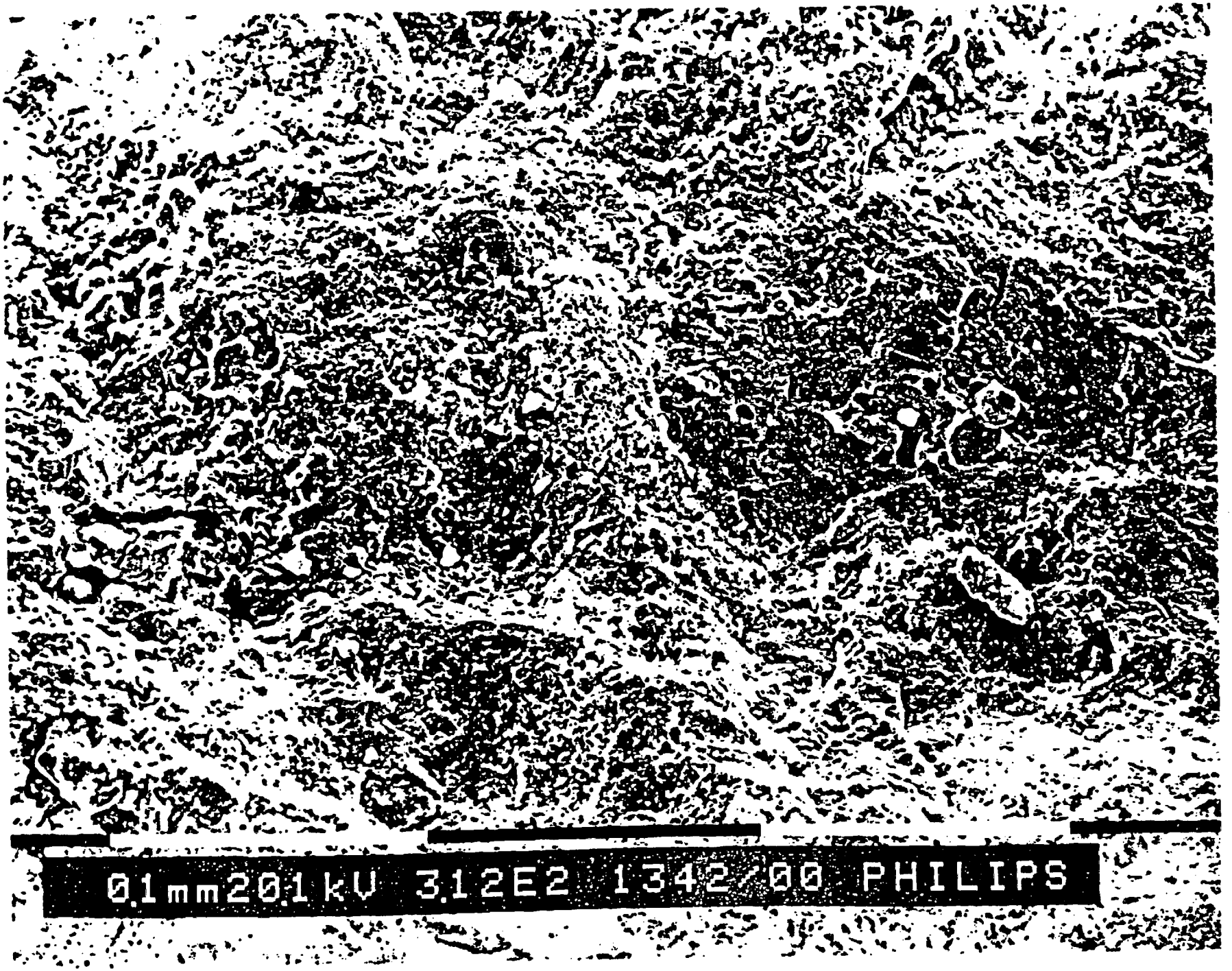
0.1mm20.1kV 3.12E2 1342.00 PHILIPS

Chemical Evolution of Reactor Solutions

The variation of Fe, Mn, pH, silica, Na, K, Ca over time for each experiment are tabulated in Appendix III and illustrated in Appendix IV. A typical profile for Fe and Mn release during experiments with devitrified and glassy tuff is shown in Figure 8. All experiments showed an initial rapid release of iron and manganese accompanied by a concomitant drop in pH. This pH drop is illustrated for a typical run in Figure 9. The pH decrease observed during the first 100 hours of operation is followed by a rapid increase in dissolved silica, sodium, potassium, and calcium concentrations (Figure 10). The experiments approach a steady-state condition after about 200 hours.

The most important factor in controlling the initial chemical evolution of reactor solutions appears to be the leaching of iron and manganese from the tuff matrix during the first 100 hours of operation. The runs with devitrified tuff produced two to three times higher concentrations of iron and manganese than did glassy tuff (Appendix III). The initial increase in iron and manganese concentrations was accompanied by a decrease in pH. The high levels of iron leached from the tuff matrix when using devitrified tuff compared to glassy results in pH values for the former as low as 3.5. Runs with glassy tuff produced pH values no lower than four. The hydrogen ions were released to the solution by the oxidation and subsequent hydrolysis of Fe^{2+} and Mn^{2+} leached from the tuff. The iron and manganese finally precipitate as iron and manganese oxyhydroxides. Iron oxyhydroxide coatings were found on tuff grains from all parts of the reactor at the termination of each experiment. The reactions proceed as follows:

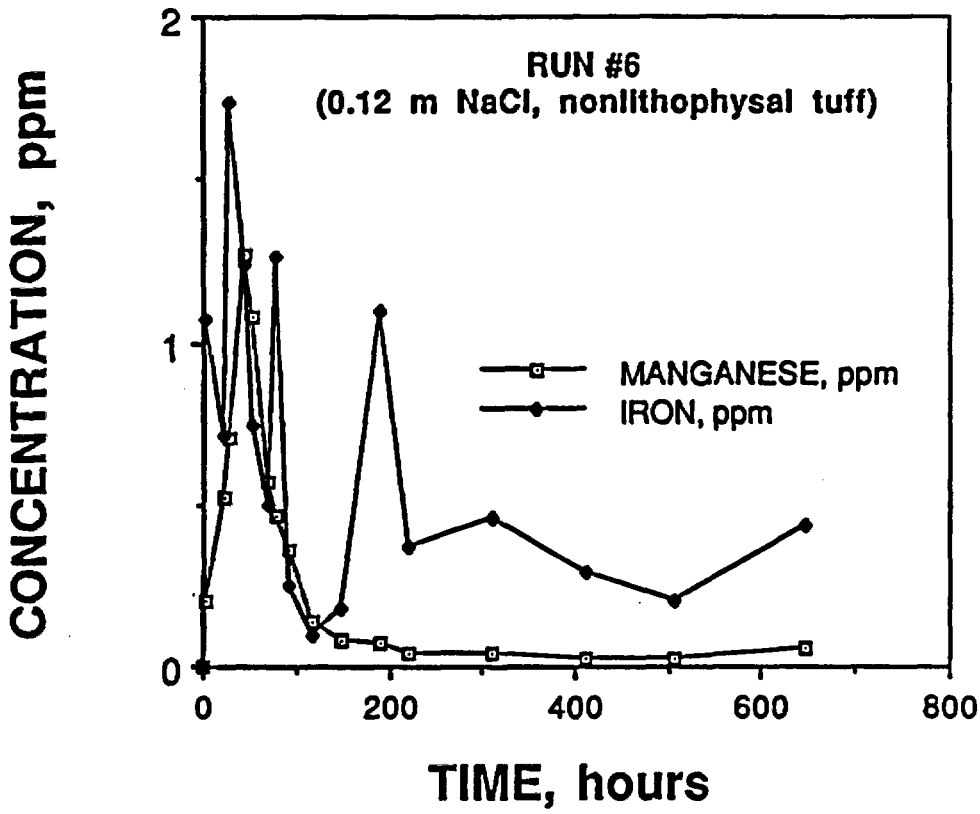

Figure 8. Typical behavior of dissolved iron and manganese for runs 5 through 10. This example is from run #6.

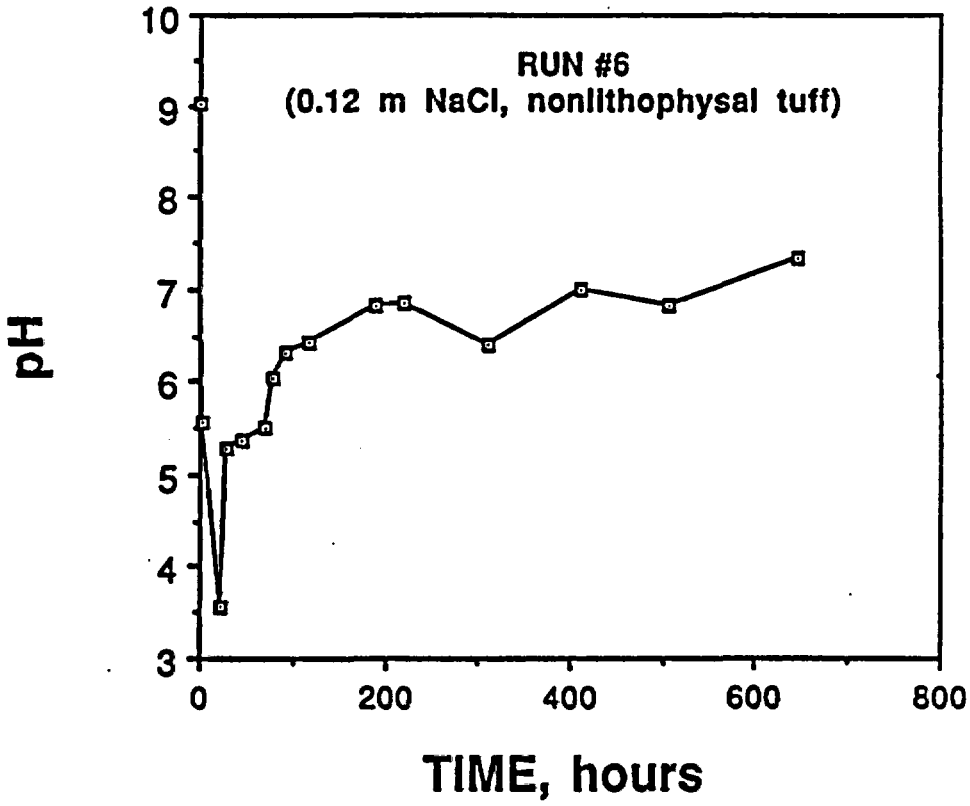

Figure 9. The pH variation of the solution for a typical run (run #6).

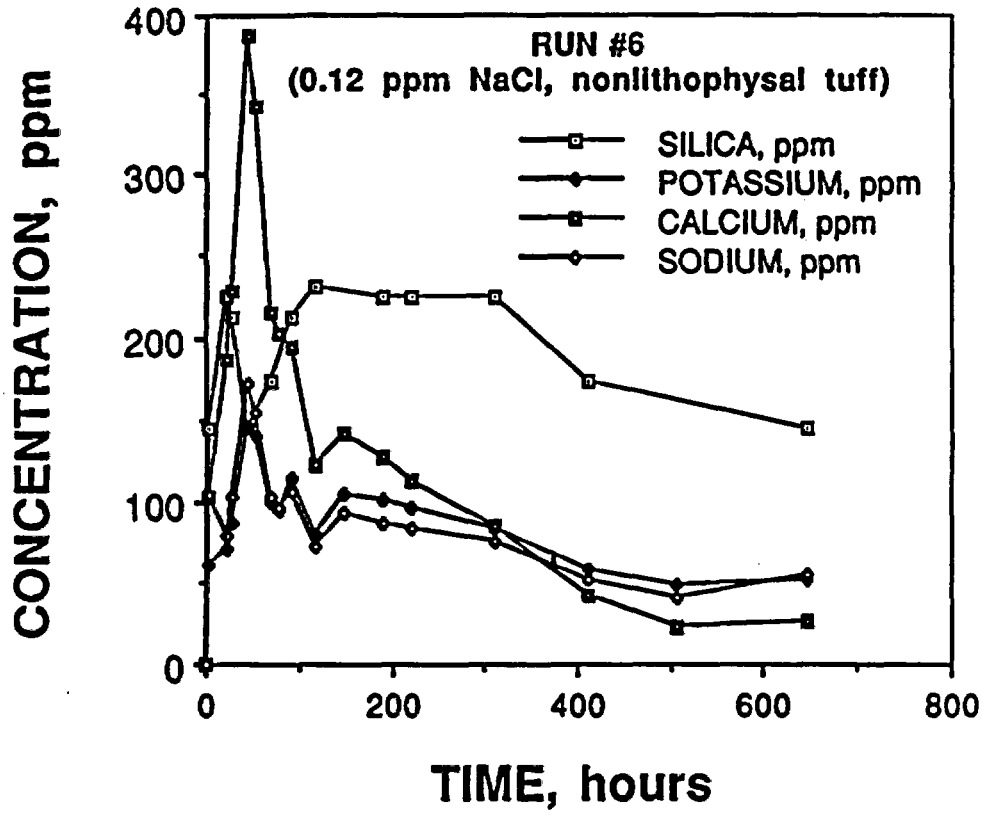

Figure 10. The variations in the concentrations of silica, potassium, calcium, and sodium for a typical run (run #6).

IRON

LEACHING $Fe^{2+}_{(s)} + 2H^{+}_{(aq)} = Fe^{2+}_{(aq)}$

OXIDATION $2Fe^{2+}_{(aq)} + 1/2\ O_2 + 2H^{+}_{(aq)} = 2Fe^{3+}_{(aq)} + H_2O$

HYDROLYSIS & PRECIPITATION $2Fe^{3+}_{(aq)} + 6H_2O = 2Fe(OH)_{3\,(s)} + 6H^{+}_{(aq)}$

OVERALL REACTION $2Fe^{2+}_{(aq)} + 1/2O_2 + 5H_2O = 2Fe(OH)_{3\,(s)} + 4H^{+}_{(aq)}$

MANGANESE

LEACHING $Mn^{2+}_{(s)} + 2H^{+}_{(aq)} = Mn^{2+}_{(aq)}$

OXIDATION $Mn^{2+}_{(aq)} + 1/2O_2 + 2H^{+}_{(aq)} = Mn^{4+}_{(aq)} + H_2O$

HYDROLYSIS & PRECIPITATION $Mn^{4+}_{(aq)} + 2H_2O = MnO_{2(s)} + 4H^{+}_{(aq)}$

OVERALL REACTION $Mn^{2+}_{(aq)} + 1/2O_2 + H_2O = MnO_{2(s)} + 2H^{+}_{(aq)}$

Runs with the devitrified tuff often showed relatively high SiO_2, Na, Ca, and K concentrations early in the experiment (see, for example, Figure 10) while their concentration in runs with glassy tuff simply rose to the near steady state value without any initial peak. Presumably, the early pulse of silica, alkali, and alkaline earth species is related to the increased rate of dissolution of Na-, Ca-, and K-bearing aluminosilicate phases in the lower pH solutions generated by the hydrolysis iron and manganese. Because

the nonlithophysal tuff released greater amounts of iron and manganese, more hydrogen ions were generated, and runs using nonlithophysal tuff samples showed an initial concentration spikes of SiO_2, Na, Ca, and K followed by rapid declines to steady-state concentrations of approximately 25% of the maximum. In contrast to the experiments with devitrified tuff, runs with the glassy tuff produced concentrations for SiO_2, Na, Ca, and K that rapidly rose to the near steady state concentrations and remained there.

The sampling of reactor liquids during the operation of the VTGE required some attention to repeatability. Samples taken within one minute of each other from near the center of the reactor core and from the margin of the PVC pipe produced pH values that differed by as much as ±0.75 pH units. pH measurements as well as the concentrations of the other dissolved species displayed wide variability. This variability in recorded pH was accompanied by fluctuations in the concentrations of dissolved silica and cations. Note that although the pH and concentrations of solution species tend to be related early in the experiments they show little or no correlation with each other or with the heat flux after the system reaches steady state. This variability no doubt arises from the very complex flow patterns of both liquid and vapor inside the reactor. A comparison of the data from runs 5 through 10 show that the variation in the concentration of dissolved species from one sample to another in a single experiment is about the same as the variation of the average steady state concentration from one experiment to another. This means that this internal variation masks any variation in solution composition that might arise from changes in the initial solution composition or from the use of different tuff samples. This is not very surprising because the chemistry and mineralogy of the tuff samples is similar and the ratio of the tuff to solution in the experiment is so large that the rock chemistry completely dominates the solution chemistry. Thus, the solution analyses for run times greater than 200 hours were pooled for all runs and averaged (Table 3).

Solution composition data from Table 3 can be used to understand the nonequilibrium nature of this experiment. When the various chemical geothermometers

Table 3. Average concentaration of dissolved species in VTGE runs (#5 through #10) at near steady state conditions (run times greater than 200 hours).

	AVERAGE	STANDARD DEVIATION
pH	6.36	1.12
Na	115 ppm	50 ppm
K	135 ppm	74 ppm
Ca	57 ppm	30 ppm
SiO_2	183 ppm	35 ppm
Fe	0.23 ppm	0.33 ppm
Mn	0.02 ppm	0.02 ppm

Table 4 Temperatures calculated for VTGE experiments using conventional chemical geothermometers that assume equilibrium between the rock and solution (Henley, 1984). The actual temperature inside of the experiment was always near 100°C.

GEOTHERMOMETER	TEMPERATURE
1. quartz (no steam loss)	174°C
2. quartz (max steam loss)	163°C
3. chalcedony	152°C
4. alpha-cristobalite	124°C
5. beta-cristobalite	74°C
6. amorphous silica	51°C
7. Na/K (Fournier)	588°C
8. Na/K (Truesdell)	813°C
9. Na-K-Ca (ß=1/3)	338°C
10. Na-K-Ca (ß=4/3)	188°C

(Henley, Truesdell, and Barton Jr., 1984), commonly used for geothermal systems, are applied to these solution data a wide range of temperatures are estimated (Table 4). The various silica geothermometers show that the solutions are supersaturated with respect to quartz, chalcedony, and alpha-cristobalite and undersaturated with beta-cristobalite and amorphous silica. Although this may be true for the average solution that accumulates in the bottom of the experiment, SEM observation of tuff grains recovered from these experiments do show that amorphous silica has precipitated from solutions throughout the experiment. Assessment of the Na, K, and Ca concentrations is somewhat more difficult. Certainly the unreasonable geothermometer temperatures show that the solution in the bottom of the experiment is not in equilibrium with the phases that equilibrate with the solutions in natural geothermal systems. It is not clear whether plotting these data on activity diagrams such as the ones constructed by Bowers and Burns (1990) will produce meaningful interpretations of the conditions in the experiment.

Understanding the behavior of the VTGE

As a first approximation the VTGE can be viewed as a simple reflux system quite similar to a Soxlet extraction apparatus. This system can be modelled as a pair of mixed flow reactors (see Levenspiel, 1972, for a discussion of ideal chemical reactors) as illustrated in Figure 11. The bottom reactor simulates the bottom part of the VTGE where liquid water contacts the tuff grains and boiling takes place. The top reactor simulates the remaining part of the VTGE column where condensation of water vapor brings distilled liquid water into contact with the tuff grains. This water is very undersaturated with respect to the minerals in the tuff grains and thus causes corrosion and etch pitting of these grains releasing dissolved species to the solution. The solution trickles downward reacting with more tuff grains and becoming progressively more saturated. After the solution accumulates in the liquid reservoir in the bottom of the reactor, boiling removes water from the solution to produce a solution supersaturated with respect to amorphous silica (opal A and possibly opal CT) and zeolites. This analysis immediately explains the very non-

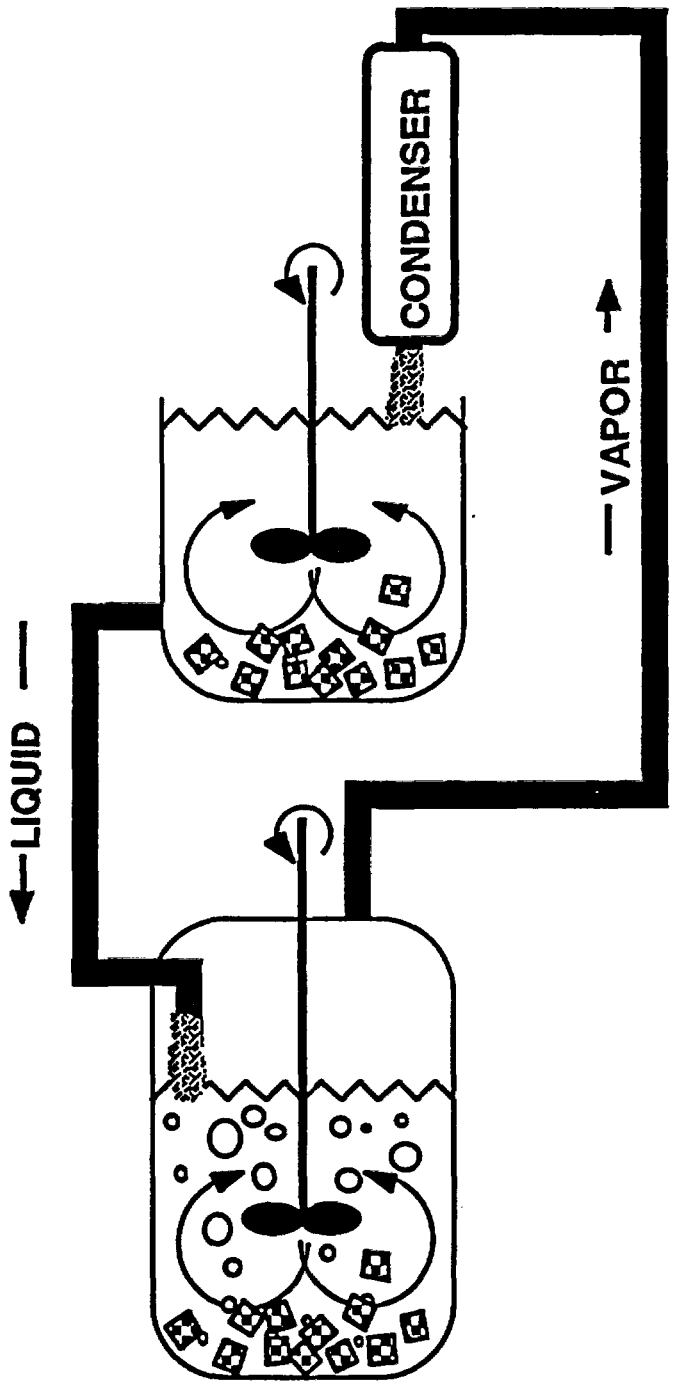

Figure 11. Schematic diagram illustrating a simple two mixed flow reactor (MFR) model of the VTGE. The bottom reactor contains tuff grains in a boiling solution while the top reactor contains tuff grains reacting with condensate.

equilibrium composition of the solutions in the experiment. Near the top of the experiment the solutions are undersaturated because distilled water is constantly added to them by condensation faster than the minerals dissolve to saturate the solution while near the bottom of the experiment the solutions tend to be supersaturated because boiling constantly removes water from them.

This analysis shows that the mass flow that is coupled to the heat flow in the VTGE creates a wide range of chemical environments. We have no way of actually observing the flow patterns in the experiment but our measurements of the thermal efficiency of the experiment shows that about 30% of the heat is lost laterally through the insulation suggesting that about 30% of the condensation should occur near the periphery of the pipe while about 70% should occur at the top of the pipe. Thus, we expect that the overall flow pattern is generally radially symmetrical with more steam rising in the center of the column and more liquid descending at the periphery (Figure 12). This would account for the variation in the composition of the solution samples taken from the bottom of the experiment as the solutions near the periphery should be more dilute and have a somewhat lower pH than those from the center of the column. A radial variation in solution composition could be modeled by adding a peripheral reservoir (Figure 13) to the ideal mixed flow reactor of Figure 11. There is also a variation of solution composition over the vertical extent of the experiment. This results from an increasing extent of reaction of the condensate with the tuff as it flows downward as a thin film covering the grains. The nature of this film is not clearly understood but it likely is composed of several layers (Figure 14). Unfortunately, we have not developed a method to sample this solution at various points along the column so we have no way to assess the nature of this downward-moving solution. One way to model this rather complex change in solution composition is by using a series of staged mixed flow reactors (Figure 15). Such a model would require empirical rate laws that describe the rate of release of important solution species as a function of solution composition. Currently no data with this level of sophistication exists,

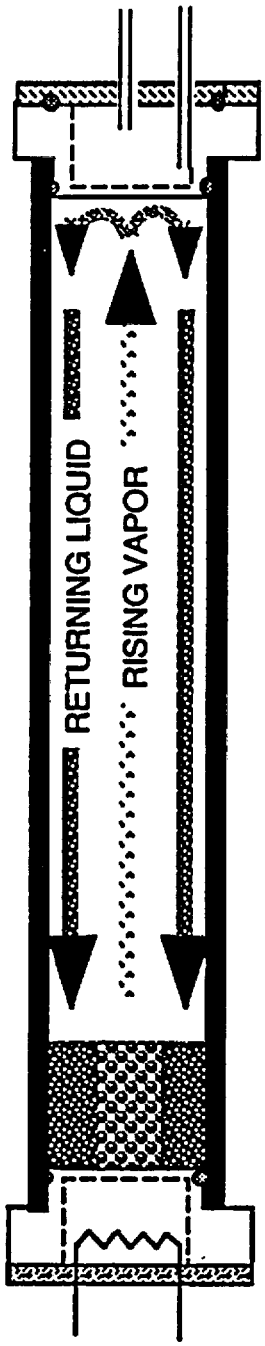

Figure 12. Schematic diagram showing the hypothesised flow pattern in the VTGE. Boiling is most vigorous near the central axis of the pipe with steam rising up the axis while heat loss at the top and through the sides of the reactor cause a net downward flow of liquid near the periphery of the pipe.

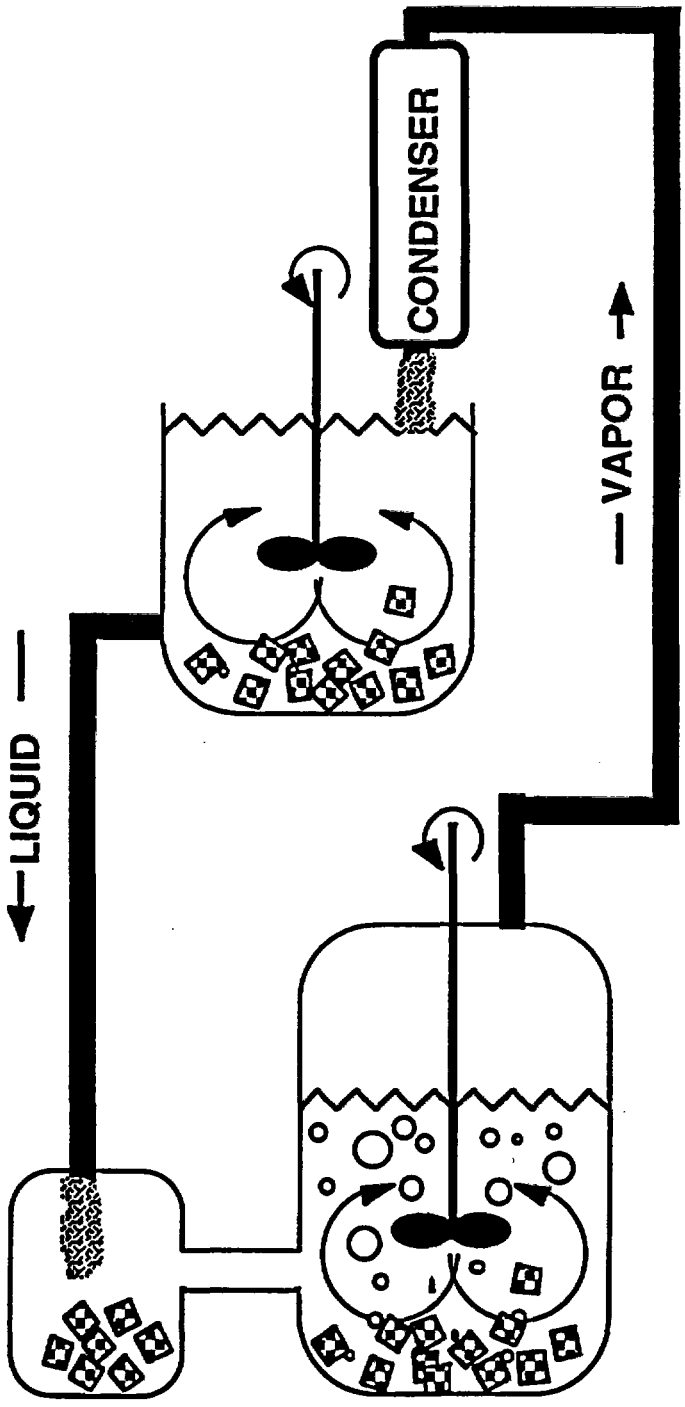

Figure 13. Modified reactor model of VTGE where the reactor repesenting the boiling zone is represented as a non-ideal mixed flow reactor.

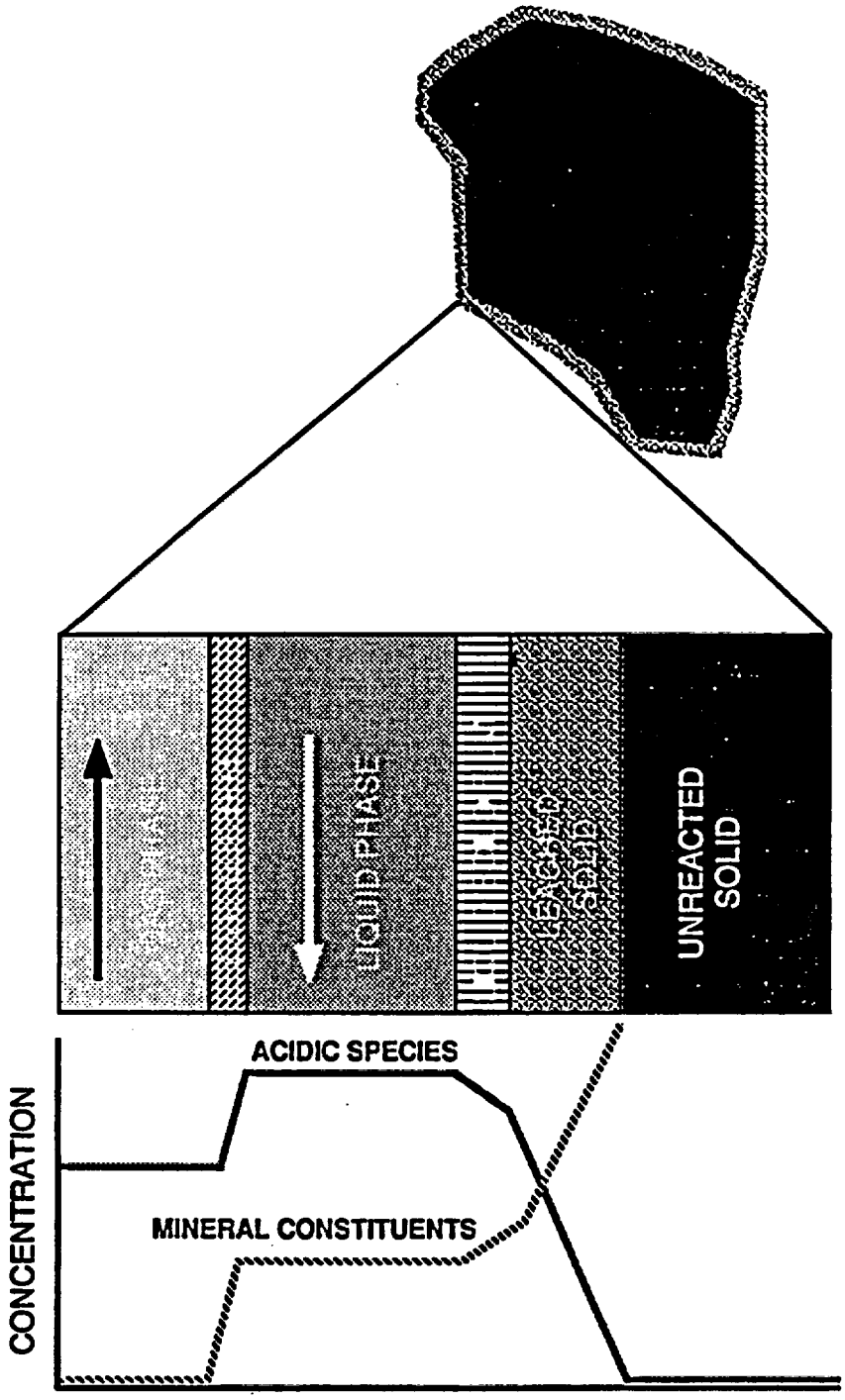

Figure 14. Diagram showing the possible compositional zones on the surface of tuff grains in the VTGE.

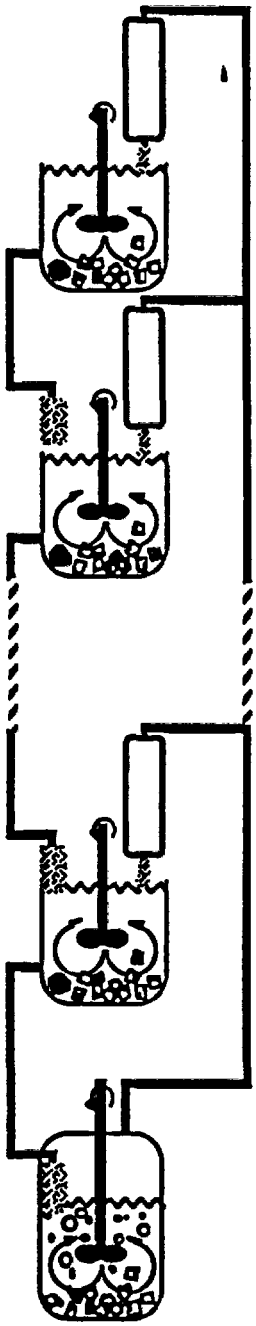

Figure 15. Schematic diagram showing staged mixed flow reactors that might simulate the variation in the environment of the reacting solution as it trickles downward in the VTGE.

and in fact, the methodology to derive it has not yet been developed. We do have some ideas along this line, however, that can be pursued when further funding becomes available. In addition, some sort of precipitation rate laws must also be developed in order to simulate the self-sealing processes near the heat source. This presents a much more difficult problem as precipitation kinetics has been much less studied than has dissolution kinetics. Development of these data probably will not be reasonable for several more years.

In addition to developing a model for the rate of chemical reactions, a model of fluid flow rates must be derived. There has been some work in this area (Pollock, 1986, Tsang and Pruess, 1987). Species transport and reaction must be coupled to such flow models in order to create a useful overall model that could predict the future behavior of the Yucca Mountain high level radioactive waste repository. However, because a sound geochemical model does not yet exist, it is beyond our current capability to create a comprehensive, coupled flow + reaction model. Rather we propose that experiments are capable of giving us only a qualitative understanding of the general behavior of a real system.

CONCLUSIONS

The vertical thermal gradient experiment (VTGE) described here simulates vapor dominated conditions in the shallow crust. The series of experiments described in this paper represent extreme conditions of heat flux and water transport that might occur adjacent to the proposed high level radioactive waste repository at Yucca Mountain, Nevada. The general behavior of the system and the composition of the solution samples were essentially independent of the kind of tuff (nonlithophysal or glassy) used in the experiment. The behavior was also unrelated to variation of the starting solution composition (ranging from distilled-deionized water to synthetic J-13 water). This is because the large mineral surface area relative to the mass of solution allows the rock to buffer the solution composition. Significant run time variations in the solution chemistry are likely the result of local variations in the liquid and vapor flow patterns in the reactor.

The solution compositions demonstrate that very nonequilibrium conditions prevail throughout most of the reactor. Presumably lower heat fluxes would allow the solution components to more nearly equilibrate with the mineral phases in the rock. Because we did not vary the heat flux in these experiments, we cannot predict how the departure from equilibrium is related to the heat flux.

The experiments produced "good news, bad news" results. In all cases it appears that this reflux system deposited iron and manganese oxyhydroxides, amorphous silica (and possibly opal CT), and zeolites in the vicinity of the heat source. These deposits would produce a self-sealing effect in the near field of the repository. Also, these phases might act as geochemical barriers to radionuclide migration. We did not, however, simulate possible nitric acid production that might occur near the waste cannisters as a result of radiolysis of atmospheric N_2 and O_2 (Reed and Van Konynenburg, 1988). This acid would likely destroy these iron and manganese oxyhydroxides and zeolites. Aside from these chemical effects, successive hydration and dehydration of the zeolite-containing rocks adjacent to the repository can set up stresses (Kranz et al., 1989) that might result in the development of additional fractures in the rock and thus increase the permeability of the rocks near the wastes. In addition, condensation of water, unsaturated with respect to any of the mineral phases, near the tips of these fractures will likely produce leaching which will destroy minerals and assist in the extension of these fractures.

It is not clear just what level of modelling of all of these effects might be necessary in order to develop a long term picture of the evolution of the repository site for licensing purposes. Models of heat and water transport for this situation already exist (Pollock, 1986, Tsang and Pruess, 1987) and a model for some chemical transport effects has been developed (Arthur and Murphy, 1989). However, there are several more important mineral dissolution and precipitation reactions that must be included into an overall model. Furthermore, these models must be coupled. For fairly constant heat flux, the chemistry shows significant fluctuations. This suggests that modelling the chemistry of vapor

dominated geothermal systems or of the vapor dominated part of the Yucca Mountain high level radioactive waste repository will be quite difficult. This is partly due to the formation of a wide range of microenvironments in the system. Finally, if the permeability and porosity of the system changes rapidly as a result of dissolution-precipitation reactions and hydration-dehydration processes (Kranz et al., 1989), these changes must be incorporated into the flow models in order to create a complete model of the time evolution of the repository.

Mass transport in a thermal field is an important source of geochemical differentiation in the earth. Many important and dramatic geological processes are driven by thermal gradients. This process has been invoked to provide explanations for a wide range of geological phenomena from the formation of ore deposits (Norton and Cathles, 1979) to geomagnetic reversals with coupled mass extinctions of flora and fauna (Courtillot and Besse, 1987). The thinning of the earth's crust in an extensional environment, or the emplacement of a shallowly seated pluton in a volcanic arc dramatically increases local heat flow. The fluid flow that is coupled to this heat flow causes significant redistribution of the elements. The experiment described in this report is designed to simulate a particular case of coupled heat and mass transport.

REFERENCES

Arthur R. C. and Murphy W. M. (1989) An analysis of gas-water-rock interactions during boiling in partially saturated tuff. *Sci. Géol. Bull.* 42, 313-327.

Bowers T. S. and Burns R. G. (1990) Activity diagrams for clinoptilolite: susceptibility of this zeolite to further diagenetic reactions. *Am. Min.* 75, 601-619.

Cline J., Bodnar R. J. and Rimstidt J. D. (1987) Quantitative evaluation of quartz transport and deposition in boiling solutions: Application to epithermal gold deposits. *G.S.A. Programs and Abstracts* 19, 621.

Courtillot V. and Besse J. (1987) Magnetic field reversals, polar wandering, and coremantle coupling. *Science* 237, 1140-1147.

Duchi V., Minissale A. A. and Rossi R. (1986) Chemistry of thermal springs in the Larderello-Travale geothermal region, southern Tuscany, Italy. *Applied Geochem.* 1, 659-667.

Ewers G. R. and Keays R. R. (1977) Volatile and precious metal zoning in the Broadlands Geothermal Field, New Zealand. *Econ. Geol.* 72, 1337-1354.

Grovett G. J. S. (1961) Critica factors in the colorometric determination of silica. *Anal. Chim. Acta* 25, 69-80.

Hedenquist J. W. and Henley R. W. (1985) Hydrothermal eruptions in the Waiotapu Geothermal System, New Zealand: Their origin, associated breccias, and relation to precious metal mineralization. *Econ. Geol.* 80, 1640-1668.

Henley R. W. and Ellis A. J. (1983) Geothermal systems ancient and modern: A geochemical review. *Earth-Science Reviews* 19, 1-50.

Henley R. W., Truesdell A. H. and Barton Jr. P. B. (1984)*Fluid-Mineral Equilibria in Hydrothermal Systems*, 1, Society of Economic Geologists, Elpaso, Texas.

Hulen J. B. and Nielson D. L. (1986) Hydrothermal alteration in the Baca Geothermal System, Redondo Dome, Valles Caldera, New Mexico. *Jour. Geophys. Res.* 91B, 1867-1886.

Kranz R. L., Bish D. L. and Blacic J. D. (1989) Hydration and dehydration of zeolitic tuff from Yucca Mountain, Nevada. *Geophysical Research Letters* **16**, 1113-1116.

Krupp R. E. and Seward T. M. (1987) The Rotokawa Geothermal System, New Zealand: An active epithermal gold-depositing environment. *Econ. Geol.* **82**, 1109-1129.

Levenspiel O. (1972)*Chemical Reaction Engineering* , 2nd, John Wiley & Sons, New York.

Moore D. E. and Morrow C. A. (1986) High-temperature permeability and groundwater chemistry of some Nevada Test Site tuffs. *J. Geophys. Res.* **91(B2)**, 2163-2171.

Muffler L. J. P., White D. E. and Truesdell A. H. (1971) Hydrothermal explosion craters in Yellowstone National Park. *Geol. Soc. Amer. Bull* **82**, 723-740.

Pollock D. W. (1986) Simulation of fluid flow and energy transport processes associated with high-level radioactive waste disposal in unsaturated alluvium. *Water Resources Research* **22**, 765-775.

Raymahashay B. C. (1968) A geochemical study of rock alteration by hot springs in the Paint Pot Hill area, Yellowstone Park. *Geochim. Cosmochim. Acta* **32**, 499-522.

Reed D. T. and Van Konynenburg A. (1988) Effect of ionizing radiation on moist air systems. *Mat. Res. Soc. Symp. Proc.* **112**, 393-404

Rose A. W. and Burt D. M. (1979) Hydrothermal Alteration. In *Geochemistry of Hydrothermal Ore Deposits* (H. L. Barnes ed.), v. Ch. 5, John Wiley & Sons, New York.

Schoen R., White D. E. and Hemley J. J. (1974) Argillization by decending acid at Steamboat Springs, Nevada. *Clays Clay Mins.* **22**, 1-22.

Truesdell A. H. and Nehring N. L. (1979) Gases and water isotopes in a geochemical section across the Larderello, Italy, geothermal field. In *Geothermics and Geothermal Energy* (L. R. a. L. Stegenas L. R. a. L. Stegena), v. Birkhauser Verlag, Basel und Stuttgart.

Tsang Y. W. and Pruess K. (1987) A study of thermally induced convection near a high-level nuclear waste repository in partially saturated fractured tuff. *Water Resources Research* 23, 1958-1966.

White D. E., Muffler L. J. P. and Truesdell A. H. (1971) Vapor-dominated hydrothermal systems compared with hot-water systems. *Econ. Geol.* 66, 75-97.

APPENDIX I

DETAILED DIAGRAMS SHOWING THE HEATING AND COOLING ASSEMBLIES OF THE VTGE

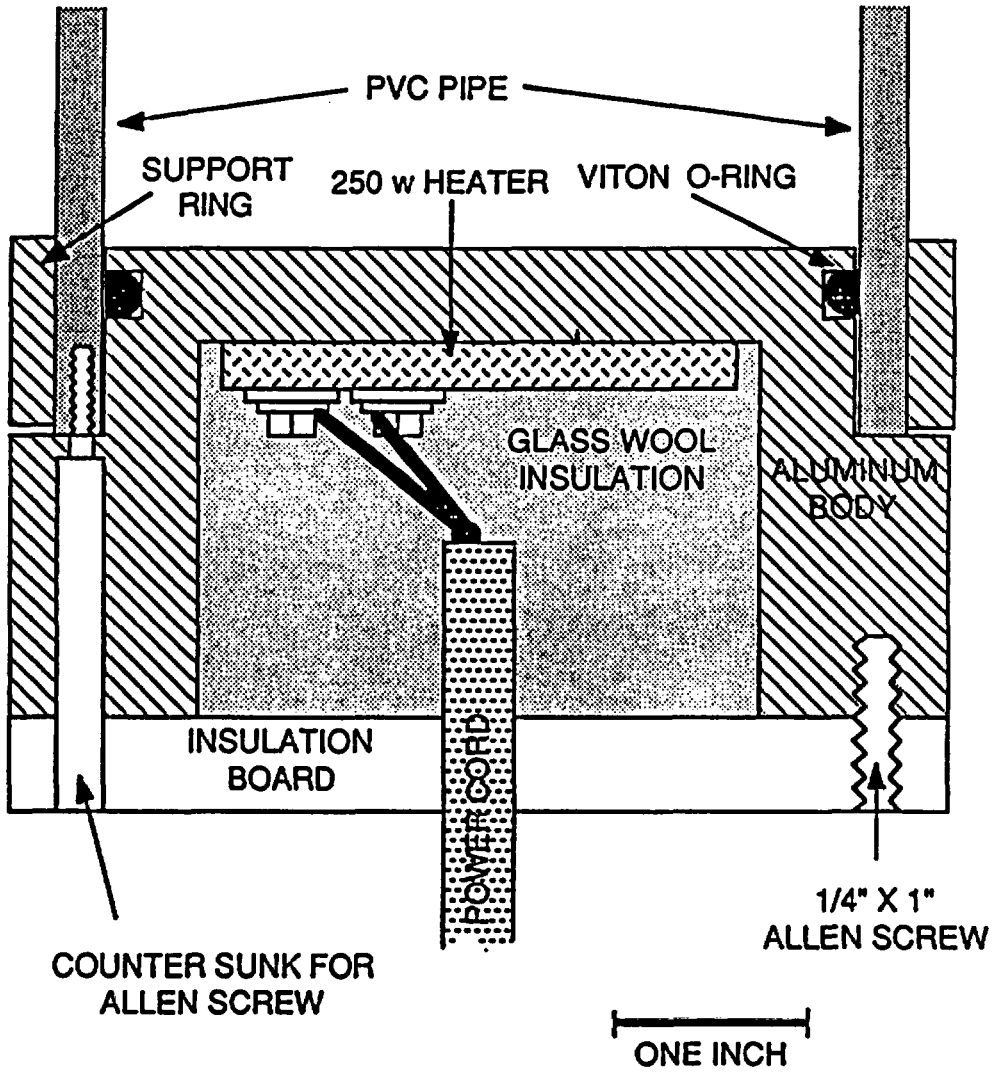

Figure I-1. Cross section of the heating assembly of the VTGE.

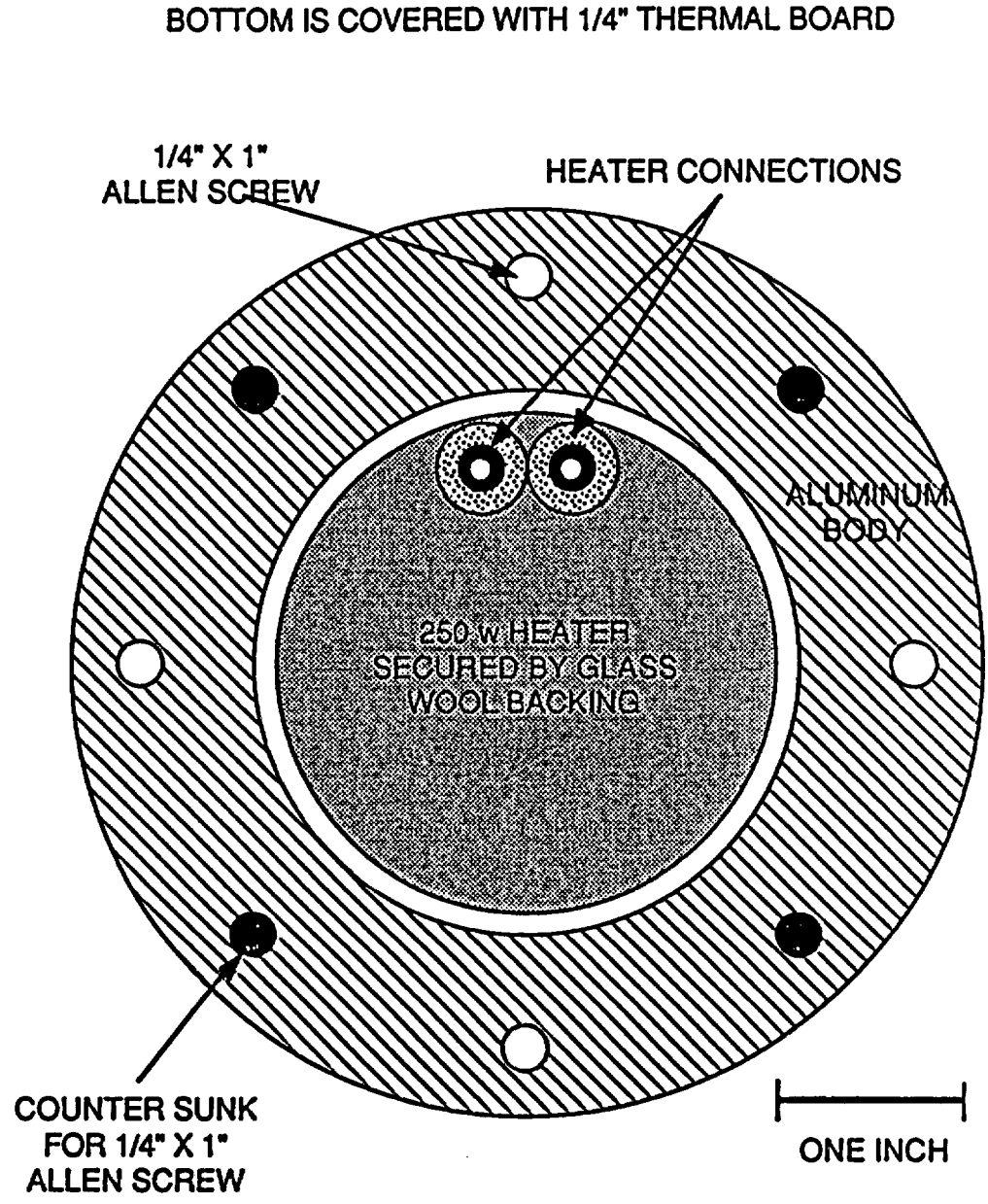

Figure I-2. Plan view of the VTGE heating assembly.

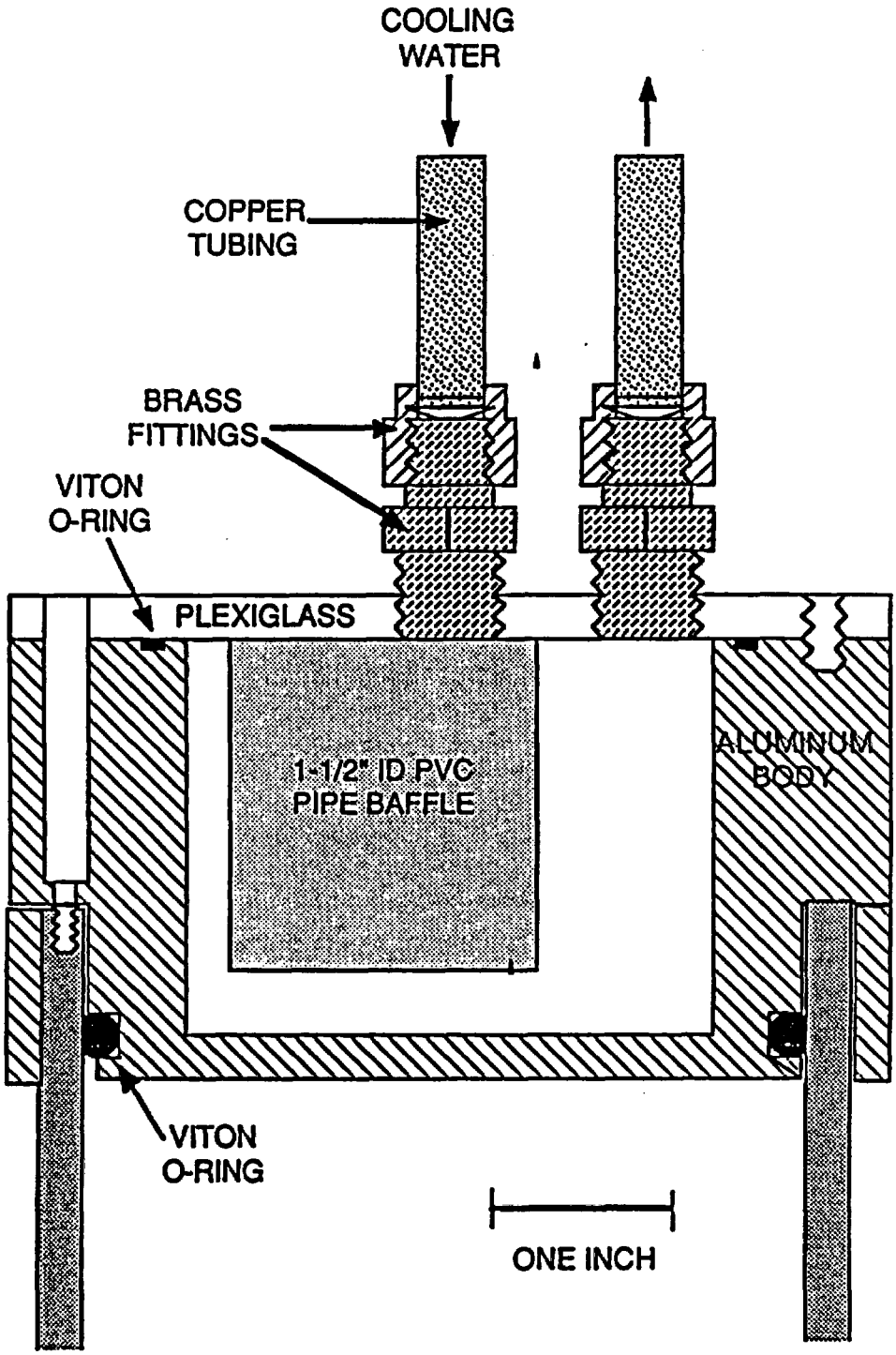

Figure I-3. Cross section of the cooling assembly for the VTGE.

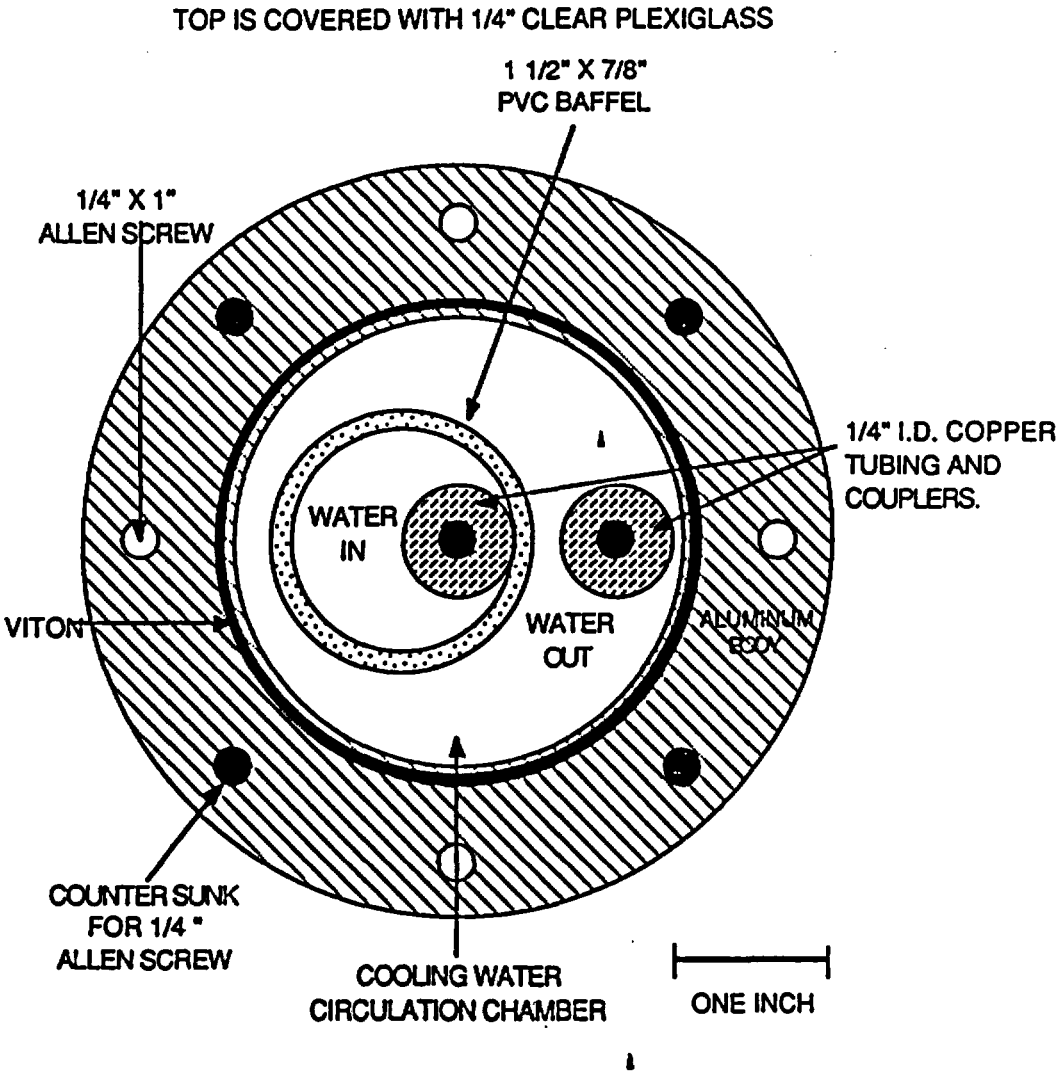

Figure I-4. Plan view of VTGE cooling assembly.

APPENDIX II

THERMAL CHARACTERISTICS OF VTGE RUNS RUNS 4 THROUGH 10

Top temp, middle temp, and bottom temp are the termperatures inside ther reactor column as measured by dial thermometers inserted so their tips lie at the center of the comumn (see Figure 2). Cooling water in and out are the temperatures of the cooling water as it flows into and out of the cooling assembly. The flow rate for these experiments were and the amount of heat absorbed form the top of the column is given by equation (2) in the text of this report. while the rate that heat was added to the bottom is given by equation 1 (V = 70 v). The heat through is the percentage of the heat that passed from the heating assembly through the cooling assembly. The remainder was lost through the insulation under the heating assembly and around the column.

Table II-1. Temperature conditions for run #4.

ELAPSED TIME (hr)	TOP TEMP (°C)	MIDDLE TEMP (°C)	BOTTOM TEMP (°C)	COOLING WATER-IN (°C)	COOLING WATER-OUT (°C)
0.0	26.04	25.7	19.3	15.5	17.5
1.0	27.08	52.5	68.6	16.5	21.5
2.0	67.2	76.8	83.2	17.5	23
3.7	92.7	100	100	17	22
4.0	94.8	100	100	17.5	30
4.5	93.8	100	100	18	28
10.0	100	100	100	18	28.5
24.0	95.3	100	100	18	29
46.0	92.7	100	99.5	18	28
48.0	92.7	100	100	17.5	26
52.0	92.7	100	100	12	26
55.0	93.8	100	100	12.5	26
74.0	93.8	100	100	14	29
96.0	93.8	100	100	14	29
118.5	93.2	100	100	14	29.5
142.0	93.2	100	100	15	30.5
148.0	91.7	100	100	14	28.5
168.0	93.2	100	100	15	30
190.0	92.7	100	100	14	28.5
197.5	91.7	100	100	12	27
215.0	91.1	100	100	13	28
219.5	90.6	100	100	12.5	27
223.0	90.6	100	100	13.5	29.5
239.5	91.7	100	100	14	30
263.5	92.2	100	100	14	30
287.0	92.2	100	100	13.5	31.5
301.0	92.7	100	100	14	33
325.5	91.7	100	100	14	34
347.5	91.1	100	100	13	28
371.5	91.7	100	100	14	32
375.0	88.5	100	100	13	29
396.5	91.7	100	100	14.5	31
419.8	90.6	100	100	14.5	29
443.5	90.6	100	100	14	29
473.5	90.6	100	100	14	30
495.5	90.6	100	100	14	30
515.5	89.6	100	100	14	30
523.5	90.6	100	100	14	30
540.0	90.6	100	100	14.5	30
563.0	90.6	100	100	15	30
588.5	89.6	100	100	13	28
619.5	89.6	100	100	13	29.5

Table II-2. Temperature conditions for run #5.

ELAPSED TIME (hr)	TOP TEMP (°C)	MIDDLE TEMP (°C)	BOTTOM TEMP (°C)	COOLING WATER-IN (°C)	COOLING WATER-OUT (°C)
0	25	25	25	12	12
45	95	99.5	100	14	27
68	95	99	100	14	25
91.5	95	99	100	15	25.5
116	95	98.5	100	15	26
140	95	99	100	14	25
165	95	99	100	14	25
189.5	95	99	100	15	25
211.5	95	99	100	14	25
236.5	95	98.5	100	14.5	25.5
285	95	98.5	99.5	14	24
309.5	95	98.5	100	14	25
340	95	99	100	15	25

Table II-3. Temperature conditions for run #6.

ELAPSED TIME (hr)	TOP TEMP (°C)	MIDDLE TEMP (°C)	BOTTOM TEMP (°C)	COOLING WATER-IN (°C)	COOLING WATER-OUT (°C)
0	24	23.5	23.5	21	21
1	24	24	75	21	23
2	31	29	97.5	21	23
4	93	99	100	21	29
5	89	99	100	21	29
22	95	99	100	22	31
27.5	97	99	100	22	32
28	97	99	100	22	32
45.5	97	99.5	100	22	34
49.5	95	99	100	22	32
53.25	97	99	100	23.5	39
70.5	97	99.5	100	22	32
73.5	96	99.5	100	22	32
77.5		99.5	100	22.5	34
93.5	97	99.5	100	22	33
117.5	96.5	99.5	100	22	32
144.5	97	99.5	100	22	32
148.5	97	99.5	100	23	33.5
165.75	97	99.5	100	22.5	33
190	97	99.5	100	23	34
214	97	99.5	100	22	32
220.5	97	99.5	100	23.5	35
238	95	99.5	100	23	34
309.5	97	99	100	24	33
410	97	99.5	100	22.5	32
507.5	91	99.5	100	22.5	31
645.5	94	99.5	100	22	32

Table II-4. Temperature conditions for run #7.

ELAPSED TIME (hr)	TOP TEMP (°C)	MIDDLE TEMP (°C)	BOTTOM TEMP (°C)	COOLING WATER-IN (°C)	COOLING WATER-OUT (°C)
0	25	25	25		
3	43.5	98.5	100	24	31
24	74	98.5	100	25	33
28.5	76	98.5	100	25	36.5
56.5	80	98.5	100	26	38
81.5	75	98.5	100	25	36
108	80	98.5	100	27	40.5
129	78	98.5	100	37	41
177	77	98.5	100	24	35
225	75	98.5	100	24	35
249	77	98.5	100	24	37
368	75	98.5	100	25	36
422	75	98.5	100	24	33
489	75	98.5	100	25	36
537	76	98.5	100	25	36

Table II-5. Temperature conditions for run #8.

ELAPSED TIME (hr)	TOP TEMP (°C)	MIDDLE TEMP (°C)	BOTTOM TEMP (°C)	COOLING WATER-IN (°C)	COOLING WATER-OUT (°C)
0	25	25	25	12	12
2	33	100	100	12	24
4	98	100	100	12	59
20.5	98	100	100	11	26
27.5	98	100	100	10	20
34.5	98	100	100	12	28
39.5	98	100	100	11	28
58	98	100	100	12	28
71	98	100	100	11	35
83	98	100	100	11	20
95	98	100	100	81	75
109	96	100	100	10	19
113	98	100	100	10	21
132	98	100	100	10	20
138	98	100	100	9	17
156	98	100	100	10	18
161	98	100	100	10	19
180	98	100	100	10	17
204	98	100	100	10	20
229	98	100	100	11	20
253	98	100	100	11	20
280	98	100	100	11	20
304	98	100	100	11	20
324	98	100	100	11	20
379	98	100	100	11	20
447	98	100	100	11	20
495	98	100	100	11	20
544	98	100	100	11	20

Table II-6. Temperature conditions for run #9.

ELAPSED TIME (hr)	TOP TEMP (°C)	MIDDLE TEMP (°C)	BOTTOM TEMP (°C)	COOLING WATER-IN (°C)	COOLING WATER-OUT (°C)
0	25	25	25	11	11
2	24	30	94	21	20
4	42	100	100	17	20
18.5	93	100	100	22	30
25	98	100	100	23	32
46.5	98	100	100	27	35
50.5	98	100	100	28	38
71	98	100	100	30	40
75.5	98	100	100	29	42
94	98	100	100	30	41
99	98	100	100	30	41
118.5	98	100	100	30	40
124	98	100	100	30	41
153.5	98	100	100	29	40
161	98	100	100	30	44
180.5	98	100	100	30	40
185.5	98	100	100	32	38
208	98	100	100	32	41
234	98	100	100	34	45
250.5	98	100	100	35	48
276	98	100	100	31	40
300	98	100	100	31	45
323	98	100	100	32	46
352	98	100	100	31	45
376.5	98	100	100	34	48
420.5	98	100	100	18	31
450.5	98	100	100	61	61

Table II-7. Temperature conditions for run #10.

ELAPSED TIME (hr)	TOP TEMP (°C)	MIDDLE TEMP (°C)	BOTTOM TEMP (°C)	COOLING WATER-IN (°C)	COOLING WATER-OUT (°C)
0	25	25	25	12	12
2	89	42	28	12	15
4	100	100	65	12	24
16	100	100	70	16	30
24.5	100	100	70	16	30
40.5	100	100	70	16	32
49	100	100	70	16	26
65	100	100	70	16	31
72	100	100	70	16	27
90	100	100	70	17	28
95.5	100	100	70	17	27
113	100	100	70	17	27
117.5	100	100	70	18	29
135.5	100	100	71	18	28
142.5	100	100	71	18	28
159	100	100	71	16	31
166.5	100	100	65	17	21
138	100	100	65	16	25
195.5	100	100	65	16	21
214.5	100	100	65	17	26
238	100	100	65	18	28
266	100	100	65	18	28
290.5	100	100	65	18	28
312	100	100	65	17	27
360.5	100	100	65	17	21
408	100	100	65	19	22
470	100	100	70	16	20
512.5	100	100	75	17	27
560.5	100	100	75	17	28
636.5	100	100	75	17	28
657.5	100	100	75	17	28

APPENDIX III

RESULTS OF CHEMICAL ANALYSIS OF SOLUTIONS EXTRACTED FROM VTGE RUNS 4 THROUGH 10 AND FROM BATCH REACTOR EXPERIMENTS

Table III-1. Solution composition data from VTGE Run 4. Nonlithophysal Yucca Mountain tuff in distilled water. Reactor initially filled to 80% of volume and solution allowed to evaporate over the experiment. This experiment was run using a different protocol than the subsequent ones and therefore should not be compared to them.

TIME hours	pH	SiO_2 ppm	Na ppm	K ppm	Ca ppm	Mn ppm	Fe ppm
0	7.00	0.0	0.00	0.0	0.0	0.000	0.000
24	6.91	155.6	21.51	54.0	111.7	0.286	0.259
48	6.82	155.6	61.31	151.6	188.8	0.138	0.145
96	8.20	144.2	98.12	240.8	219.8	0.072	0.138
144		220.8	59.92	147.0	144.0	0.060	0.120
148	8.20						
190	8.82	393.7	56.33	136.0	107.3	0.038	0.204

Table III-2. Solution composition data from VTGE Run 5 (distilled water, nonlithophysal tuff).

TIME hours	pH	SiO_2 ppm	Na ppm	K ppm	Ca ppm	Mn ppm	Fe ppm
0	7.00	0.0	0.00	0.0	0.0	0.000	0.000
48	6.13	328.5	74.27	162.8	336.1	0.925	0.263
144	6.70	127.2	16.23	36.9	65.8	0.172	0.757
238	8.03	141.4	25.70	60.6	73.1	0.036	0.177
288	8.82	132.9	74.89	185.7	127.3	0.031	0.066
362	8.85	168.3	70.33	152.2	104.7	0.031	0.077

Table III-3. Solution composition data from VTGE Run 6 (0.125 ppm NaCl, nonlithophysal tuff).

TIME hours	pH	SiO_2 ppm	Na ppm	K ppm	Ca ppm	Mn ppm	Fe ppm
0	9.02	0.0	0.13	0.0	0.0	0.000	0.000
4	5.57	144.0	103.76	61.2	102.2	0.205	1.069
22	3.57	224.5	78.35	71.3	186.3	0.522	0.711
27.5	5.27	211.9	102.78	86.2	228.4	0.706	1.737
45.5	5.37	144.0	172.37	146.2	387.3	1.266	1.235
53.25			154.66	139.8	342.3	1.074	0.749
70.5	5.51	173.7	102.74	99.0	215.7	0.568	0.498
77.5	6.04		95.91	95.0	202.3	0.466	1.265
93.5	6.32	211.8	106.25	114.7	194.2	0.364	0.248
117.5	6.42	231.6	72.46	80.7	122.2	0.137	0.100
148.5			92.69	104.6	140.7	0.079	0.179
190	6.82	224.5	87.05	101.4	127.5	0.073	1.092
220.5	6.86	224.5	83.50	96.8	111.8	0.041	0.370
309.5	6.40	224.5	75.81	83.0	85.0	0.039	0.458
410	6.99	173.7	50.62	58.3	41.0	0.025	0.290
507.5	6.82		40.10	47.7	22.3	0.022	0.200
645.5	7.33	144.0	54.25	50.9	25.7	0.058	0.434

Table III-4. Solution composition data from VTGE Run 7 (distilled water, glassy tuff).

TIME hours	pH	SiO_2 ppm	Na ppm	K ppm	Ca ppm	Mn ppm	Fe ppm
0	7.00	0.0	0.00	0.0	0.0	0.000	0.000
3	3.96	192.6	23.07	54.6	49.3	0.017	0.202
24	7.45	165.6	137.39	245.0	308.1	0.015	0.131
28.5	7.52	154.1	94.18	175.5	198.1	0.015	0.254
56.5	7.75	138.6	134.53	254.2	239.4	0.014	0.115
81.5	7.77	154.1	132.77	272.7	198.1	0.009	0.086
108	8.25	163.0	116.71	264.9	162.7	0.007	0.062
129	8.20	173.3	134.09	311.2	176.8	0.007	0.069
177	8.19	173.3	133.98	333.5	164.2	0.007	0.056
225	8.00	170.1	137.28	362.5	147.1	0.001	0.006
249	8.10	169.5	139.37	370.0	145.3	0.001	0.006
368	7.59	181.0	88.44	240.2	87.5	0.022	0.051
422	7.68	211.8	111.21	295.5	96.6	0.001	0.006
489	8.76	177.2	66.76	176.0	62.9	0.018	0.041
537	8.21	188.7	82.76	207.2	71.1	0.012	0.046

Table III-5. Solution composition data from VTGE Run 8 (0.125 ppm NaCl, nonlithophysal tuff).

TIME hours	pH	SiO_2 ppm	Na ppm	K ppm	Ca ppm	Mn ppm	Fe ppm
0		0.0	0.13	0.0	0.0	0.000	0.000
2	4.60	69.2	100.10	77.0	71.3	0.047	1.700
4	4.57	99.8	121.77	77.2	92.4	0.038	1.639
20.5	5.54	189.1	120.12	71.4	47.6	0.033	1.482
27.5	6.12	253.1	155.87	97.8	56.8	0.015	0.768
34.5	6.61	226.4	153.01	120.3	51.4	0.010	0.376
39.5	6.49	221.9	128.59	99.9	46.7	0.012	0.346
58	6.07	226.4	148.72	125.1	48.9	0.015	0.388
71	6.58	213.2	124.19	109.8	44.0	0.015	0.288
83	6.37	200.8	159.83	144.5	48.6	0.012	0.326
95	6.54	194.8	193.27	157.1	52.1	0.015	0.496
109	6.70	198.8	170.28	120.7	43.1	0.012	0.237
113	6.22	208.9	121.11	89.3	37.3	0.002	0.095
132	6.03	250.5	160.27	122.3	47.3	0.007	0.164
138	6.00	255.7	163.90	126.5	46.8	0.010	0.214
156	5.93		193.82	147.7	58.1	0.010	0.339
161	5.93	250.5	154.55	125.3	49.3	0.017	0.333
180	5.87		149.93	124.3	46.7	0.003	0.085
204	5.76	245.4	170.61	139.4	51.3	0.007	0.136
229	5.69		188.98	158.7	56.1	0.007	0.125
253	5.61	250.5	156.20	133.8	45.5	0.012	0.339
280	5.59	221.9	166.10	143.9	50.2	0.008	0.137
304	5.54	231.0	187.44	163.2	56.2	0.012	0.201
324	5.53	204.8	150.59	133.0	45.3	0.010	0.151
379	5.47	213.2	175.56	170.3	51.9	0.007	0.150
447	5.26	181.6	163.46	139.9	53.3	0.030	0.335
495	5.24	189.1	175.67	151.4	51.4	0.012	0.139
544	5.21	189.1	171.71	150.6	49.7	0.027	0.140

Table III-6. Solution composition data from VTGE Run 9 (syn. J13 water, glassy tuff).

TIME hours	pH	SiO_2 ppm	Na ppm	K ppm	Ca ppm	Mn ppm	Fe ppm
0	7.00	0.0	46.50	5.5	9.4	0.000	0.000
2	4.66	20.5	53.97	26.7	64.9	0.013	0.493
4	4.71	58.3	58.18	27.0	46.9	0.022	0.722
18.5	4.57	188.0	112.31	68.2	186.7	0.030	1.014
25	4.72	233.9	134.86	93.0	194.4	0.018	0.411
46.5	5.18	201.5	114.62	77.6	122.8	0.013	0.083
50.5	5.22	205.5	125.29	86.1	127.8	0.007	0.055
71	5.24	201.5	96.32	65.7	79.2	0.010	0.269
75.5	5.24	205.5	94.60	69.7	82.0	0.012	0.192
94	5.29	197.6	116.93	87.5	90.5	0.010	0.172
99	5.31	201.5	106.33	79.8	82.1	0.007	
118.5	5.34	182.4	89.89	70.5	65.8	0.010	0.175
124	5.64	178.9	87.15	68.8	63.1	0.012	0.179
153.5	5.81	197.6	101.33	79.2	68.3	0.008	0.059
161	5.99	193.6	94.28	73.7	63.4	0.008	
180.5	6.06	222.5	106.27	83.3	63.7	0.007	0.050
185.5	6.01		120.67	95.2	70.9	0.010	
208	5.88	158.4	86.75	69.2	51.0	0.015	0.018
234	5.76		78.91	65.2	43.4	0.003	0.008
250.5	5.69	158.4	87.45	68.0	45.7	0.008	0.118
276	5.66		94.71	73.1	45.1	0.010	
300	5.58	186.1	84.60	67.4	39.2	0.007	
323	5.38		76.55	59.9	36.5	0.007	
352	5.15		87.01	65.2	40.9	0.003	
376.5	5.19		79.67	62.5	35.3	0.003	
420.5	5.18		75.33	58.2	31.5	0.007	
450.5	5.14						

Table III-7. Solution composition data from VTGE Run 10 (syn. J13 water, nonlithophysal tuff).

TIME hours	pH	SiO_2 ppm	Na ppm	K ppm	Ca ppm	Mn ppm	Fe ppm
0	7.50	0.0	46.50	5.5	9.4	0.000	0.000
2	4.86	17.2	35.32	48.5	75.2	0.093	2.929
4	4.88	22.1	40.19	48.5	72.4	0.045	0.591
16	4.88	101.0	59.70	77.1	124.0	0.173	0.618
24.5	4.55	156.9	83.63	104.5	155.9	0.175	0.437
40.5	4.85		56.23	74.7	86.0	0.110	2.338
49	4.77	170.1	93.94	117.7	134.2	0.084	0.797
65	5.02	125.6	58.47	76.1	70.7	0.043	0.705
72	5.04	139.9	72.88	95.3	80.1	0.053	1.041
90	5.16	112.3	61.53	85.8	59.8	0.038	0.884
95.5	5.16	125.6	65.04	87.5	63.6	0.021	0.130
113	5.28	131.2	68.56	92.1	60.3	0.015	0.183
117.5	5.34	117.6	58.59	79.3	49.3	0.015	0.134
135.5	5.55		70.81	96.5	52.8	0.017	0.152
142.5	5.57	120.2	70.52	95.7	51.9	0.015	0.242
159	5.60	142.9	85.80	114.1	59.0	0.022	0.308
166.5	5.92	122.9	64.13	84.9	44.5	0.027	0.434
138	5.76		72.19	94.2	46.8	0.069	1.751
195.5	5.54	137.0	92.38	118.0	57.3	0.024	0.431
214.5	5.41		71.43	93.4	39.9	0.019	0.336
238	5.41	125.6	80.70	102.5	42.4	0.026	0.497
266	5.99		107.16	128.5	51.8	0.027	0.395
290.5	5.98	131.2					
312	5.89		101.61	117.6	39.4	0.015	0.122
360.5	5.83	134.1	106.82	119.5	36.4	0.039	0.413
408	5.80		120.78	125.7	37.4	0.022	0.235
470	6.18	161.7	155.21	148.2	40.0	0.048	0.157
512.5	7.02		160.82	148.5	33.8	0.039	0.637
560.5	6.77		195.80	170.1	32.4	0.015	0.107
636.5	7.31	197.6	215.16	178.1	32.2	0.118	1.814
657.5	7.16		203.94	155.2	29.8	0.070	1.162

Table III-8. Solution composition data from the batch reactor experiment (100°C, distilled water.

TIME hours	pH	SiO_2 ppm	Na ppm	K ppm	Ca ppm	Mn ppm	Fe ppm
0	7.00	0.0	0.00	0.0	0.0	0.000	0.000
24	6.48	44.7	10.85	34.2	50.5	0.277	6.035
48	5.78	49.9	10.34	27.2	59.8	0.273	9.681
96	6.82	62.7	15.18	35.2	74.3	0.735	31.44
220	7.38						
288	8.03	61.7	18.50	28.0	73.7	1.453	66.24
672	5.76	53.0	17.09	42.1	70.4	0.988	49.67
1200	5.75	44.7	15.33	36.8	79.1	0.604	29.82

APPENDIX IV

GRAPHS THAT COMPARE THE COMPOSITIONS OF SOLUTIONS EXTRACTED FROM RUNS 4 THROUGH 10

RUN #4

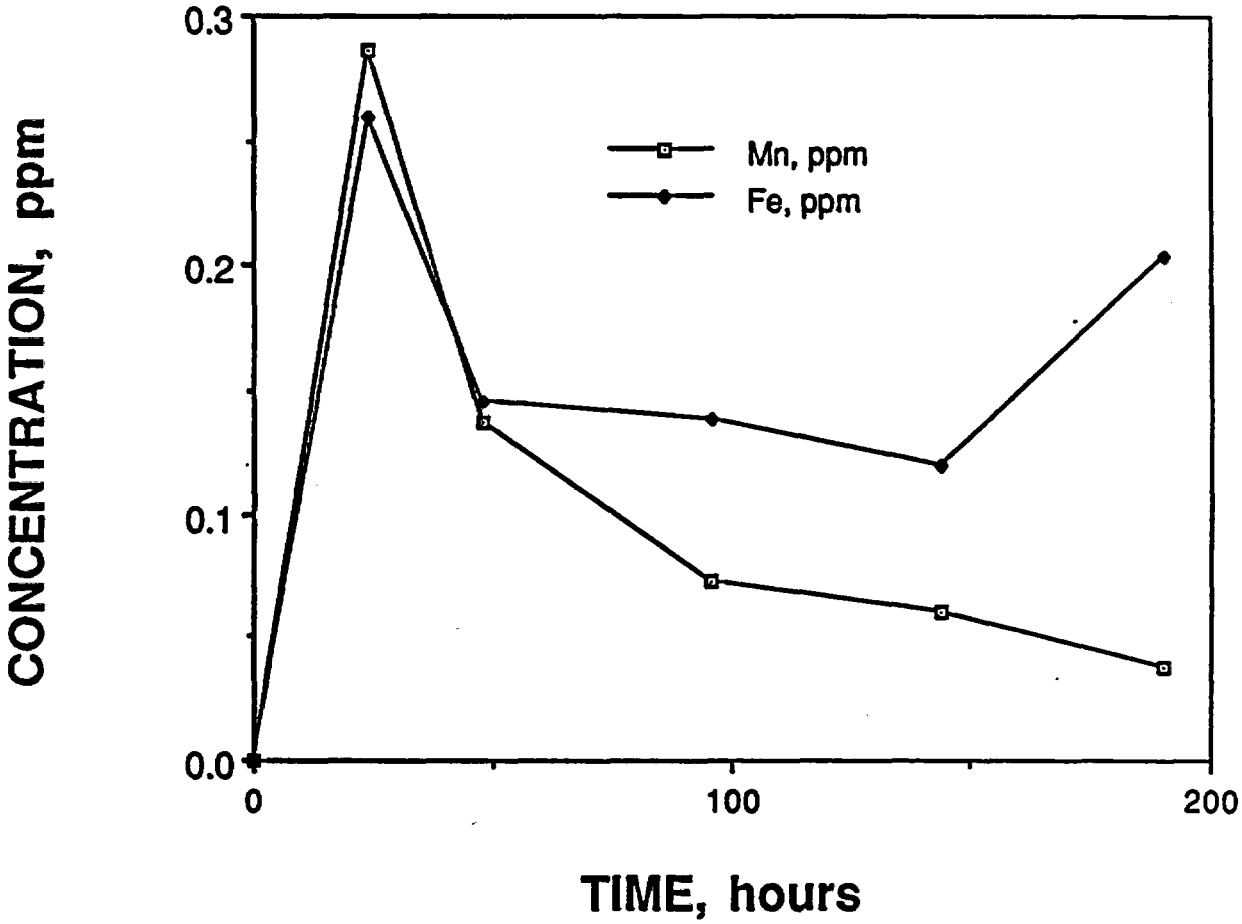
0.3
0.2
0.1
0.0
0
100
200
Mn, ppm
Fe, ppm
CONCENTRATION, ppm
TIME, hours

RUN #4

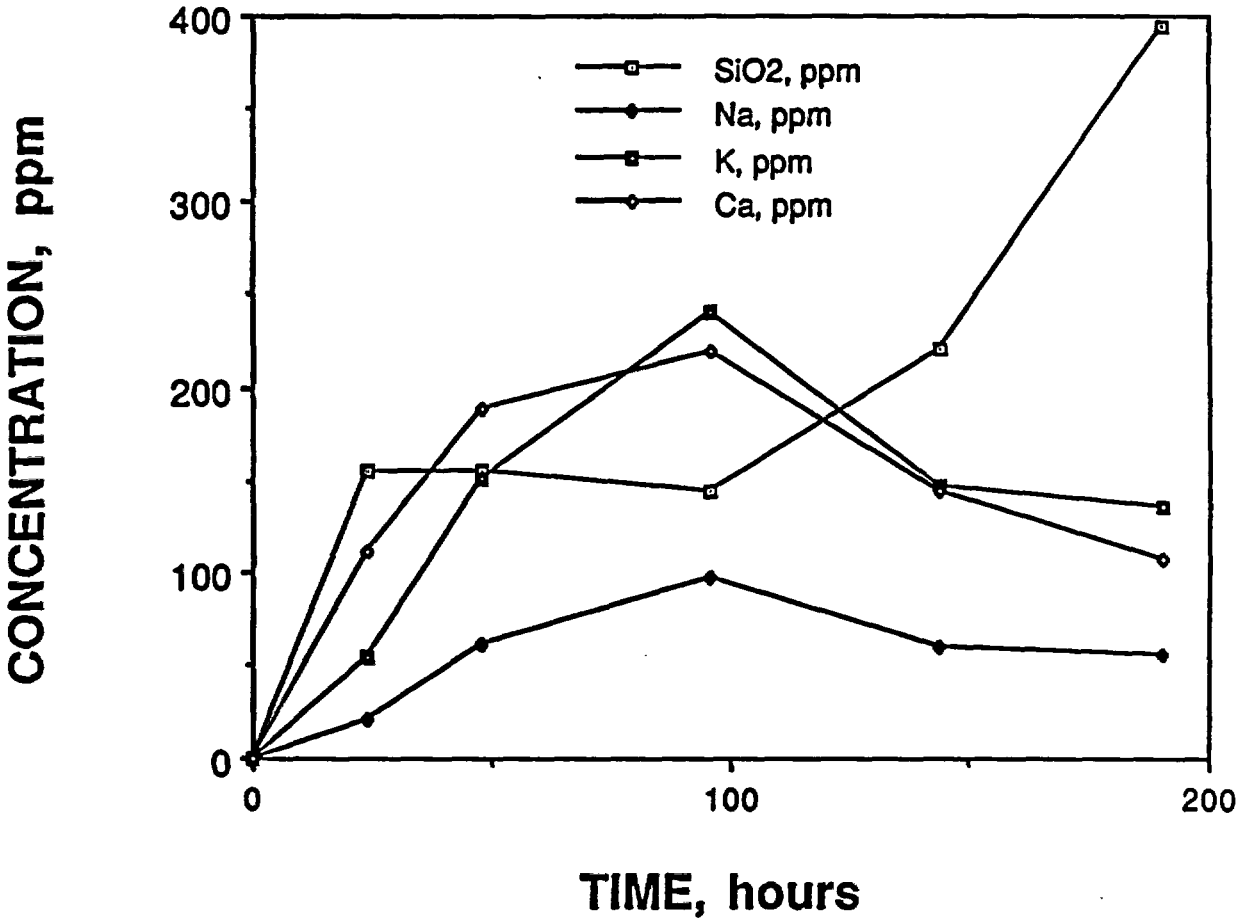
400
300
200
100
0
0
100
200
SiO2, ppm
Na, ppm
K, ppm
Ca, ppm
CONCENTRATION, ppm
TIME, hours

RUN #4

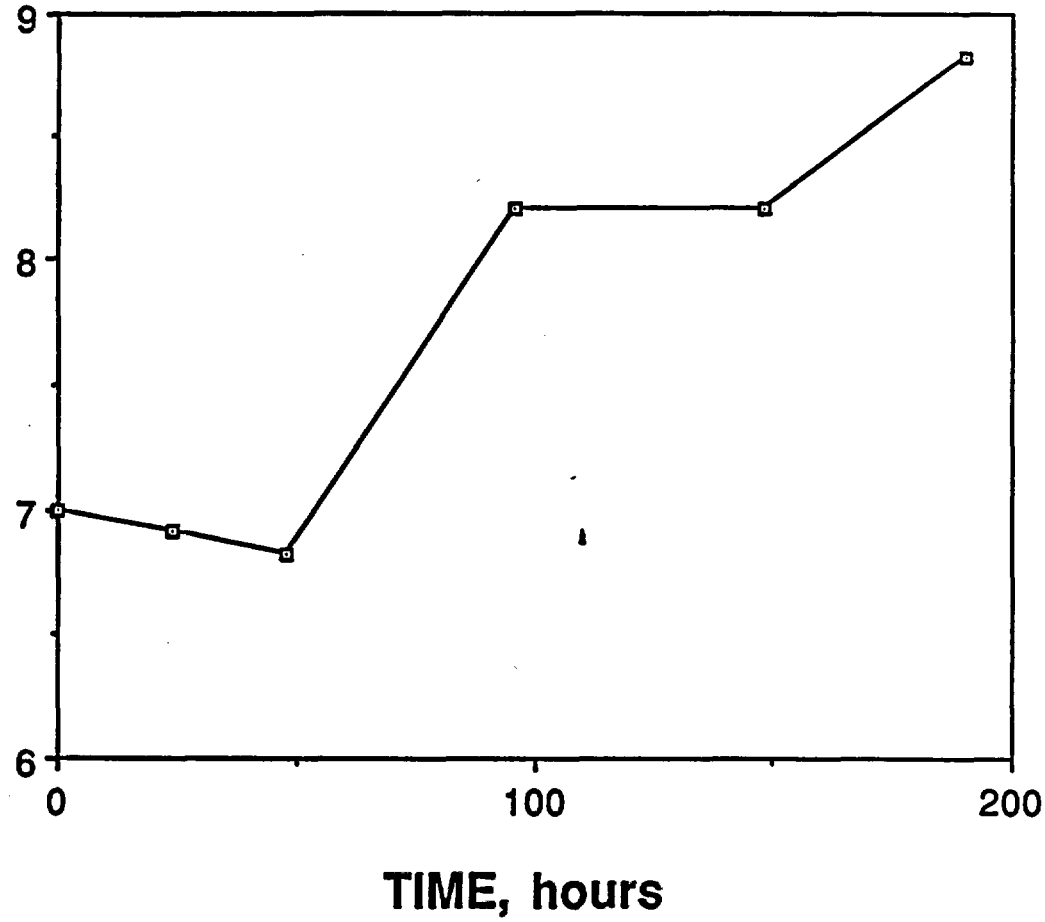

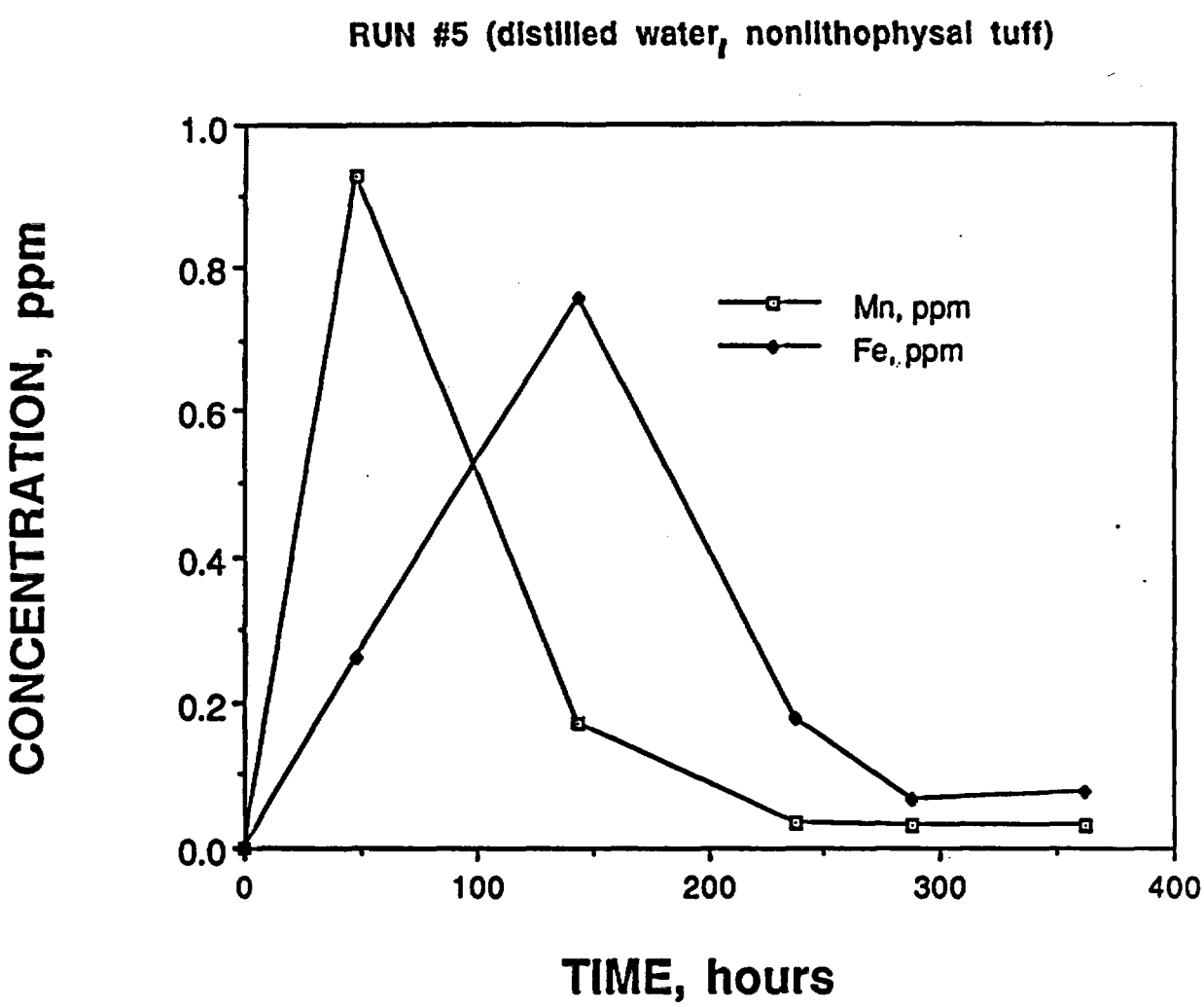
RUN #5 (distilled water, nonlithophysal tuff)
CONCENTRATION, ppm
1.0
0.8
0.6
0.4
0.2
0.0
0
100
200
300
400
TIME, hours
Mn, ppm
Fe, ppm

RUN #5 (distilled water, nonlithophysal tuff)

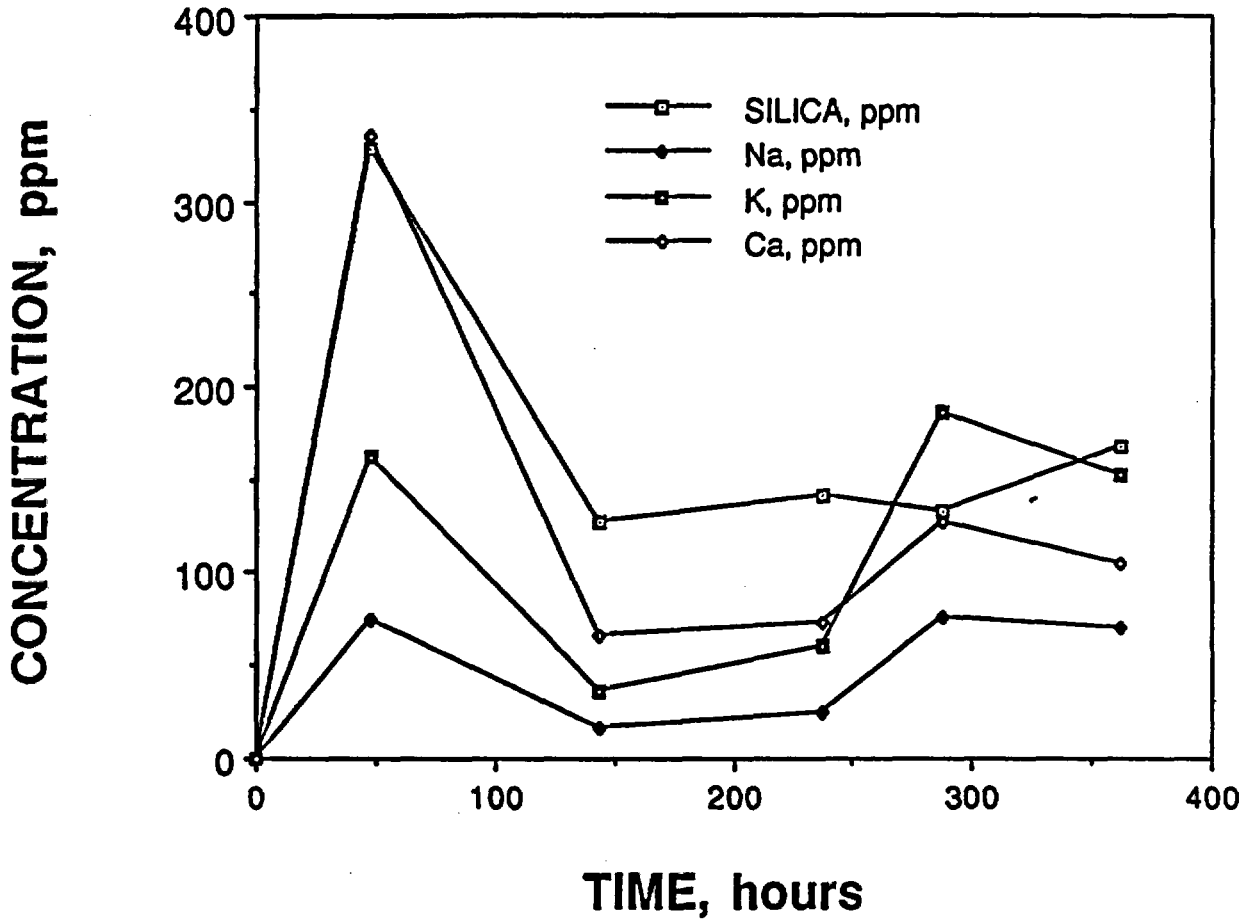

RUN #5 (distilled water, nonlithophysal tuff)

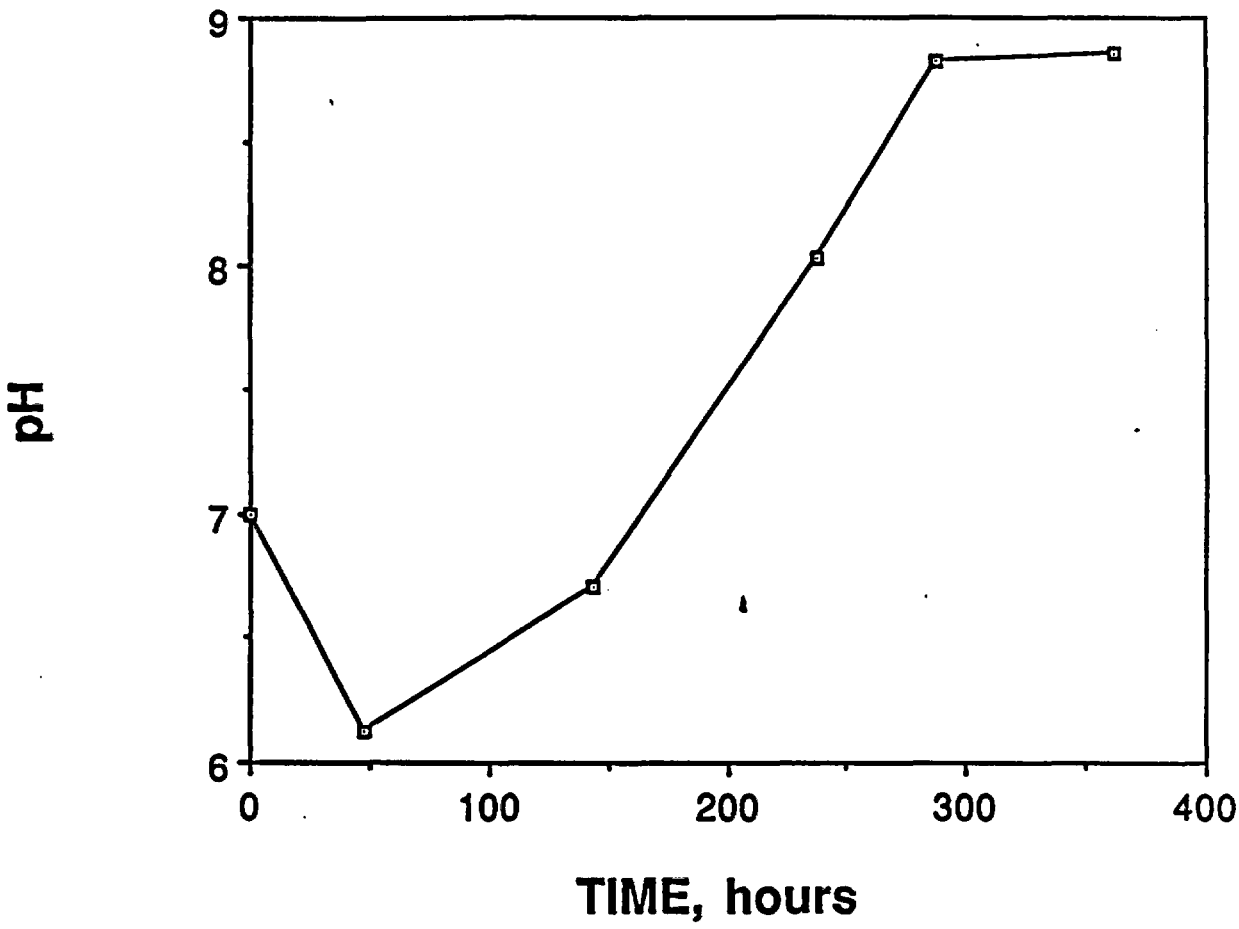

RUN #6 (0.12 m NaCl, nonlithophysal tuff)

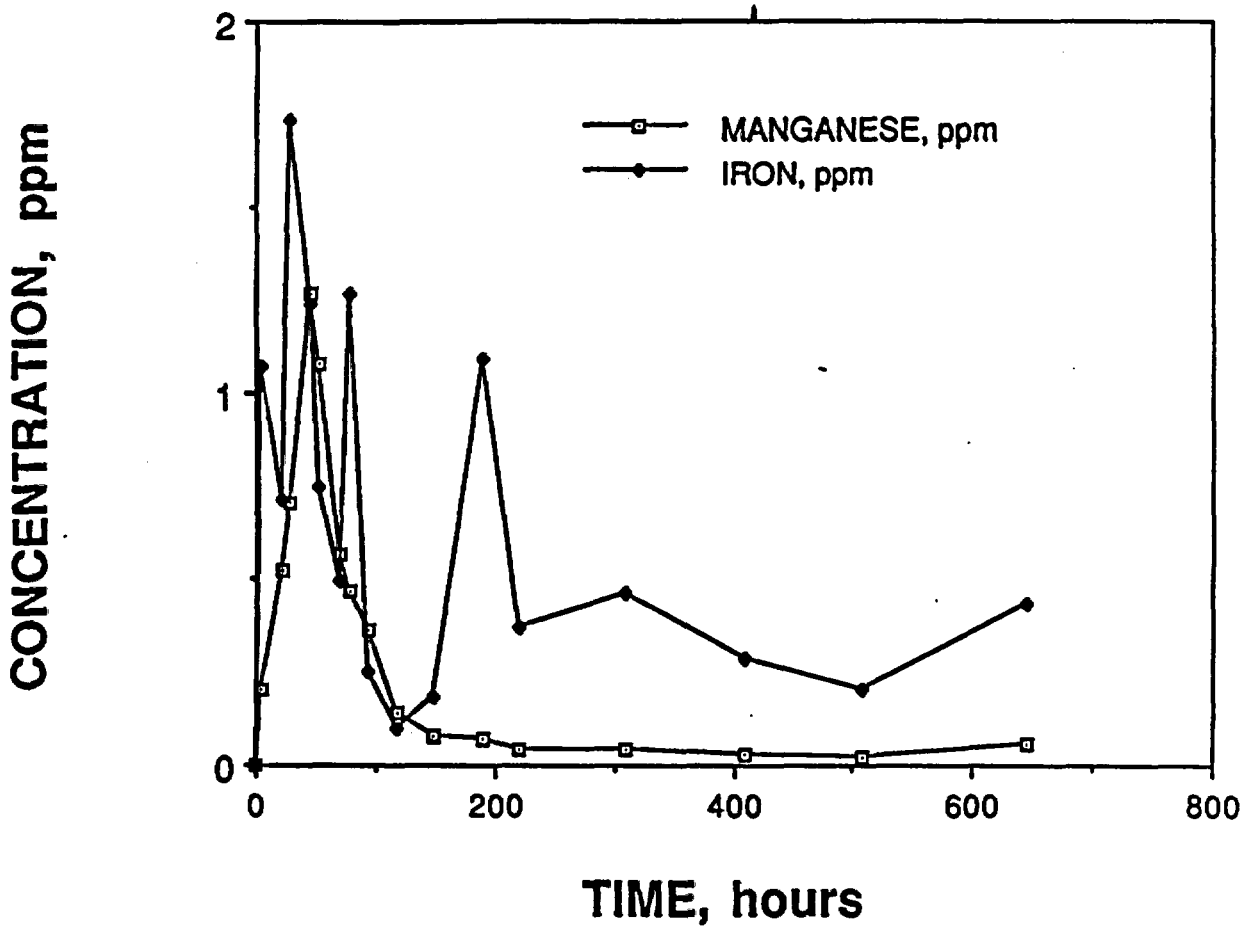

RUN #6 (0.12 ppm NaCl, nonlithophysal tuff)

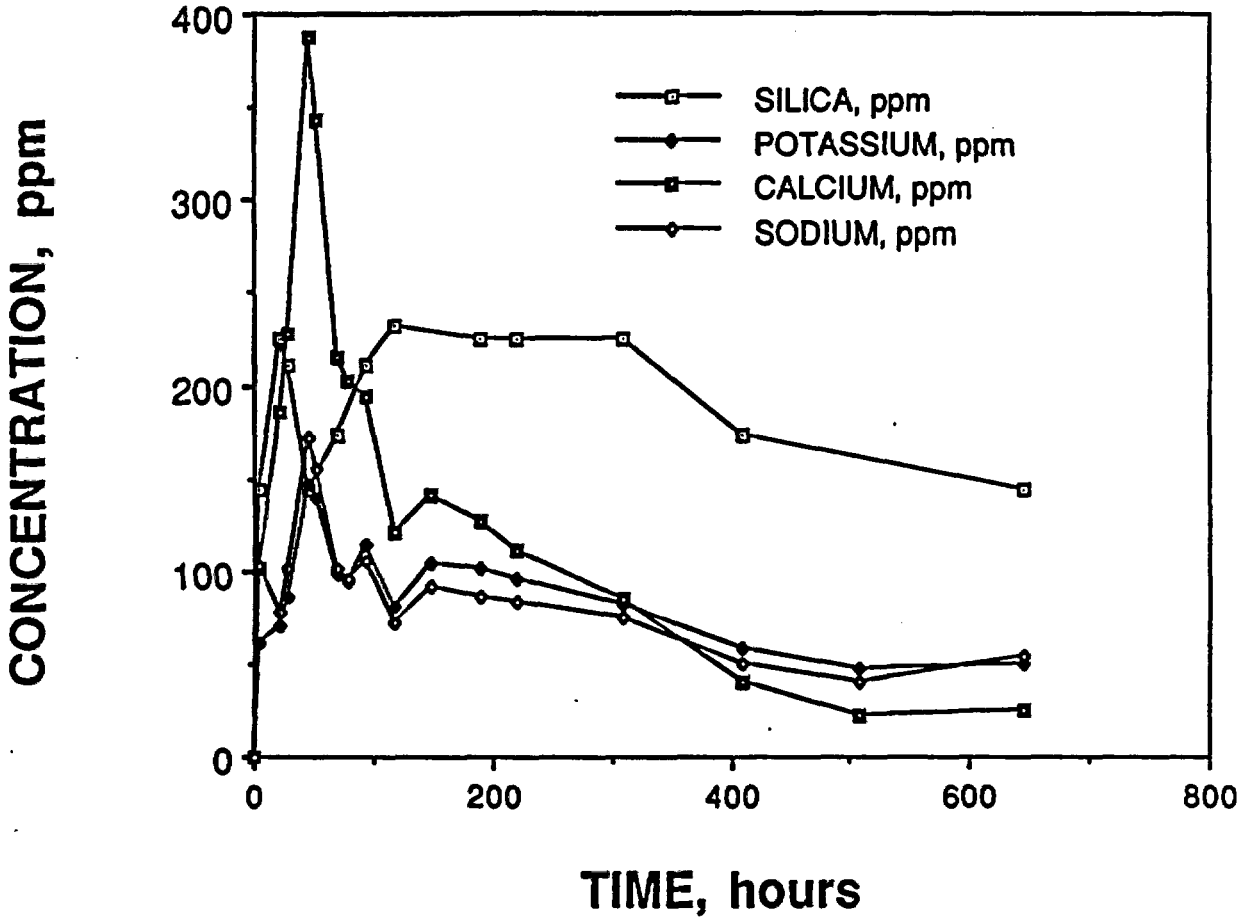

RUN #6 (0.12 m NaCl, nonlithophysal tuff)

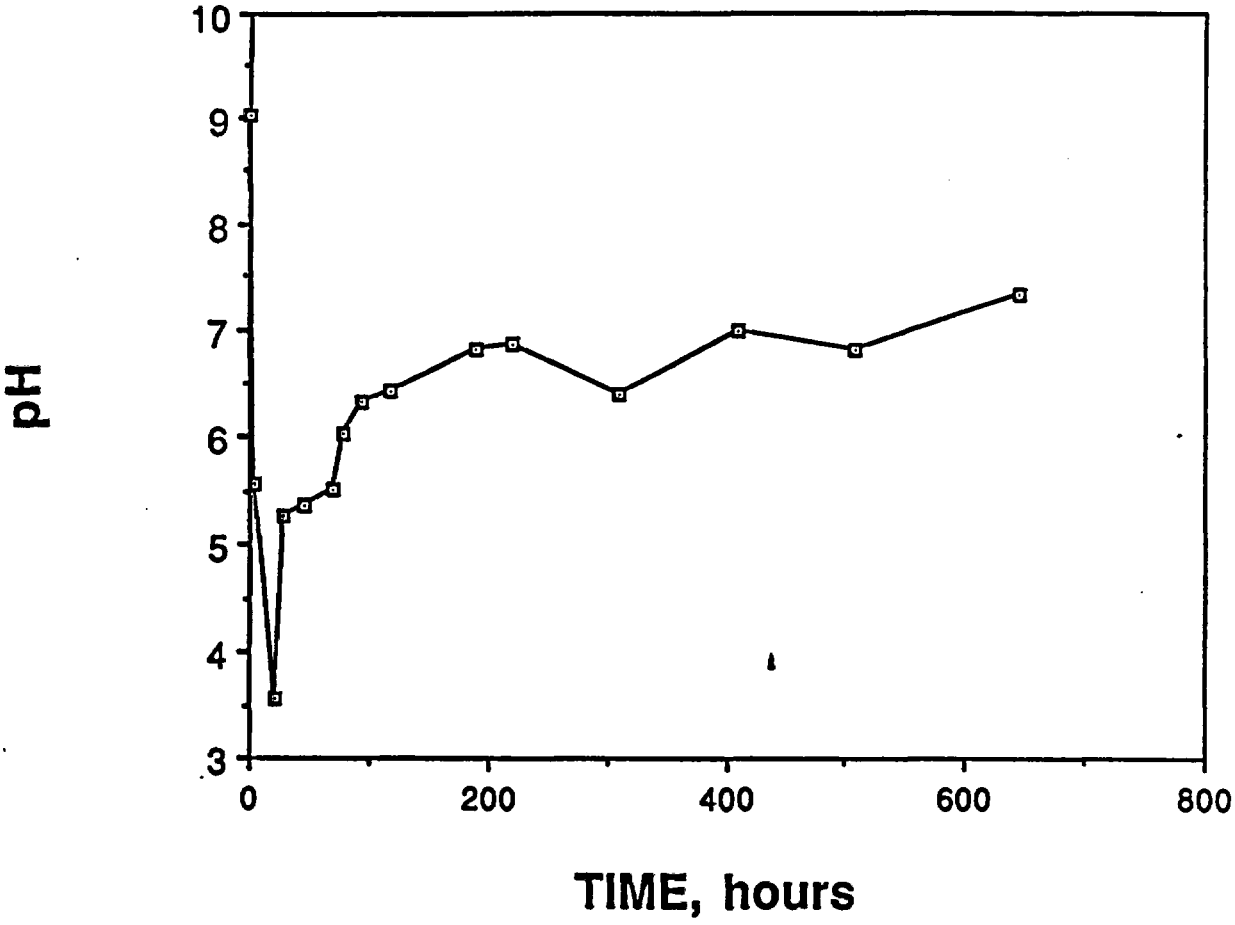

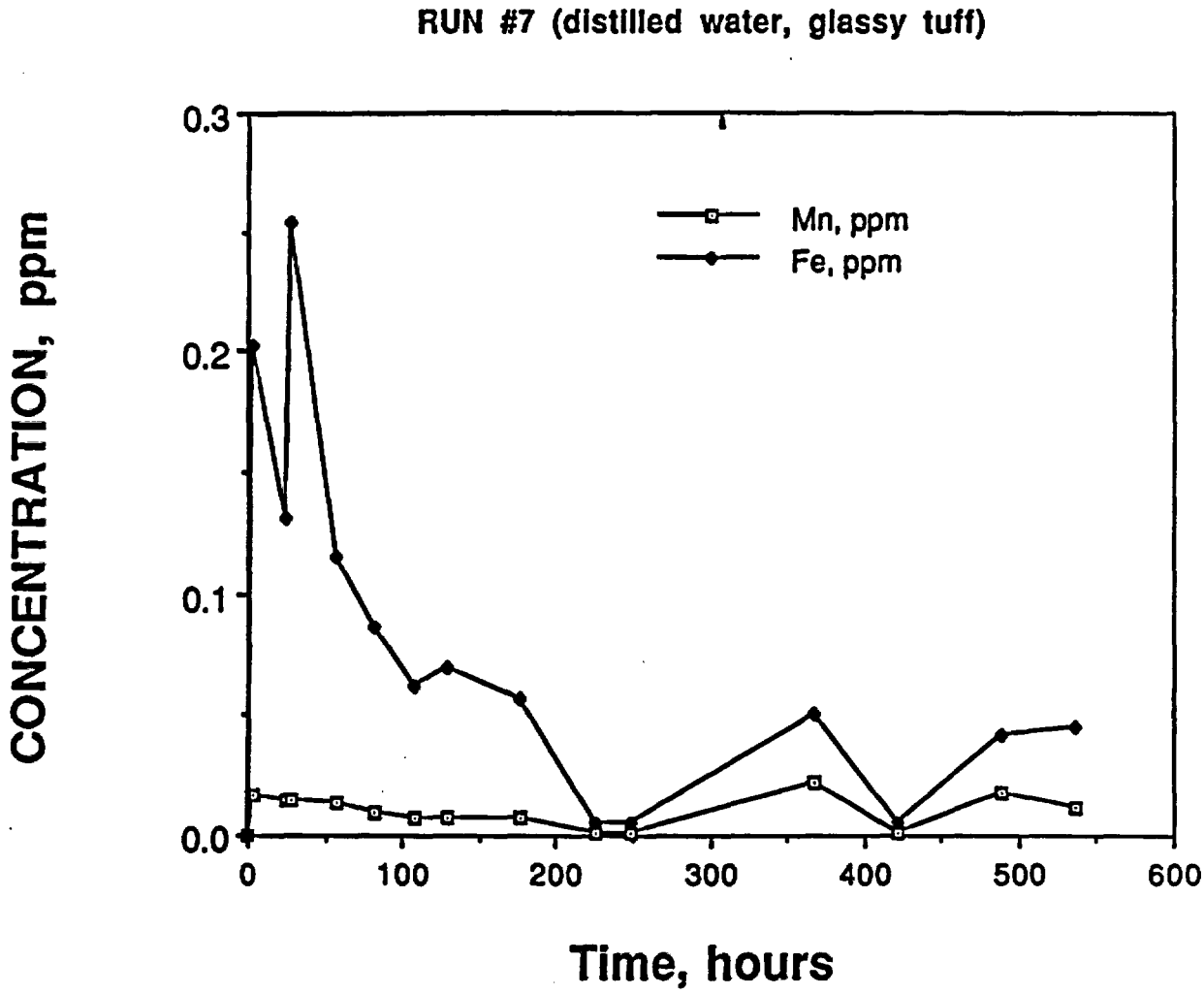
RUN #7 (distilled water, glassy tuff)
CONCENTRATION, ppm
0.3
0.2
0.1
0.0
Mn, ppm
Fe, ppm
0
100
200
300
400
500
600
Time, hours

RUN #7 (distilled water, glassy tuff)

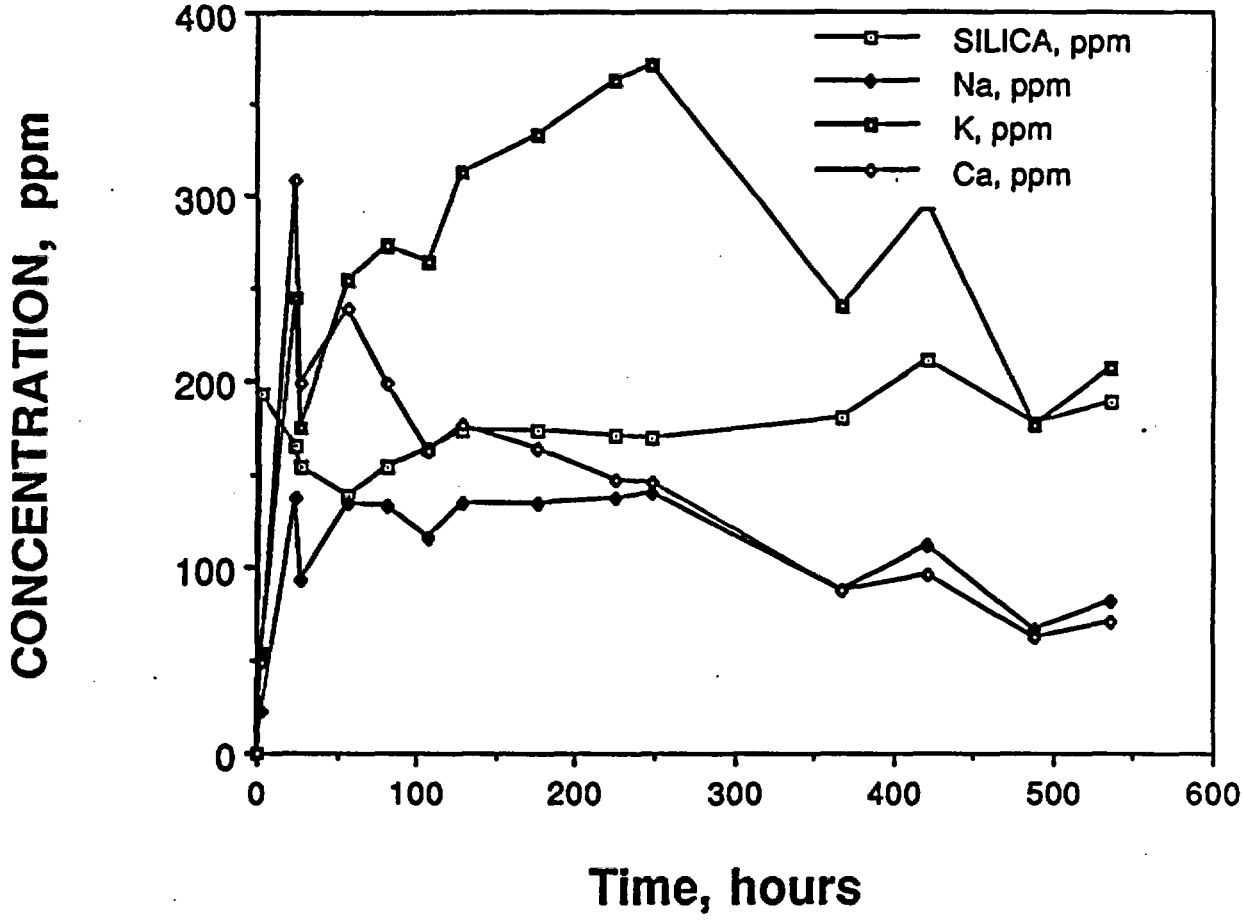

RUN #7 (distilled water, glassy tuff)

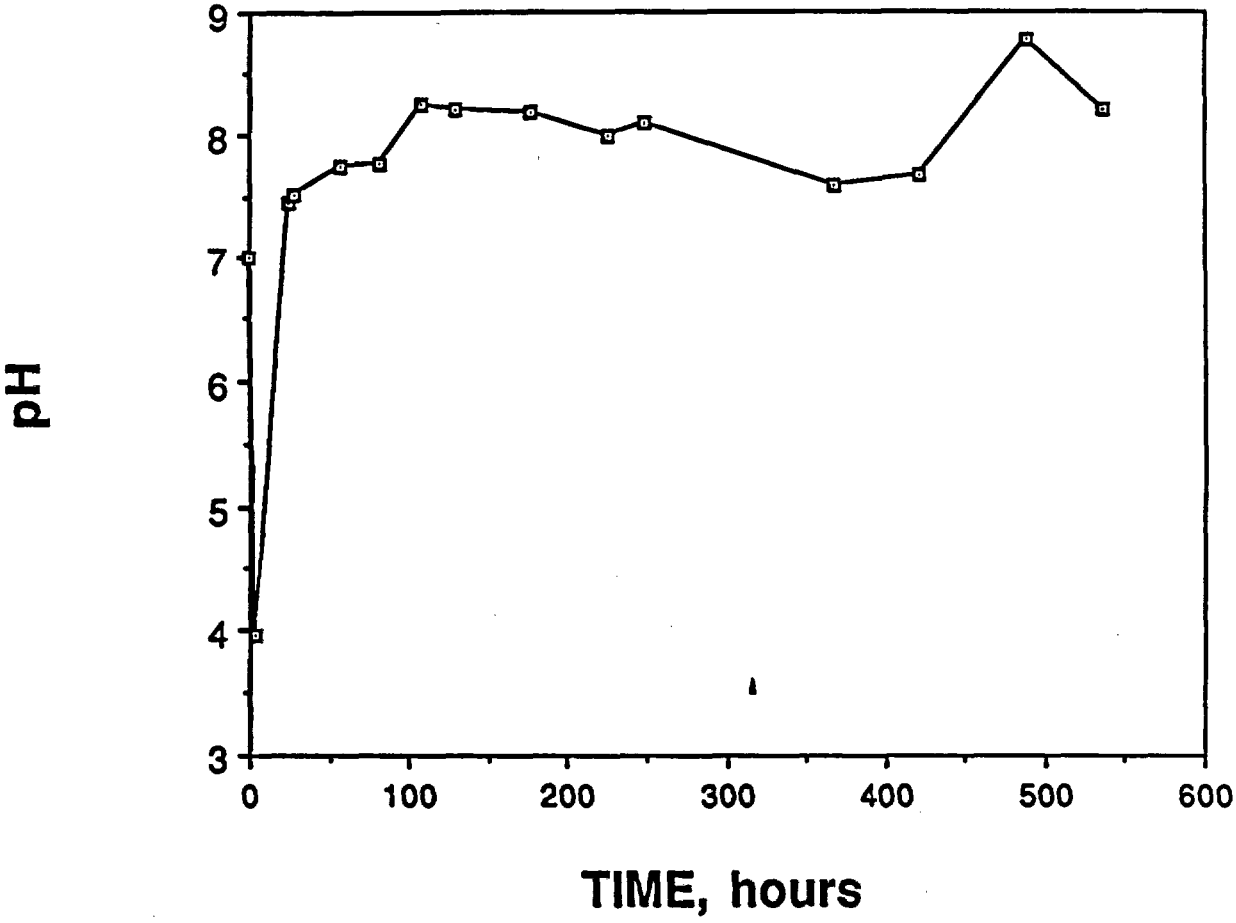

RUN #8 (0.12 ppm NaCl, glassy tuff)

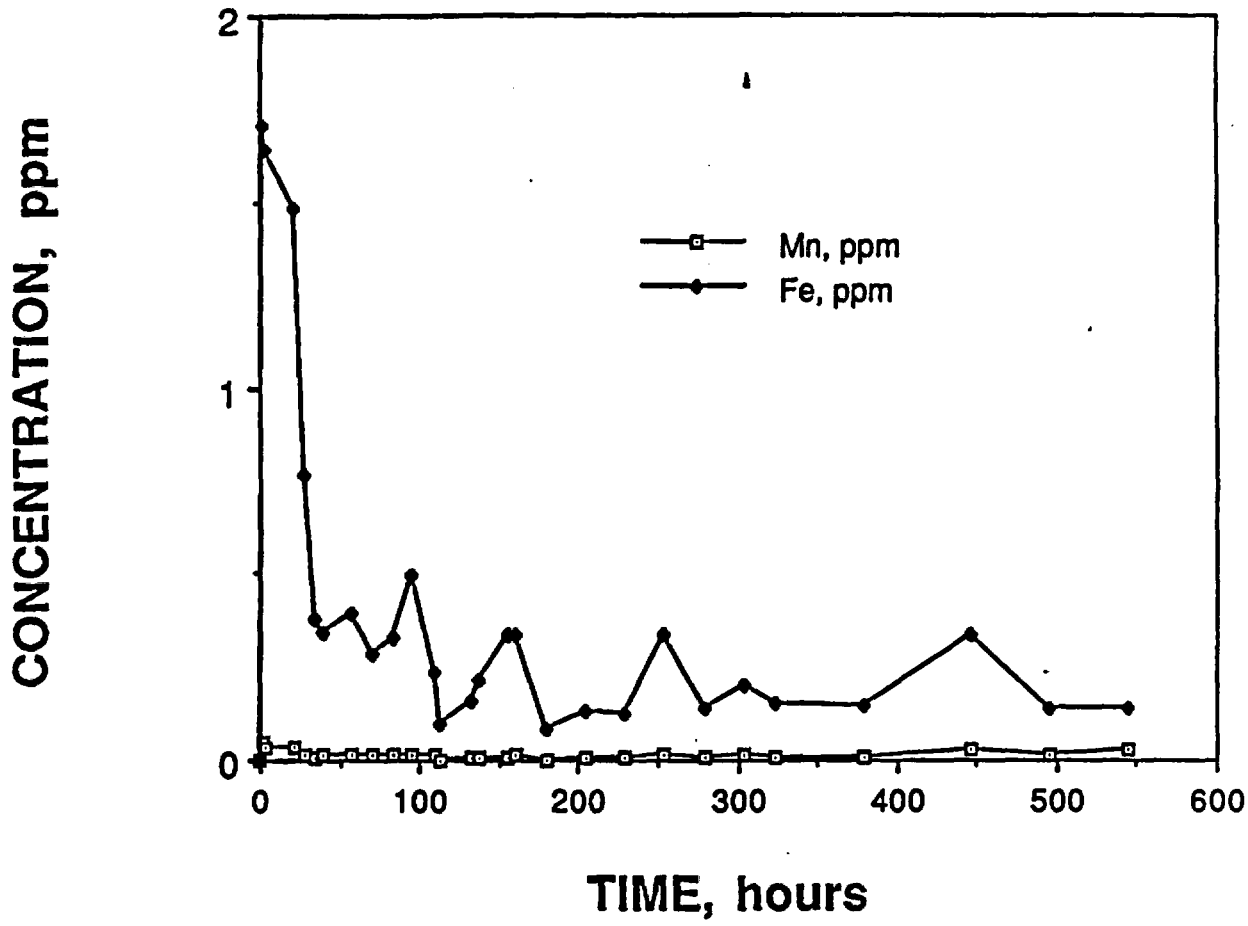

RUN #8 (0.12 ppm NaCl, glassy tuff)

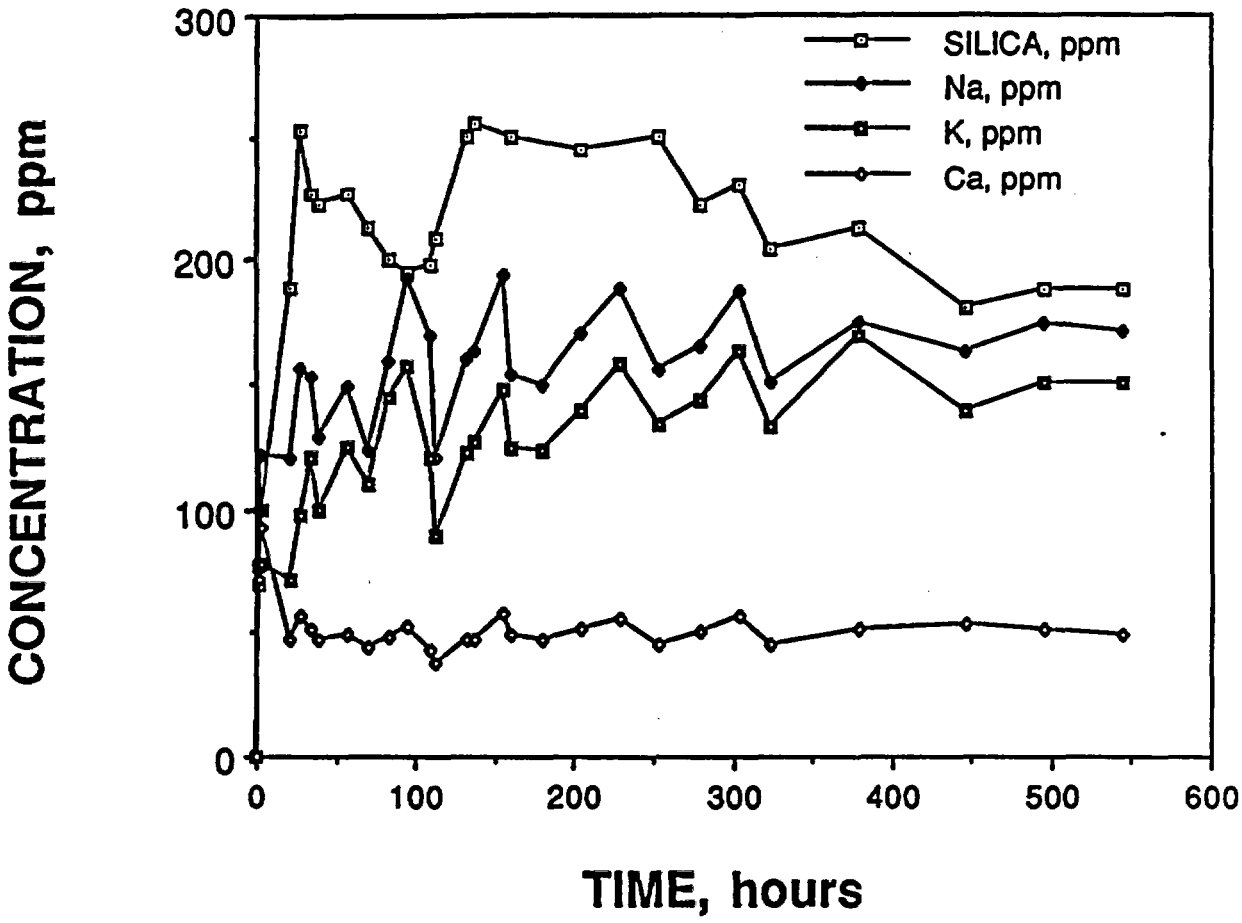

RUN #8 (0.12 ppm NaCl, glassy tuff)

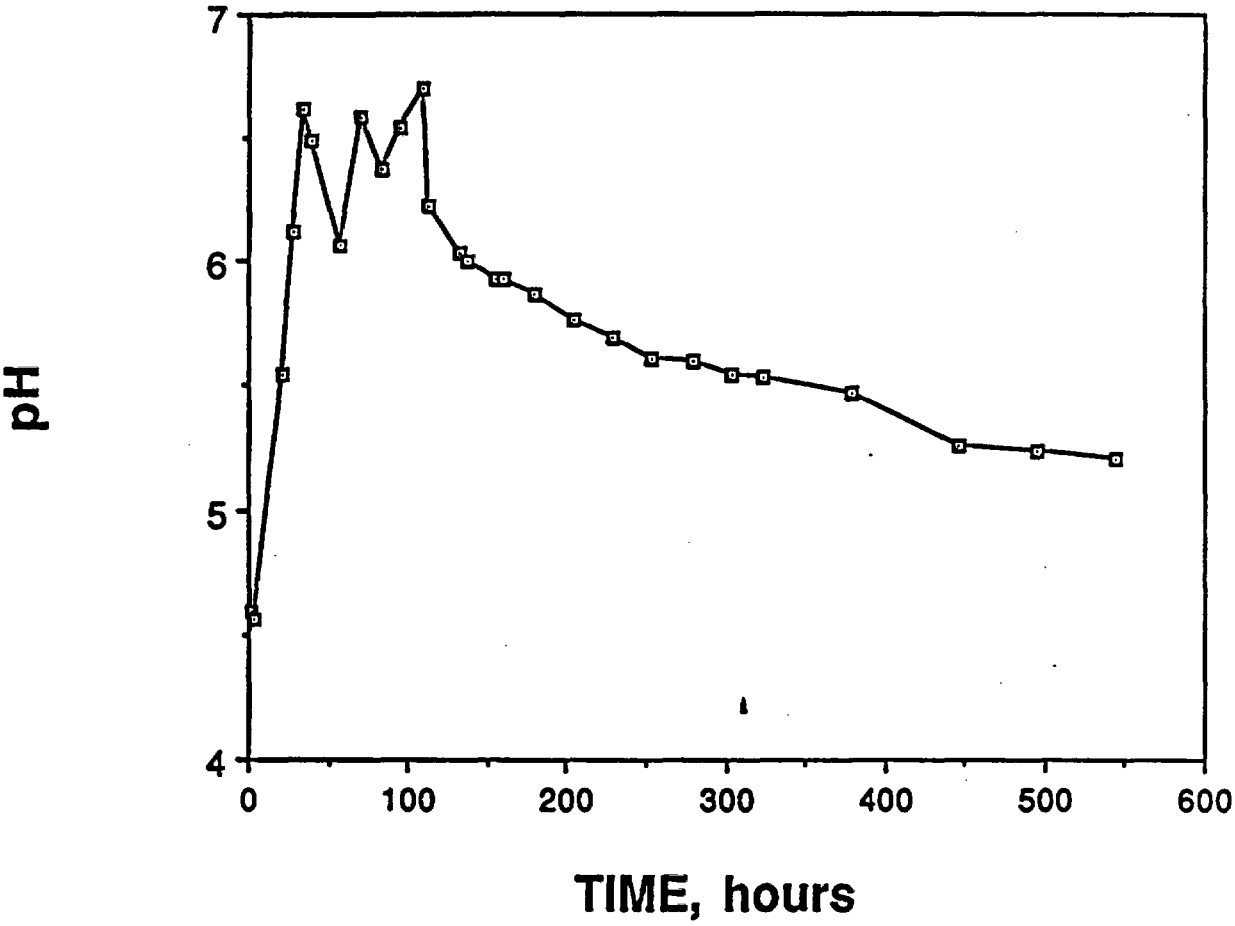

RUN #9 (syn. J13 water, glassy tuff)

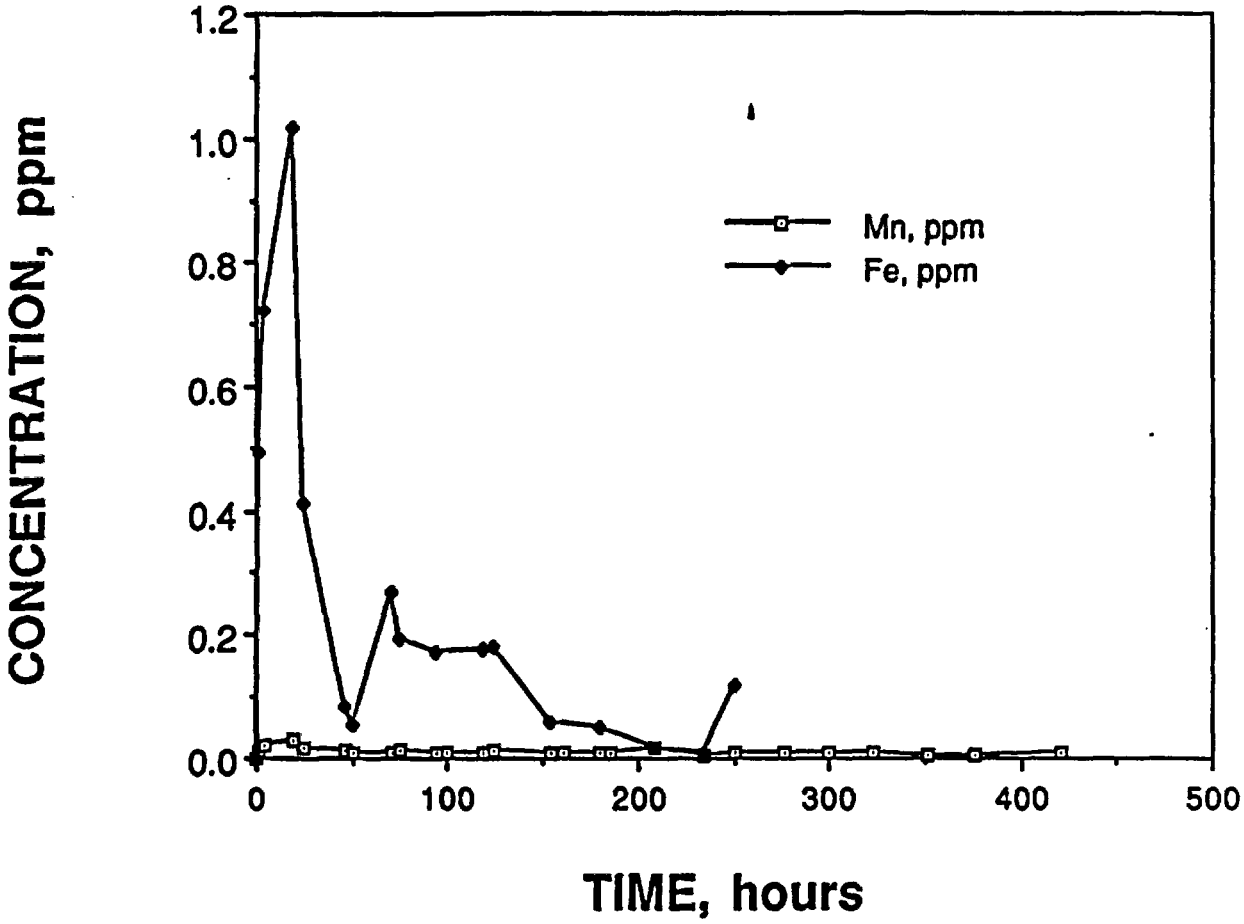

RUN #9 (syn. J13 water, glassy tuff)

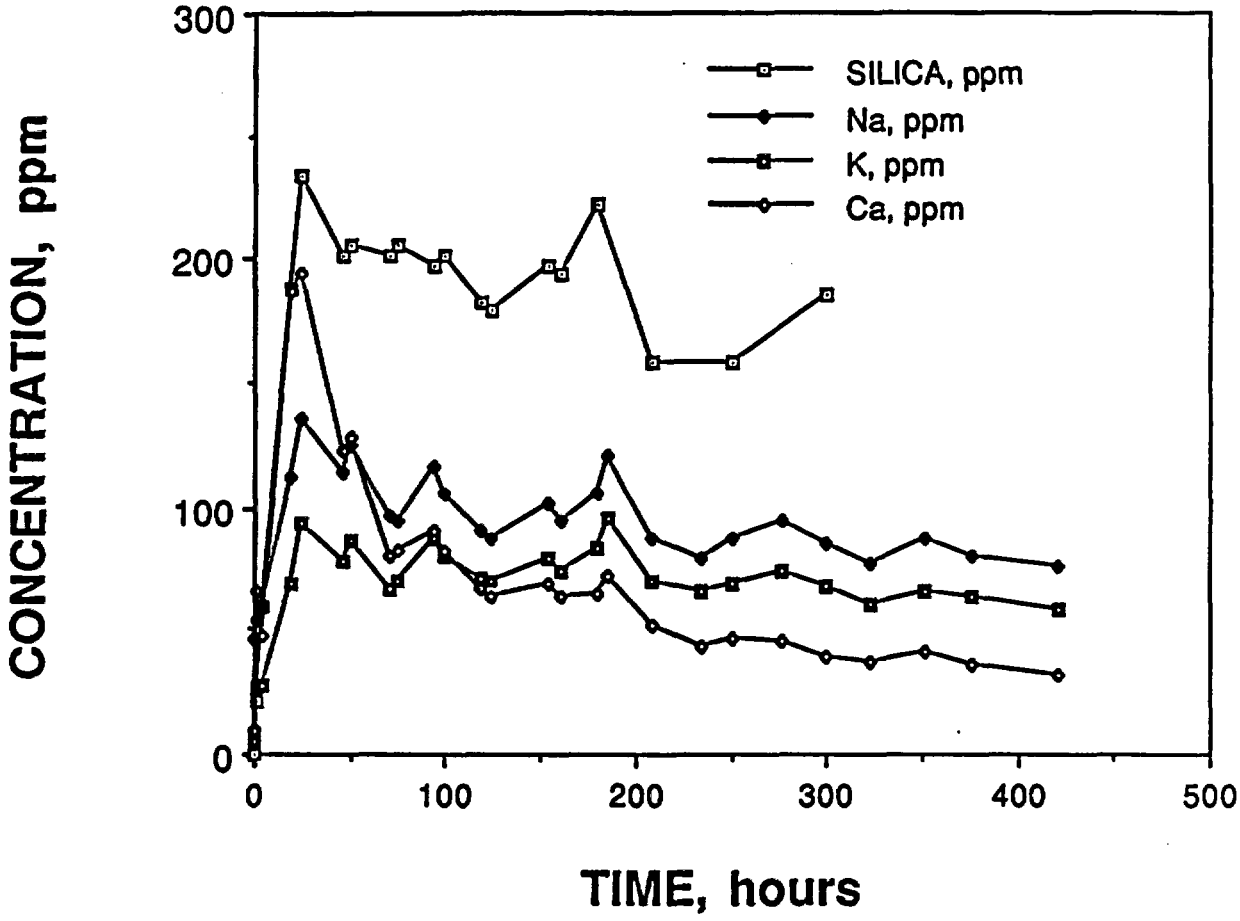

RUN #9 (syn. J13 water, glassy tuff)

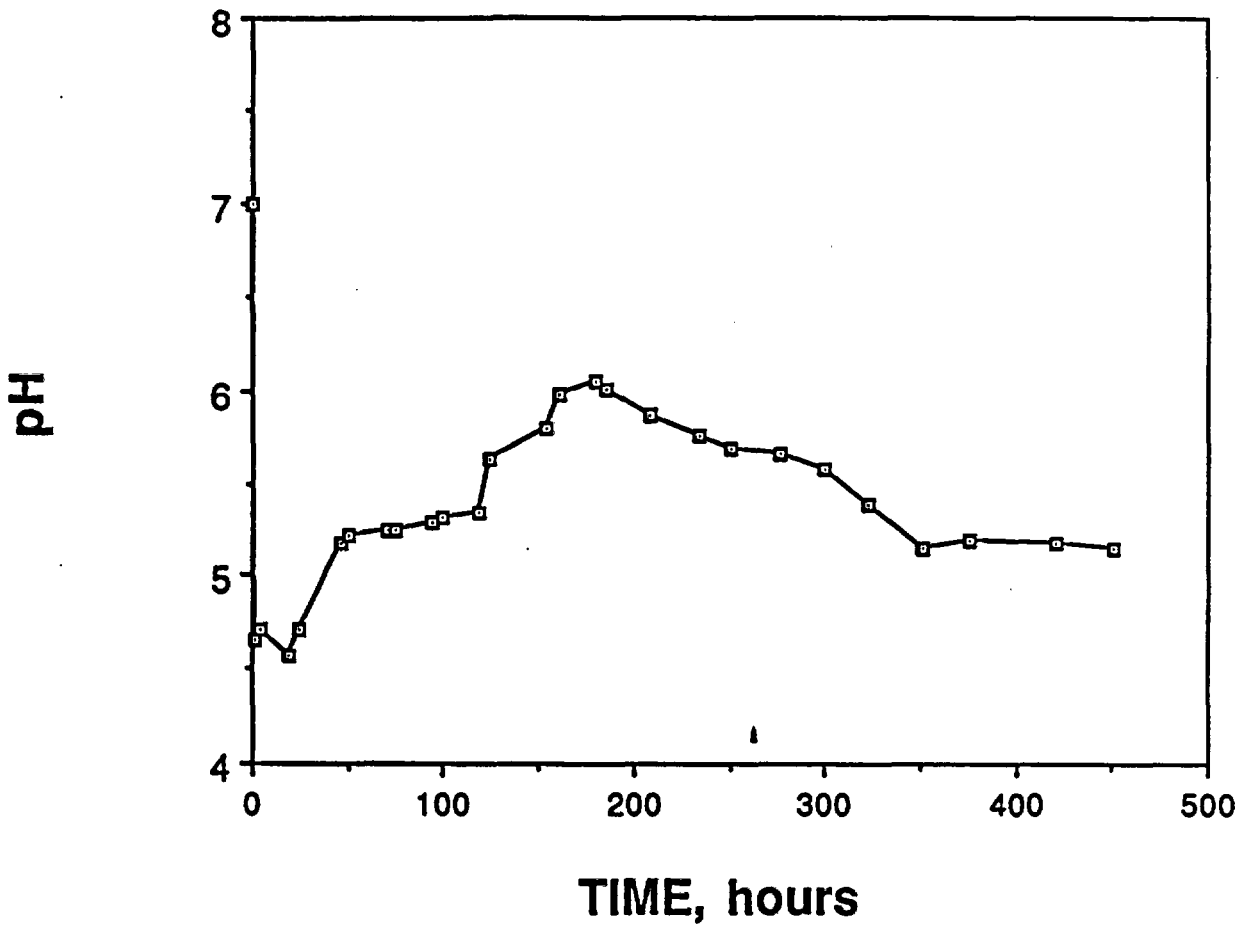

RUN #10 (syn. J13 water, nonlithophysal tuff)

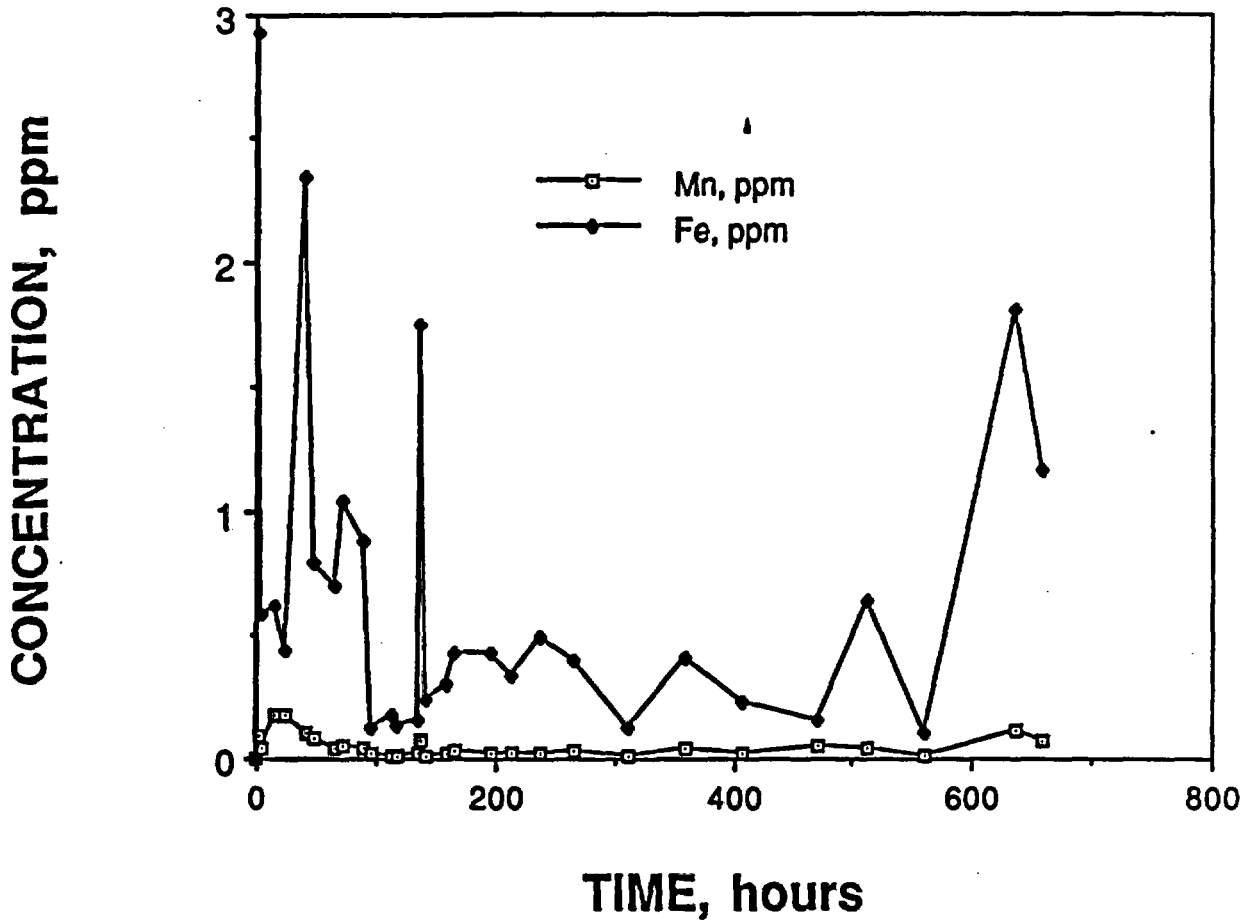

RUN #10 (syn. J13 water, nonlithophysal tuff)

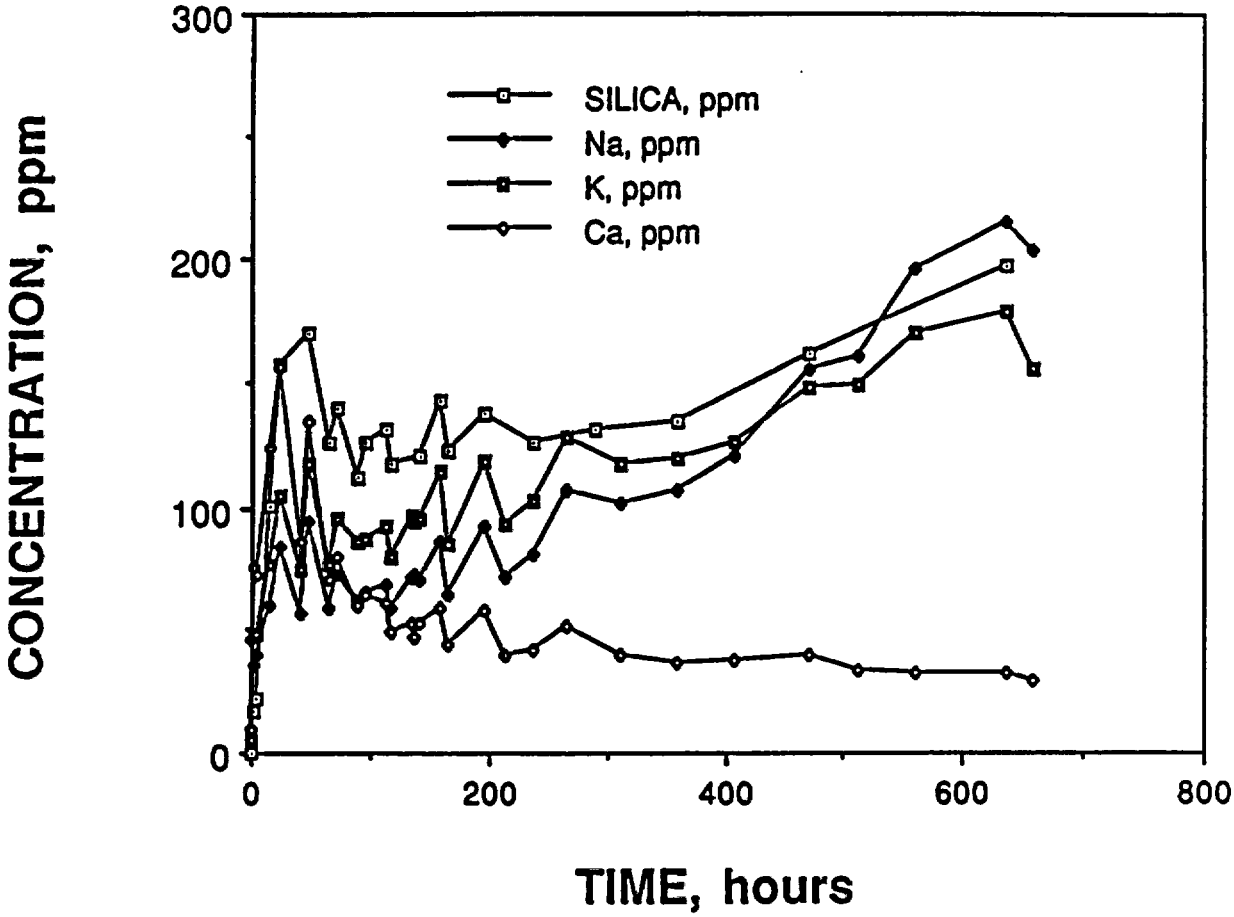

RUN #10 (syn. J13 water, nonlithophysal tuff)

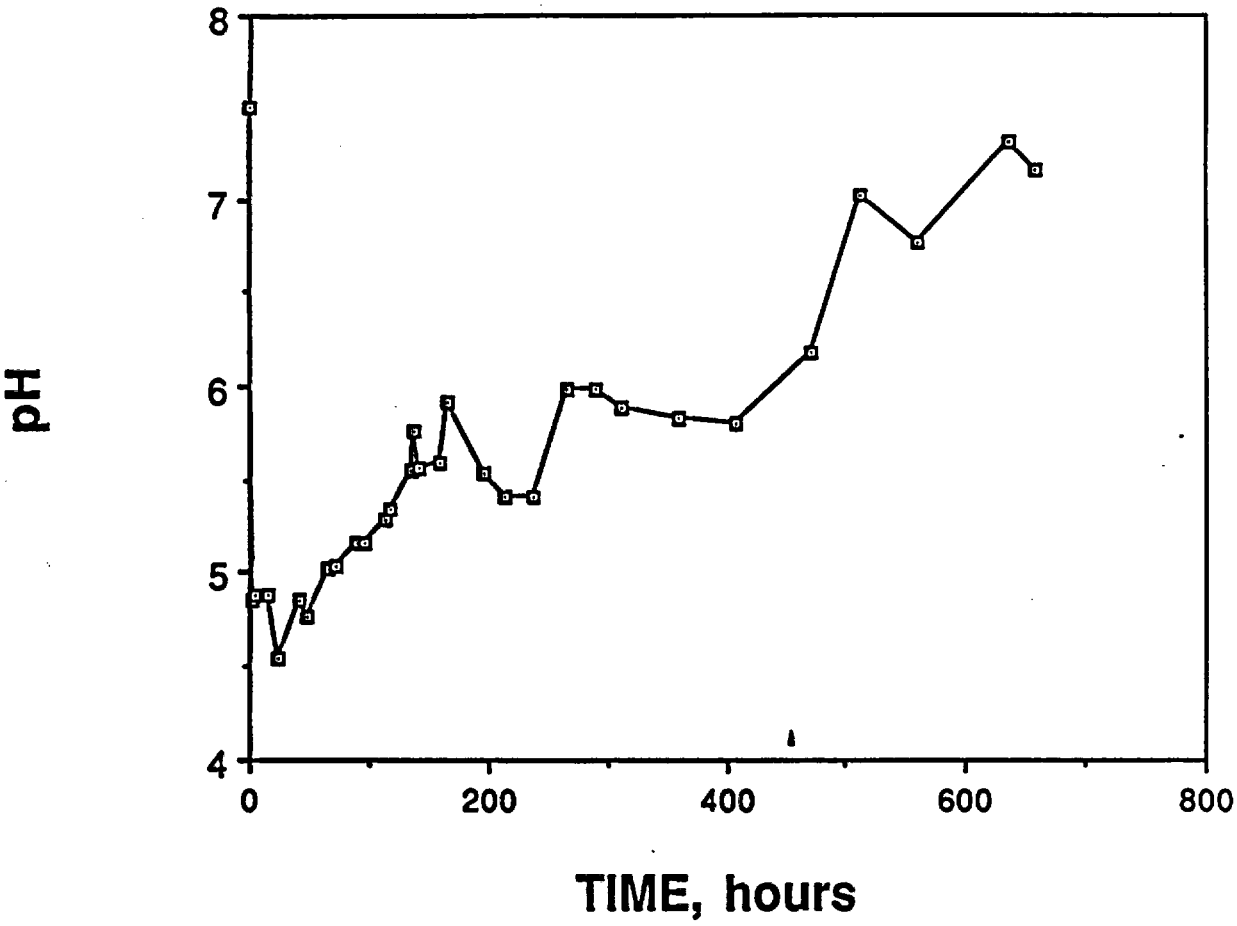

Fe (ALL RUNS)

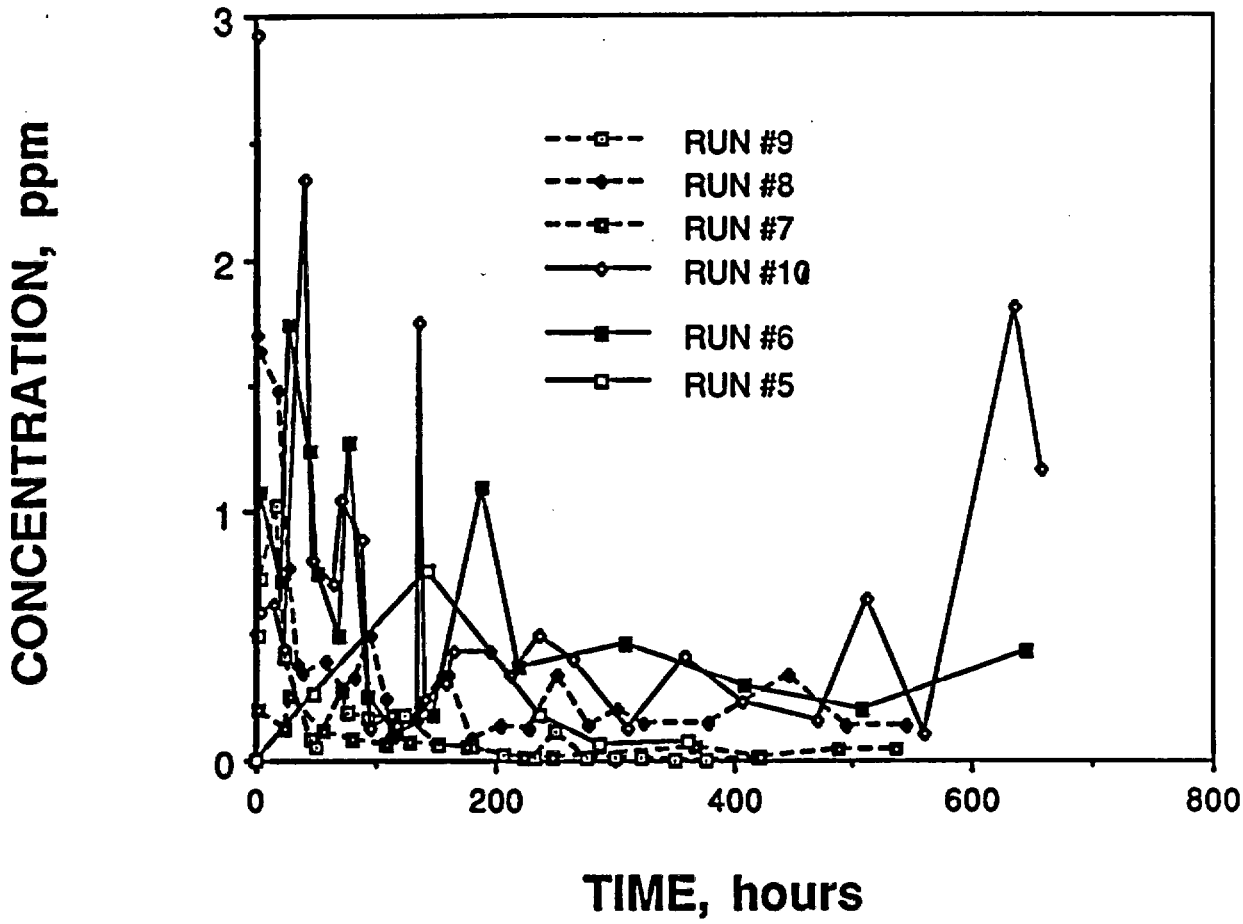
CONCENTRATION, ppm
3
2
1
0
0
200
400
600
800
RUN #9
RUN #8
RUN #7
RUN #10
RUN #6
RUN #5
TIME, hours

Mn (ALL RUNS)

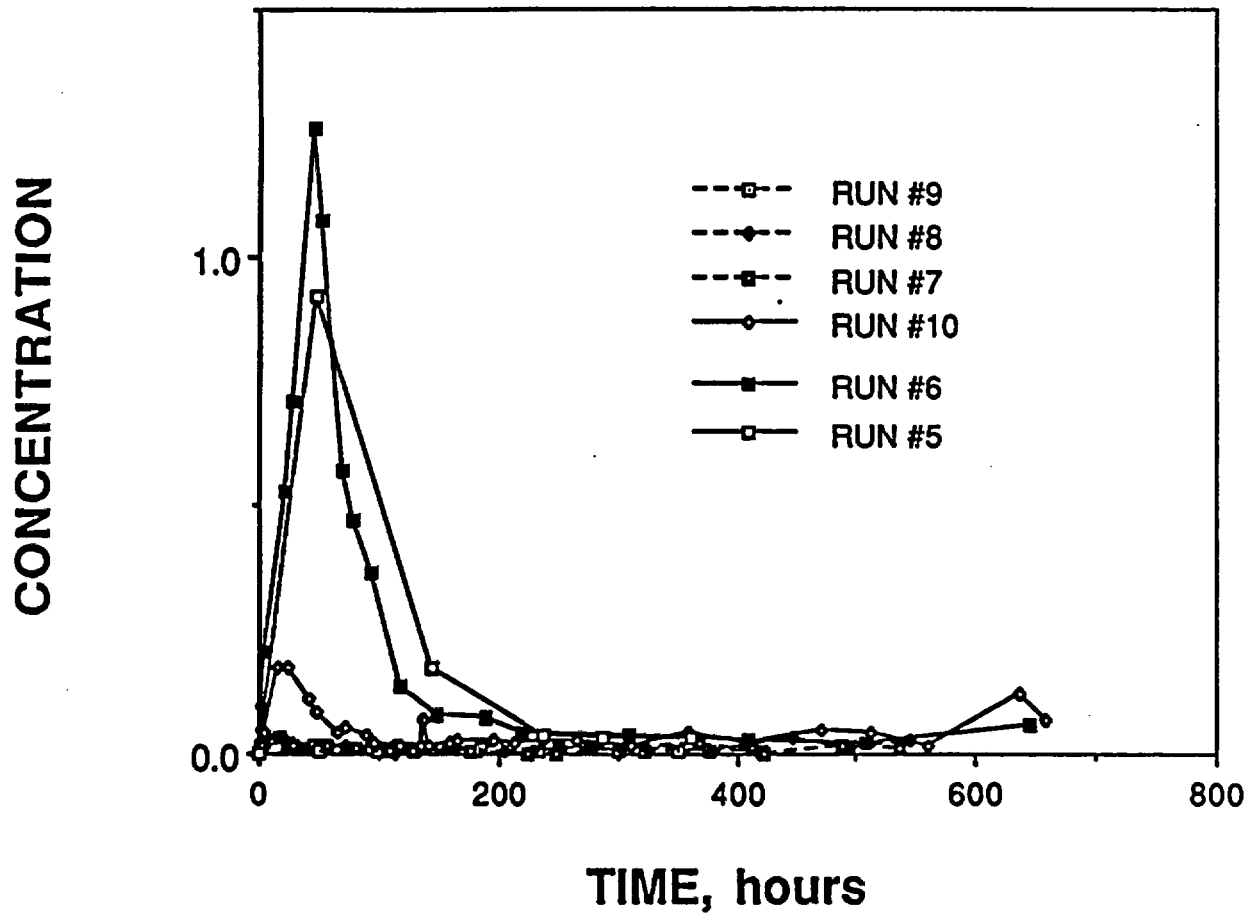
CONCENTRATION
1.0
0.0
0
200
400
600
800
RUN #9
RUN #8
RUN #7
RUN #10
RUN #6
RUN #5
TIME, hours

Na (ALL RUNS)

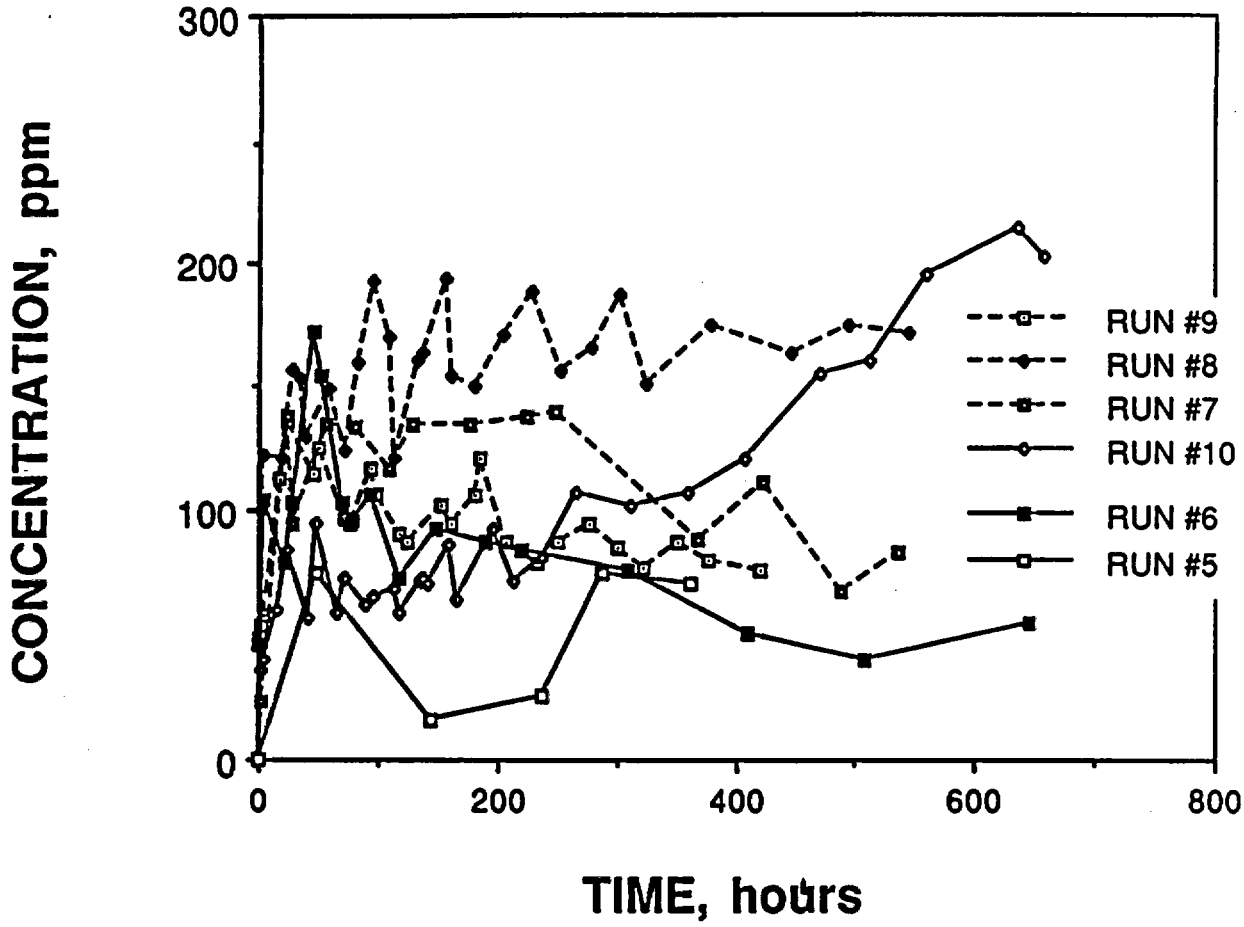
CONCENTRATION, ppm
300
200
100
0
0
200
400
600
800
TIME, hours
RUN #9
RUN #8
RUN #7
RUN #10
RUN #6
RUN #5

Ca (ALL RUNS)

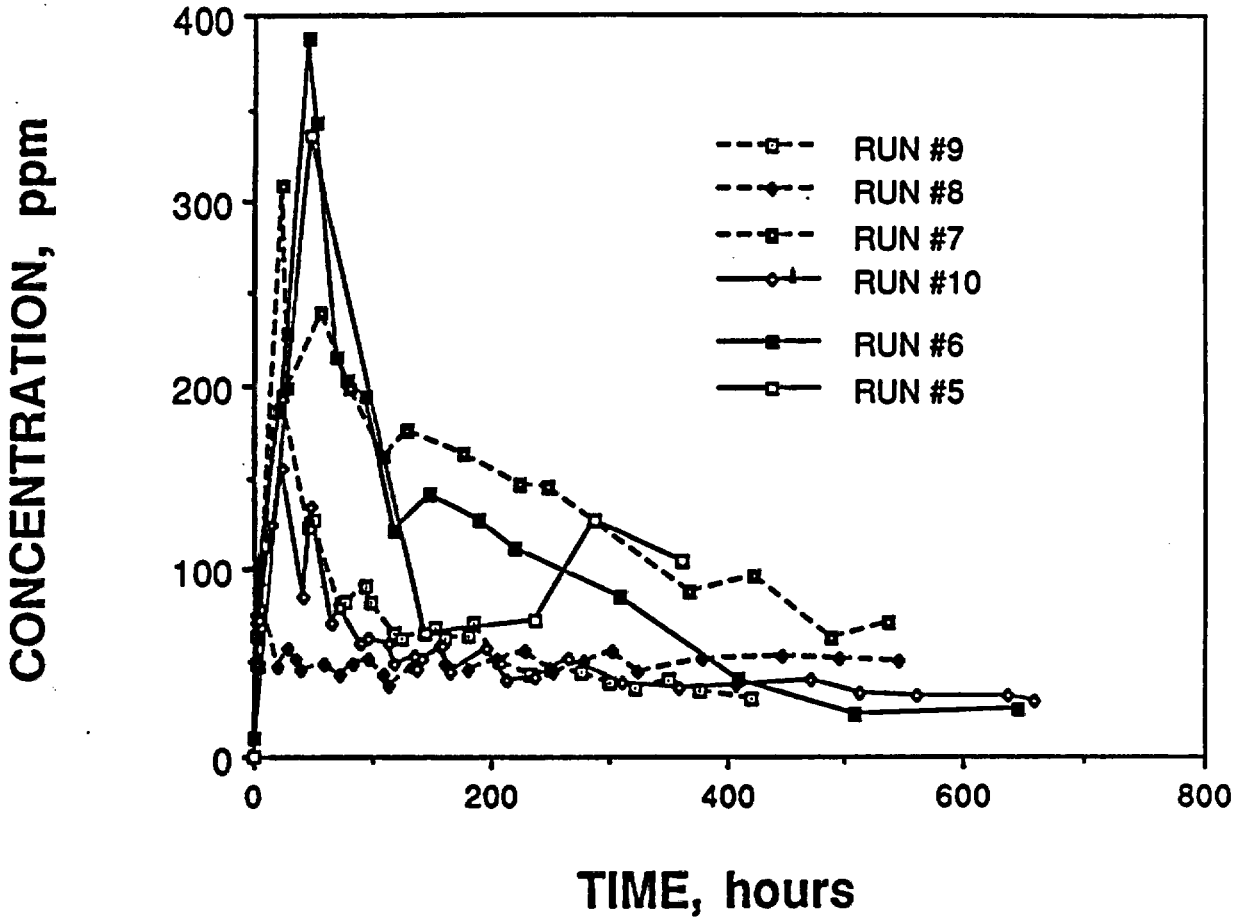
CONCENTRATION, ppm
400
300
200
100
0
0
200
400
600
800
TIME, hours
RUN #9
RUN #8
RUN #7
RUN #10
RUN #6
RUN #5

K (ALL RUNS)

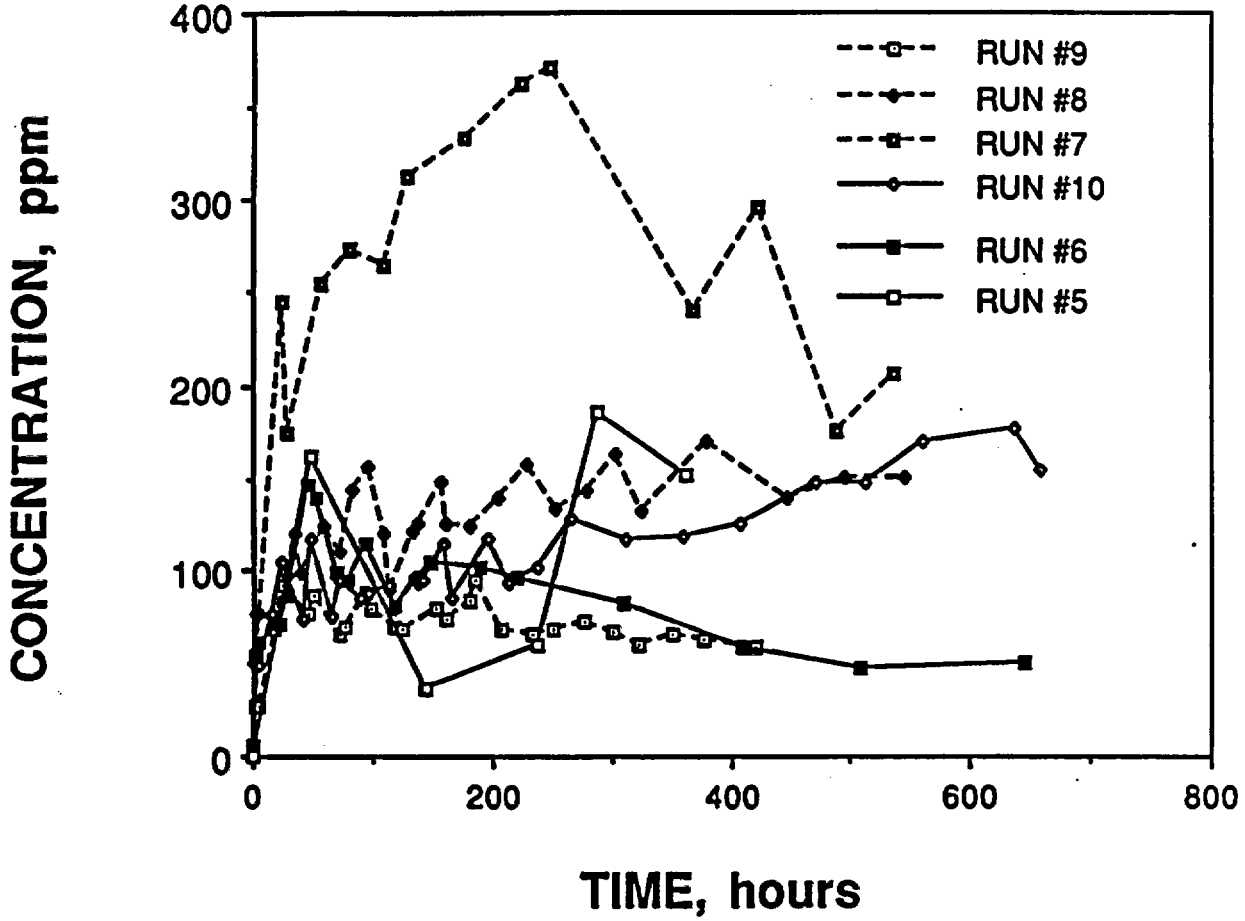
CONCENTRATION, ppm
400
300
200
100
0
0
200
400
600
800
TIME, hours
RUN #9
RUN #8
RUN #7
RUN #10
RUN #6
RUN #5

SILICA CONCENTRATIONS (ALL RUNS)

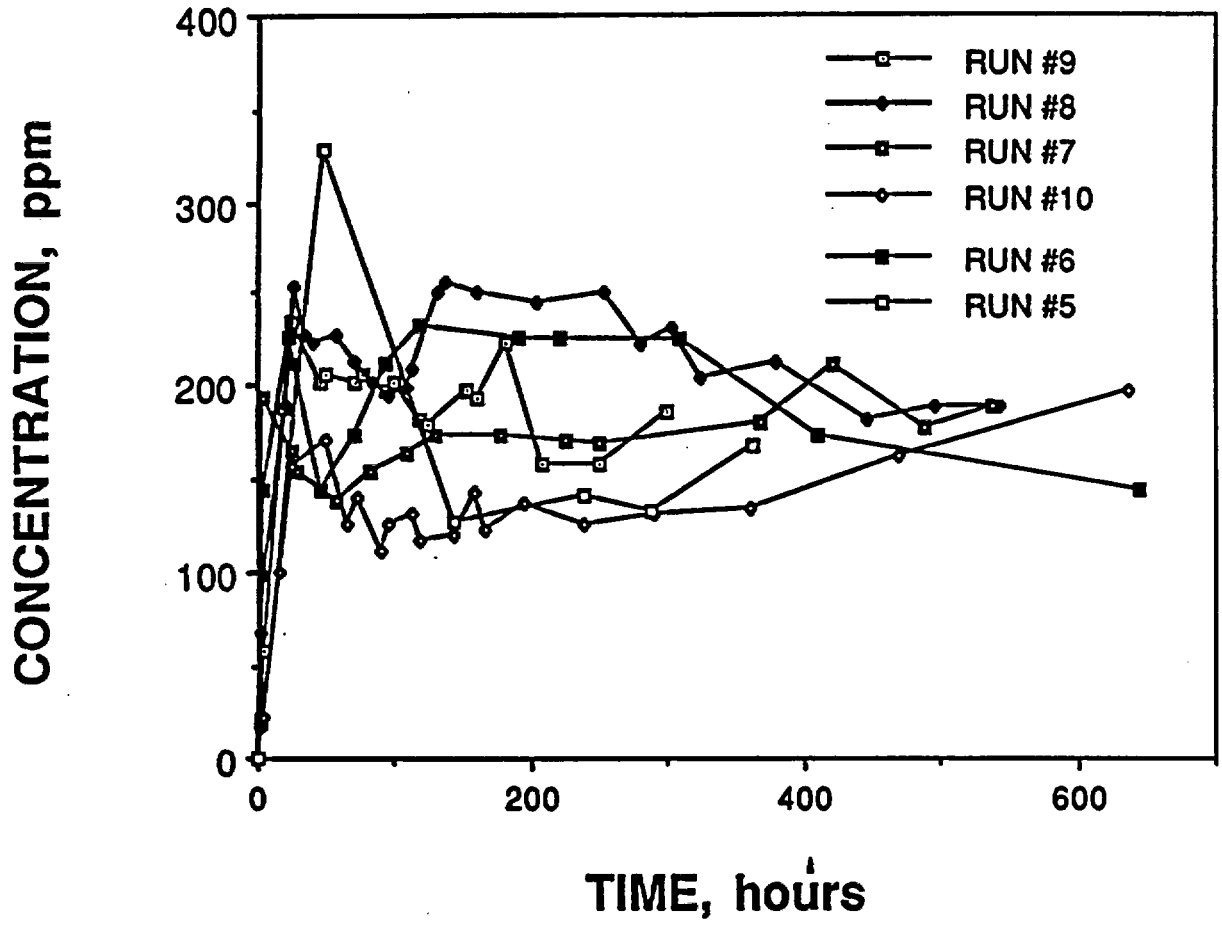

pH (ALL RUNS)

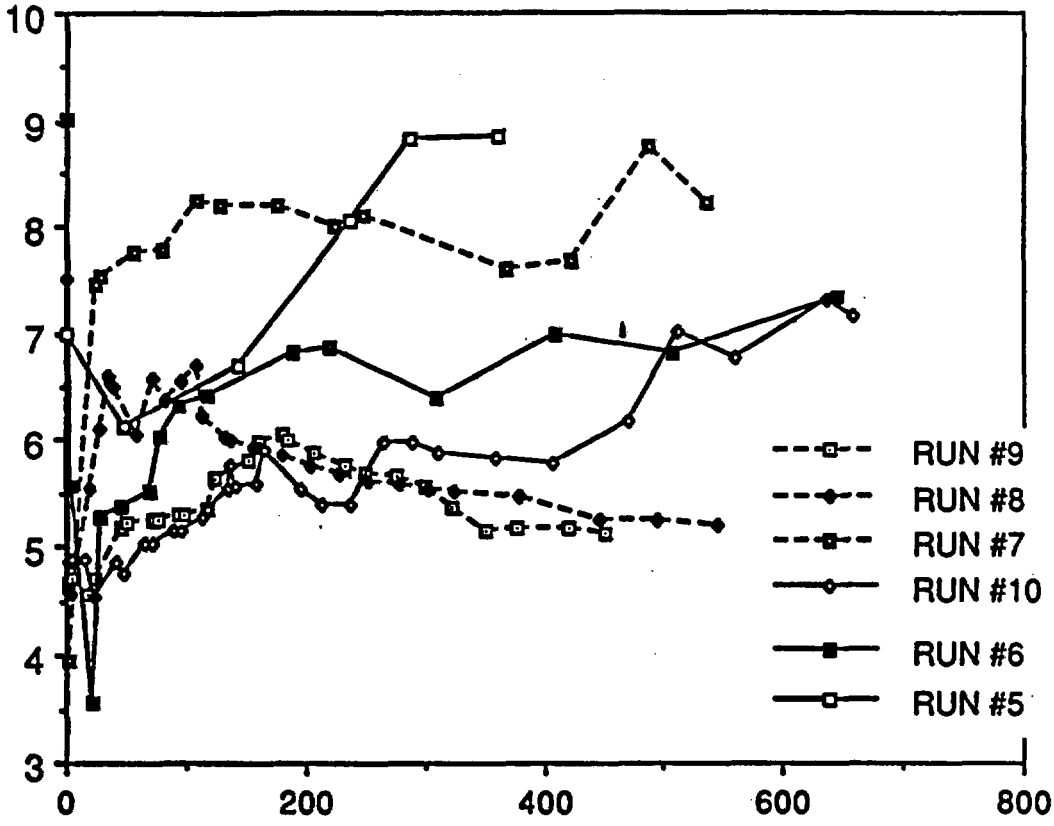
10
9
8
7
6
5
4
3
0
200
400
600
800
pH
TIME, hours
RUN #9
RUN #8
RUN #7
RUN #10
RUN #6
RUN #5